

NATURAL CONVECTION HEAT TRANSFER
WITHIN HORIZONTAL SPENT NUCLEAR
FUEL ASSEMBLIES

DISTRIBUTION OF THIS DOCUMENT IS UNLIMITED

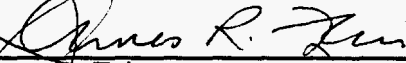


MASTER

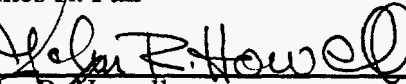
APPROVED BY
DISSERTATION COMMITTEE:



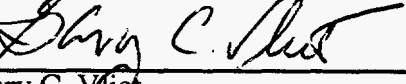
Dale E. Klein, Supervisor



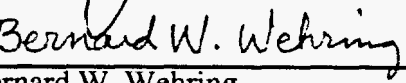
James R. Fair



John R. Howell



Gary C. Vliet



Bernard W. Wehring

DISCLAIMER

This report was prepared as an account of work sponsored by an agency of the United States Government. Neither the United States Government nor any agency thereof, nor any of their employees, makes any warranty, express or implied, or assumes any legal liability or responsibility for the accuracy, completeness, or usefulness of any information, apparatus, product, or process disclosed, or represents that its use would not infringe privately owned rights. Reference herein to any specific commercial product, process, or service by trade name, trademark, manufacturer, or otherwise does not necessarily constitute or imply its endorsement, recommendation, or favoring by the United States Government or any agency thereof. The views and opinions of authors expressed herein do not necessarily state or reflect those of the United States Government or any agency thereof.

DISCLAIMER

**Portions of this document may be illegible
electronic image products. Images are
produced from the best available original
document.**

The Government reserves for itself and others acting on its behalf a royalty free, nonexclusive, irrevocable, world-wide license for governmental purposes to publish, distribute, translate, duplicate, exhibit, and perform any such data copyrighted by the contractor.

1995

Dedication

For Linda Suzanne, my star

Always∞

**NATURAL CONVECTION HEAT TRANSFER
WITHIN HORIZONTAL SPENT NUCLEAR
FUEL ASSEMBLIES**

by

ROBERT ERNST CANAAN, B.S., M.S.

DISSERTATION

Presented to the Faculty of the Graduate School of

The University of Texas at Austin

in Partial Fulfillment

of the Requirements

for the Degree of

DOCTOR OF PHILOSOPHY

THE UNIVERSITY OF TEXAS AT AUSTIN

December, 1995

Acknowledgements

This dissertation was performed under appointment to the Office of Civilian Radioactive Waste Management (OCWRM) Fellowship program administered by the Oak Ridge Institute for Science and Education and was additionally supported by grants from Sandia National Laboratories. I would like to thank both organizations for their funding, confidence, and administrative assistance.

To Dr. Dale Klein, who is primarily responsible for orange tinting my maroon blood, I am deeply grateful for four years of sound technical advice, excellent moral support, unfailing financial assistance, and good friendship (Not to mention all the green chile parties and questionable Aggie jokes). Gig'em.

My deepest appreciation to those faculty members who served on my dissertation committee: Dr. John Howell for his open door and technical guidance; Dr. Bernard Wehring for many well taught classes and good times, Dr. Gary Vliet for keeping me on my toes, and Dr. Jim Fair for his good nature and interest in my progress.

I would also like to thank fellow graduate students and good friends: Steve Manson, Shawn Burns, Jason Butler, and Eric Triplett (Data Boy). Each of you has made major contributions to this work in many ways. I could not have done it

without you. The good times we've shared have been a highlight of my experiences in Austin.

To Sandy Taylor, your support through the years has been invaluable. I know how lucky I am to have had you on my side. Thank you.

Thanks to all those at Sandia who made my practicum experience exceptional and greatly inspired me: Ned Keltner, T.Y. Chu, Walt Gill, Larry Kent, and Dave Schulze.

I would also like to thank Dr. Lyman Bilhartz at UT Southwestern. Your technical advice and support, although not related to spent nuclear fuel heat transfer, is greatly appreciated.

And most of all, I thank my wonderful parents, Gershon and Doris Canaan. Your steadfast support, enduring confidence, and undying love are my eternal strength. I love you dearly.

**NATURAL CONVECTION HEAT TRANSFER
WITHIN HORIZONTAL SPENT NUCLEAR
FUEL ASSEMBLIES**

Publication No. _____

Robert Ernst Canaan, Ph.D.

The University of Texas at Austin, 1995

Supervisor: Dale E. Klein

Natural convection heat transfer is experimentally investigated in an enclosed horizontal rod bundle, which characterizes a spent nuclear fuel assembly during dry storage and/or transport conditions. The basic test section consists of a square array of sixty-four stainless steel tubular heaters enclosed within a water-cooled rectangular copper heat exchanger. The heaters are supplied with a uniform power generation per unit length while the surrounding enclosure is maintained at a uniform temperature. The test section resides within a vacuum/pressure chamber in order to subject the assembly to a range of pressure statepoints and various backfill gases.

The objective of this experimental study is to obtain convection correlations which can be used in order to easily incorporate convective effects

into analytical models of horizontal spent fuel systems, and also to investigate the physical nature of natural convection in enclosed horizontal rod bundles in general. The resulting data consist of: 1) measured temperatures within the assembly as a function of power, pressure, and backfill gas; 2) the relative radiative contribution for the range of observed temperatures; 3) correlations of convective Nusselt number and Rayleigh number for the rod bundle as a whole; and 4) correlations of convective Nusselt number as a function of Rayleigh number for individual rods within the array.

For the rod bundle as a whole, the data suggest the presence of conduction and convection regimes, distinguished by a critical Rayleigh number. The correlation of the convection regime suggests turbulent flow conditions. On an individual rod basis, the data indicate that rods in the lower regions of the bundle tend to preheat the ambient fluid surrounding upper rods, resulting in decreased convection up the array. Hence, Nusselt numbers tend to decrease as one considers rod positions progressively higher in the enclosed rod bundle. Furthermore, there is evidence that individual rods within the array are in different but co-existing flow regimes at a given power/pressure statepoint.

Table of Contents

List of Figures	xv
List of Tables	xxiii
Nomenclature	xxv
Chapter 1 - Introduction	1
1.1 Prologue	1
1.2 Introduction to the Management of Spent Nuclear Fuel	3
1.2.1 Overview	3
1.2.2 Spent Nuclear Fuel (SNF)	4
1.2.3 Spent Fuel Storage Requirements	6
1.2.4 Options for Increasing At-Reactor Storage Capacity	10
1.2.4.1 Pool Expansion	11
1.2.4.2 Rerack	11
1.2.4.3 Fuel Consolidation	12
1.2.4.4 Dry Storage	12
1.2.5 Transportation of SNF	14
1.2.6 Monitored Retrievable Storage (MRS)	19
1.2.7 Permanent Disposal	21
1.2.8 The Multi-Purpose Canister (MPC) System	24
1.3 Importance of SNF Thermal Analyses	28
1.4 Experimental Objectives	29
Chapter 2 - Literature Survey	31
2.1 Organization	31
2.2 Experimental Simulations of Horizontal Spent Nuclear Fuel	31
2.3 Experimental Studies of Natural Convection in Similar Geometries	42
2.4 The Present Work	54
Chapter 3 - Heat Transfer in Spent Fuel Systems	56
3.1 Introduction	56

3.2 SNF Heat Transfer Fundamentals	57
3.2.1 Spent Fuel Decay Power	57
3.2.2 Multimode Heat Transfer	61
3.2.2.1 Overview	61
3.2.2.2 Importance of Accurate Thermal Analysis	66
3.2.3 Natural Convection in Horizontal Spent Fuel Assemblies	69
3.2.3.1 The SNF Convection Debate	69
3.2.3.2 The Rayleigh and Nusselt Number	72
3.2.3.3 Factors Which Influence Natural Convection in SNF ...	74
3.2.4 Thermal Radiation in Horizontal Spent Fuel Assemblies	78
3.2.4.1 General	78
3.2.4.2 Importance of Isolating Radiation from Convection	83
3.3 Experimental Methodology for SNF Heat Transfer Measurements	87
Chapter 4 - Preliminary Analyses and Scoping Calculations	94
4.1 Overview	94
4.2 Isolated Fuel Rod	95
4.3 Natural Convection in a Horizontal Concentric Annulus	100
4.4 Convective Analysis of a Horizontal BWR Assembly	108
4.5 Radiative/Convective Analysis of a BWR Assembly Subregion	120
4.6 Axial Analysis of a Horizontal Fuel Rod	127
4.7 Summary	141
Chapter 5 - Experimental Apparatus Design Description	143
5.1 Introduction	143
5.2 The Heater Rods	146
5.2.1 General	146
5.2.2 Heater Rod Construction	152
5.2.3 Heater Rod Arrangement	156
5.2.4 End Effects Revisited	159
5.3 The Copper Boundary Enclosure	164
5.4 The Pressure Vessel and Related Components	166
5.5 The Power System	182

5.6 The Cooling System	183
5.7 The Data Acquisition and Control System (DAQCS)	185
5.8 Integrated System	193
Chapter 6 - Assembly, Configuration, and Debugging	195
6.1 Overview	195
6.2 Heater Rod Testing and Preparation	196
6.3 CuBE Preparation and Loading	197
6.4 Power System Configuration	200
6.4.1 Circuit Wiring and Grounding	200
6.4.2 Rod Power Measurement	204
6.5 DAQCS Configuration And Testing	207
6.5.1 Overview	207
6.5.2 Hardware Configuration	208
6.5.2.1 Thermocouple Wiring, Routing, and Configuration	208
6.5.2.2 Shunt Wiring, Routing, and Configuration	214
6.5.3 Software Configuration	215
6.6 Initial Testing and Debugging	222
Chapter 7 - Experimental Procedure and Data Reduction	231
7.1 Overview	231
7.2 Test Matrix	231
7.3 Experimental Procedure	234
7.4 Data Reduction	238
7.5 Looking Ahead	244
Chapter 8 - Determination of the Radiative Heat Transfer Component	245
8.1 Background	245
8.2 Numerical Computation of Thermal Radiation in Rod Arrays	247
8.2.1 Introduction	247
8.2.2 Finite Element Based Radiation Methods	248
8.2.3 Assumptions Relevant to the Applied Finite Element Model	249
8.2.4 Derivation of the Applied Finite Element Formulations	251

8.2.5	Visibility Considerations: Shadowing and Line of Symmetry	263
8.2.5.1	Shadowing	263
8.2.5.2	Line of Symmetry	267
8.2.6	Solution Procedure and Code Structure	270
8.2.6.1	Solution Procedure	270
8.2.6.2	RADERA Code Structure	272
8.3	Determination of Total Hemispherical Emissivities	274
8.3.1	Reported Emissivity for Pyromark 2500 Coated Surfaces	276
8.3.1.1	SNL Reported Emissivity Values	276
8.3.1.2	NASA Reported Emissivity Values	280
8.3.2	Summary of Reported Emissivity Values for Pyromark-2500	284
8.3.3	Experimental Measurements of Emissivity at UT	285
8.4	Benchmarking and RADERA Code Assessment	287
8.4.1	The Concentric Annulus	287
8.4.2	The Enclosed Rod Array	292
8.5	Summary	299
Chapter 9	- Uncertainty Analysis	300
9.1	General	300
9.2	Estimation of Surface Temperature Uncertainties	302
9.2.1	Individual Thermocouple Error	302
9.2.1.1	Discussion of Temperature Bias Errors	302
9.2.1.2	Discussion of Temperature Precision Error	306
9.2.1.3	Estimation of Temperature Bias Using Manufacturer Specifications	306
9.2.1.4	Estimation of Temperature Bias Using Direct Calibration	314
9.2.2	Uncertainty of the Mean Temperature of a Given Rod	317
9.2.3	Uncertainty of the Mean Temperature of All Rods in the Bundle	319
9.2.4	Uncertainty of the Mean CuBE Temperature	319
9.2.5	Uncertainty of the Individual Rod Reference Temperature	320

9.2.6	Uncertainty of the Rod Bundle Reference Temperature	320
9.3	Estimation of the Individual Rod Power Uncertainty	321
9.3.1	Estimation of Rod Power Uncertainty Using Manufacturer's Data	321
9.3.2	Estimation of Rod Power Uncertainty Using Direct Calibration	325
9.4	Estimation of System Pressure Uncertainty	329
9.5	Uncertainty of the Calculated Radiative Heat Transfer Component ...	329
9.5.1	Overview	329
9.5.2	Sequential Perturbation of RADERA Parameters	330
9.5.2.1	Emissivity Perturbation	332
9.5.2.2	Temperature Perturbation	333
9.5.2.3	Mesh Spacing Perturbation	334
9.5.2.4	Overall Radiative Uncertainty	336
9.6	Uncertainties Associated with Various Physical Parameters	337
9.6.1	Fluid Property Uncertainty	337
9.6.2	Length Scale Uncertainty	338
9.6.2.1	Uncertainty in the CuBE Height	338
9.6.2.2	Uncertainty in the Heated Rod Length	339
9.6.2.3	Uncertainty in the Heater Rod Diameter	339
9.7	Uncertainties of Non-dimensional Parameters: Rayleigh and Nusselt Number	339
9.7.1	Full Array Non-dimensional Uncertainties	340
9.7.1.1	Uncertainty of the Bundle Averaged Rayleigh Number	340
9.7.1.2	Uncertainty of the Bundle Averaged Nusselt Number	343
9.7.1.3	Uncertainty of the Peak Rod Rayleigh Number 1	344
9.7.1.4	Uncertainty of the Peak Rod Rayleigh Number 2	344
9.7.1.5	Uncertainty of the Peak Rod Nusselt Number	345
9.7.2	Individual Rod Non-dimensional Uncertainties	346
9.7.2.1	Uncertainty of the Individual Rod Rayleigh Number ..	346
9.7.2.2	Uncertainty of the Individual Rod Nusselt Number	347

9.8 Nonessential Thermocouple Measurements	348
9.9 Additional Sources of Uncertainty	351
9.10 Summary	352
Chapter 10 - Results and Discussion	354
10.1 Overview.....	354
10.2 Assembly Temperatures, Power, and Radiative Power	354
10.3 General Trends.....	360
10.4 Full Array Rayleigh/Nusselt Number Correlations	364
10.5 Individual Rod Nusselt/Rayleigh Number Correlations	371
10.6 Applications of Convective Correlations.....	381
10.6.1 General.....	381
10.6.2 The Wooten-Epstein Relationship	384
10.6.3 Comparison of Experimental Correlations to Wooten & Epstein	386
10.6.4 Other Considerations	388
Chapter 11 - Conclusions and Future Work	408
Appendix 1 - RADERA Code Listing	413
Appendix 2 - Array Temperature Data	451
Appendix 3 - Heater Rod Measured Power	493
Appendix 4 - Heater Rod Radiative Power	535
Appendix 5 - Heater Rod Resistances	577
Bibliography	578
Vita	589

List of Figures

Figure 1.1	A typical boiling water reactor (BWR) fuel assembly	5
Figure 1.2	At-reactor dry storage and shutdown reactor pool storage data	9
Figure 1.3	A typical spent nuclear fuel dry storage canister	13
Figure 1.4	Conceptual horizontal at-reactor dry storage concept	15
Figure 1.5	Babcock & Wilcox BR-100 100 ton rail/barge SNF cask	18
Figure 1.6	Cross section of the B&W BR-100 cask (52 BWR configuration)	20
Figure 1.7	General concept of a MGDS employing vertical boreholes	22
Figure 1.8	Horizontal drift emplacement concept for SNF waste packages ...	23
Figure 1.9	Adaptability of the MPC system.....	25
Figure 1.10	MPC system in storage, transportation, and disposal roles	27
Figure 2.1	BWR assembly mock-up used by Lovett (1991).....	33
Figure 2.2	Test apparatus used by Bates (1986)	36
Figure 2.3	Cross-section of test apparatus used by Klima (1975) and Sanchez & Hudson (1986).....	37
Figure 2.4	Cross-section of experimental apparatus used by Tokura <i>et. al.</i> ...	45
Figure 2.5	The effect of horizontal cylinder separation distance on the convective heat transfer of upper rods	48
Figure 3.1	Thermal energy produced by PWR and BWR fuel assemblies	58
Figure 3.2	Decay power for a single BWR fuel rod	60

Figure 3.3	The multimode heat transfer processes associated with spent fuel	62
Figure 3.4	Comparison of core radial and axial neutron flux distribution	65
Figure 3.5	Symmetry considerations associated with horizontally oriented SNF assemblies.....	67
Figure 3.6	Thermal analysis of a B&W rail cask using an effective conductivity approach.....	68
Figure 3.7	Non-uniform incident radiative flux in spent fuel assemblies.....	80
Figure 3.8	Local radiative heat transfer both to and from a given fuel rod	81
Figure 3.9	Concentric cylinders exposed to the same inner body heat flux and outer body surface temperature, but possessing different emissivities.....	85
Figure 3.10a	System dependent convection correlation	86
Figure 3.10b	Universal convection correlation (radiation subtracted).....	86
Figure 3.11	Schematic of heated rod arrangement for determination of SNF assembly heat transfer.....	88
Figure 4.1	Horizontal convecting cylinder in a quiescent environment	96
Figure 4.2	Biot number analysis for a single fuel rod in an quiescent medium	98
Figure 4.3	Concentric annulus in which the interior of the inner body is exposed to a uniform heat flux while the outer body is isothermal	101
Figure 4.4	Modeling a spent fuel rod with a uniform interior clad heat flux	103

Figure 4.5	Outer surface temperature of inner cylinder for $Ra_L=10^4$	106
Figure 4.6	Outer surface heat flux of inner cylinder for $Ra_L=10^4$	107
Figure 4.7	TEXSAN model of a BWR assembly indicating boundary conditions.....	109
Figure 4.8	Computational mesh for convective analysis of a horizontal BWR fuel assembly	112
Figure 4.9	Non-dimensional temperature, $Ra_D = 10$	114
Figure 4.10	Non-dimensional temperature, $Ra_D = 10^3$	115
Figure 4.11	Dimensionless outer surface heat flux for rod C	117
Figure 4.12	Dimensionless outer surface heat flux for rod B	118
Figure 4.13	TEXSAN model for radiative/convective analysis of a BWR assembly corner region	122
Figure 4.14	Corner rod surface temperature as a function of ϑ	124
Figure 4.15	Corner rod surface temperature variation as influenced by emissivity perturbation	126
Figure 4.16	Energy balance associated with a finite length spent fuel rod.....	129
Figure 4.17	End effects as a function of rod length (uniform axial heating) ..	130
Figure 4.18	Modified fin approach to fuel rod axial analysis	131
Figure 4.19	Limiting examples of fuel rod end support structures	136
Figure 4.20	Dimensionless surface temperature at a zircalloy fuel rod's axial midpoint as a function of rod length and end condition	138
Figure 4.21	Variation of effective infinite rod length (within 1% of infinite case) with fuel rod conductivity for $C_f=10.0$	139

Figure 5.1	Watlow Co. drawing of an uninstrumented heater rod	148
Figure 5.2	Watlow Co. drawing of a double TC instrumented heater	149
Figure 5.3	Watlow Co. drawing of a triple TC instrumented heater.....	150
Figure 5.4	Cut-away view of an instrumented heater rod	153
Figure 5.5	Manufacturing steps required for an instrumented rod.....	155
Figure 5.6	Instrumentation scheme for the UT test apparatus	157
Figure 5.7	Heater rod axial temperature profile as a function of C_f	162
Figure 5.8	Heater rod end losses as a function of total supplied power and C_f	163
Figure 5.9	End view of CuBE	167
Figure 5.10	Top/bottom wall of CuBE	168
Figure 5.11	Side wall of CuBE	169
Figure 5.12	Heater rod support plate, material: brass, quantity: two	170
Figure 5.13a	Top/bottom view of CuBE indicating inner surface mounted foil TC locations	171
Figure 5.13b	Side view of CuBE indicating inner surface mounted foil TC locations	171
Figure 5.14	Cross sectional view of CuBE midpoint, viewed from the East wall	172
Figure 5.15	Pressure vessel cut-away viewed from the North wall	176
Figure 5.16	Vessel penetrations, feedthroughs, and valves within the UT apparatus	177
Figure 5.17	Effective gas conductivity as a function of vacuum pressure.....	180
Figure 5.18	One to four line valved manifold with flow meters	184

Figure 5.19	The UT data acquisition and control system	186
Figure 5.20	The main LabVIEW® front panel for DAQCS operation.....	190
Figure 5.21	LabVIEW® strip chart for real time temperature observation	191
Figure 5.22	Front panel for power supply control and communication.....	192
Figure 5.23	The overall UT experimental apparatus	194
Figure 6.1	The fully loaded CuBE with top removed.....	199
Figure 6.2	Electrical configuration of the test apparatus	202
Figure 6.3	Heater rod electrical connections and power line nomenclature .	203
Figure 6.4	Nichrome wire resistance deviation (from $T_o = 20^{\circ}\text{C}$) as a function of temperature.....	206
Figure 6.5	Temperature measurement aspects of the UT DAQCS	209
Figure 6.6	DAQCS configuration legend for heater rod TCs [view of the assembly from the TC lead end (East end)].....	211
Figure 6.7	DAQCS configuration legend for CuBE TCs	213
Figure 6.8	LabVIEW® data acquisition program flow chart.....	217
Figure 6.9	Front panel for DAQCS configuration/timing input	218
Figure 6.10	Front panel used for single channel thermocouple calibrations ..	224
Figure 6.11a	Power supply/heater rod coupling results in amplifier saturation.....	229
Figure 6.11b	Grounding the rod sheath resolves the problem	229
Figure 7.1	Data analysis and reduction using an Excel® worksheet	239
Figure 8.1	The radiative flux vector associated with dA	252
Figure 8.2	Quantities relating the intensity to the radiative flux vector.....	254

Figure 8.3	Radiant exchange between nodes i and j in Cartesian coordinates	256
Figure 8.4	Determination of the nodal net radiative heat rate.....	263
Figure 8.5	Shadowing related visibility tests	265
Figure 8.6	Line of symmetry considerations in visibility calculations	268
Figure 8.7	RADERA algorithm structure	273
Figure 8.8	Variation of the total normal emissivity of Pyromark coated surfaces	282
Figure 8.9	Comparison of the radiant flux of a Pyromark coated SS-321 surface with Lambert's Cosine Law for diffuse emission.....	283
Figure 8.10	Arrangement for experimental emissivity measurement using an IR camera	286
Figure 8.11	The concentric annulus benchmark problem	288
Figure 8.12	RADERA model for radiative transport analysis	294
Figure 9.1	Temperature measurement system schematic depicting sources of potential error	303
Figure 9.2	Thermocouple mounting error associated with instrumented heaters	308
Figure 9.3	Circuit representation of heater rod power calibration experiment	326
Figure 10.1	Sample page from Appendix 2	357
Figure 10.2	Sample page from Appendix 3	358
Figure 10.3	Sample page from Appendix 4	359
Figure 10.4	Maximum array ΔT variation with pressure (Nitrogen backfill)	361

Figure 10.5	Maximum array ΔT variation with pressure (Helium backfill) ...	361
Figure 10.6	Radiative contribution over the range of experimental conditions.....	363
Figure 10.7	Rod bundle convective Nusselt Number based upon ΔT_{max} ($Ra_Q = f(Q'_c)$).....	365
Figure 10.8	Rod bundle convective Nusselt Number based upon ΔT_{max} ($Ra_{max} = f(\Delta T_{max})$).....	367
Figure 10.9	Rod bundle convective Nusselt Number based upon ΔT_b ($Ra_b = f(\Delta T_b)$).....	368
Figure 10.10	Convective Nusselt Number for Rod D8.....	391
Figure 10.11	Convective Nusselt Number for Rod D7.....	391
Figure 10.12	Convective Nusselt Number for Rod D6.....	392
Figure 10.13	Convective Nusselt Number for Rod D5.....	392
Figure 10.14	Convective Nusselt Number for Rod D4.....	393
Figure 10.15	Convective Nusselt Number for Rod D3.....	393
Figure 10.16	Convective Nusselt Number for Rod D2.....	394
Figure 10.17	Convective Nusselt Number for Rod D1.....	394
Figure 10.18	Convective Nusselt Number for Rod C8.....	395
Figure 10.19	Convective Nusselt Number for Rod C7.....	395
Figure 10.20	Convective Nusselt Number for Rod C6.....	396
Figure 10.21	Convective Nusselt Number for Rod C5.....	396
Figure 10.22	Convective Nusselt Number for Rod C4.....	397
Figure 10.23	Convective Nusselt Number for Rod C3.....	397
Figure 10.24	Convective Nusselt Number for Rod C2.....	398

Figure 10.25	Convective Nusselt Number for Rod C1	398
Figure 10.26	Convective Nusselt Number for Rod B8	399
Figure 10.27	Convective Nusselt Number for Rod B7	399
Figure 10.28	Convective Nusselt Number for Rod B6	400
Figure 10.29	Convective Nusselt Number for Rod B5	400
Figure 10.30	Convective Nusselt Number for Rod B4	401
Figure 10.31	Convective Nusselt Number for Rod B3	401
Figure 10.32	Convective Nusselt Number for Rod B2	402
Figure 10.33	Convective Nusselt Number for Rod B1	402
Figure 10.34	Convective Nusselt Number for Rod A8	403
Figure 10.35	Convective Nusselt Number for Rod A7	403
Figure 10.36	Convective Nusselt Number for Rod A6	404
Figure 10.37	Convective Nusselt Number for Rod A5	404
Figure 10.38	Convective Nusselt Number for Rod A4	405
Figure 10.39	Convective Nusselt Number for Rod A3	405
Figure 10.40	Convective Nusselt Number for Rod A2	406
Figure 10.41	Convective Nusselt Number for Rod A1	406
Figure 10.42	Predicted velocity vectors for a horizontal BWR assembly, $Ra \approx 10^3$	407

List of Tables

Table 1.1	Dry storage requirements before 1998	7
Table 1.2	Spent fuel pools and SNF storage at reactors shutdown before 1998	8
Table 3.1	Comparative fuel rod heat fluxes for active and spent fuel	61
Table 3.2	Dimensions of typical LWR fuel	63
Table 4.1	Sensitivity of results to variation in surface emissivity, $(Ra_D = 1,400, T_h = 200^\circ\text{C} \text{ \& } T_C = 160^\circ\text{C})$	125
Table 5.1	Thermal conductivity of UT heater rods and actual BWR fuel (W/m-K averaged from 200 °C to 1000 °C)	146
Table 5.2	Heater rod specifications	151
Table 5.3	UT experimental assembly dimensions	158
Table 5.4	Percentage end loss as a function of C_f	164
Table 5.5	Pressure vessel specifications	174
Table 7.1	The primary experimental test matrix	232
Table 7.2	Supplementary test matrix	233
Table 8.1	SNL measurements of total hemispherical emissivity for a Pyromark coated mild steel substrate	279
Table 8.2	Concentric annulus analysis using RADERA with $\theta_o = 0.5$ and $\varepsilon = 0.5$	290
Table 8.3	Concentric annulus analysis with $\theta_o = 0.2$ and $N_i=29$	290
Table 9.1	TC mounting bias for instrumented heater rods	309

Table 9.2	Results of thermocouple calibration for selected channels.....	316
Table 9.3	Results of heater rod power calibration for selected rods.....	328
Table 9.4	Difference quantities for the perturbation of emissivity	332
Table 9.5	Difference quantities for the perturbation of temperature	334
Table 9.6	Difference quantities corresponding to the mesh spacing	335
Table 9.7	Overall maximum and average RADERA calculated uncertainties	336
Table 9.8	Symmetry TC measurements (temperature differences shown), averaged over all datasets	349
Table 9.9	Temperature differences between midpoint and axially offset TCs, averaged over all datasets	350
Table 10.1	Ra_{max} at atmospheric pressure (101.3kPa) and $T_{f,b} = 400K$	370
Table 10.2	Convective Nusselt number correlations for rods in column D ..	372
Table 10.3	Convective Nusselt number correlations for rods in column C...373	
Table 10.4	Convective Nusselt number correlations for rods in column B...374	
Table 10.5	Convective Nusselt number correlations for rods in column A ..375	
Table 10.6	Wooten and Epstein predictions of T_{max} for selected data (percent error given)	386
Table 10.7	Comparison of UT experimental correlations to Wooten- Epstein	388
Table A5.1	Heater rod resistances by array position (Ω)	577

Nomenclature

A_s	Surface area
A_c	Cross-sectional area
B	Bias error
Bi	Biot number, $Bi = \frac{hD}{k}$
c_p	Specific heat at constant pressure
C_f	Area correction factor
D	Diameter of a heater rod
e	Percentage error
E	Emissive power
E_q	A matrix of vectors representing the direct emission configuration factors
F_{cond}	Conduction factor, [see Manteufel, (1991)]
g	Gravitational acceleration
h	Convective heat transfer coefficient for each rod, $h = \frac{q'_c}{\pi D \Delta T}$
h_b	Convective heat transfer coefficient for the rod bundle, based upon the mean temperature difference for the bundle, $h_b = \frac{Q'_c}{4H \Delta T_b}$

- h_{max} Convective heat transfer coefficient for the rod bundle, based upon the maximum temperature difference for the bundle, $h_{max} = \frac{Q_c'}{4H \Delta T_{max}}$
- H Height of enclosure
- i Current or radiation intensity
- k Thermal conductivity
- k^* Dimensionless thermal conductivity
- k_{eff} Effective thermal conductivity
- k_{cond} Effective thermal conductivity for conduction/convection
- k_{rad} Effective thermal conductivity for radiation
- L Characteristic length
- L_h Heated rod length
- M Molecular weight or total number of surfaces in a numerical model
- \hat{n} Surface normal vector
- N Total number of nodes in a numerical model
- N_d Total number of independent data points
- N_{rods} Number of rods in an array
- Nu Convective Nusselt number for each rod, $Nu = \frac{hD}{k_f}$

- Nu_b Convective Nusselt number for the rod bundle, based upon h_b ,

$$Nu_b = \frac{h_b H}{k_f}$$
- Nu_{max} Convective Nusselt number for the rod bundle, based upon h_{max} ,

$$Nu_{max} = \frac{h_{max} H}{k_f}$$
- p System pressure
- P Rod pitch or precision error
- Pr Prandtl number
- q Rod power
- q' Rod power per unit length, $q' = \frac{q}{L_h}$
- q'_c Rod power per unit length due to convection, $q'_c = q' - q'_{r,net}$
- $q'_{r,net}$ Rod power per unit length due to radiation
- q'' Heat flux
- q''_r Radiative flux vector
- q^* Dimensionless heat flux
- Q Total rod bundle power
- Q' Total rod bundle power per unit length, $Q' = \frac{Q}{L_h}$
- Q'_c Total rod bundle power per unit length due to convection, $Q'_c = Q' - Q'_{r,net}$
- $Q'_{r,net}$ Total rod bundle power per unit length due to radiation

- r radius
- \mathbf{r} A three dimensional vector
- r^* Dimensionless radius
- R Heater rod resistance or dimensionless radius as defined
- \bar{R}_q A matrix of tensors representing the indirect reflection configuration factors
- Ra Rayleigh number for each rod, $Ra = \frac{g\beta \Delta T D^3}{\nu\alpha}$
- Ra_b Rayleigh number for the rod bundle, based upon ΔT_b ,
 $Ra_b = \frac{g\beta \Delta T_b H^3}{\nu\alpha}$
- Ra_{max} Rayleigh number for the rod bundle, based upon ΔT_{max} ,
 $Ra_{max} = \frac{g\beta \Delta T_{max} H^3}{\nu\alpha}$
- Ra_Q Rayleigh number for the rod bundle, based upon Q'_c ,
 $Ra_Q = \frac{g\beta Q'_c H^4}{4H \nu\alpha k_f}$
- Ra_{cr} Critical Rayleigh number
- s A two dimensional vector in the S direction
- \hat{s} Unit vector in the S direction, $\hat{s} = \frac{s}{S}$
- s Rod to enclosure gap width
- S_f Standard deviation

- T_C Mean temperature of the enclosure
- T_f Reference temperature for fluid property evaluation (individual rod),

$$T_f = \frac{T_r + T_C}{2}$$
- $T_{f,b}$ Reference temperature for fluid property evaluation (rod bundle),

$$T_{f,b} = \frac{T_{r,b} + T_C}{2}$$
- T_r Mean temperature of a given rod
- $T_{r,b}$ Mean temperature of all rods in the bundle
- T_{ref} Convective reference temperature
- T_s Surface temperature
- T_{sur} Surroundings temperature
- ΔT Characteristic temperature difference (individual rod), $\Delta T = T_r - T_C$
- ΔT_b Characteristic temperature difference (mean rod bundle), $\Delta T_b = T_{r,b} - T_C$
- ΔT_{max} Characteristic temperature difference (maximum rod bundle),

$$\Delta T_{max} = T_{max} - T_C$$
- v Fluid velocity
- V Voltage

Greek Symbols

- α Thermal diffusivity, $\alpha = \frac{k}{\rho c_p}$; or temperature coefficient of resistance
- β Coefficient of thermal expansion

δ	Cladding thickness
$\delta x, \Delta x$	Uncertainty in variable x , as defined
ε	Total hemispherical emissivity
μ	absolute viscosity
ν	Kinematic viscosity, $\nu = \frac{\mu}{\rho}$
φ	Angle between the surface normal and a given unit vector
ρ	density or total hemispherical reflectivity
Ψ	Finite element basis function
σ	Stefan-Boltzmann constant or Seebeck coefficient
ϑ	Circumferential rod angle
θ, θ^*	Dimensionless temperature or excess temperature as defined
ω	Solid angle
$\partial\Omega$	Region of the computational domain

Subscripts

b	Rod bundle
bb	Black body
c	Convective or cladding value
cal	Calibration value

<i>ch</i>	Characteristic value
<i>cr</i>	Critical value
<i>C</i>	Enclosure value
<i>DAQ</i>	Data acquisition and control system value
<i>DMM</i>	Digital multimeter obtained value
<i>f</i>	Reference value or fluid property
<i>h</i>	'Hot' value as defined
<i>i</i>	Inner surface value
<i>int</i>	Internal value
<i>ij</i>	Nodal quantities
<i>inf</i>	Infinite case value
∞	Ambient value
<i>loss</i>	Axial end loss component
<i>max</i>	Maximum value
<i>n</i>	normal component
<i>o</i>	Outer surface value or nominal value
<i>r</i>	Heater/fuel rod or radiative
<i>s</i>	Surface value
<i>sur</i>	Surroundings value

tc Thermocouple junction value
1, 2 Refers to specific regions of data

Superscripts

p Perturbed value
" units of inches or a nodal quantity

Acronyms and Abbreviations

AC Alternating Current
A/D Analog to Digital
ASME American Society of Mechanical Engineers
B&W Babcock and Wilcox Company
BWR Boiling Water Reactor
CFR Code of Federal Regulations
CPU Central Processing Unit
CuBE Copper Boundary Enclosure
DAQCS Data Acquisition and Control System
DC Direct Current
DMM Digital Multimeter
DOE U.S. Department of Energy
emf Electromotive force

GPIB	General Purpose Interface Bus
GW-d	Giga-watt • days
IR	Infra-Red
LMFBR	Liquid Metal Fast Breeder Reactor
LSB	Least Significant Bit
LWR	Light Water Reactor
LWT	Legal Weight Truck
MAC	Apple® Macintosh® Personal Computer
MGDS	Mined Geologic Disposal System
MIMS	Mineral Insulated Metal Sheath
MPC	Multi-Purpose Canister
MRS	Monitored Retrievable Storage Facility
MTIHM	Mega-tons of initial heavy metal (uranium)
MUX	Multiplexer
NASA	National Aeronautics and Space Administration
NBS	National Bureau of Standards
NI	National Instruments
NIST	National Institute for Standards and Technology (formerly NBS)
NPT	National Pipe Thread

NRC	Nuclear Regulatory Commission
NWPA	Nuclear Waste Policy Act
ORNL	Oak Ridge National Laboratory
PC	Personal Computer
PGIA	Programmable Gain Instrumentation Amplifier
PWR	Pressurized Water Reactor
RADERA	Radiation in Enclosed Rod Arrays algorithm
R/B	Rail/Barge
RSS	Root-Sum-Square
SCXI	Signal Conditioning Extensions for Instrumentation
SNL	Sandia National Laboratories
TC	Thermocouple
USCEA	United States Center for Energy Awareness
UT	The University of Texas at Austin
VI	Virtual Instrument

Chapter 1 - Introduction

1.1 PROLOGUE

For nearly forty years nuclear power in the United States has demonstrated that it can provide substantial resources of energy in a safe, technically sound manner. The United States has come to rely upon nuclear energy as a significant source of electricity, second only to coal. Its potential benefits with regard to environmental issues have further established its value as a vital national energy source. However, the general public remains worried over the safety of nuclear power, despite the fact that no human death can be attributed to radiation produced by U.S. commercial nuclear power plants, including the Three Mile Island incident. One of the key reasons for public concern over nuclear power in this country stems from a fear of the potential hazards of nuclear waste. Critics of our government's plans to site a high level nuclear waste repository have charged that the project is grossly mismanaged and technically unfeasible. They maintain that the safe disposal of such waste is a problem which cannot be solved. Interestingly enough, extensive studies by our nation's foremost geologists, hydrologists, and engineers conclude just the opposite - that the safe storage and disposal of nuclear waste is in fact a tractable technical problem. The issue seems political, not technological.

Nevertheless, there are technological issues which have yet to be fully resolved, and which will continue to require considerable focus in the coming years. The intent of this dissertation is to address a technological concern associated with the storage, transportation, and ultimate disposal of a form of high-level nuclear waste known as spent nuclear fuel. Spent nuclear fuel, or SNF, consists of used nuclear fuel assemblies which are regularly discharged from commercial nuclear power reactors. The forthcoming discussions and analyses focus upon the characterization of SNF from a *thermal* standpoint. In particular, the natural convection heat transfer process is experimentally investigated in a SNF assembly mock-up. The objective of this study is to obtain convection correlations which can be used in order to easily incorporate convective effects into numerical models of horizontal spent fuel systems, and also to investigate the physical nature of natural convection in enclosed horizontal rod bundles in general. Specifically, questions have arisen regarding the importance of natural convection heat transfer in SNF geometries. The natural convection process may play a key role in the passive cooling of SNF during transportation and disposal and therefore is a significant design consideration.

However, before delving into the details of this topic, it will be useful to provide an overview of spent fuel management practices in this country, both presently and in the foreseeable future. The technological and political issues which affect the management of SNF will be reviewed in the remaining sections of this chapter. Furthermore, the case for a sound thermal characterization of SNF

will be made, and a more detailed statement of experimental objectives will follow.

1.2 INTRODUCTION TO THE MANAGEMENT OF SPENT NUCLEAR FUEL

1.2.1 Overview

When commercial nuclear power plants were first constructed in the United States, plans called for the recycling, or reprocessing, of spent nuclear fuel. Reprocessing not only allows recovery of the valuable fissile fuel components, but also significantly reduces the concentration of long-lived radioactive isotopes in the waste stream, greatly simplifying the disposal process and long term safety. However, during the Carter Administration, plans for reprocessing were scuttled, despite the fact that in other countries, such as France and Great Britain, nuclear fuel continues to be successfully reprocessed. Although the U.S. reprocessing ban was recalled during the Reagan Administration, the economic and political tide had already been turned against reprocessing. As a result, there has been a steady increase in the volume of high level nuclear waste, namely SNF, to be permanently disposed, and the nation's nuclear utilities are faced with an interim storage need for spent fuel. Current plans rely upon the opening of an interim storage site, or monitored retrievable storage facility (MRS), in order to accept SNF ultimately bound for permanent disposal. An MRS should not be expected before the year 2000. The Nuclear Waste Policy Act of 1982 (NWPA) specifies that the mode of permanent disposal will be in a subterranean repository, or Mined Geologic Disposal System (MGDS). Although the NWPA initially

required federal government acceptance of SNF by January 31, 1998, a MGDS is not expected before 2010.

1.2.2 Spent Nuclear Fuel (SNF)

Nuclear fuel material is contained in fuel assemblies, which consist of a large array of individual fuel rods. Each fuel rod consists of an outer shell of zirconium alloy cladding which contains the uranium dioxide fuel as well as any radioactive fission products. Typically, the fuel rods are arranged in a square array separated by axially offset rod spacer grids, resulting in an approximate pitch-to-diameter ratio (P/D) of 1.3. In the case of a boiling water reactor (BWR) fuel assembly (Figure 1.1), the square array of fuel rods consists of an eight row by eight column matrix and is enclosed by a square fuel channel. Pressurized water reactor (PWR) assemblies are larger, generally consisting of square arrays ranging from 15 X 15 to 17 X 17 rods. A typical light water reactor (LWR) core consists of approximately 200 nuclear fuel assemblies.

During the course of power production, fissile isotopes within the fuel such as U^{235} undergo nuclear fission, leaving behind radioactive fission products such as barium, cesium, zirconium, and niobium, among others. Eventually, as these fission products build up in the fuel and the number of U^{235} atoms is decreased by the fission process, the nuclear chain reaction can no longer be sustained and the reactor will shut down for refueling. The nuclear fuel is normally removed when it has reached an average burnup of about 35,000 MWD/MT (MW-Day per Metric Ton of total uranium) and thus becomes a

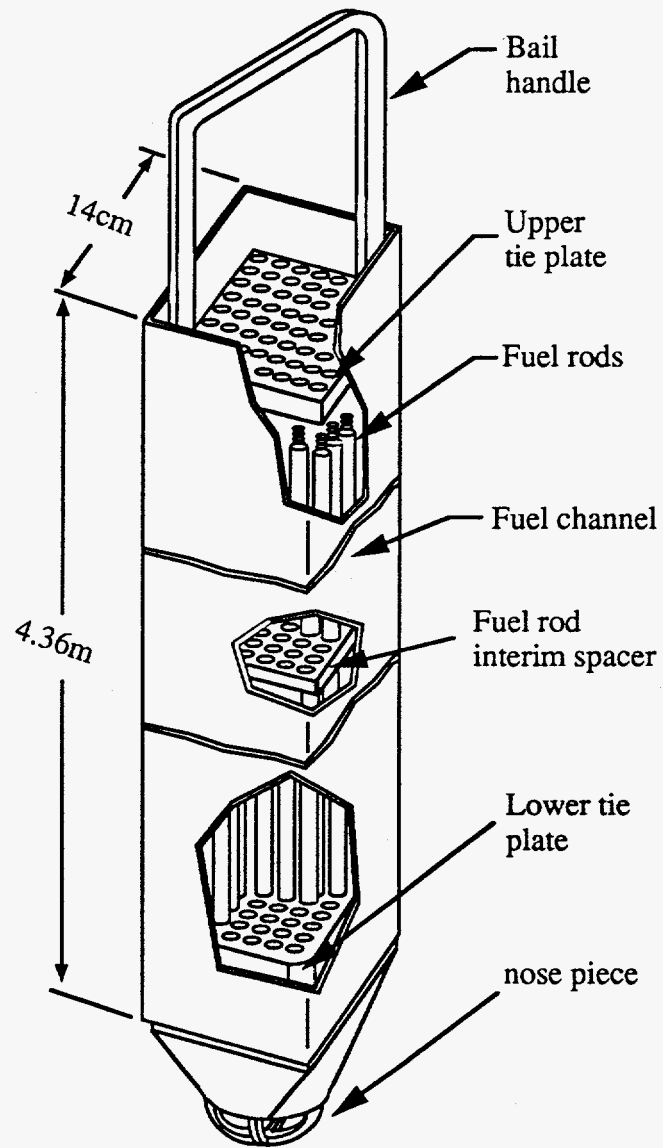


Figure 1.1 A typical boiling water reactor (BWR) fuel assembly

"spent" fuel. Since SNF contains a significant concentration of radioactive fission products, it is both radioactively and thermally "hot", and therefore must continue to be cooled following its removal from the reactor core. This is accomplished by directly placing the spent fuel assemblies in specially treated, water filled pools lined with concrete and steel. Water not only cools the SNF but also acts as a natural barrier to shield workers from radiation.

1.2.3 Spent Fuel Storage Requirements

Although essentially all SNF is currently stored on-site (at-reactor) in spent fuel pools, this is not intended to be a permanent solution. Presently, the federal government is legally required to take responsibility for SNF in 1998, although the timeline is not likely to be met. The earliest date at which SNF could be accepted by an interim facility, such as an MRS, is the year 2000. The permanent disposal of such waste in a MGDS will not occur before 2010. In the meantime, reactor cooling pools across the country are rapidly reaching capacity. When many U.S. commercial plants were first built, spent fuel pools were typically designed to hold only two to three cores, because at that time reprocessing was expected within a few years of discharge. It is presently estimated that before 1998, 20 spent fuel storage pools will have reached their maximum capacity and will require additional storage capacity, such as at-reactor dry storage. Dry storage involves heavy concrete or steel containers, called dry casks, placed on a concrete pad or in a concrete bunker above-ground at the reactor site. Like pool storage, dry storage has been proven safe but is not

intended to be a permanent solution for waste disposal. Table 1.1 presents the list of pools and the total number of SNF assemblies requiring at-reactor dry storage before 1998 (Emami, *et al.*, 1994).

Table 1.1 Dry storage requirements before 1998

Pool Name	Fuel Type	Number of Assemblies
Arkansas Nuclear 1	PWR	48
Arkansas Nuclear 2	PWR	48
Calvert Cliffs 1, 2	PWR	264
Pilgrim	BWR	85
Brunswick 1	BWR	468
Robinson 2	PWR	128
Big Rock 1	BWR	34
Palisades	PWR	168
Oconee 1, 2	PWR	648
Oconee 3	PWR	168
Oyster Creek	BWR	156
Maine Yankee	PWR	24
Nine Mile Point	BWR	312
Milestone 1	BWR	52
Prairie Island 1, 2	PWR	288
Fort Calhoun	PWR	70
Limerick 1, 2	BWR	156
Davis-Besse	PWR	48
Surry 1, 2	PWR	592
Point Beach 1, 2	PWR	96

Furthermore, it is expected that before 1998, ten reactor facilities will be shutdown. Each of the shutdown reactor pools is anticipated to have a number of SNF assemblies stored in the pool after shutdown, including the last core load. Table 1.2 lists the pools which will require reactor shutdown before 1998, and the number of SNF assemblies each pool is expected to contain (Emami, *et al.*, 1994).

Table 1.2 Spent fuel pools and SNF storage at reactors shutdown before 1998

Pool Name	Fuel Type	Number of Assemblies
Indian Point 1	PWR	160
Lacrosse	BWR	333
Three Mile Island	PWR	b
Shoreham	BWR	560
Humboldt Bay	BWR	390
Trojan	PWR	c
Fort St. Vrain	HTGR ^a	a
Rancho Seco	PWR	493
San Onofre 1	PWR	256
Yankee-Rowe	PWR	533

Notes:

- a) High Temperature Gas Reactor (HTGR) fuel, requires different storage technology
- b) SNF stored at the Idaho National Engineering Laboratory
- c) Not available

The question remains, what will happen to SNF after 1998? Figure 1.2 shows aggregate at-reactor dry storage data for a system in which the federal

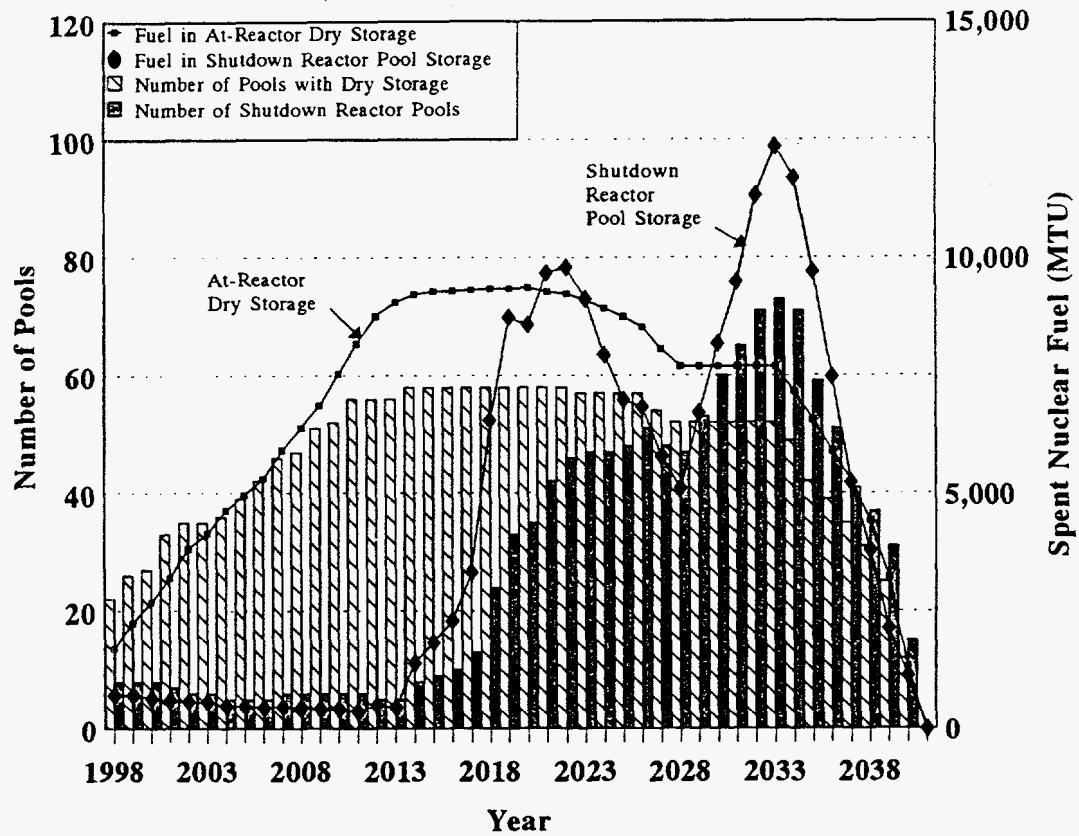


Figure 1.2 At-reactor dry storage and shutdown reactor pool storage data
[from Emami, et. al., (1994)]

government begins picking up SNF from the reactor sites in the year 2000. This figure depicts 1) the total metric tons uranium (MTU) of SNF requiring at-reactor dry storage, 2) the total MTU of SNF in spent fuel pools at shutdown reactors, 3) the total number of spent fuel pools requiring dry storage, and 4) the total number of pools associated with shutdown reactors. These data are evaluated from 1998 until the time all SNF has been removed from the reactor sites. It has been assumed that the SNF already in dry storage prior to 1998 will continue to be stored in that manner. Furthermore, the data of Figure 1.2 assumes that a MRS begins operations in the year 2000 and that the MGDS begins operations in 2010. The steady state throughput rates for these scenarios, as well as the storage capacities of the MRS and MGDS, are based upon projections made by TRW Environmental Safety Systems Inc. (1993). The assumption for the total amount of SNF projected to be discharged is based on Department of Energy (DOE) data contained in *Spent Fuel Storage Requirements 1992-2036* (1993), which assumes no new nuclear plant orders and no plant life-time extensions. The figure indicates that the need for at-reactor dry storage of SNF is expected to rise sharply over the next decade, even with a MRS and a MGDS facility in place. The following section will discuss the options that nuclear utilities have in order to address their at-reactor storage requirements.

1.2.4 Options for Increasing At-Reactor Storage Capacity

Many of the early reactors in this country were built such that their spent fuel cooling pools could only accommodate two to three cores. While more recent

reactors have incorporated larger cooling pools in their designs, it is inevitable that all reactors must develop options for increasing their at-reactor storage capacities. Several options have been considered. These are to expand existing pool storage, rerack the pool, consolidate fuel, and develop on-site dry storage.

1.2.4.1 Pool Expansion

Pool expansion refers to building another pool or expanding an existing one. This approach requires the least development, as water pool storage is well-accepted and proven technology. However, this option is very expensive and often unfeasible due to space limitations.

1.2.4.2 Rerack

Because of early Nuclear Regulatory Commission (NRC) conservatism and the unforeseen need for large storage capacity, nuclear fuel assemblies were initially stored on 53cm (21in) centers in the pools. However, experience in spent fuel storage and improved calculation techniques have demonstrated that plants may increase their storage capacity by changing to storage racks with closer spacings, such as 23cm (9in) centers. This "reracking" still allows plants to meet their seismic requirements and accommodate the additional floor loadings. Furthermore, by taking into account the burnup of the fuel, and adding additional neutron poisons to the rack material, the sub-criticality of the reracked system is ensured. Such schemes make it possible to store five times as much fuel in the same storage pool (Tang & Saling, 1990).

1.2.4.3 Fuel Consolidation

In fuel consolidation, the fuel assembly is dismantled and the spent fuel rods are rearranged into a hexagonal close-packed geometry in which the rods are essentially in contact ($P/D=1$). Demonstrations of fuel consolidation have shown that a two-to-one reduction in storage space can be safely made. Fuel consolidation in conjunction with the use of high-density racks allows a pool storage density of up to 1.02MTU per square foot for PWR fuel and up to 1.25MTU per square foot for BWR fuel (Tang & Saling, 1990).

1.2.4.4 Dry Storage

Despite the increase in pool storage capacity offered by the above options, many utilities have had to develop dry storage options. And as Figure 1.2 indicates, the need for at-reactor dry storage is expected to increase considerably. In dry storage, the SNF is stored in a shielded container outside the reactor containment building. Figure 1.3 illustrates a typical dry storage container, or cask, in which a number of fuel assemblies can be stored (Bahney, 1993). The primary internal features of such a cask include the fuel basket, a grid-like structure which separates individual fuel assemblies. The basket performs a number of important functions, including a high conductivity heat conduction pathway, criticality control (boron is incorporated in the basket), and structural support. The basket is surrounded by one or more layers of corrosion resistant material, which also provides for radiation shielding. Typically, the cask is filled

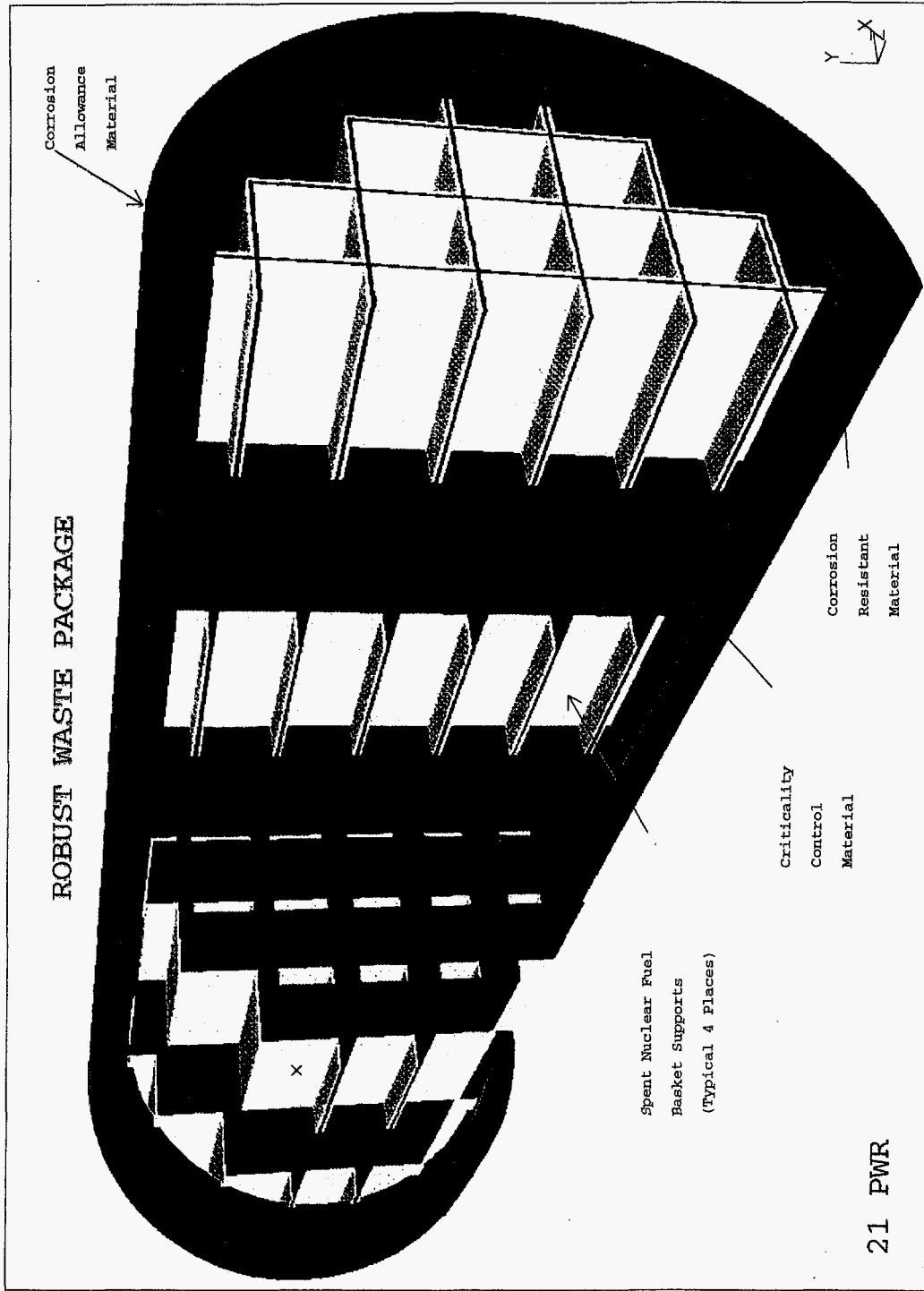


Figure 1.3 A typical spent nuclear fuel dry storage canister, [from Bahney, (1993)]

with an inert gas such as helium or nitrogen, is sealed, and placed on a concrete pad or above-ground bunker as shown in Figure 1.4.

The storage of SNF is governed by the regulatory requirements established in 10CFR part 72 (Code of Federal Regulations). These regulations are similar to those imposed upon transportation casks; however, they are less stringent. Two key provisions of 10CFR72 include:

- 1) Storage casks must survive intact a drop test from 1.8m (6ft) onto an unyielding surface.
- 2) The maximum fuel rod cladding temperature must be maintained below 385°C (725°F) while stored under an inert atmosphere.

Recently, at-reactor dry storage facilities have been developed at the Prairie Island and Point Beach plants, allowing them to continue operation until a permanent solution to the high level waste problem can be enacted.

1.2.5 Transportation of SNF

It seems inevitable that SNF will one day be transported from reactor facilities to a centralized storage/disposal site, either an MRS or MGDS. Pool storage and/or at-reactor dry storage are not intended to be permanent SNF disposal sites. According to the NWPA of 1982, and its 1987 amendment, the DOE will take title to SNF at commercial power reactor sites and transport it to federally owned and operated storage or disposal facilities. Already, over the past

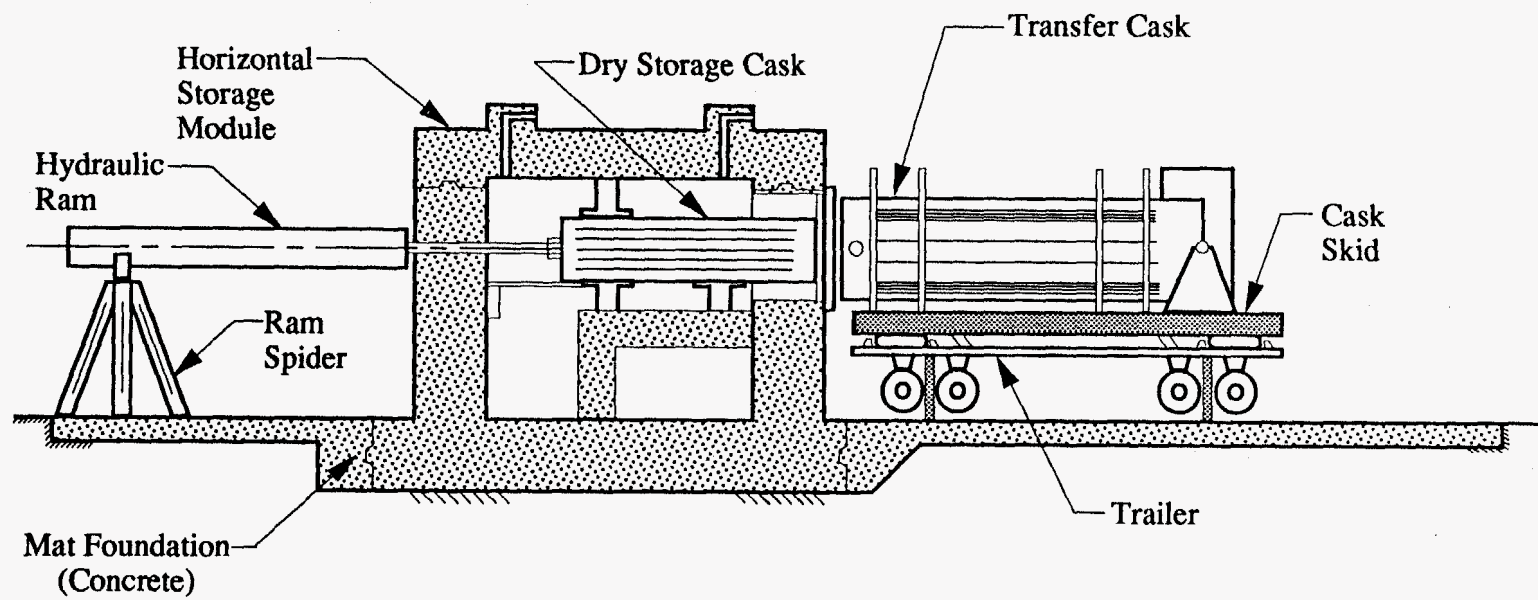


Figure 1.4 Conceptual horizontal at-reactor dry storage concept

25 years, more than 2500 shipments of SNF (primarily non-commercial sources) have been transported safely over America's highways, waterways, and railroads. An exemplary safety record has been established with regard to these shipments, with no fatalities, injuries, or environmental damage caused by the radioactive nature of the cargo. One of the primary reasons for this success is attributable to the design and construction of SNF shipping or transportation casks. Each shipping cask is designed to maintain its integrity under routine transportation conditions as well as during severe accidents. The casks must ensure radiological safety even after being subjected to the NRC's hypothetical accident conditions. These tests, which are administered in sequence include:

- 1) A 9m (30ft) free fall onto an unyielding surface
- 2) A puncture test allowing the cask to free-fall 1m (40in) onto a steel rod 15cm (6in) in diameter
- 3) A 30 minute, all-engulfing fire at 802°C (1475°F)
- 4) An 8 hour immersion under 0.9m (3ft) of water

These regulations are given under 10CFR part 71, which also includes the following provisions:

- 1) The radiation level at any point on the external surface of the shipping cask during transport may not exceed 200mrem/h and also may not exceed 10mrem/h at 2m (6.6ft) from that surface.

- 2) The maximum accessible surface temperature of the waste package during transport is limited to 82°C (180°F).
- 3) The maximum allowed fuel basket temperature is 177°C (350°F).
- 4) The peak fuel cladding temperature during transport is limited to 360°C (680°F).

The thermal limits, listed above for the various shipping cask components, must be met for the 10CFR71 requirement of a 38°C (100°F) ambient temperature day with insolation of 388 W/m² and a fuel payload generating the maximum heat credible within the bounds of expected transport conditions. During normal operation, the casks are pressurized with an inert gas to a value slightly less than atmospheric. The maximum internal pressure is that which would result if all fuel rods ruptured [$< 0.69\text{MPa}$ (100psig)]. Such an event is highly unlikely but has been used in order to establish highly conservative design requirements.

Currently, transportation cask activities are focusing on developing legal weight truck (LWT) casks and rail/barge (R/B) casks. Figure 1.5 illustrates the Babcock & Wilcox BR-100 rail/barge cask (DOE/ID/12701-1, 1990). This cask capacity is 21 PWR or 52 BWR assemblies. The cask design has a circular cross section and a stainless steel structure with a lead gamma shield. Neutron shielding is provided by an internal layer of borated concrete. The concrete neutron shield contains an array of imbedded copper fins in order to improve the heat transfer characteristics of the package (DOE/ID/12701-1, 1990). A cross

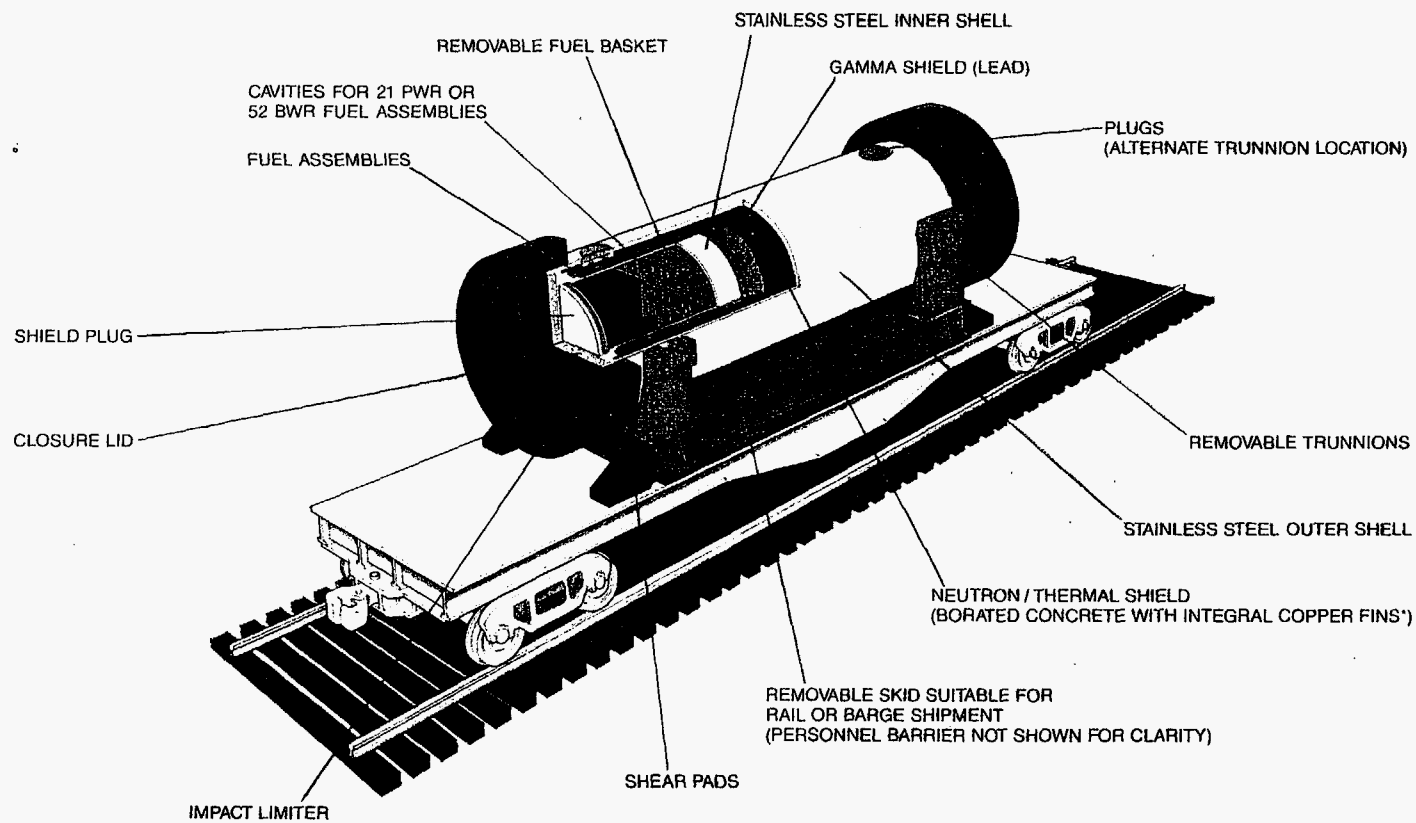


Figure 1.5 Babcock & Wilcox BR-100 100 ton rail/barge SNF cask

section of the BR-100, in the 52 BWR assembly configuration, is depicted in Figure 1.6.

1.2.6 Monitored Retrievable Storage (MRS)

Monitored retrievable storage is the long-term isolation of SNF in facilities that permit continuous monitoring, ready retrieval, and periodic maintenance as necessary to ensure containment of the radioactive materials. An MRS would provide a collection point for some of the nation's SNF while a permanent repository is being built. The initial NWPA required the DOE to evaluate the need and feasibility of an MRS facility. The 1987 amendment to the act established an MRS Review Commission to consider inclusion of such a facility as part of the nation's nuclear waste management system. The MRS would have the following principal functions (Tang & Saling, 1990):

- 1) Prepare SNF for emplacement in a repository
- 2) Serve as the central receiving station for SNF
- 3) Provide limited temporary storage for SNF with a capacity of up to 15,000 MTU

An MRS would make use of dry storage technology, such as concrete cask or bunker storage (similar to Figure 1.4). Presently, the Mescalero Apache tribe of New Mexico has agreed to host an MRS and efforts in this regard are progressing.

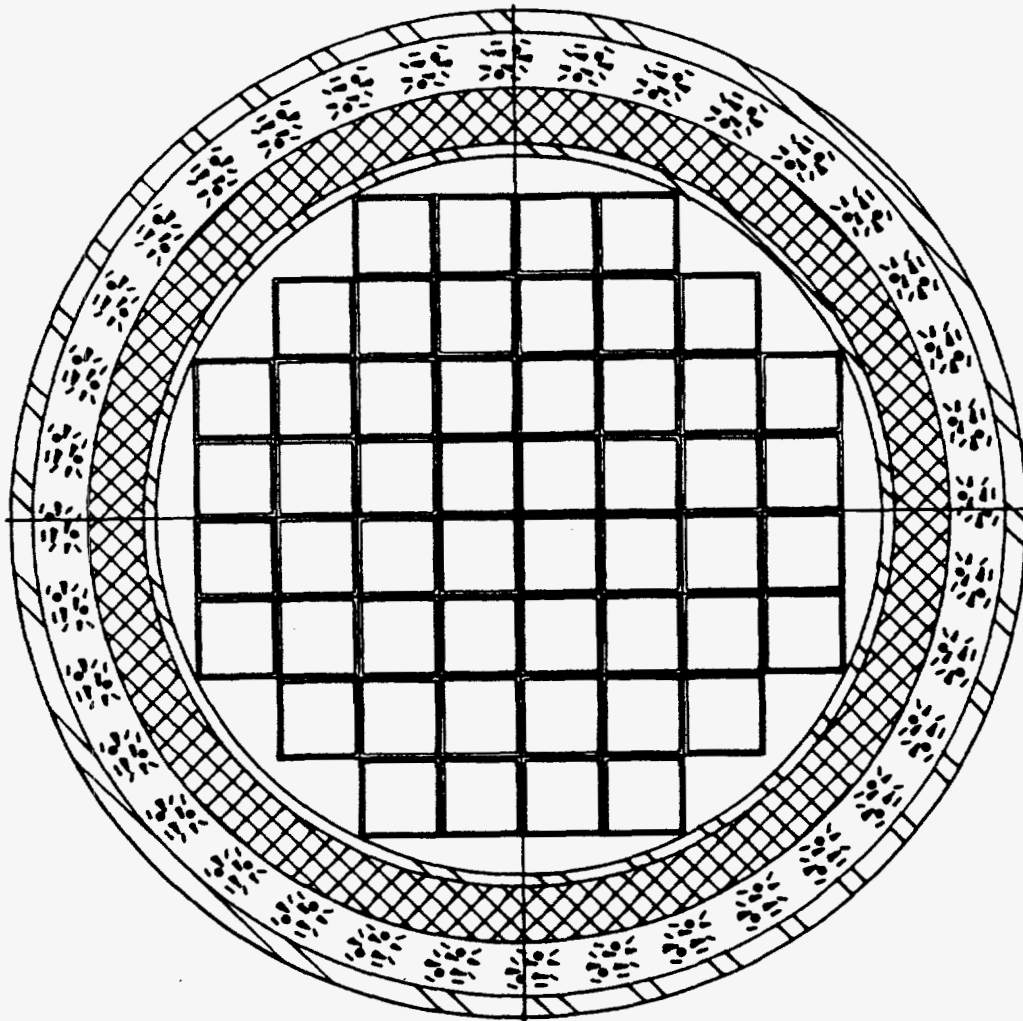


Figure 1.6 Cross section of the B&W BR-100 cask (52 BWR configuration)

1.2.7 Permanent Disposal

The permanent solution in a SNF disposal system is a repository. Many permanent disposal options have been considered in order to determine the best environment for isolating radioactive SNF for long periods of time. For instance, leaving the waste at the reactor site, burying it in the ocean floor, putting it in polar ice sheets, and sending it into outer space have all been considered. However, the consensus of the scientific community has recommended subterranean geologic disposal.

The 1987 amendment to the NWPA directed the DOE to concentrate site characterization studies on Yucca Mountain, Nevada. Yucca Mountain is in an arid climate approximately 100 miles from Las Vegas. The proposed depth of the repository is 300m (1,000ft) below the surface, but still about 240m (800ft) above the water table in a very hard rock known as volcanic tuff. Figure 1.7 illustrates the general design considerations associated with a MGDS such as Yucca Mountain (U.S Council for Energy Awareness, 1992). SNF may be placed within the repository in vertical boreholes drilled in tunnels excavated at great depth (as shown in Figure 1.7), or in horizontal drift emplacements as indicated in Figure 1.8 (Bahney, 1993). Presently, site characterization is underway, and involves a large number of activities designed to determine whether Yucca Mountain is a suitable location for the MGDS. Geologists are examining the surface, taking core samples from deep drills into the mountain, digging trenches and studying strata, and investigating the propagation of sound waves through the

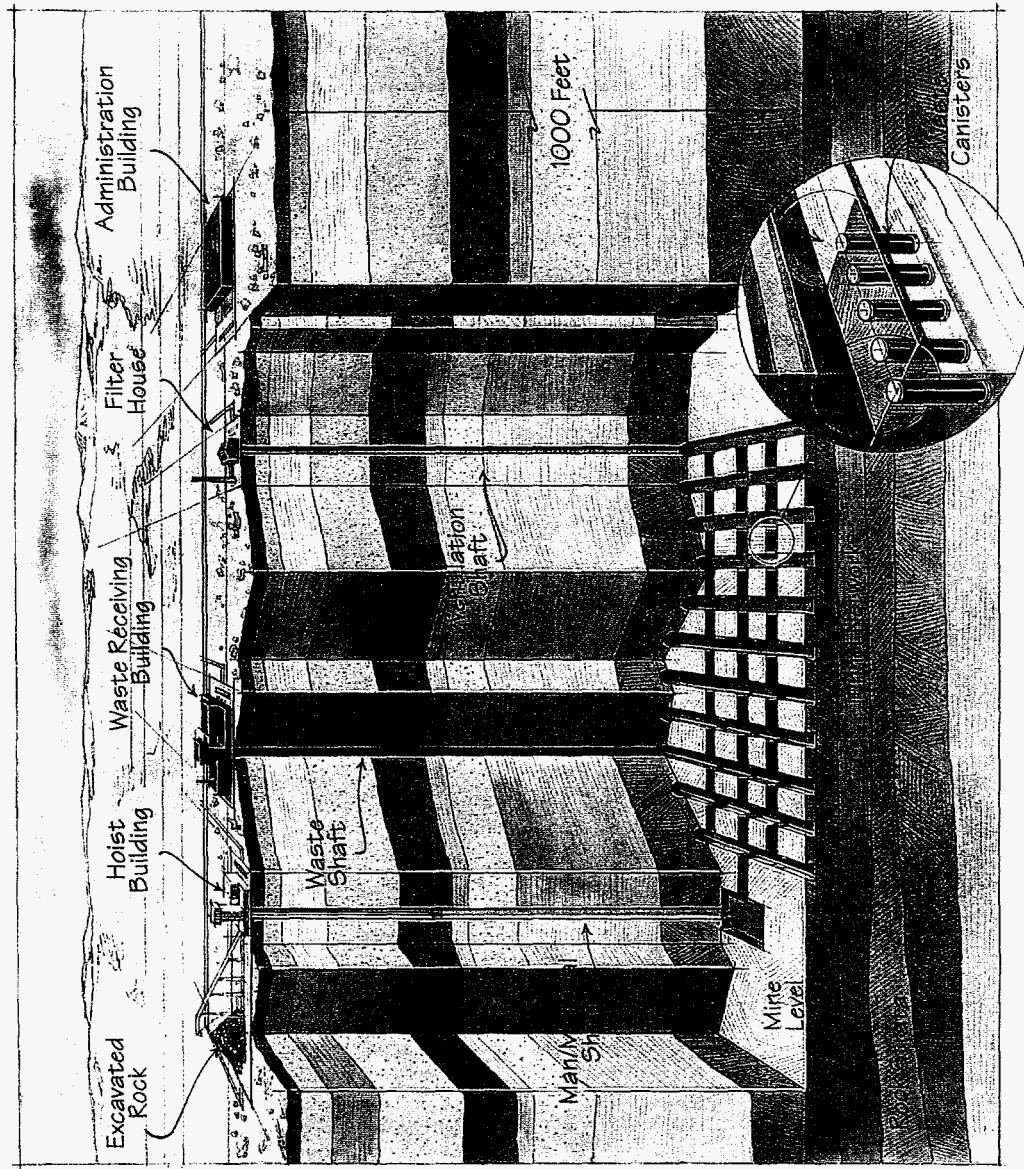


Figure 1.7 General concept of a MGDS employing vertical boreholes (copyright USCEA)

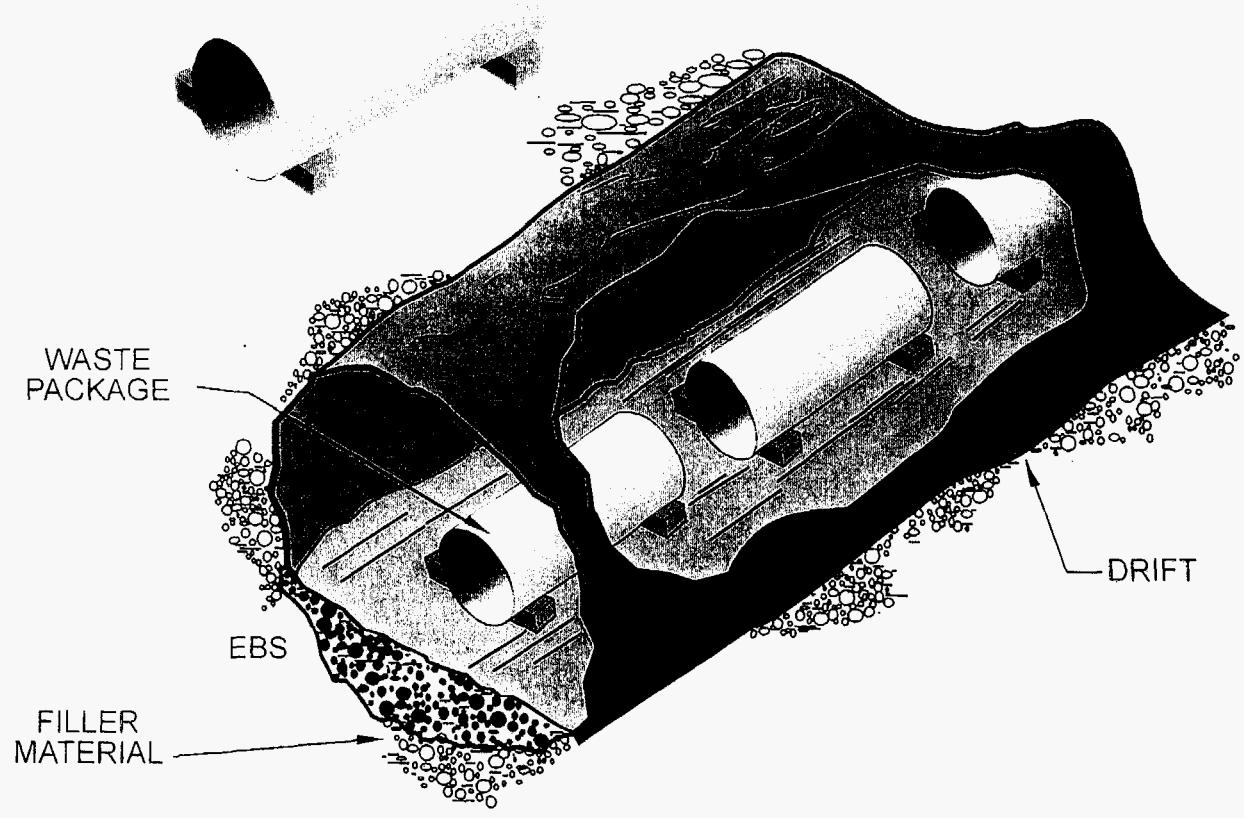


Figure 1.8 Horizontal drift emplacement concept for SNF waste packages, [from Bahney, (1993)]

mountain. Tunneling into Yucca Mountain has already begun in order to construct an Exploratory Studies Facility, which will allow internal observation of the mountain and its structure.

1.2.8 The Multi-Purpose Canister (MPC) System

Over the years, the DOE has considered several different cask systems and numerous casks have been NRC approved for SNF storage or transportation. Typically, a cask is independently licensed for either storage, transportation, or disposal. In early 1994 however, a decision was made to pursue the development of a canister-based system, known as the multi-purpose canister or MPC, that could be used for all stages of the waste management system. The MPC system would use sealed metal canisters to maintain multiple spent nuclear fuel assemblies in a dry, inert environment, as the SNF moves through the stages of at-reactor storage, transportation, MRS storage, and ultimately permanent disposal at a MGDS. Once spent nuclear fuel assemblies are loaded into the MPC, it is sealed and not reopened. The MPC can then be placed inside separate casks or overpacks for storage, transportation, and disposal. This is in contrast with a non-MPC system, in which individual, uncanistered spent fuel assemblies would be transferred between the various stages of the storage, transportation, and disposal modes. The MPC concept is depicted in Figure 1.9.

The MPC is currently being designed to contain SNF from both PWRs and BWRs. It will also come in two sizes - 125 tons and 75 tons. The 125 ton MPC will be used at power plants with crane capacities of at least 125 tons; whereas,

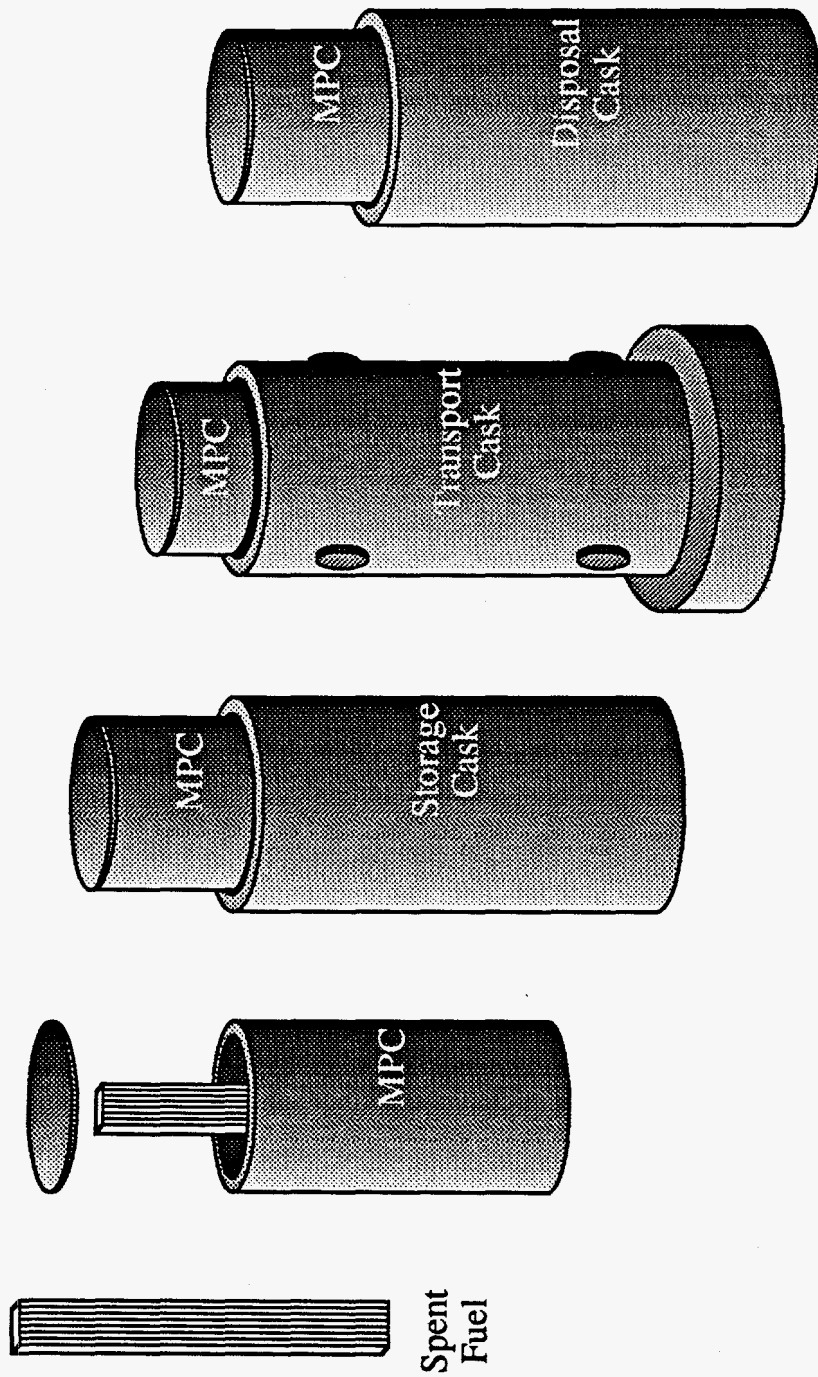


Figure 1.9 Adaptability of the MPC system

the 75 ton MPC will be used at plants with a minimum 75 ton crane capacity. Because of its weight, the MPC is intended for rail shipment. The larger MPC is expected to contain either 21 PWR or 40 BWR assemblies. The small rail MPC will carry 12 PWR or 24 BWR assemblies (DOE/RW-0358/Rev. 1, 1994).

Under the MPC system scenario, SNF would be stored in pools at the reactor facilities. Facilities that can accommodate MPCs and which run out of pool storage space would load SNF assemblies into MPCs rigged for on-site dry storage. At the time of federal government waste acceptance, the MPCs would be transferred to transportation overpacks, and shipped by rail to an MRS. Upon arrival at the MRS, the MPCs are again transferred to storage overpacks. Upon the completion of a MGDS, the MPCs could be transferred from the MRS to the MGDS by rail. There, the MPCs would be transferred to disposal containers, which would be placed in the underground repository. This scenario is depicted in Figure 1.10, which illustrates the versatility of an MPC based system. The use of multi-purpose casks is beneficial in that it reduces the complexity of the waste management system. Furthermore, it may significantly lower the occupational radiation exposure attributed to working with SNF assemblies during the various operational modes.

The preceding discussions have provided a brief overview of the technical and political challenges associated with the transportation, storage, and disposal of spent nuclear fuel in this country. Now, however, the focus of this dissertation

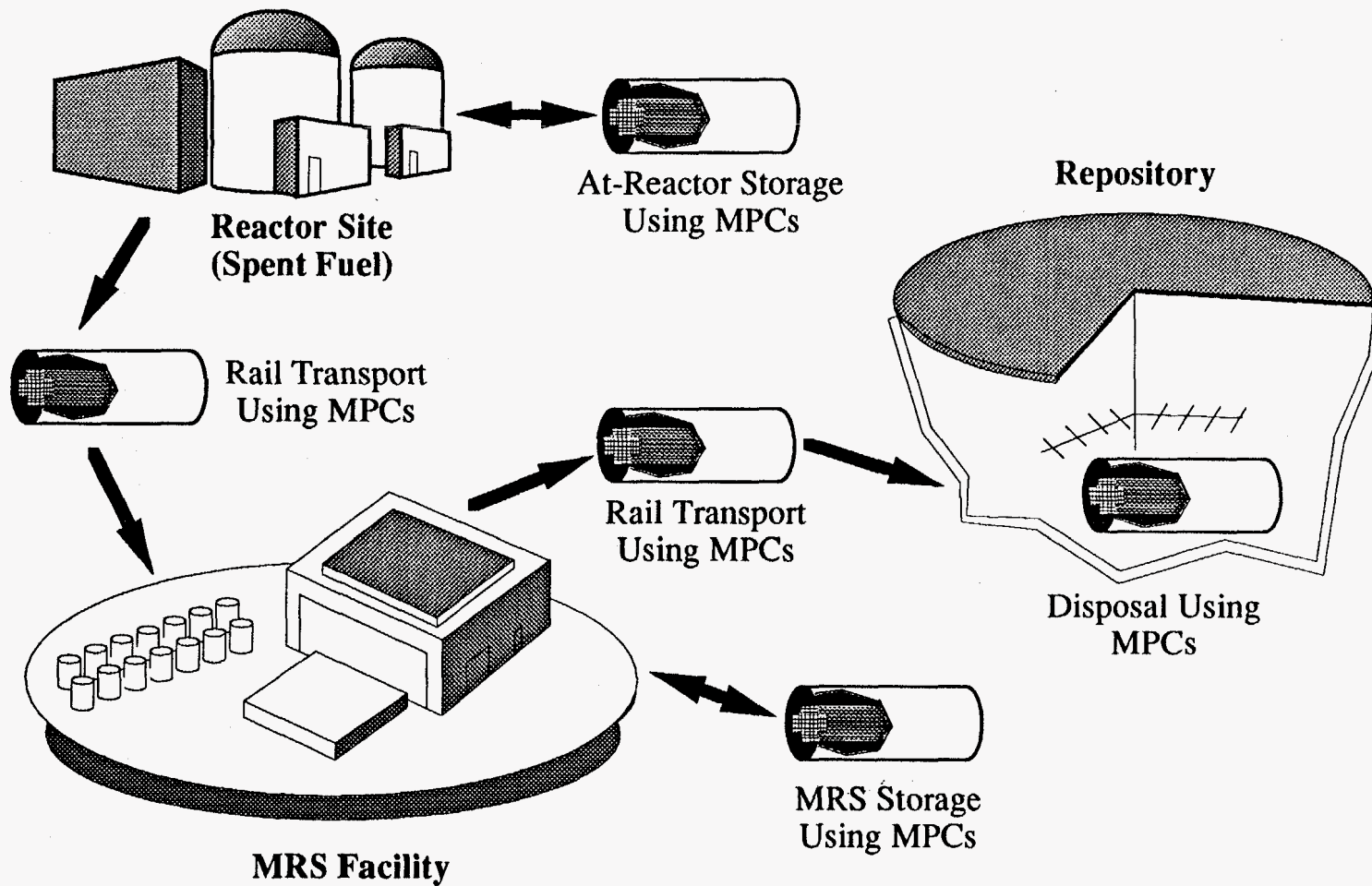


Figure 1.10 MPC system in storage, transportation, and disposal roles

will turn to the engineering challenges associated with the thermal analysis of SNF.

1.3 IMPORTANCE OF SNF THERMAL ANALYSES

A key issue among the engineering challenges associated with spent fuel transportation and storage involves the thermal characterization of the waste package. Although the energy generated by SNF is not sufficient to melt fuel or supporting structures, the temporal and spatial variation of temperature within the fuel assembly directly affects the material properties of the entire waste package and therefore determines the package's structural integrity. Additionally, the thermal energy source that the spent fuel represents will significantly influence the surroundings of the waste package, which is of particular concern with regard to siting and loading a geologic repository. These considerations make thermal analysis of SNF systems an important component of the overall waste package/cask design process.

The prediction of temperature fields within spent fuel casks is typically carried out using numerical models which simulate the various heat transfer mechanisms present in the actual physical system. However, numerical analysis of multimode heat transfer in geometries as complex as those associated with SNF represents a difficult problem. A comprehensive, combined mode, numerical thermal analysis is presently possible; however, such a study requires significant computational resources and expense. Engineering correlations based upon

applicable *experimental* data represent a viable option for either direct analysis or the simplification of available numerical models. However, systematic and fundamental experimental studies of spent fuel configurations are essentially nonexistent in the open literature. Most of the currently available data come from coarsely instrumented mock-ups of spent fuel and therefore do not provide the detailed spatial characterization of temperature that is required for a comprehensive thermal investigation.

1.4 EXPERIMENTAL OBJECTIVES

A BWR fuel assembly mock-up has been designed, constructed, and tested at The University of Texas at Austin (UT) in order to investigate the multimode heat transfer processes associated with the horizontal transportation and storage of spent nuclear fuel. The primary objective of this experimental study is to obtain natural convection correlations which can be used in order to incorporate convective effects into analytical models of horizontal spent fuel systems. Investigation of the physical nature of natural convection in enclosed horizontal rod bundles is also of interest. The focus of the work is on the natural convection process; however, all modes of heat transfer must be independently characterized in order to isolate convective effects.

Among the lingering questions regarding heat transfer processes in SNF systems, the importance of natural convection remains unanswered. The existence of natural convection currents within horizontal fuel assemblies may be of paramount importance to the safe and efficient storage, transport, and disposal

of SNF with regard to two interrelated physical processes. Firstly, natural convection may have a significant influence on the overall heat transfer mechanisms present and thus have impact upon spent fuel and cask thermal behavior. Secondly, the presence of natural convection induced flow fields may prove important with regard to the potential transport of activated particulate material within the cask. However, the existence of fundamental and detailed experimental data relating to natural convective processes under the geometrical and thermal conditions of interest here are lacking. Furthermore, the majority of past studies have focused primarily upon the determination of coarse thermal effects such as the measurement of peak rod temperatures within simulated fuel bundles as a function of limited variational parameters. The significance of free convective processes in SNF cask geometries remains an issue, and is certainly not fundamentally quantified.

This dissertation addresses these points, and provides the reader with the detailed information necessary for the reproduction of results, using either experimental or numerical approaches. First, however, a review of past work relevant to this study is presented in Chapter 2.

Chapter 2 - Literature Survey

2.1 ORGANIZATION

A literature review has been conducted in order to provide the reader with a background of previous work pertinent to this dissertation. This survey focuses on previously published experimental work related to heat transfer within horizontally oriented, heat-producing rod bundles. Particular attention is paid to natural convection in dry nuclear spent fuel assemblies and closely related geometries. Computational studies are not reviewed although many are referenced and discussed in later chapters. Work involving vertically oriented rod bundles is excluded as well. The literature review provided by Manteufel (1991), references many works with regard to these latter subjects, which the interested reader may wish to consult. This chapter will review works categorized as either 1) Experimental simulations of spent fuel (Section 2.2), or 2) Experimental studies of natural convection in similar geometries (Section 2.3). The investigations are reviewed in reverse chronological order.

2.2 EXPERIMENTAL SIMULATIONS OF HORIZONTAL SPENT NUCLEAR FUEL

Lovett (1991) conducted an experimental study in which a BWR assembly was simulated under horizontal transport or storage conditions. The test section was comprised of a square 8 X 8 rod array enclosed in an aluminum box. The

0.95cm diameter rods were electrically heated as was the surrounding aluminum enclosure. A single thermocouple was embedded in the center of each rod, which essentially consisted of a 0.61m long copper tube filled with a MgO insulating powder. Figure 2.1 depicts the cross-sectional view of the test section. Although the test apparatus was designed to simulate a BWR assembly, the rod diameter coincides with a PWR fuel rod. Various fill gases were utilized and the system pressure was varied between atmospheric, 101.3kPa (0 psig), and 239.1 kPa (20 psig). It was reported that all data were taken at steady state. During the course of experimentation, it was determined that the enclosure could not be uniformly heated in order to maintain an isothermal enclosure boundary condition. Thus, most of the data were obtained with the enclosure temperature uncontrolled so that as the assembly power increased, the box temperature reached increasingly higher equilibrium values.

The reported data consist of plots relating the maximum recorded temperature within the array to the electrical power supplied to the bundle. Nusselt-Rayleigh number correlations are not given and no effort was made in order to separate and individually quantify the convective and radiative heat transfer components. Furthermore, the placement of thermocouples in the center of the heater rods makes estimation of rod *surface* temperature difficult.

Irino *et al.* (1986) report an experimental study in which a 15 X 15 rod pressurized water reactor (PWR) assembly was simulated in a horizontal orientation using stainless steel electric heaters 2.0m in length, surrounded by a steel basket enclosure. The surface temperatures of 19 heater rods (out of 225

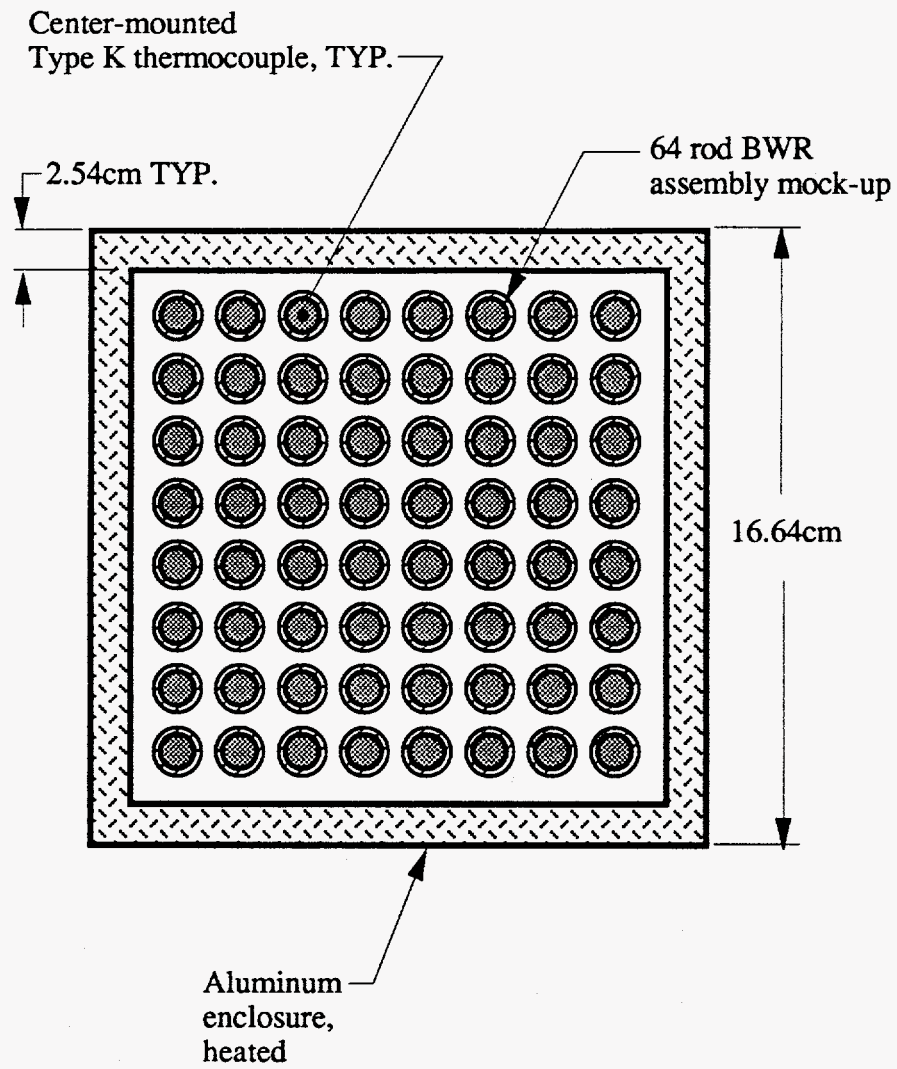


Figure 2.1 BWR assembly mock-up used by Lovett (1991)

total) as well as the surrounding basket were monitored using Type K thermocouple instrumentation. Measurements were taken for three power settings (0.01W/cm, 0.03W/cm, and 0.06W/cm), with backfills of helium and nitrogen (at steady state). The basket enclosure was electrically heated and data were taken at three enclosure temperatures (200°C, 250°C, and 300°C). Apparently all experiments were performed at either atmospheric pressure or vacuum.

The experimental results consist of individual rod temperature variations at the various bundle powers. No quantitative separation of measured radiative and convective effects are given and no Nusselt/Rayleigh correlations are included. The experimental results were compared to a developed numerical algorithm (SICOH-3D) which solves the mass, momentum, and energy equations in an isolated assembly cell using a k- ϵ model for turbulent natural convection. This code also accounts for radiation heat transfer in the energy equation source term using the Net Radiation method. The model assumes that a given rod participates radiatively with its nearest 16 neighbors. In general, agreement between the code results and the measured temperatures is good for fuel rods located in the center of the assembly. The edge rod temperatures are overpredicted, however.

Bates (1986) conducted a series of experimental tests in a simulated full-scale 15 X 15 rod PWR assembly. The electrically powered, thermocouple instrumented rod bundle was enclosed in a rectangular basket which resided within a cylindrical annulus. The inner wall of the cylinder was instrumented with guard heaters to control the wall temperature to the desired set point of

200°C. The heater rods were 1.07cm in diameter and were 3.66m in length (full-scale). The test apparatus used by Bates (1986) is illustrated in cross-section in Figure 2.2. Tests were conducted in horizontal, vertical and inclined orientations using air and helium backfills at two power levels. The primary reported results consist of rod-to-wall temperature differences plotted as a function of assembly power and pressure.

Sanchez and Hudson (1986) of Sandia National Laboratories (SNL) report on experimental measurements taken in a 217 rod liquid metal fast breeder reactor (LMFBR) fuel assembly mock-up. The 0.64cm diameter, 1.22m long, wire-wrapped electrical heater rods were arranged in an equilateral-triangular array with a pitch to diameter ratio (P/D) of 1.24. The horizontal rod bundle was enclosed in a hexagonal enclosure which was located within a steel pipe. The surface temperatures of 13 heater rods, as well as the hexagonal assembly enclosure, were measured using thermocouple sensors. A total of 14 heat flux sensors were additionally mounted on the hex-can and the surrounding pipe. The SNL test assembly was the same one utilized in an experimental study conducted by Klima (1975) at Oak Ridge National Laboratory (ORNL), see Figure 2.3. Helium was the primary backfill utilized for all experiments. Data were taken at approximate bundle powers of 1000W, 1250W, and 1500W. The data primarily consist of direct sensor measurements of heater rod temperature and enclosure heat flux. Since the heater rods within the assembly were tightly packed and individually wire-wrapped, natural convection within the enclosure was precluded.

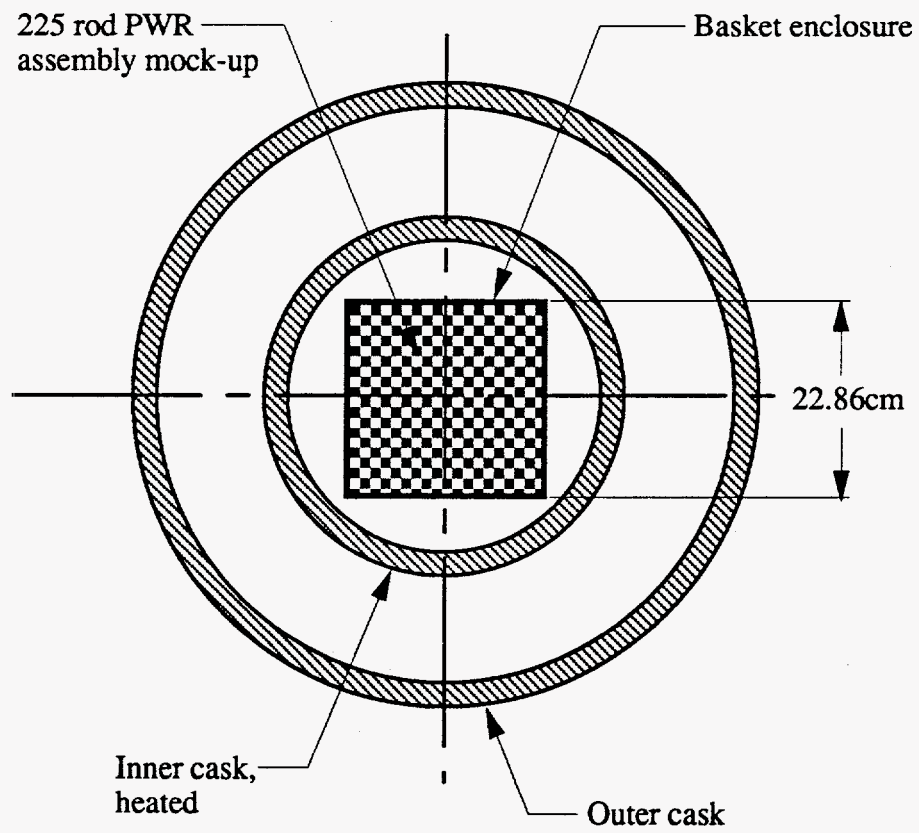


Figure 2.2 Test apparatus used by Bates (1986)

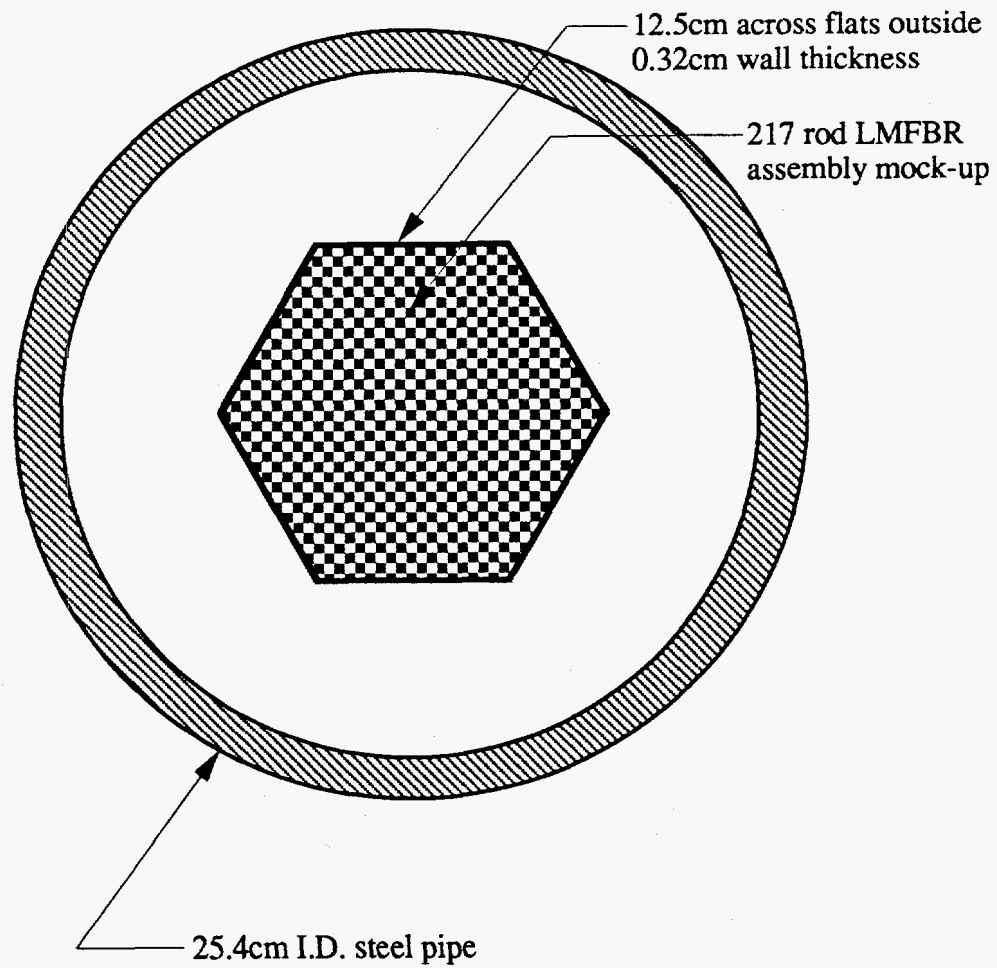


Figure 2.3 Cross-section of test apparatus used by Klima (1975) and Sanchez & Hudson (1986)

Eggers (1983) also fabricated an experimental model of a BWR fuel assembly. The apparatus consisted of sixty-four, 1.22cm diameter, 60.9cm long electrical heaters arranged in an 8 X 8 square array with a pitch/diameter ratio of 1.3. The array was enclosed within a square fuel tube which was wrapped with electrical heating tape and covered in insulation. Only six of the sixty-four heater rods were instrumented with thermocouples; thus, the data lacked the sufficient detail required for quantification of individual heat transfer components.

The primary reported data consist of plots of instrumented rod surface temperature as a function of supplied power and backfill gas, either air or helium. In all, six data sets are reported which include two power levels and two backfill conditions (air and helium). A later study by Eggers (1985) describes results obtained in a compressed version of the same test apparatus, which utilized 126 heater rods consolidated into a two-to-one ratio. In a consolidated array, the fuel rods are essentially in contact with each other and natural convection is prevented.

Fry *et al.* (1983) conducted a series of experiments using an electric heater rod simulation of a 16 X 16 enclosed PWR assembly in the horizontal orientation. The data were compared to predictions obtained using the RIGG code (a two dimensional model of radiation and lumped conduction) in order to determine the validity of the code toward prediction of the peak fuel rod temperature. The experimental apparatus consisted of 256, 0.95cm diameter Zircaloy-4 tubes, held together by nine axially off-set spacer grids (the assembly was full-scale). The array resided within a tight-fitting aluminum box, which was air-cooled to obtain

an isothermal boundary condition. Instrumentation consisted of 200 heater rod thermocouples and twenty-four enclosure thermocouples, axially spaced. Twenty-six heater rods were instrumented at a given assembly cross-section, with six enclosure-mounted thermocouples at a given cross-section. The heater rod thermocouples were attached to the internal heater elements and thus did not measure the rod surface temperature directly. A separate experiment was carried out using a single heater rod to determine the typical ΔT between the rod center (where the thermocouples were located) and the surface. A correlation was developed in order to back out the heater rod surface temperature, given the measured internal temperature. Equilibrium data were taken for air and helium backfills at atmospheric pressure.

Fry initially states that heat transfer within horizontal assemblies is a radiation governed process, with only a small contribution from convection. However, experimental results indicate a strong convective effect, causing as much as an 84°C difference in heater rod temperature from top to bottom of the array with air as a backfill. With helium, the isotherms are center-symmetric and the maximum rod temperature was noticeably reduced. Originally, data were taken with the enclosure emissivity equal to 0.4. The enclosure interior was later painted black in order to raise its emissivity to 0.85. With an air backfill, this action resulted in reducing the peak rod temperature by 10°C. The presented experimental results consist of the measured temperatures for three of the seventeen conducted tests. The rod average temperatures are plotted as a function of position in the array, and no indication of the measured power is given. The

selected data sets are compared to results from the RIGG computer code, which does not include a convection model. The code results compare well to experimental helium data, but significantly overpredicts heater rod temperatures for air backfills, when natural convection is present.

Anderson (1979) conducted an experimental study using a simulated, full-scale 15 X 15 rod PWR assembly, which was later used by Bates (1986), [Figure 2.2]. Both horizontal and vertical geometries were investigated using air and helium backfills. Tests were also performed with just single heater rods in vertical and horizontal containers. The presented data consists of peak array temperature, average array temperature, and basket temperature, plotted as a function of supplied electrical power. The test apparatus is not described or depicted.

Wooten and Epstein (1963) conducted both theoretical and experimental investigations of spent fuel assembly heat transfer in a variety of orientations and backfills. Their complete work has not been published. However, their analysis of natural convection and radiative cooling in horizontal assemblies has been published in a study by Bucholz (1983). This condensed version of the original work considers horizontal assemblies in an air backfill. The Wooten and Epstein simulated fuel assembly consisted of a 17 X 18 rod array, comprised of 0.86cm diameter, 2.44m long steel tubes, which are smaller (in diameter) than PWR fuel rods (0.95cm diameter). The pitch/diameter ratio was 1.24, a tighter packing than typical PWR assemblies (PWRs have a $P/D=1.32$). The assembly was electrically heated, with power ranging from 0 to 50kW, and the total power was calculated

from measurements of the electrical resistance of the heater rods and the current input. During the experiment, the rod bundle was centered inside a steel pipe with an inside diameter of 30.4cm. A larger tube surrounded this structure, and water was passed through the annulus to obtain an isothermal inner cylinder boundary condition. The instrumentation scheme is not discussed, other than a statement to the effect that "thermocouples were placed along the length of the assembly."

The presented data are the maximum heater rod surface temperature as a function of the total electrical power supplied to the assembly. A simple, algebraic, semi-empirical correlation is offered based upon a coarse radiation/convection model, the latter of which assumes turbulent natural convection. The correlation predicts the array-maximum rod temperature as a function of total bundle power.

It should be noted from the preceding reviewed material, that in general, previous investigations relevant to the transportation and horizontal storage/disposal of spent nuclear fuel have been limited to the testing of electrically heated, coarsely instrumented mock-ups, which do not provide the detailed spatial characterization of temperature that is required for a comprehensive thermal investigation. In these studies, no attempt has been made to conduct a systematic and fundamental analysis of the individual radiation/convection heat transfer processes. Furthermore, the raw experimental data are often unavailable, either because the data were not adequately recorded or because the data are proprietary.

The following section reviews works which are more fundamental in nature, particularly with regard to the natural convection process. None of the forthcoming discussions involve exact spent fuel geometries, but rather simplified systems of general similarity.

2.3 EXPERIMENTAL STUDIES OF NATURAL CONVECTION IN SIMILAR GEOMETRIES

This section reviews experimental studies which focus upon fundamental natural convection processes in geometries which are similar to those discussed above. Specifically, 'similar' will be defined as configurations of heat-producing, horizontal cylinders (rods), which thermally interact in a gaseous environment. All of the described investigations were conducted at steady state.

Choi (1983) and Choi & Cha (1990) conducted an experimental study of natural convection in both square (in-line) and staggered horizontal tube arrays. Both enclosed and unbounded rod bundles were utilized. The rods were hollow SS304 tubes, uniformly heated by passing a direct current directly through the tube walls. The rod pitch was fixed at 1.25cm, and diameters of 0.32 and 0.64cm were employed. This resulted in a respective pitch to diameter ratio (P/D) of approximately 4 and 2. The rod bundle consisted of 84 rods, arranged in a 12 X 7 matrix which could be pivoted about an axis to examine either square or staggered geometries. The backfill was air. The local and rod average Nusselt numbers were determined for various tubes using a Mach-Zehnder interferometer. The local Nusselt number was calculated from the non-dimensional temperature

gradient at the tube surface. The rod average Nusselt number was found by numerically integrating the local values over the rod surface.

Choi reports that the heat transfer generally decreases as one considers rods located at higher positions in the horizontal array. The authors speculate that this is due to the increased ambient temperature which results from preheating by lower rods. As the ambient temperature progressively increases (up the array), the density gradients about a given rod tend to decrease, resulting in reduced buoyant potential and less vigorous flow fields. Choi also reports that the heat transfer in a staggered rod bundle is better than in a corresponding square array since the convection-induced buoyant plumes have more room for complete development and diffusion cooling before impinging upon higher rods. Also, for staggered arrays, the local heat transfer coefficient is a maximum at the bottom of a given rod, regardless of the rod's position in the bundle. However, Choi finds that for square arrays, this is only the case for the bottom positioned rods. Upper rods have peak local heat transfer coefficients on their sides (for small spacings).

A limitation of this work is that no correction for radiation heat transfer is made. The temperature gradient about each rod, from which the reported Nusselt number is determined, results from combined-mode convection *and* radiation heat transfer. Furthermore, the Rayleigh number is defined in terms of the total heat flux, not just the convective contribution. Thus, the reported convection correlations will be somewhat system specific, dependent upon the test apparatus' radiative surface properties. Choi reports that $Nu \sim Ra^{0.5}$, which Manteuffel (1991) asserts is inflated by including radiative heat transfer.

Vdovets *et al.* (1986) conducted a major experimental study involving horizontally oriented rod bundles surrounded by an enclosure. Rod bundles containing up to 331 rods were considered. Backfill media included air, carbon dioxide, water, and oil. Numerous geometries were involved, including: hexagonally arranged arrays in hexagonal enclosures; hexagonal arrays in circular enclosures; concentric circular arrays in a circular enclosure; and staggered (triangular pitched) arrays in a square enclosure. In all cases, the enclosure was cooled and isothermal, and steady state was achieved. No data for square arrays are reported. Vdovets reports array averaged Nusselt number vs. array averaged Rayleigh number correlations for natural convection. The radiative component of heat transfer was calculated using an approximate analytical technique in which only the two outer layers of rods within an array were assumed to participate with the surrounding enclosure. Furthermore, each layer of rods is assigned a single temperature equal to the mean temperature of all rods in that layer. Vdovets indicates that natural convection is a significant mechanism in all tests involving gaseous backfills. In a 37 rod hexagonal bundle ($P/D = 1.38$), as the air pressure is increased from 0.1 to 0.9 MPa (11 W power per rod), the maximum temperature in the array drops from 181 to 81 °C.

Tokura *et al.* (1983) report on an experimental study in which 2, 3, and 5 horizontal rods were stacked in a single vertical column to determine the average rod Nusselt number as a function of rod spacing (pitch). The vertical array was set between two vertical and parallel plates open to an 'infinite' medium, as depicted in Figure 2.4. The local flow field about each rod was

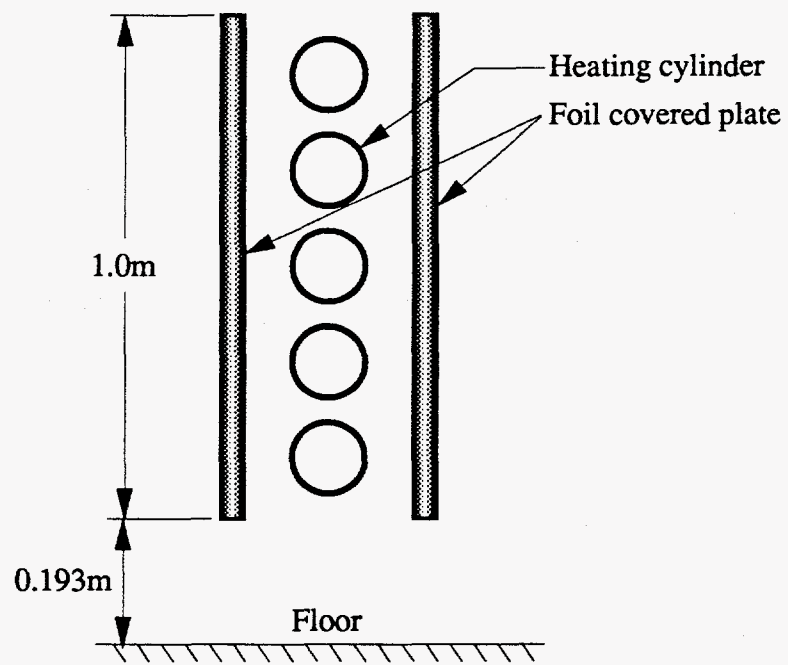


Figure 2.4 Cross-section of experimental apparatus used by Tokura *et. al.*

also characterized qualitatively using Mach-Zehnder photographic interferometry. The copper rods (tubes) were 0.6m long, 1mm in thickness, and 2.85cm in outer diameter. The rods were heated electrically with internal Nichrome wire heaters. The temperature of the rod surfaces was measured using Type T thermocouples attached to the upper surface of each rod, with an axial spacing of 0.1m. The power to each rod was adjusted to obtain uniform temperatures for all rods in the array to within 1.0°C. Thus, the rods were subject to a uniform surface temperature boundary condition, as opposed to the uniform heating condition typical of spent fuel assemblies. Tokura also verified, by rotating the rods, that the circumferential temperature difference about a given rod was less than 0.3°C. The copper rods were highly polished ($\epsilon \approx 0.072$) and the adjacent parallel plates were covered with foil in order to reduce the emissivity of all surfaces. The radiative heat transfer was subsequently calculated using an approximate analytical technique whose basic assumption is that each rod is exchanging radiation primarily with the ambient surroundings, not with the other rods. The authors indicate that radiation heat transfer was less 9% of the total heat transfer.

Tokura's results indicate that for small rod spacings, ($P/D < 3$), natural convection heat transfer decreases as one considers rods located progressively higher in the column. Similar observations were reported by Choi (1983). However, for larger rod spacings, ($P/D > 3$), the buoyant plumes created by lower rods can actually increase the Nusselt number of the rods they impinge upon, creating in essence a forced convection environment for upper rods. Yet, this

convective enhancing effect has a limit, which Tokura reports, reaches a maximum for $P/D \approx 7$.

In most cases, the Nusselt number for the bottom rod in the column is essentially the same as that for a single, isolated cylinder. The exception is for very small separation distances ($P/D \approx 1.1$), when the heat transfer from the bottom rod is less. In this case, the spacing is so small that the buoyant flow around a cylinder cannot penetrate the narrow gap between cylinders, and stagnation regions may consequently form at the tops and bottoms of downstream rods. These stagnation regions may form hot spots which reduce local heat transfer coefficients. Thus, for pitch to diameter values of the order of $P/D \sim 1.1$, a given rod's boundary layer is perturbed by both its upstream and downstream neighbors. As the rod spacing increases, only the upstream rod is influential - sometimes enhancing convection, sometimes hindering, dependent upon the actual pitch to diameter ratio (Figure 2.5).

Sparrow & Niethammer (1981) conducted experiments using two horizontal, electrically heated rods, arranged in a vertical column. They discuss extensively the two seemingly opposing effects that the lower cylinder can impose upon the upper. Namely, the lower rod can preheat the ambient fluid surrounding the upper rod, resulting in a decrease in natural convection heat transfer for the upper rod. Or, the buoyant plume created by the lower rod can impinge upon the upper rod in a forced convection manner, increasing the upper rod's convective heat transfer. The magnitudes of these effects depend primarily upon the vertical spacing between cylinders. Sparrow and Niethammer observed that at

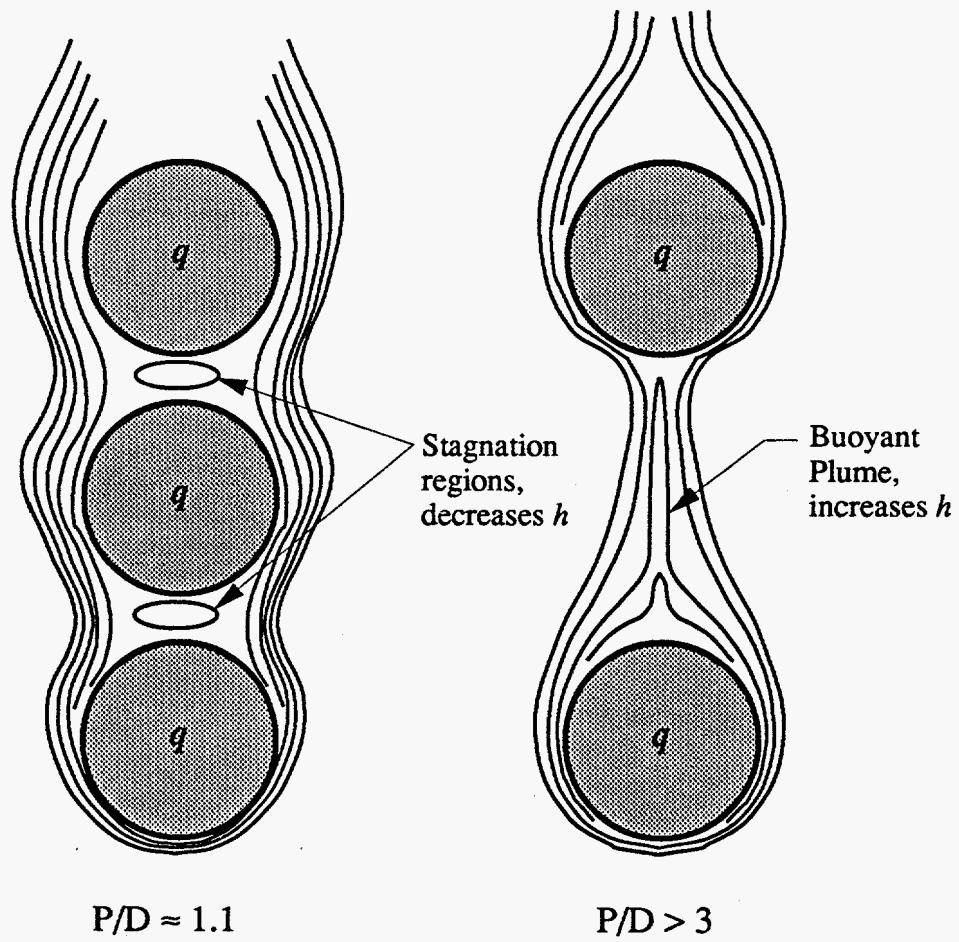


Figure 2.5 The effect of horizontal cylinder separation distance on the convective heat transfer of upper rods

low separation distances ($P/D \approx 2-3$), the preheating effect dominates, resulting in a Nusselt number for the upper cylinder which is below that of a single, isolated cylinder at the same Rayleigh number. As the separation distance increases, the preheating effect lessens and the buoyant plume's cooling ability becomes increasingly significant. However, the plume must have room to fully develop and cool in order to effectively increase the Nusselt number of the upper rod. Sparrow reports that an observed peak in the upper rod Nusselt number occurs at vertical separation of $P/D \approx 7-9$. This is in accordance with the results observed by Tokura *et. al.* Beyond this separation distance, one would of course expect the situation to more closely resemble two isolated cylinders.

Sparrow and Niethammer also report that slight variations in rod emissivity (± 0.02) produced a negligible effect upon their reported rod averaged Nusselt numbers. Conductive end losses for the 0.76m long, end-insulated heater rods, were deemed negligible as well. This was proven by performing a separate experiment involving only one horizontal heater, and subsequently comparing the results to previously published, single, isolated cylinder data. Had conductive end losses been significant in Sparrow's apparatus, his single cylinder Nusselt numbers would have been consistently overpredicted, since escaping end loss energy would end up being counted as having been removed by convection.

Warrington and Crupper (1979) present convection correlations for an experiment involving four horizontal cylinders arranged in a 2 X 2 square array, and surrounded by a water-cooled cubical enclosure. The heater rods were

17.8cm in length, 4.12cm in outer diameter, and had a $P/D \approx 3$. The power to each of the four heater rods was independently controlled to maintain the rods at the same surface temperature. The investigation utilized air, water, glycerin, and oil as working fluids, giving a Prandtl number variation of $0.7 < Pr < 31,000$. The four horizontal rods were supported by stems attached to a central spherical body. Although conduction losses from the horizontal rods down the supports were corrected for, the supports may have disrupted the flow field between cylinders. The radiative heat transfer component was determined experimentally, although the procedure was not fully described.

The data consist of rod and array averaged Nusselt number plotted against corresponding Rayleigh number. The upper row of rods had an average Nusselt number which was 84% of the bottom row value, with an air backfill. The authors additionally report that the data are best correlated as $Nu \sim Ra^{0.25}$, which is typical of laminar natural convective flows.

Warrington and Weaver later expanded upon this work, including staggered arrays consisting of 8 and 14 cylinders (Warrington & Weaver, 1984). In this study, the staggered rod arrangement produced a higher array average heat transfer coefficient than the square array of comparable size and spacing. Even more pronounced was the increase in heat transfer coefficient when the spacing between rods was increased. This increase was not as prominent for the higher Prandtl number fluids however.

Tillman (1979) conducted a study using 1.27cm diameter, 10.16cm long, electrically heated horizontal rods arranged in a 4 X 4 square array, and a fourteen heater rod staggered array. Each metal-clad heater rod was equipped with one thermocouple, soldered to the outer surface at the rod's midpoint. The rod bundle was not enclosed and all experiments were conducted in air at atmospheric pressure. The heaters were operated at near isothermal conditions (all rods were within $\pm 5.6^{\circ}\text{C}$), although the power of each heater was not independently controlled. Instead, each row of heaters was connected to independent transformers. Thus, the center rods of each row ran hotter than the edge heaters. Tillman also claims that "since each heater in a horizontal row was controlled by the same transformer, each row operated under conditions of constant heat flux." The implication that each heater is subject to a uniform outer surface heat flux is not valid, given the apparatus design and the presence of combined natural convection and radiation processes (cf. Chapter 4). Tillman also assumes that heater end losses are negligible. However, despite the insulation provided at each heater's end (as support), the short length of the heater rods makes conductive as well as convective end effects likely.

Tillman presents array averaged convective correlations (heat transfer coefficient and Nusselt number), which indicate that for closely packed rods, the heat transfer is diminished compared to that of a single, isolated cylinder. Tillman also concludes that the rod spacing is more influential on the convective heat transfer than the array pattern. However, Tillman assumes that radiation is negligible and thus no radiation correction is made. The data are correlated in

terms of $Nu \sim Ra^{0.5}$, which gives the indication of being inflated due to the inclusion of radiative effects, as was the data of Choi (1990, 1983).

Marsters (1972) utilized a single column of stacked horizontal rods, supported at each end and exposed to an open environment at atmospheric pressure. This experiment was similar to that of Tokura *et. al.* (1983), except no enclosure was present. The rods were 0.635cm outer diameter, 58.5cm long steel tubes, heated directly by passage of a direct current through the sheaths. The number of tubes and their spacing were varied, as well as the applied power. Voltage was measured over an interior portion of each rod; thus, an effective guard section on each end was created which minimized end effects. These losses were estimated to be less than 1% of the total supplied power and were thus neglected. Marsters claims that "because of the low heat transfer coefficients and the relatively high conductivity of the tube material, circumferential temperature is constant to within the accuracy of the experiment." Thus, only one thermocouple per rod was used to measure the outer surface temperature. Because the thermocouple was in direct contact with the rod sheath, which was heated directly by an electric current, the current leads had to be reversed for each data point in order to determine the voltage drop induced over the thermocouple junction.

Thermal radiation is deemed important by Marsters. He uses an approximate method to correct for it. Since his tubes are generally far apart, Marsters assumes that each tube is exchanging radiation only with the ambient surroundings, and not with other tubes. However, Marsters does correct for the

decreased view factor due to obstruction of the surroundings by other tubes. The radiative contribution is subsequently linearized by defining a radiative heat transfer coefficient. Marsters justifies the approximation since the uncertainty of the rod's emissivity is of the same order.

The presented results indicate that the upper rods in the column have reduced Nusselt numbers at close rod spacing ($P/D \approx 3$) and enhanced Nusselt numbers at large spacing ($P/D \approx 5 - 21$), compared to the single, isolated cylinder case. The temperature of upper rods is increased with respect to the bottom rod at $P/D = 3-5$, but beyond that the upper rods are cooled compared to the bottom rod. The minimum pitch to diameter ratio investigated was $P/D = 3$. The presented Nusselt numbers are normalized by the Nusselt number predicted from previous work for a single, isolated cylinder at the same Rayleigh number.

Lieberman and Gebhart (1969) conducted experiments dealing with the thermal interaction between heated wires arranged in a plane array. The 0.127mm diameter, 0.184m long wires were oriented in a stacked vertical column, which could be rotated with respect to the vertical. The wire spacing was varied from 37.5 diameters to 225 diameters, and data were taken at inclinations of 0° , 30° , 60° , and 90° from the vertical. The arrangement provided for very low Grashof numbers, of the order of 0.15 for the array average. Moreover, the wire spacing was much larger than might be expected in applications such as nuclear fuel assemblies or practical heat exchangers.

One of the earliest studies of interacting horizontal cylinders was performed by Eckert and Soehngen (1948). They measured Nusselt numbers for three horizontal copper rods of 2.23cm diameter. It was found that when the rods were arranged in a vertical column, the Nusselt number progressively decreased for the upper rods. While the bottom rod had a Nusselt number comparable to a single, isolated cylinder, the next highest rod's Nusselt number was 83% of that of the bottom rod, and the highest rod's Nusselt number was only 65% of the bottom rod. The rods were also arranged so that the axes of the highest and lowest rods were in the same vertical plane, while the axis of the middle rod was offset by a half rod diameter. In this configuration, the bottom rod still had the same Nusselt number as before, but the middle rod's Nusselt number was 103% of that of the bottom rod, and the highest rod had a Nusselt number which was 86% of the bottom rod's value. The increase in the heat transfer from the middle tube was attributed to the higher velocity past this tube induced by the wake from the lower tube. Thus, the staggered arrangement had a higher array average Nusselt number than the in-line array.

2.4 THE PRESENT WORK

The objective of this investigation is to quantitatively assess the natural convective process within horizontal spent fuel. Additionally, basic heat transfer data for an enclosed horizontal rod bundle undergoing coupled conduction, natural convection, and radiation heat transfer is provided for computer model validation. This work is intended to expand the base of experimental knowledge

relevant and applicable to the thermal characterization of SNF, and to address questions concerning the thermal behavior of SNF which have remained unanswered in prior efforts.

The chapter which follows provides an overview of the fundamental heat transfer processes inherent to spent nuclear fuel systems. The specific characteristics of SNF which influence these processes are discussed in detail. Chapter 3 also provides the theoretical basis for the experimental methodology and procedure which will be described in later chapters.

Chapter 3 - Heat Transfer in Spent Fuel Systems

3.1 INTRODUCTION

Heat transfer within dry, spent nuclear fuel systems is complicated by two primary factors; namely, the inherent complexity of the geometry and the presence of combined conduction, convection, and radiative processes. These heat transfer processes depend upon the rate of heat generation by the spent fuel, the thermal boundary conditions on the enclosing surfaces, the backfill media, system pressure, SNF surface properties, and the orientation of the waste package, - as well as internal geometric parameters. This chapter will detail the fundamental heat transfer mechanisms associated with SNF storage and transportation, both on an individual fuel assembly and entire cask basis. Emphasis will be given to horizontally oriented fuel assemblies, and the debate surrounding the importance of the natural convection process will be reviewed. The latter sections of the chapter provide an experimental methodology, based on theoretical considerations, which will allow resolution of the stated experimental objectives.

3.2 SNF HEAT TRANSFER FUNDAMENTALS

3.2.1 Spent Fuel Decay Power

The heat generated by a spent nuclear fuel assembly evolves from the radioactive decay of various isotopes, produced either directly or indirectly by the nuclear fission process. Some of these isotopes are fission products or their radioactive daughters, primarily confined within the fuel region itself; while some radioactive isotopes are neutron activation products and are located in the non-fuel support structures. The heat level at a given time is primarily dependent upon specific operating conditions such as the fuel burnup, expressed in giga-watt days per metric ton of initial heavy metal (GWD/MTIHM), the type of fuel assembly, and the age or cooling period following removal of the assembly from the reactor core. Figure 3.1 illustrates the decay power produced per fuel assembly, for both BWR and PWR assemblies, as a function of burnup and age (DOE/RW-0184, 1988). The greater the burnup, the greater the concentration of fission-produced radionuclides, and therefore the greater the thermal decay power. The average burnup for light water reactor (LWR) fuel assemblies is of the order of 35 GWD/MTIHM. Also, a typical PWR assembly contains 0.464 MTIHM (uranium); whereas, a typical BWR fuel assembly contains 0.189 MTIHM. Thus, on a per fuel assembly basis, a PWR assembly has a greater thermal energy production rate than a corresponding BWR assembly.

Note from Figure 3.1 that the thermal energy production rate of SNF is highly dependent upon the age of the fuel assembly, or the length of time that the

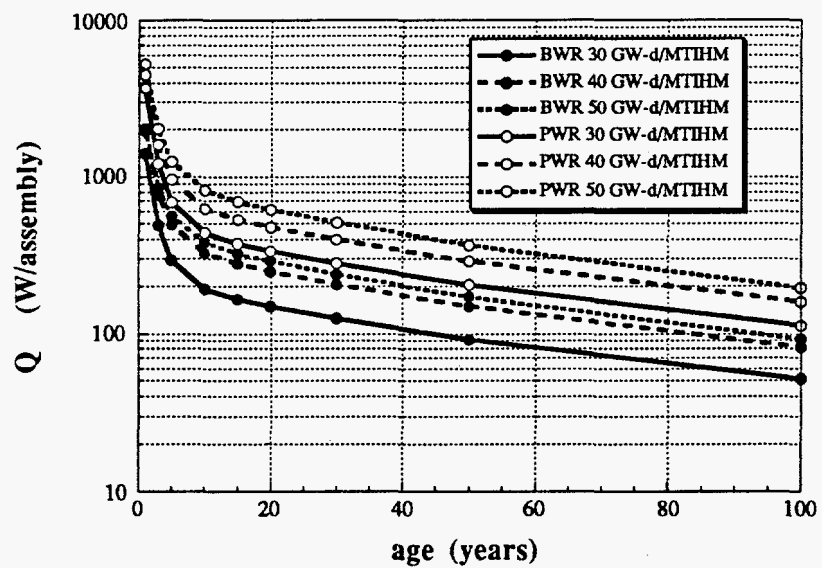


Figure 3.1 Thermal energy produced by PWR and BWR fuel assemblies

assembly has cooled following core removal. This is due to the fact that all radionuclides eventually decay to stable, non-radioactive states. Right out of the reactor, both types of LWR assemblies produce thousands of watts per assembly. However, after ten years, the PWR assembly is producing 400-900W and the BWR assembly is generating 200-400W. After twenty five years, these rates have dropped further; the PWR assembly produces about 300-600W while the BWR assembly produces only 150-275W. In light of the current political and legislative climate, it is expected that essentially all SNF will be cooled to 15+ years before transportation or dry storage is considered. Thus, the thermal energy source that SNF represents with regard to transportation and disposal is relatively small. Figure 3.2 re-emphasizes this point, by plotting the thermal energy generated by a single BWR fuel rod as a function of burnup and age (A BWR assembly contains 64 rods). In the time frame of interest (> 10 yr cooled), thermal decay power is typically less than 5W per fuel rod. Table 3.1 depicts the heat flux at the cladding surface of nuclear fuel, both during operation in the reactor core and following removal (Anderson, 1979). Without question, the heat flux at the cladding surface for aged spent fuel is extremely low. Nevertheless, thermal concerns arise when many spent fuel assemblies are grouped together, such as in transportation casks and geologic repositories. Federal regulations limit the fuel cladding temperature, the temperature of the cask/container surface, and the total repository heat load (kW per acre). Design considerations call for the minimization of thermal gradients within SNF packages in order to reduce thermal stress and ensure the long-term safety of such systems.

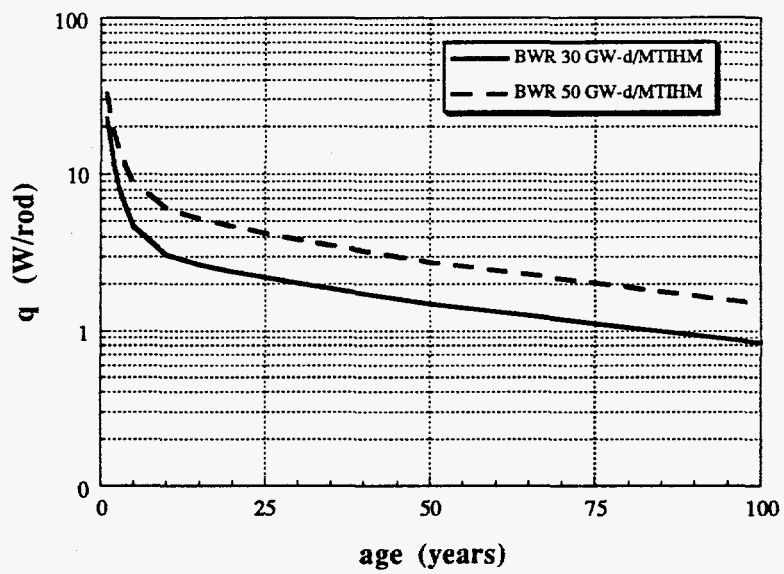


Figure 3.2 Decay power for a single BWR fuel rod

Table 3.1 Comparative fuel rod heat fluxes for active and spent fuel

Condition	Heat flux (W/m ²)
Maximum (local) nuclear fuel during operation	$\approx 2.76 \times 10^{+06}$
Average nuclear fuel during operation	$\approx 7.10 \times 10^{+05}$
Spent fuel after 10 years cooling	$\approx 20-35$
Typical light bulb (incandescent)	4700

3.2.2 Multimode Heat Transfer

3.2.2.1 Overview

Figure 3.3 depicts a cross section of a single LWR fuel rod. The vast majority of the thermal energy produced by a spent fuel rod comes from the radioactive decay of fission products trapped within the central, uranium dioxide fuel pellet region. In most thermal analyses, the fuel pellet region is treated as a uniformly generating volumetric energy source (Incropera & DeWitt, 1990). The thermal energy generated in the UO₂ pellet is conducted and radiated across a narrow helium filled gap, conducted through the metallic fuel rod cladding, and eventually transported to the surroundings by combined natural convection and thermal radiative processes. The physical dimensions associated with typical LWR fuel are given in Table 3.2 (Duderstadt & Hamilton, 1976).

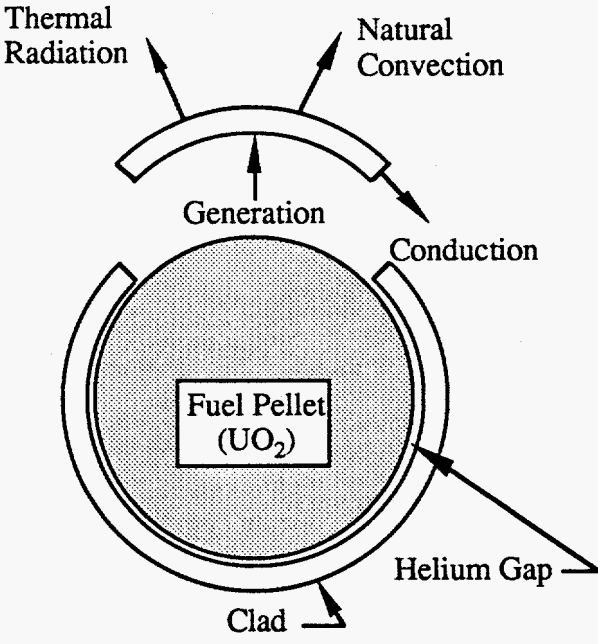


Figure 3.3 The multimode heat transfer processes associated with spent fuel

Table 3.2 Dimensions of typical LWR fuel

	PWR	BWR
fuel pellet diameter	0.819cm	1.056cm
helium gap width	0.0082cm	0.008cm
clad thickness	0.0572cm	0.0864cm
fuel rod outer diameter	0.94cm	1.23cm
rod pitch	1.25cm	1.62cm
assembly dimension	21 X 21cm	14 X 14cm
assembly length	409cm	436cm
active fuel length	366cm	376cm

Recall from Chapter 1, Section 1.2.2, that a light water reactor fuel assembly is comprised of anywhere from 64 to 289 individual rods (a typical BWR and PWR assembly, respectively). In the case of the BWR assembly, the rod bundle is enclosed in a rectangular fuel channel; whereas, a PWR assembly is not enclosed. However, when a SNF assembly is loaded into a storage, transportation, or disposal cask, the assembly is nevertheless typically enclosed in a given cell of the fuel basket (Figure 1.3). Thus, the thermal energy released by the decay of radioactive nuclides within each fuel rod is ultimately transported to the surrounding fuel channel/basket enclosure by combined natural convection and thermal radiation. During either transportation from a reactor site to a repository, or during storage in a dry environment, proposed procedures call for keeping the spent fuel assemblies in a horizontal orientation, sealed within a shipping/storage

cask containing a gaseous atmosphere such as nitrogen or helium (DOE/RW-0184, 1988). Hence, from a heat transfer perspective, the spent fuel thermal problem can be generalized as one of multimode heat transport within an enclosed array of horizontal cylinders.

Note from Table 3.2 that LWR fuel assemblies are over four meters in length, but are only 14 X 14cm or 21 X 21cm square (for a BWR and PWR assembly, respectively). Hence, essentially all engineering thermal analyses of horizontal spent fuel systems consider only two dimensional heat transfer mechanisms, neglecting axial effects. This is a good assumption despite the fact that in a nuclear reactor, the neutron flux is axially non-uniform over the length of the core (an assembly's length); consequently, the resulting burnup, and hence decay power, is axially non-uniform (the reported axial peak to average ratio is 1.1 - 1.2 [Manteuffel, 1991]). Furthermore, SNF assemblies are treated as uniformly generating thermal structures. In other words, the energy generation rate for all rods in a given assembly is assumed equal. Radially though, the neutron flux over an entire reactor core is not uniform either. However, over the dimensions associated with *single* fuel assembly, the radial flux gradient is negligible in comparison with the axial (Figure 3.4).

Thermally, the orientation of SNF only affects the convective heat transfer process. The thermal boundary layer length is significantly larger for vertically oriented assemblies undergoing natural convection than for corresponding

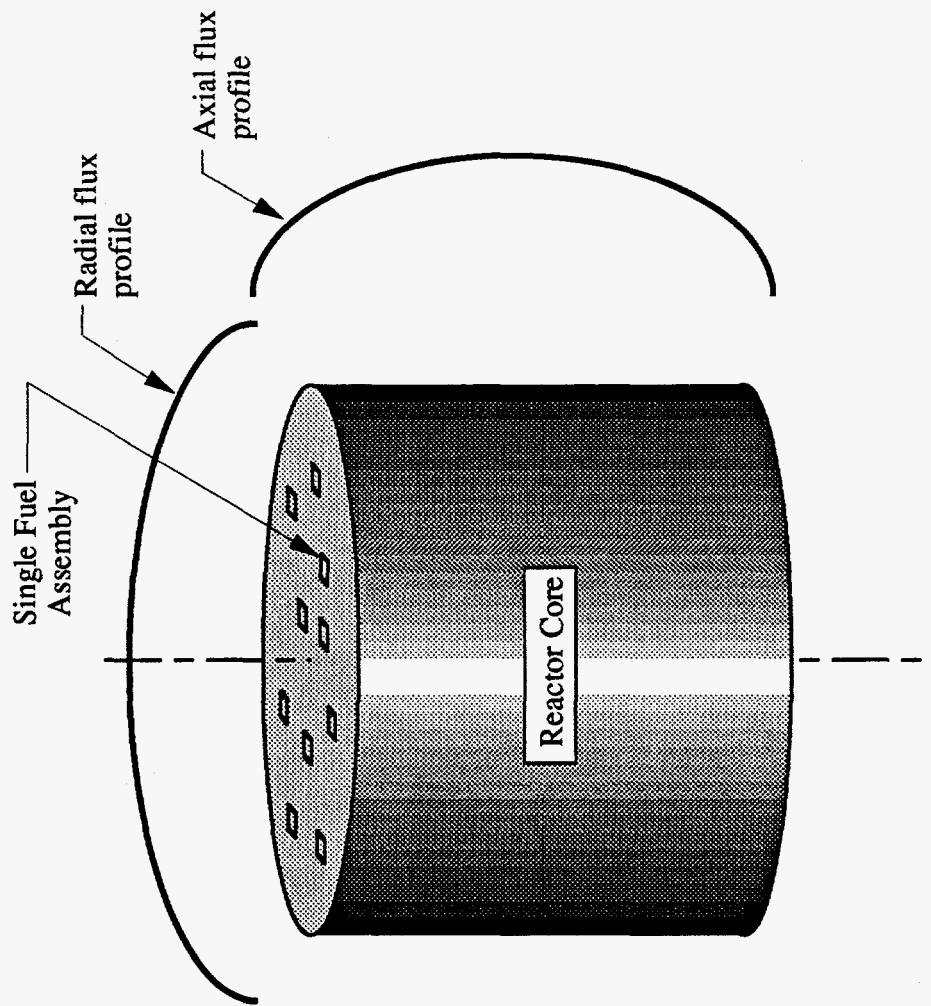


Figure 3.4 Comparison of core radial and axial neutron flux distribution

horizontal orientations. In the absence of natural convection, a fuel assembly's temperature distribution is 1/8 symmetric, and independent of assembly orientation. However, for horizontal SNF in which convection is significant, thermal symmetry only exists along a vertical plane (Figure 3.5). The natural convective contribution to the overall assembly heat transfer will be further discussed in Section 3.2.3.

3.2.2.2 Importance of Accurate Thermal Analysis

Figure 3.6 is an example of results obtained from a commercial code-based thermal analysis of a spent fuel cask (Bahney, 1993). These results correspond to a horizontal cask, identical to the one depicted in Figure 1.3, containing 21 PWR assemblies which have a burnup of 40 GW-d/MTIHM and have been cooled for 40 years. The cask is shown in cross section. The left-hand side of the figure is a heat flux plot; whereas, the right-hand side depicts the temperature distribution throughout the cask. In this model, each cell of the honeycomb-structured fuel basket contains a 40 year old spent fuel assembly. From the heat flux plot, it is evident that the majority of the thermal energy generated by the enclosed fuel assemblies is conducted via the high thermal conductivity basket material to the cask surface. From the temperature plot, the basket wall temperature is shown to be circumferentially variant for intermediate basket positions; whereas, the center position and the edge positions are nearly isothermal. A key aspect of these results however, concerns not the predicted thermal features, but rather the details of the numerical model. Typically,

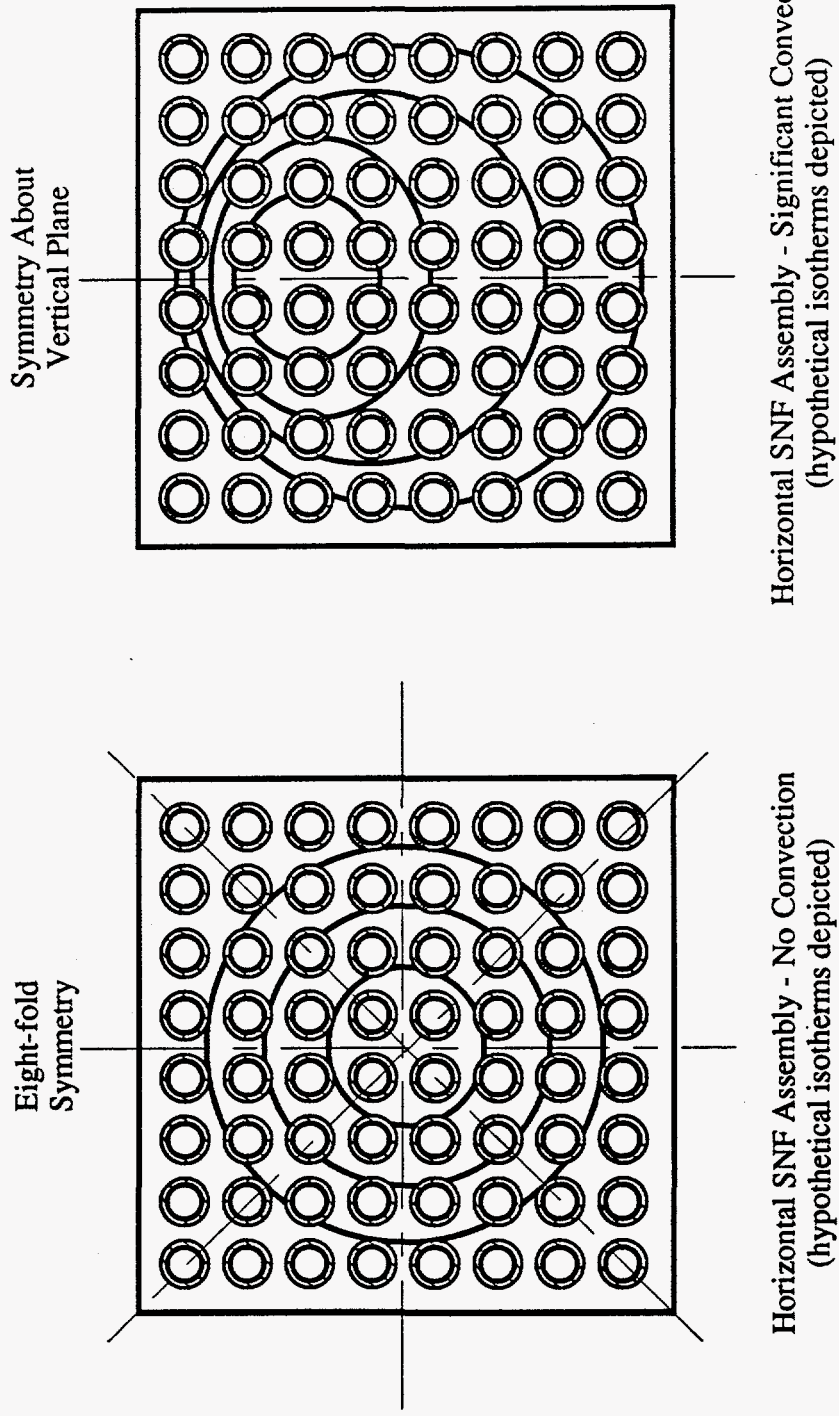


Figure 3.5 Symmetry considerations associated with horizontally oriented SNF assemblies

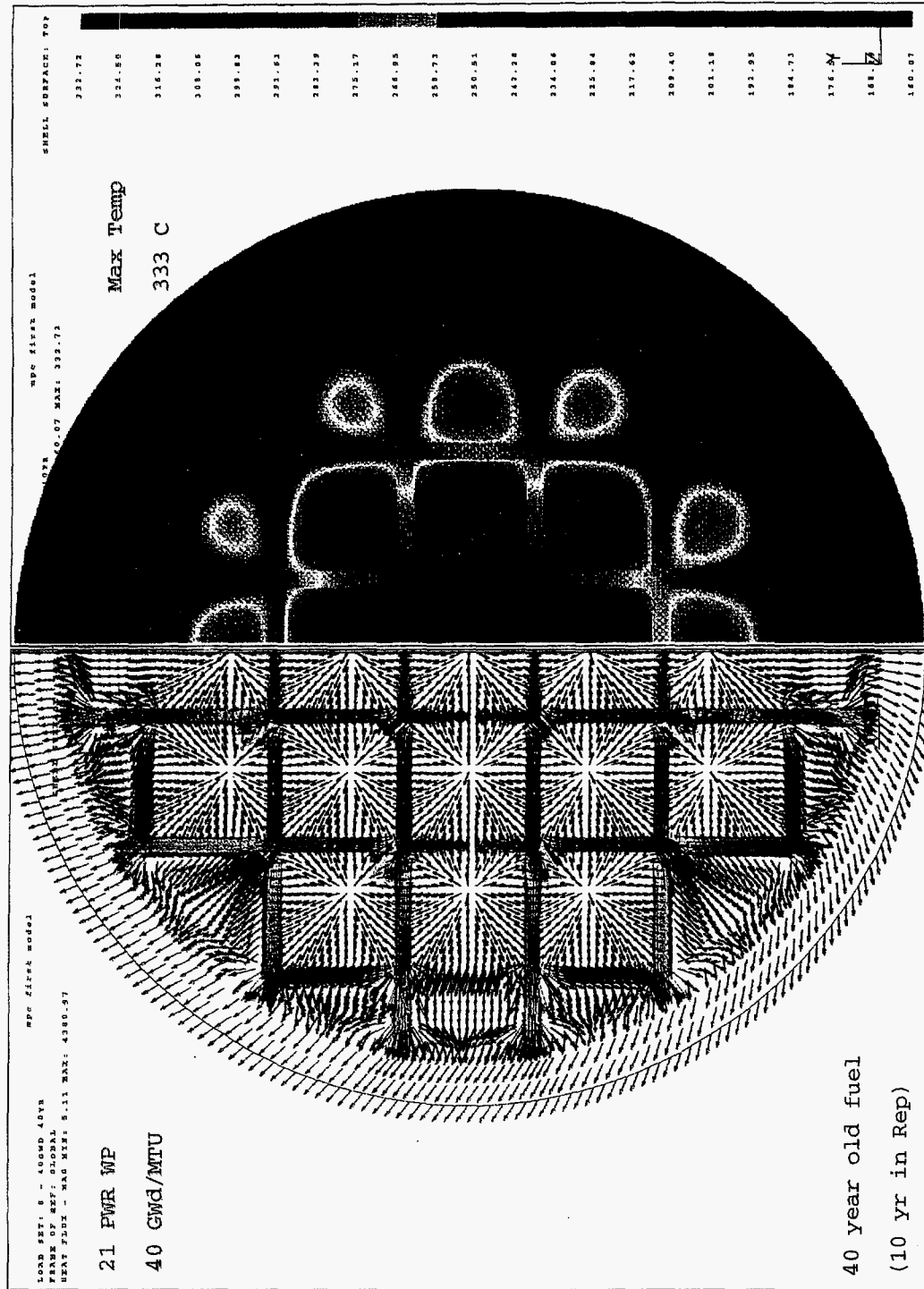


Figure 3.6 Thermal analysis of a B&W rail cask using an effective conductivity approach, [from Bahney, (1993)]

analyses such as these are made by assuming that conduction is the only heat transfer mechanism present. As such, the spent fuel assemblies are homogenized, and are represented by an effective thermal conductivity which is generally an area averaged quantity based upon the known conductivities of the present materials. By neglecting natural convection and radiation heat transfer, the door is open for significant thermal inaccuracy (temperature overprediction). The result may be an overly conservative design from a thermal perspective. This is of potential concern in any fuel cycle since one strives to maximize the number of fuel assemblies in a given shipping/storage cask in order to minimize the total number of SNF transfers, thus minimizing public and worker radiation exposure and the potential for accident. The relative importance of natural convection and radiative heat transfer in spent fuel systems is the subject of Sections 3.2.3 and 3.2.4, respectively.

3.2.3 Natural Convection in Horizontal Spent Fuel Assemblies

3.2.3.1 The SNF Convection Debate

There has been considerable discussion about whether natural convection is a significant heat transfer mechanism within horizontal spent fuel systems. Because of the difficulties associated with numerically modeling natural convection in a geometry as complex as a nuclear fuel assembly, most SNF thermal analysts have ignored the process entirely, or in some instances have used gross approximations of the convective process. For example, Wix and Koski (1993) modeled a single horizontal spent fuel assembly using a commercial finite

element conduction/radiation code, which did not contain an explicit convective capability. Rather, free convection experimental correlations from the code's internal library, corresponding to data obtained from a single, isolated horizontal cylinder in a quiescent medium, were used for each rod position within the fuel assembly. Clearly this is a rough approximation of the convection process at hand. However, no other reasonable correlations were available. The alternatives would have been to either ignore convection entirely, or explicitly solve the Navier-Stokes equations in combination with the radiatively coupled energy equations - a task requiring significant computational resources and expense (Butler, 1994). Certainly, some evidence is needed which indicates the importance of free convection in SNF systems such that these decisions may be more knowledgeably addressed.

Manteuffel (1991) concludes following his extensive review of previously published experimental data, that SNF fuel assemblies in a horizontal orientation, whether exposed to a helium or nitrogen backfill, will remain within a conduction regime. In other words, fluid motion is not expected to affect the overall assembly heat transfer. He states:

From the available experimental data, it can be concluded that a PWR (assembly) with a helium backfill will remain in the conduction regime. With nitrogen backfill, it will remain in the conduction regime for all horizontal orientations. If it is vertically oriented and resides in a loose enclosure with nitrogen, then it may go into the convection regime. Admittedly, all of these assessments are approximations.

Subsequently, Manteuffel offers an effective thermal conductivity approach to SNF assembly thermal analysis which includes radiative and conductive contributions, but ignores natural convection. Yet, his theoretically based model consistently overpredicts experimentally measured temperatures obtained in rod bundles subject to convective backfills. For example, when comparing the results of his effective conductivity model to experimental data reported by Eggers (1983) for an unconsolidated 8X8 enclosed horizontal rod bundle in air, Manteuffel overpredicts the peak rod to enclosure temperature difference by over 100%. However, for the same rod bundle in a consolidated form, which physically precludes natural convection (Eggers, 1985), Manteuffel's model improves considerably.

Despite the fact that there are few detailed systematic studies of combined radiation/convection within enclosed rod bundles, several researchers offer further evidence that natural convection may be an important mechanism in this geometry. Keyhani and Luo (1994) have recently conducted a numerical study of natural convection in enclosed horizontal rod bundles containing up to 81 individual rods. They report that:

there is significant flow activity in the enclosure...The isotherms clearly show that the majority of the energy generated within the enclosure is transferred to the top and side plates. This indicates that, as suspected, convection is a major factor in heat transfer in transportation casks.

The previously discussed experimental data of Fry *et al.* (1983) and Irino *et al.* (1986) [cf. Chapter 2.2] provide additional support for the argument that natural

convection plays an important role in the heat transfer of horizontally oriented SNF systems. One of the primary objectives of this dissertation is to further address this debate and subsequently quantify the role of free convection under a range of SNF thermal environments.

3.2.3.2 *The Rayleigh and Nusselt Number*

Typically, the results of natural convection studies are presented in terms of the dimensionless Rayleigh and Nusselt numbers. Developing correlations between these non-dimensional parameters allows convenient application of the results to similar systems and further provides some physical insight as to the fundamental nature of the free convection process of interest. In general, the Nusselt number is defined as the product of the heat transfer coefficient, h , and an appropriate length scale, L , divided by the thermal conductivity of the fluid medium:

$$Nu = \frac{hL}{k_f} \quad (3.1)$$

This parameter is equal to the dimensionless fluid temperature gradient at the surface of the convecting body and provides a measure of the convection heat transfer occurring at the surface. Often, the Nusselt number is defined to be equal to 1.0 for the lower limiting condition of no fluid motion, and hence no convective heat transfer enhancement beyond stagnant fluid conduction. Using Newton's law of cooling, the Nusselt number may be expressed in terms of the convective heat transfer rate, q_c'' , and a characteristic temperature difference

between the convecting body's surface and some fluid reference temperature, i.e.

$$\Delta T = T_s - T_{ref}$$

$$Nu = \frac{q_c'' L}{\Delta T k_f} \quad (3.2)$$

When describing natural convection in a given geometry, the Nusselt number is often taken to be a universal function of the Rayleigh number, Ra . The Rayleigh number as traditionally defined represents the ratio of the natural convection inducing buoyancy force to that of the viscous force acting on the fluid. The Rayleigh number takes into account the particular fluid's Prandtl number, the latter being a measure of a fluid's effective potential for momentum and thermal diffusion. Generally, the Rayleigh number is defined in terms of a characteristic temperature difference and the transport/thermodynamic properties of the fluid:

$$Ra = \frac{g \beta \Delta T L^3}{\nu \alpha} \quad (3.3)$$

where

g is the gravitational constant

β is the thermal expansion coefficient of the fluid

ν is the kinematic viscosity of the fluid, and

α is the thermal diffusivity of the fluid.

Physically, the Rayleigh number provides a measure of the local fluid buoyancy. The greater the Rayleigh number, the greater the local fluid buoyancy, and the greater the potential for fluid motion and subsequent natural convection heat transfer enhancement. Thus, the Nusselt number generally increases monotonically with increasing Rayleigh number.

For a horizontal SNF assembly, or in general an enclosed rod array, it makes sense to define a Nusselt/Rayleigh number for each rod within the array, as well as an array averaged Nusselt/Rayleigh number. These definitions will be discussed later in greater detail (cf. Chapter 7).

3.2.3.3 Factors Which Influence Natural Convection in SNF

Natural convection heat transfer occurs when there is a temperature difference between a body immersed in a fluid and the surrounding fluid. The resulting temperature gradient which forms in the fluid produces a density gradient, which, in the presence of a body force such as gravity, induces buoyant fluid flow. This increase in local fluid velocity enhances the heat transfer from the body to the surrounding fluid beyond that which would occur if the gas were stagnant and only conduction were present. The thermal boundary layer is the physical region in which the temperature gradient is formed and is thus the region in which natural convection heat transfer occurs. The effectiveness of a given natural convection process depends upon conditions in the boundary layer, which are in turn influenced by surface geometry, the nature of the fluid motion, and a number of fluid thermodynamic and transport properties.

In the enclosed rod bundle geometry characteristic of SNF assemblies, a key factor which influences the magnitude of natural convection is the backfill gas. The importance of the backfill gas can be seen by observing the influence of the thermophysical properties on the Rayleigh number. For example, consider the Rayleigh number ratio of a given gas to that of helium at atmospheric pressure and at a mean fluid temperature of 300K:

$$\frac{Ra_{gas}}{Ra_{He}} = \frac{(\nu\alpha)_{He}}{(\nu\alpha)_{gas}} = \left(\frac{M_{gas}}{M_{He}}\right)^2 \left(\frac{c_{p,gas}}{c_{p,He}}\right) \left(\frac{\mu_{He}}{\mu_{gas}}\right) \left(\frac{k_{He}}{k_{gas}}\right) \quad (3.4)$$

Here, M is the molecular weight and ideal gas behavior has been assumed. Consider this ratio for the following backfills at the stated conditions (Manteuffel, 1991):

<u>gas</u>	<u>ratio</u>
He	1
N ₂	65
Ar	75
CO ₂	250
SF ₆	2400

Note the effect that the dense gases have on the Rayleigh number. The potential for natural convection heat transfer enhancement is certainly tied to the Rayleigh number; thus, the given ratios indicate which backfills have a greater convective potential. Current SNF transportation/storage scenarios call for the use of either helium or nitrogen backfills. A choice of nitrogen over helium (for a given ΔT),

results in a 65 fold increase in the Rayleigh number, significantly increasing the potential for convective fluid motion.

The Rayleigh number, and thus the potential for natural convection, is also highly dependent upon the global system pressure. Note from equation (3.3) that

$$Ra \sim \frac{1}{v\alpha} \quad (3.5)$$

since

$$v = \frac{\mu}{\rho}, \quad (3.6)$$

and

$$\alpha = \frac{k}{\rho c_p} \quad (3.7)$$

then

$$Ra \sim \rho^2 \sim p^2 \quad (3.8)$$

again, assuming ideal gas behavior ($\rho = pM / R_u T$). Thus, doubling the system pressure results in a four fold increase in the Rayleigh number, and so on. Current proposals call for shipping and storing SNF at or slightly below atmospheric pressure.

Of course, the potential for natural convection is dependent upon the temperature difference between the convecting body and the surrounding reference fluid. It is this temperature difference which gives rise to fluid density

gradients and the resulting buoyant force. Thus, to a large degree, the convective process in SNF assemblies is tied to the decay power or age of the fuel. However, this does not imply that the 'hotter' (or less aged) fuel is most likely to be convection dominated. In fact, it is more probable that spent fuel cooled less than five years will be dominated by thermal radiation heat transfer processes (Anderson, 1979). Some insight into this assertion may be gained by examining the effect of the mean backfill gas temperature on the Rayleigh number, as before. Recalling the Rayleigh number definition given by equation (3.3), note that the thermal expansion coefficient for an ideal gas is:

$$\beta = \frac{1}{T} \quad (3.9)$$

Also note from the kinetic theory of gases that the thermal conductivity and viscosity are only functions of temperature, roughly:

$$k \sim \sqrt{T} \quad (3.10)$$

$$\mu \sim \sqrt{T} \quad (3.11)$$

And the ideal gas density is inversely proportional to temperature:

$$\rho \propto \frac{1}{T} \quad (3.12)$$

Hence, it follows from equation (3.3) and equations (3.9) through (3.12), that the Rayleigh number scales as the inverse of the fourth power of temperature:

$$Ra \sim \frac{1}{T^4} \quad (3.13)$$

Thus, when the bulk fluid temperature within a spent fuel assembly is increasing, the Rayleigh number, as far as its dependencies on fluid thermophysical properties is concerned, is suppressed. Conversely however, as temperatures rise within the assembly, thermal radiation tends to become increasingly significant. Thermal radiation in spent fuel assemblies is the subject of the following section.

3.2.4 Thermal Radiation in Horizontal Spent Fuel Assemblies

3.2.4.1 General

Thermal radiation heat transfer occurs when matter at differing temperatures exchange thermal energy in the form of electromagnetic waves (or alternatively photons). When spent fuel assemblies are transported or stored in a dry environment, they reside inside containers which are filled with non-reacting gases such as helium or nitrogen. These gases are transparent to thermal radiation and are said to be non-participating. Thus, thermal radiation exchange in spent fuel assemblies occurs between assembly component *surfaces*, separated by a gaseous interface, which are at different temperature. The radiative heat transfer rate (flux) associated with a given surface and its surroundings (large) can be expressed as function of the temperature of the participating surfaces raised to the fourth power:

$$q''_{r,net} = \epsilon\sigma (T_s^4 - T_{sur}^4) \quad (3.14)$$

where,

σ is the Stefan-Boltzmann constant, and

ϵ is the emissivity of the surface

In a spent fuel assembly, the situation is more complicated however, as the visibility of the closely packed fuel rods and their surrounding enclosure must be taken into account. However, equation (3.14) indicates that the radiative heat transfer in dry spent fuel assemblies is dependent upon the SNF decay power, the temperature of the enclosure or fuel basket, and the surface properties of the spent fuel material. Note from equation (3.14) that even slight increases in overall SNF component temperatures result in significant increases in the radiative contribution, which gives rise to the added importance of thermal radiation for relatively short-term cooled spent fuel (< 5 years of cooling).

Since all of the fuel rods in a given spent fuel assembly are generating approximately the same thermal power, each fuel rod will have a unique surface temperature, and a temperature gradient will exist across the fuel assembly (Figure 3.7). Thus, a given fuel rod in a spent fuel assembly will be subject to an incident radiative flux which is spatially non-uniform around the circumference of the rod. This flux is related to the emissive power of neighboring fuel rods ($\epsilon\sigma T^4$). When no temperature gradient exists within the array, no non-uniform incident flux exists, no heat transfer occurs, and the problem is trivial. Although the *net* radiative heat transfer must be away from the rod, there will be local radiative heat transfer both to and from a given rod (Figure 3.8). The magnitude of a rod's radiative heat transfer is thus dependent upon the rod's position in the

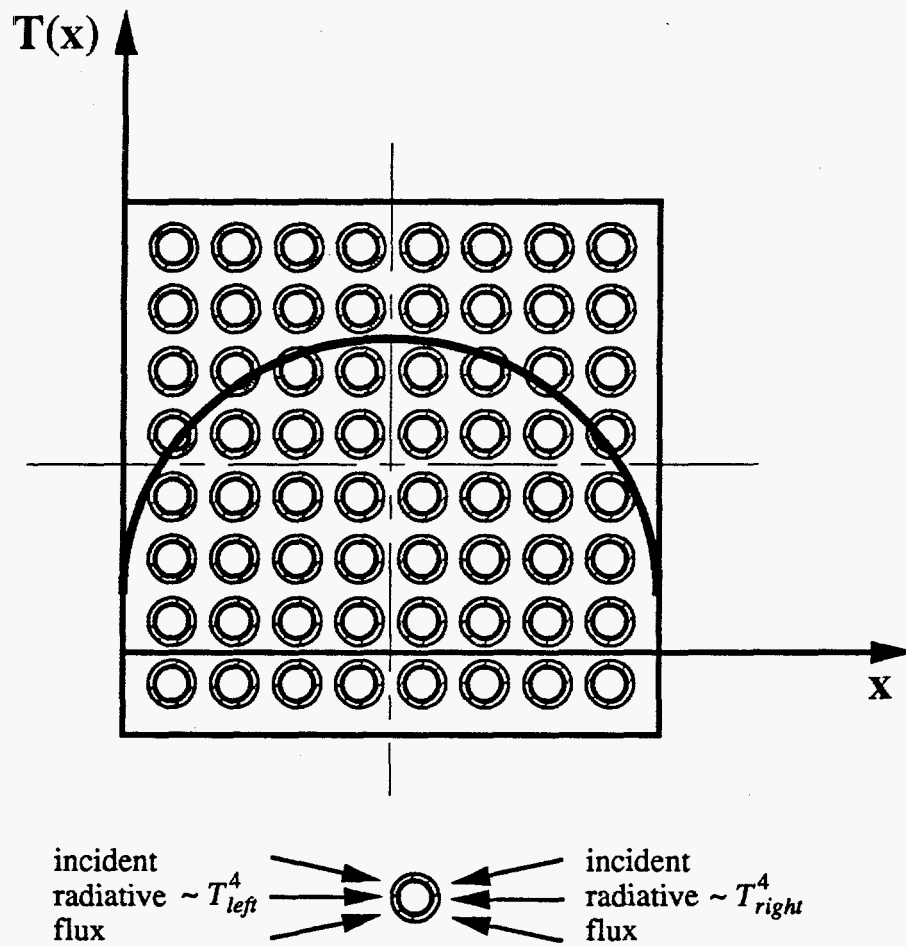


Figure 3.7 Non-uniform incident radiative flux in spent fuel assemblies,
[adapted from Manteuffel, 1991]

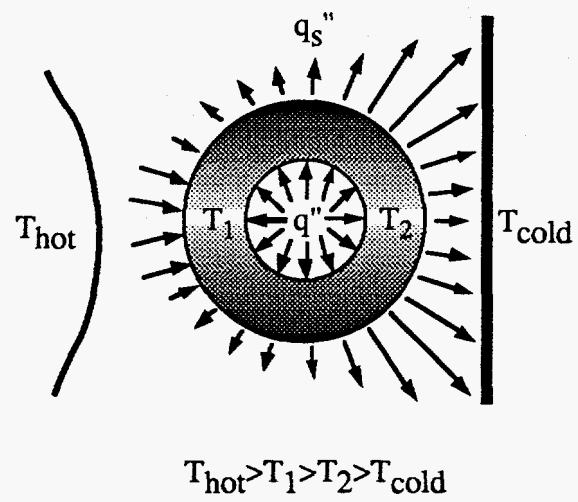


Figure 3.8 Local radiative heat transfer both to and from a given fuel rod

array. For example, in a horizontal spent fuel assembly, it is likely that fuel rods at the center of the array will be surrounded by neighboring rods which are of similar temperature. These rods will additionally be very nearly radiatively blind to the surrounding (cool) fuel enclosure/basket. Conversely, rods located on the periphery of the array will be exposed to both hot fuel rods and a good portion of the relatively cool enclosure. Thus, it is probable that the potential for heat transfer by thermal radiation is greater for the outer rods than that of the rods located in the core of the assembly (Kulacki & Keyhani, 1987). However, this condition will also be influenced by the presence of natural convection circulation patterns within the array, if any.

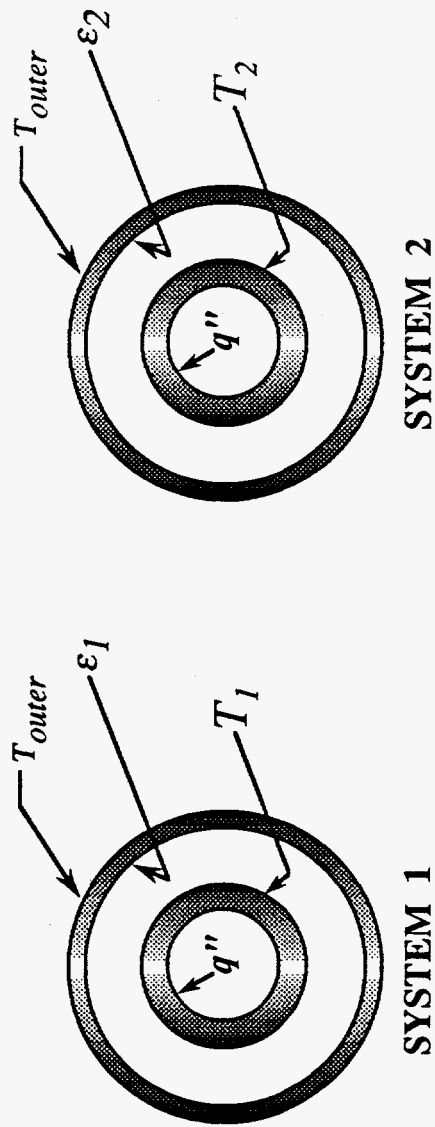
For the problem of radiative heat transfer in an enclosed spent fuel assembly, the assumptions of gray and diffuse surface behavior are often invoked. The gray assumption implies that the emissivity, ϵ , of all surfaces in the assembly is equal to the absorptivity, α , and that both are independent of wavelength. Thus, the surfaces have no special preference with regard to their abilities to emit or absorb energy at a particular wavelength. No real materials are gray over all wavelengths; however, pragmatically speaking a surface is gray if the energy that is being exchanged is concentrated in a wavelength band for which the emissivity and absorptivity are nearly independent of wavelength. The diffuse assumption implies that the radiation reflected or emitted from any surface is diffusely or uniformly distributed according to Lambert's cosine law (see Chapter 8.3.1.2). In a spent fuel assembly, the assumptions of gray and diffuse are a result of the oxidized rod/enclosure surfaces. Increasing oxidation provides an increasingly

rough surface which approximates the gray/diffuse behavior. There have been several experimental measurements of the emissivity of spent fuel rods subject to varying levels of surface oxidation. These data are included in the material properties library MATPRO (1990), a collection of properties and parameters distributed with several NRC thermal-hydraulics codes. The MATPRO recommended value for spent fuel rod emissivity is $\epsilon = 0.8 \pm 0.2$, implying that if one were to measure the emissivity of a given spent fuel rod, there would be 95% chance that the surface would have an emissivity between 0.6 and 1.0. Although this value appears consistent throughout the available literature, one should be mindful that there is often significant variance in the radiative surface properties measured by different investigators, regardless of how similar the measured materials may be. An important consideration regarding the accurate determination of the radiative surface properties of spent fuel is discussed in the following section.

3.2.4.2 Importance of Isolating Radiation from Convection

In the experimental study of systems characterized by combined or multi-mode heat transfer, it is often desirable to quantify the convective and thermal radiative processes in an independent manner. This is particularly true with regard to the presentation of correlations of convective Nusselt number and Rayleigh number. Simply stated, convective correlations should be expressed solely in terms of the convective heat transfer contribution, obtained by subtracting the radiative heat transfer contribution from the total heat transfer.

Failure to do this will result in convection correlations which are system dependent, or limited in use to systems which are identical to the one in which the data were obtained. In this case, 'identical', refers not only to geometry, but also to the exact radiative surface properties and absolute temperatures of the original system. Due to the wide variance in these properties from one system to the next, there is no guarantee that the correlations will have universal accuracy - unless they are fully radiation independent. Furthermore, failure to isolate the radiative contribution from the convective will result in convection correlations which do not have a true physical interpretation. Consider the two systems depicted in Figure 3.9. In this representative case, the geometry is one of two concentric cylinders, the inner one being exposed to a uniform heat flux, while the outer one is maintained at an isothermal state. Assume that the systems are characterized by combined convection and radiation heat transfer. The only difference between System 1 and System 2 is the radiative surface properties of the cylinders, namely the emissivity, ϵ . Because $\epsilon_1 \neq \epsilon_2$, the temperature difference between the inner and outer cylinders will not be equal either, i.e. $T_1 \neq T_2$. Thus, if one were to attempt to define an average heat transfer coefficient for the inner body in terms of the *total* heat transfer rate (q''), as in Figure 3.10a, a universal/system independent correlation would *not* result. However, if the convective contribution (q_c'') were independently known for both systems, and the heat transfer coefficient were defined in terms of this parameter, a system independent universal correlation could be constructed (Figure 3.10b). Of course, the ability to individually quantify the radiative and convective components is a prerequisite to this task. The remaining sections of this chapter will utilize the theoretical



Note: $\epsilon_1 \neq \epsilon_2$; thus, $T_1 \neq T_2$

Figure 3.9 Concentric cylinders exposed to the same inner body heat flux and outer body surface temperature, but possessing different emissivities

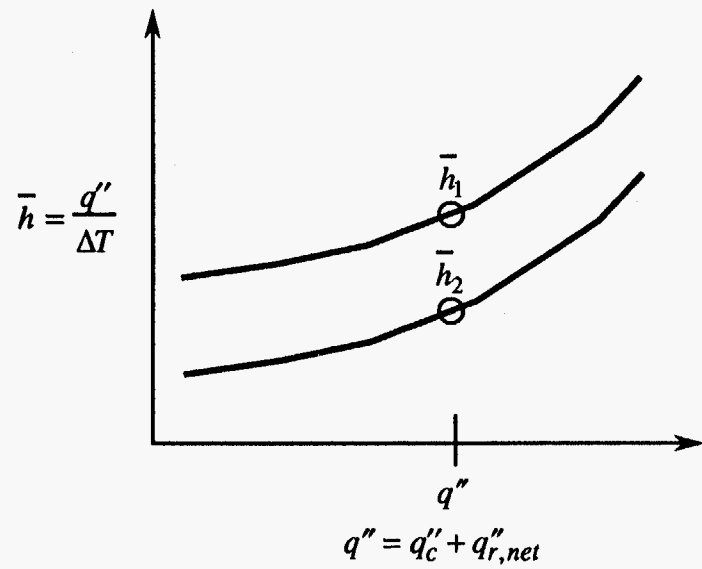


Figure 3.10a System dependent convection correlation

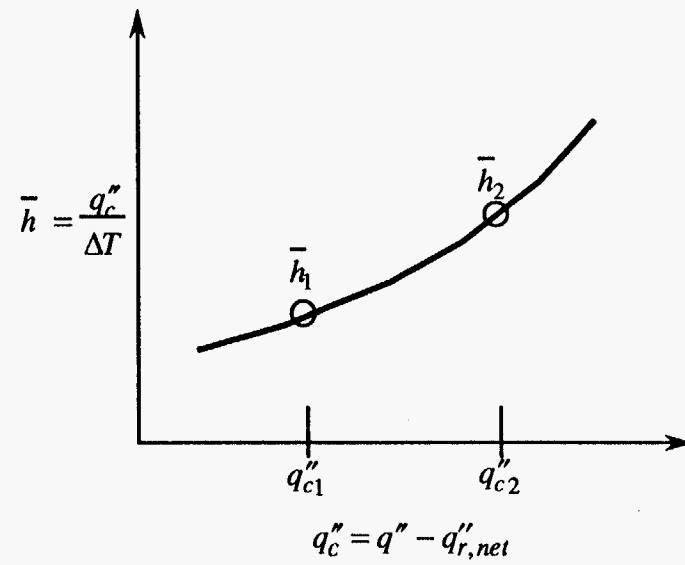


Figure 3.10b Universal convection correlation (radiation subtracted)

considerations previously discussed in order to develop a general methodology which will allow the experimental determination and quantification of the independent convective and radiative heat transfer processes associated with a horizontal dry spent fuel assembly.

3.3 EXPERIMENTAL METHODOLOGY FOR SNF HEAT TRANSFER MEASUREMENTS

An objective of this dissertation is to independently quantify the convective and radiative heat transfer mechanisms associated with a horizontal spent nuclear fuel assembly exposed to a gaseous backfill. This section will demonstrate the fundamental experimental methodology, based upon the theoretical concepts discussed earlier, which will allow this objective to be met. Consider the experimental arrangement depicted in Figure 3.11. This figure shows one of the multiple rods which constitute a nuclear fuel assembly. In this case, the spent nuclear fuel rod is simulated using an electrically powered resistance heater, which is geometrically and thermally equivalent to the actual fuel rod. It is assumed that the heater rod is sufficiently long (and/or insulated) such that axial conduction losses are negligible in comparison to the total supplied electrical power. Thus, the supplied electrical power, q' , is dissipated as illustrated in Figure 3.3 by the convective and radiative components, q'_c and $q'_{r,net}$, respectively. The total heat loss from the heater rod to the environment at steady state is given by the following relation, expressed on a per unit length basis by dividing through by the rod's heated length, L_h :

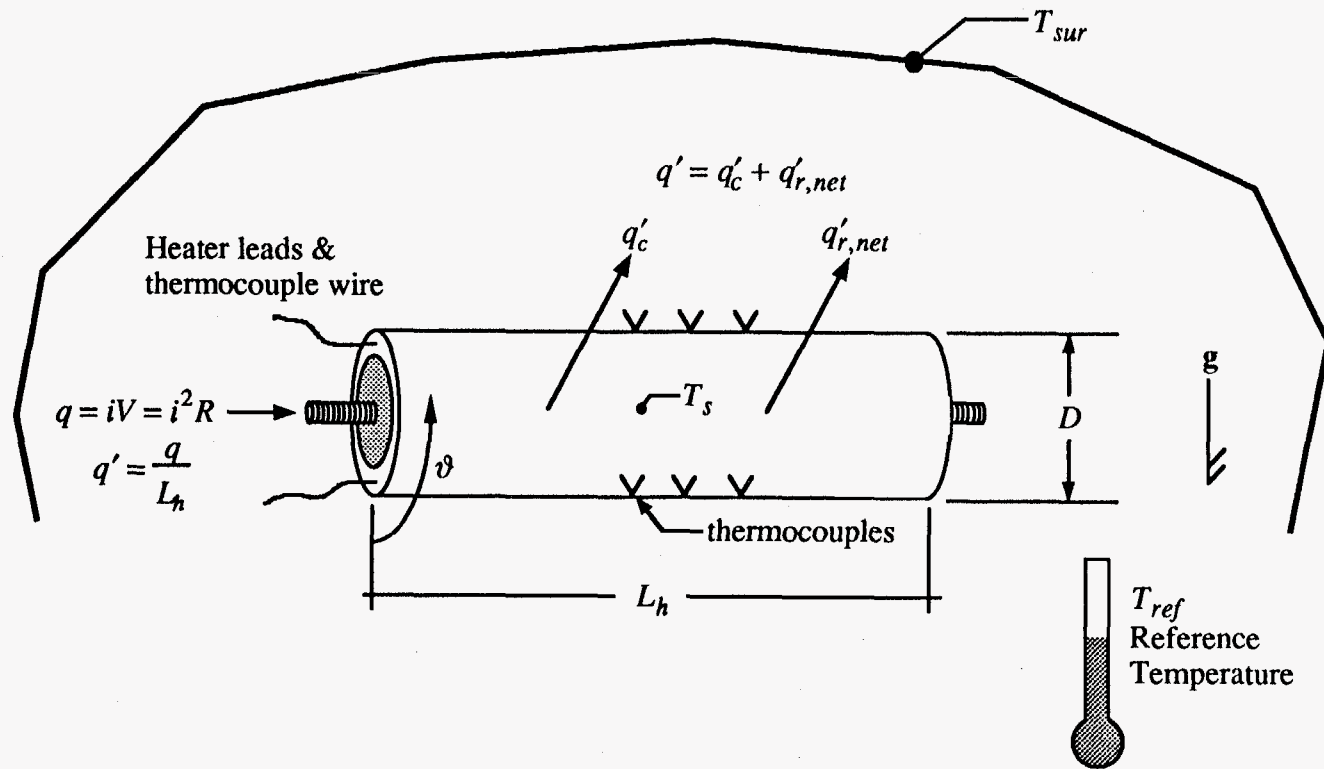


Figure 3.11 Schematic of heated rod arrangement for determination of SNF assembly heat transfer

$$q' = q'_c + q'_{r,net} \quad (3.15)$$

The total power supplied to the heater rod is measured either by taking the product of the line current and the rod's voltage drop,

$$q = iV \quad (3.16)$$

or by taking the product of the square of the current and the rod's electrical resistance:

$$q = i^2 R \quad (3.17)$$

where in general $R = f(T)$.

It is also a requirement that the surface temperature of the heater rod as well as an appropriate reference temperature be known. In the schematic of Figure 3.11, it is assumed that the heater rod is well equipped with thermocouples, mounted such that an accurate surface temperature measurement can be made.

The convective component of equation (3.15) may be expressed via Newton's law of cooling as a local heat flux, dependent upon the circumferential rod angle, ϑ .

$$q''_c = h(\vartheta) \{T_s(\vartheta) - T_{ref}\} \quad (3.18)$$

Provided that the heat dissipated by the heater rod is uniform in the axial direction, the heat rate per unit length may be related to the local heat flux by the following relation:

$$q' = \left(\frac{D}{2}\right) \int_0^{2\pi} q''(\vartheta) d\vartheta \quad (3.19)$$

Substitution of equation (3.18) for the flux term of equation (3.19), yields the following expression for the convective heat transfer rate per unit length:

$$q'_c = \left(\frac{D}{2}\right) \int_0^{2\pi} h(\vartheta) \{T_s(\vartheta) - T_{ref}\} d\vartheta \quad (3.20)$$

where,

T_s is the surface temperature of the heater rod

T_{ref} is an appropriate reference temperature

D is the heater rod diameter

ϑ is the circumferential rod angle, and

h is the convective heat transfer coefficient.

Due to the relatively low heat transfer coefficients expected within the confines of a horizontal spent fuel assembly, and the relatively high thermal conductivity of the fuel rod cladding, the surface temperature of a spent fuel rod will most likely be isothermal. In other words, it is expected that the surface temperature is circumferentially uniform. Thus, it is possible to rewrite equation (3.20) as follows:

$$q'_c = \left(\frac{D}{2}\right) \{T_s - T_{ref}\} \int_0^{2\pi} h(\vartheta) d\vartheta \quad (3.21)$$

For a cylindrical body, an average convective heat transfer coefficient may be defined by:

$$\bar{h} = \frac{1}{2\pi} \int_0^{2\pi} h(\vartheta) d\vartheta \quad (3.22)$$

Equation (3.22) may be substituted into equation (3.21) in order to yield the following expression for the convective component:

$$q'_c = \bar{h} \pi D \{T_s - T_{ref}\} \quad (3.23)$$

The radiative component of equation (3.15) can be simply expressed only for the case in which it is assumed that the heater rod interacts radiatively with surroundings which are 'large', such that a blackbody enclosure is approximated [see equation (3.14)]. In this elementary treatment, the radiative heat transfer from the heater rod per unit length is given as:

$$q'_{r,net} = \epsilon \sigma \pi D (T_s^4 - T_{sur}^4) \quad (3.24)$$

In an actual fuel rod array, a simple expression such as the one above is not possible. This is due to the complexities associated with the geometrical configuration factors which determine the radiative line of sight between adjacent fuel rods and their surrounding enclosure, as well as the reflected radiative components associated with a given rod's neighboring surfaces. This topic will be addressed in detail in Chapter 8 with regard to the SNF assembly problem, however; for convenience equation (3.24) will be assumed to be presently

applicable. Hence, substitution of equations (3.24), (3.23), (3.17), and (3.16), into equation (3.15), yields the following energy balance:

$$\frac{i^2 R}{L_h} = \frac{iV}{L_h} = \bar{h} \pi D \{T_s - T_{ref}\} + \epsilon \sigma \pi D (T_s^4 - T_{sur}^4) \quad (3.25)$$

If the objective of an experimental study is the determination of the average convective heat transfer coefficient for a given rod in an enclosed bundle, the above relation can be used, provided the appropriate quantities are known from measurement. Given the instrumentation scheme depicted in Figure 3.11 for *each* heater rod location in the bundle, and the capacity to measure the electrical properties of the resulting circuit, this task is relatively straight forward - provided care is taken to ensure the validity of equation (3.25). Namely, that axial effects have been made negligible via design (or correction) such that the resulting data are fully two dimensional. Also note from equation (3.25), that the emissivity of the radiatively participating surfaces must be known and/or measurable. The importance of this consideration was discussed briefly in Chapter 3.2.4.2; however, it will be reviewed in greater detail in Chapters 8 and 9.

The methodology described in this section serves as an introduction to the detailed experimental methodology and procedure which will be presented in Chapter 7. Furthermore, the explicit variable definitions and correlations which will be used to present the results of this investigation will be thoroughly reviewed in Chapter 7 as well. Now however, consideration will be given to the design aspects of an experimental mock-up of a horizontal spent nuclear fuel assembly. Chapter 4 will establish the design criteria which are pre-requisite to a

functional and effective test apparatus. Emphasis will be given to the design scoping calculations which were performed in order to determine the appropriate experimental thermal boundary conditions and the required instrumentation.

Chapter 4 - Preliminary Analyses and Scoping Calculations

4.1 OVERVIEW

The intent of this chapter is to describe a series of scoping calculations which were performed in order to accomplish the following objectives:

- 1) To develop a better understanding of the heat transfer processes associated with horizontal spent nuclear fuel assemblies.
- 2) To aid in the design of an experimental apparatus which thermally simulates a horizontal spent fuel assembly (in 2 dimensions).
- 3) To determine the type and level of instrumentation necessary to adequately quantify the heat transfer in an experimental mock-up of a spent fuel assembly.

Furthermore, it is hoped that the viability of the proposed experimental methodology (given in the previous chapter) can be ascertained by gaining further insight into the thermal nature of the spent fuel problem.

The results of five independent scoping analyses are presented, ranging from 'back-of-the-envelope' hand calculations to numerically evaluated finite element formulations of the Navier-Stokes equations in a full assembly. Specifically, the following cases were examined:

- 1) A Biot number calculation for a single horizontal fuel rod in a quiescent ambient environment.
- 2) A numerical convection analysis of a single horizontal fuel rod contained within a concentric enclosure (2 dimensional).
- 3) A numerical convection analysis of a complete SNF assembly in the horizontal orientation (2 dimensional).
- 4) A numerical radiative/convective analysis obtained in a corner region of a spent fuel assembly (2 dimensional).
- 5) An end effects analysis of a single horizontal fuel rod (1 dimensional)

These analyses are presented in the order in which they were carried out; accordingly, there is a logical progression in the calculational complexity (the last case being an exception). The following sections of this chapter review the respective cases in detail.

4.2 ISOLATED FUEL ROD

Consider a single horizontal cylinder undergoing natural convection in a quiescent ambient environment as shown in Figure 4.1. Such a cylinder might be considered a reasonable first order approximation for an individual fuel rod within a fuel assembly. Churchill and Chu (1975) have recommended a single natural convection correlation for a wide Rayleigh number range, ($10^{-5} < Ra_D < 10^{12}$):

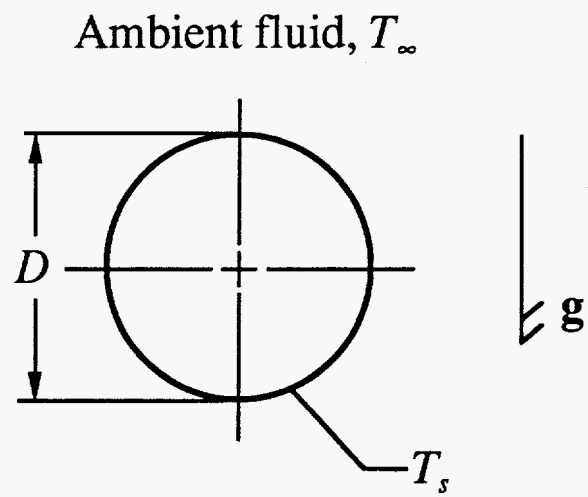


Figure 4.1 Horizontal convecting cylinder in a quiescent environment

$$Nu_D = \left\{ 0.60 + \frac{0.387 Ra_D^{1/6}}{\left[1 + (0.559 / Pr)^{9/16} \right]^{8/27}} \right\}^2 \quad (4.1)$$

where,

$$Ra_D = \frac{g\beta(T_s - T_\infty)D^3}{\nu\alpha} \quad (4.2)$$

and Pr is the Prandtl number of the convecting fluid.

The correlations represented by equations (4.1) and (4.2) provide the average Nusselt number over the entire circumference of the horizontal cylinder. By defining the conductivity ratio of the fuel cladding to the surrounding fluid, $k^* = k_c/k_f$, the Biot number for the single cylinder of Figure 4.1 may be expressed as:

$$Bi = \frac{Nu_D}{k^*} \quad (4.3)$$

The Biot number is a dimensionless parameter which provides a measure of the temperature drop in the solid cylinder relative to the temperature difference between its surface and the fluid. From equations (4.1) to (4.3), a plot of the variation of the Biot number for various values of the Rayleigh number and conductivity ratio may be developed, as shown in Figure 4.2. The two Rayleigh number cases indicated, $Ra_D = 1$ and $Ra_D = 10^5$, represent the limiting values expected within a spent fuel assembly containing either helium or air backfills.

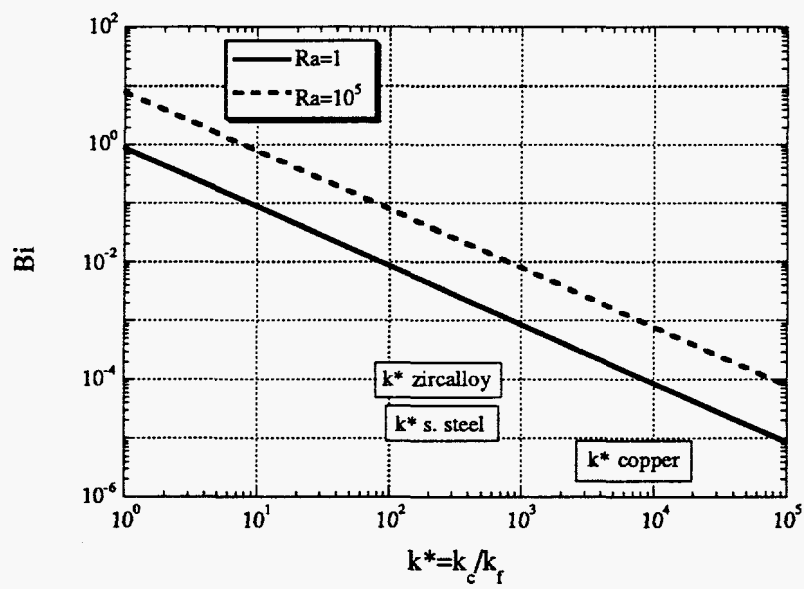


Figure 4.2 Biot number analysis for a single fuel rod in an quiescent medium

Also shown in Figure 4.2 are the ranges of conductivity ratio which correspond to various cylinder materials including zircalloy, stainless steel, and copper. The thermal conductivity ranges illustrated in the figure assume that the backfill gas is any of air, nitrogen, or helium.

Figure 4.2 clearly shows that the Biot number is less than unity for thermal conductivity ratios $k^* > 10$, even under the most vigorous natural convection environments expected within a horizontal fuel assembly. Furthermore, the thermal conductivity ranges for zircalloy, steel, and copper cylinders ($100 < k^* < 10^4$) produce Biot numbers which are less than 0.1, and thus suggest that the resistance to conduction within the solid cylinder is much less than the resistance to convection across the fluid boundary layer. Hence, it is reasonable to assume that the horizontal cylinder will be isothermal under a broad range of convective environments.

The above analysis is for a single isolated fuel rod and the question remains as to how these results should be interpreted in an actual fuel assembly such as the one depicted in Figure 3.5. The interaction of the thermal plumes generated by individual fuel rods within the assembly will undoubtedly influence the overall convective heat transfer. Specifically, the gas in the upper region of the assembly will have a higher bulk temperature due to heating from fuel rods lower in the array. Furthermore, the flow restriction caused by the proximity of the fuel rods in the array will restrict the convective motion of the backfill gas. The combination of these effects may tend to decrease the Nusselt number for a

given rod in an assembly relative to that of a single isolated rod at a similar Rayleigh number. This conclusion is consistent with the work of Tokura *et al.* (1983) and Marsters (1972), as reviewed in Chapter 2.3. Thus, from equation (4.3), it is apparent that a decrease in the Nusselt number represents a decrease in the Biot number. Therefore, the lines shown in Figure 4.2 would tend to shift downward in an actual fuel assembly, resulting in lower Biot numbers for a given conductivity ratio. The principle observation of this first order analysis is that, under reasonable natural convective conditions, the individual fuel rods which make up a fuel assembly will tend to be isothermal. This conclusion is reasonable considering the high conductivity of the fuel rods and the relatively low heat transfer coefficients expected in this geometry.

4.3 NATURAL CONVECTION IN A HORIZONTAL CONCENTRIC ANNULUS

The Biot number analysis of the previous section inherently assumed that the spent fuel rod was composed of a homogeneous high conductivity material. In an actual spent fuel rod, the thickness of the high conductivity cladding is quite small (see Table 3.2), and the vast majority of the fuel rod is composed of a low thermal conductivity pellet region (Figure 3.3). The relatively thin cladding may thus act to impede the flow of thermal energy in the circumferential direction about the fuel rod, which can alter the previous conclusion that the rod will remain isothermal. In order to investigate this possibility, as well as account for boundary layer effects, a more sophisticated convection analysis was carried out. Figure 4.3 depicts a single horizontal fuel rod (the inner body) surrounded by a

Model Dimensions

$$D = 2r_o = 12.24\text{mm}$$

$$\delta = 1.98\text{mm}$$

$$L = r_o = 6.12\text{mm}$$

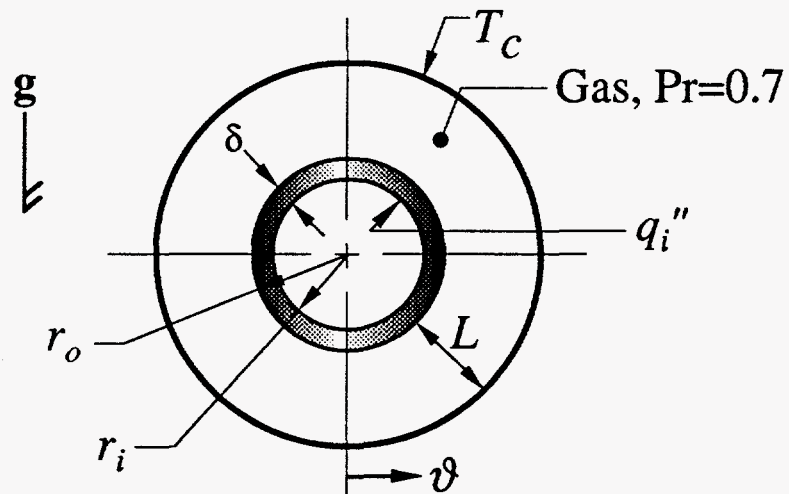


Figure 4.3 Concentric annulus in which the interior surface of the inner body is exposed to a uniform heat flux while the outer body is isothermal

concentric enclosure (the outer body), forming an annulus. The annulus is filled with a convecting backfill gas with a Prandtl number of 0.7. The interior surface of the inner body is subjected to a uniform heat flux, q_i'' , while the outer body is maintained at an isothermal temperature, T_c . Because the fuel pellet region of a fuel rod is commonly treated as a uniformly generating volumetric energy source, and the thermal resistance of the ceramic fuel pellet is much greater than that of the metallic cladding material, it is appropriate in this two dimensional analysis to simulate the fuel contained within the cladding by applying a uniform heat flux to the *inner* surface of the inner body [see Figure 4.4]. The solution to the problem will then suggest the appropriate boundary condition which should be applied at the *outer* surface of each fuel rod in order to simulate the effect of the entire rod.

The convection problem depicted by Figure 4.3 was solved numerically using the TEXSAN code (thermal radiation was not modeled). TEXSAN is a hybrid finite element/finite difference algorithm capable of solving conjugate heat transfer problems in complex geometries (Burns & Klein, 1993). TEXSAN solves the coupled mass, momentum, and energy equations in order to explicitly model the buoyant fluid motion and heat transfer associated with natural convection processes. The code employs an iterative method based on the SIMPLER algorithm developed by Patankar (1980). The results of the present simulation are expressed in terms of the dimensionless outer surface temperature of the inner body, θ , and the dimensionless outer surface heat flux of the inner body, q_o^* . The former parameter is defined as follows:

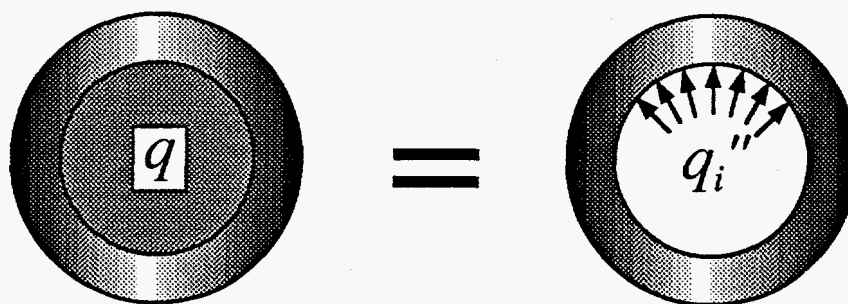


Figure 4.4 Modeling a spent fuel rod with a uniform interior clad heat flux

$$\theta = \frac{T(\vartheta) - T_C}{\Delta T} \quad (4.4)$$

where $T(\vartheta)$ is the outer surface temperature of the inner body,
 T_C is the uniform temperature of the outer body,
 and the characteristic temperature difference ΔT is defined as:

$$\Delta T = \frac{q_i'' L}{k_f} \quad (\text{where } L \text{ is indicated in Figure 4.3}) \quad (4.5)$$

The dimensionless heat flux on the outer surface of the inner body is given via:

$$q_o^* = \frac{q_o''(\vartheta)}{q_i''} \quad (4.6)$$

The actual heat flux on the outer surface of the fuel rod, $q_o''(\vartheta)$, was obtained by interpolating the nodal cladding temperatures using a bilinear finite element expansion. The gradient of this expansion, evaluated at the clad surface and multiplied by the thermal conductivity, is $q_o''(\vartheta)$.

Figure 4.5 indicates the variation of θ as a function of circumferential rod angle, ϑ , and conductivity ratio, k^* . The Rayleigh number for this case was chosen to be $Ra_L = 10^4$, where Rayleigh number is presently defined by the following relation:

$$Ra_L = \frac{g\beta q_i'' L^4}{\nu \alpha k_f} = \frac{g\beta \Delta T L^3}{\nu \alpha} \quad (4.7)$$

Figure 4.6 similarly depicts the variation of q_o^* as a function of k^* for the case where $Ra_L = 10^4$. Note from Figure 4.5 that as the clad/fluid conductivity ratio, k^* , increases, the outer surface temperature of the simulated fuel rod becomes increasingly isothermal. For a zircalloy or stainless steel cladding in a helium backfill, $k^* \approx 100$; whereas, in a nitrogen backfill $k^* \approx 600$. Thus, the arguments of the previous section appear valid in the present analysis; namely, the fuel rod's relatively high conductivity combined with its low heat transfer coefficient result in an essentially isothermal boundary condition. Further insight into the boundary conditions associated with the inner body (fuel rod) is gained from Figure 4.6, which plots the dimensionless outer surface heat flux of the fuel rod as a function of ϑ . Note that as opposed to temperature, the heat flux on the outer surface of the fuel rod for $k^* \geq 100$ is highly non-uniform, peaking on the lower rod surfaces where the convective heat transfer coefficient is greatest. However, as the thermal conductivity of the cladding is reduced, the outer surface heat flux becomes increasingly uniform, eventually approaching the uniform value which would exist if no convective effects were present (as indicated in Figure 4.6). The explanation for these observations is as follows. For relatively high thermal conductivity claddings (i.e. $k^* > 100$), the thermal resistance to circumferential energy flow in the cladding is small. This results in a nearly isothermal cladding which conversely has a highly non-uniform outer surface convective heat flux. For low conductivity claddings (i.e. $k^* < 10$), the circumferential cladding thermal resistance is great, which results in a variable outer surface temperature and a fairly uniform outer surface heat flux.

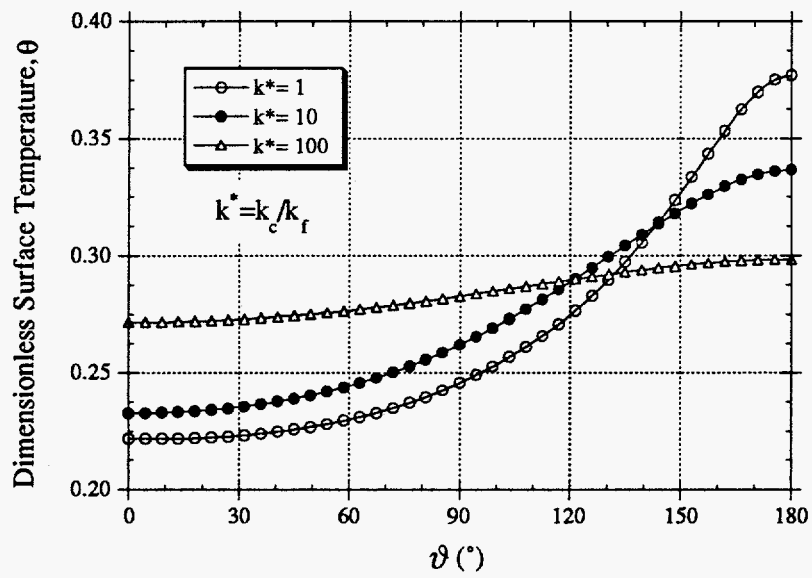


Figure 4.5 Outer surface temperature of inner cylinder for $Ra_L = 10^4$

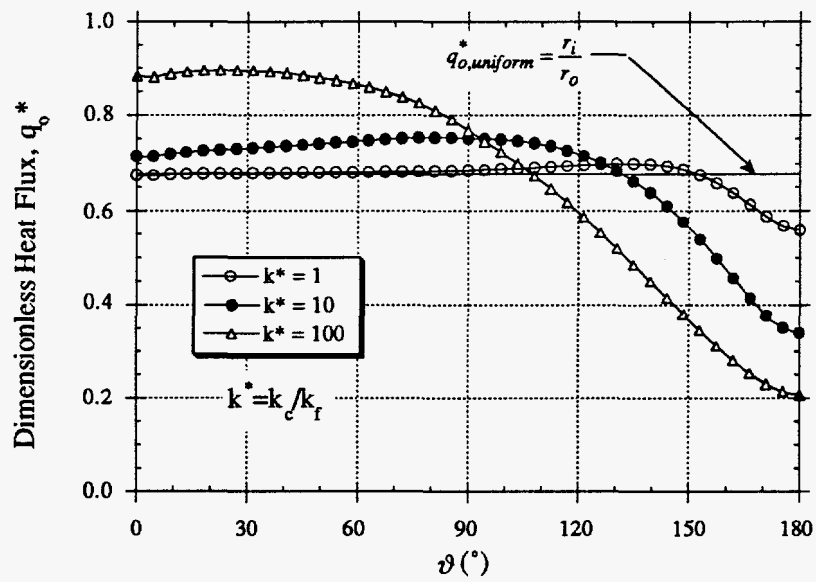


Figure 4.6 Outer surface heat flux of inner cylinder for $Ra_L=10^4$

In summary, the previous two analyses indicate that a horizontal spent fuel rod (or any heat generating rod of similar construction), undergoing natural convection in a gaseous backfill, will most likely be isothermal about its outer surface. Furthermore, the convective heat flux about the rod's outer surface will be significantly *non-uniform*. These conclusions were obtained for a single horizontal rod however, and do not include the thermal interactions which can be expected to occur in a full assembly. These interactions will be examined in the following section.

4.4 CONVECTIVE ANALYSIS OF A HORIZONTAL BWR ASSEMBLY

In order to verify the conclusions of the previous first order analyses, a numerical simulation of the buoyant fluid flow and heat transfer within an entire SNF assembly was conducted for a range of Rayleigh number. This section will provide an overview of the model and its results. For further information or greater detail, the reader is encouraged to review the work of Butler (1994). In this simulation, a horizontal BWR fuel assembly was considered as depicted in Figure 4.7. The numerical analysis of the full fuel assembly in two dimensions was conducted using the TEXSAN thermal hydraulic code (as in the previous section). Thermal radiation was not included in the simulation.

Figure 4.7 illustrates the numerical boundary conditions as well as the overall geometry. Note that symmetry about the assembly's vertical mid-plane was invoked as discussed in Chapter 3.2.2. The cladding of each of the fuel rods

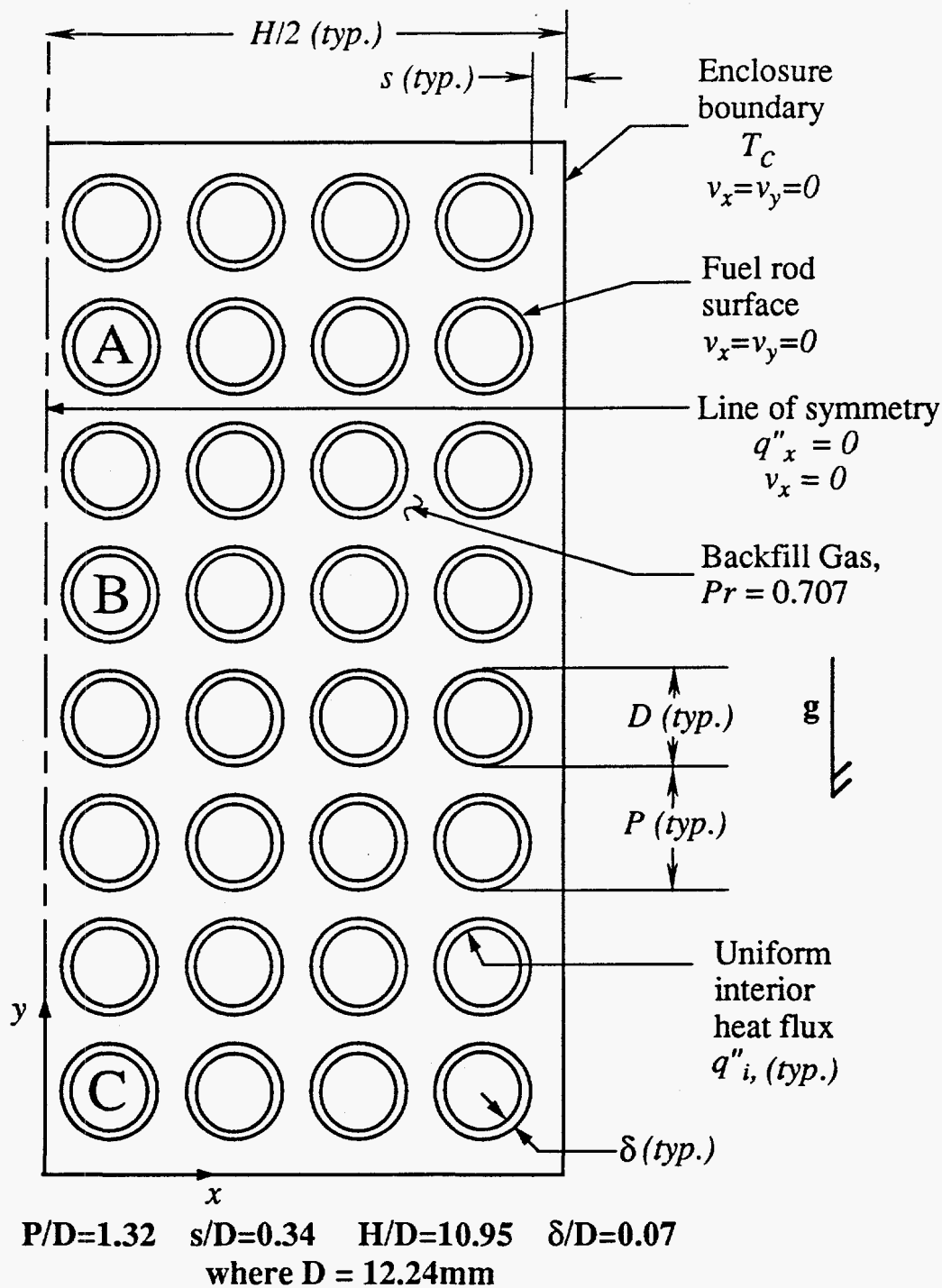


Figure 4.7 TEXSAN model of a BWR assembly indicating boundary conditions

in the assembly was explicitly modeled and, as discussed in the previous section, a uniform heat flux was applied to the interior cladding surface of each fuel rod. The assembly walls were assumed to be isothermal. No slip boundary conditions were applied at all real surfaces and the symmetry line was modeled as an adiabatic zero traction boundary.

It is convenient to express the governing heat transfer and fluid flow equations in dimensionless forms. This is accomplished in general by dividing each of the primary variables by a characteristic quantity. For non-dimensionalizing temperature, velocity, and dynamic pressure, a characteristic temperature difference (ΔT), a characteristic velocity (v_{ch}), and a characteristic dynamic pressure (p_{ch}) are respectively defined. The associated dimensionless temperature (θ), velocity (v^*), and dynamic pressure (p^*) are then related to the dimensional variables as follows:

$$\theta = \frac{T - T_c}{\Delta T}; \quad \Delta T = \frac{q_i'' D}{k_f} \quad (4.8)$$

$$v^* = \frac{v}{v_{ch}}; \quad v_{ch} = \frac{\alpha}{D} \quad (4.9)$$

$$p^* = \frac{p}{p_{ch}}; \quad p_{ch} = \rho v_{ch}^2 \quad (4.10)$$

Furthermore, all material properties are scaled by the corresponding fluid property giving rise to the thermal conductivity ratio, $k^* = k/k_f$, i.e. in the fluid, $k^* = 1$, and in the cladding, $k^* = k_c/k_f$. Physical dimensions in the model are non-

dimensionalized by scaling with the fuel rod diameter, D . Substitution of the above quantities into the governing equations for heat transfer and fluid flow results in the following dimensionless forms of the equations for the fluid region:

$$\text{Mass or continuity:} \quad \nabla \cdot \mathbf{v}^* = 0 \quad (4.11)$$

$$\text{Momentum (y):} \quad \nabla \cdot (\mathbf{v}_y^* \mathbf{v}^* - Pr \nabla v_y^*) = Ra_D Pr \theta - \nabla p^* \quad (4.12)$$

$$\text{Energy:} \quad \nabla \cdot (\mathbf{v}^* \theta - k^* \nabla \theta) = 0 \quad (4.13)$$

Equations (4.11) through (4.13) assume steady, two dimensional, constant property conditions in which the gravity force acts in the negative y direction. Also, with one exception, the fluid is assumed to be incompressible. The exception involves accounting for the effect of variable density in the buoyancy force (the Boussinesq approximation), since it is this variation which induces natural convective fluid motion. The Rayleigh number as seen in equation (4.12) is defined as follows:

$$Ra_D = \frac{g\beta q_i'' D^4}{\nu \alpha k_f} \quad (4.14)$$

Note that this Rayleigh number is defined in terms of the uniform heat flux applied to the cladding interior of each fuel rod. This quantity is equal for all rods in the assembly.

The finite element mesh for the present problem is depicted in Figure 4.8. This mesh contains a total of 4222 nodes. The cladding of each of the fuel rods in

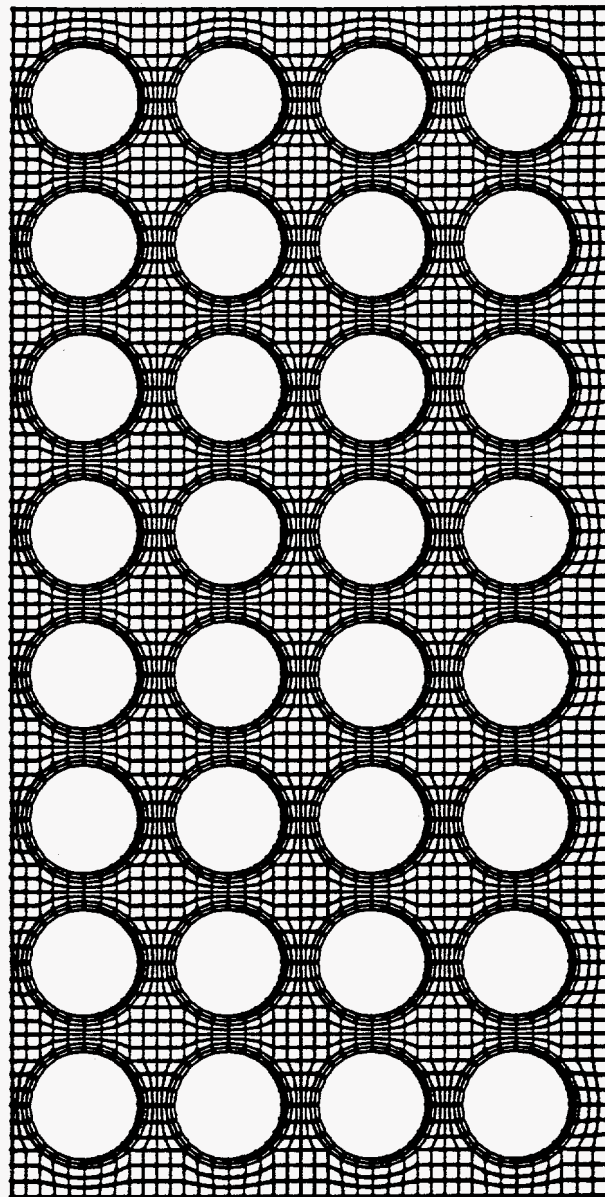


Figure 4.8 Computational mesh for convective analysis of a horizontal BWR assembly

the assembly is explicitly meshed as well as the backfill gas. All of the elements employed were four node quadrilaterals. The geometric parameters of the model are consistent with those of typical BWR fuel assemblies containing an 8X8 fuel rod matrix. The fuel rod diameter, D , equals 12.24mm and the pitch, P , is 16.2mm, resulting in a pitch to diameter ratio of 1.32. The thermal conductivity of the modeled rods corresponds to that of zircalloy cladding. The cladding thickness is $\delta = 0.864\text{mm}$. All analyses were performed for an air backfill at standard temperature and pressure ($Pr=0.707$). The Rayleigh number was varied over five cases in order to simulate varying levels of heat input (decay power). Butler (1994) reports results corresponding to the present model for the following cases: $Ra_D = 0, 10, 100, 1,000, \text{ and } 2,000$.

Only a representative set of the results obtained by Butler will be presented in this discussion. Figures 4.9 and 4.10 are plots of the non-dimensional temperature field, $\theta(x^*, y^*)$, for cases corresponding to $Ra_D=10$ and $Ra_D=1,000$, respectively. A key feature of the $Ra_D=10$ case (Figure 4.9) is the pattern of concentric temperature contours, essentially symmetric about both the horizontal and vertical assembly mid-planes. Gradients are relatively low near the center of the assembly and steepen significantly near the enclosure boundary. These isotherms are characteristic of a conduction dominated scenario in which the assembly resembles a solid experiencing uniform internal heat generation. The situation is dramatically different however, for the $Ra_D=1,000$ case. Not only has the maximum assembly temperature decreased, but the isotherms indicate significant upward skewing due to buoyancy driven fluid flow. Rods in the lower

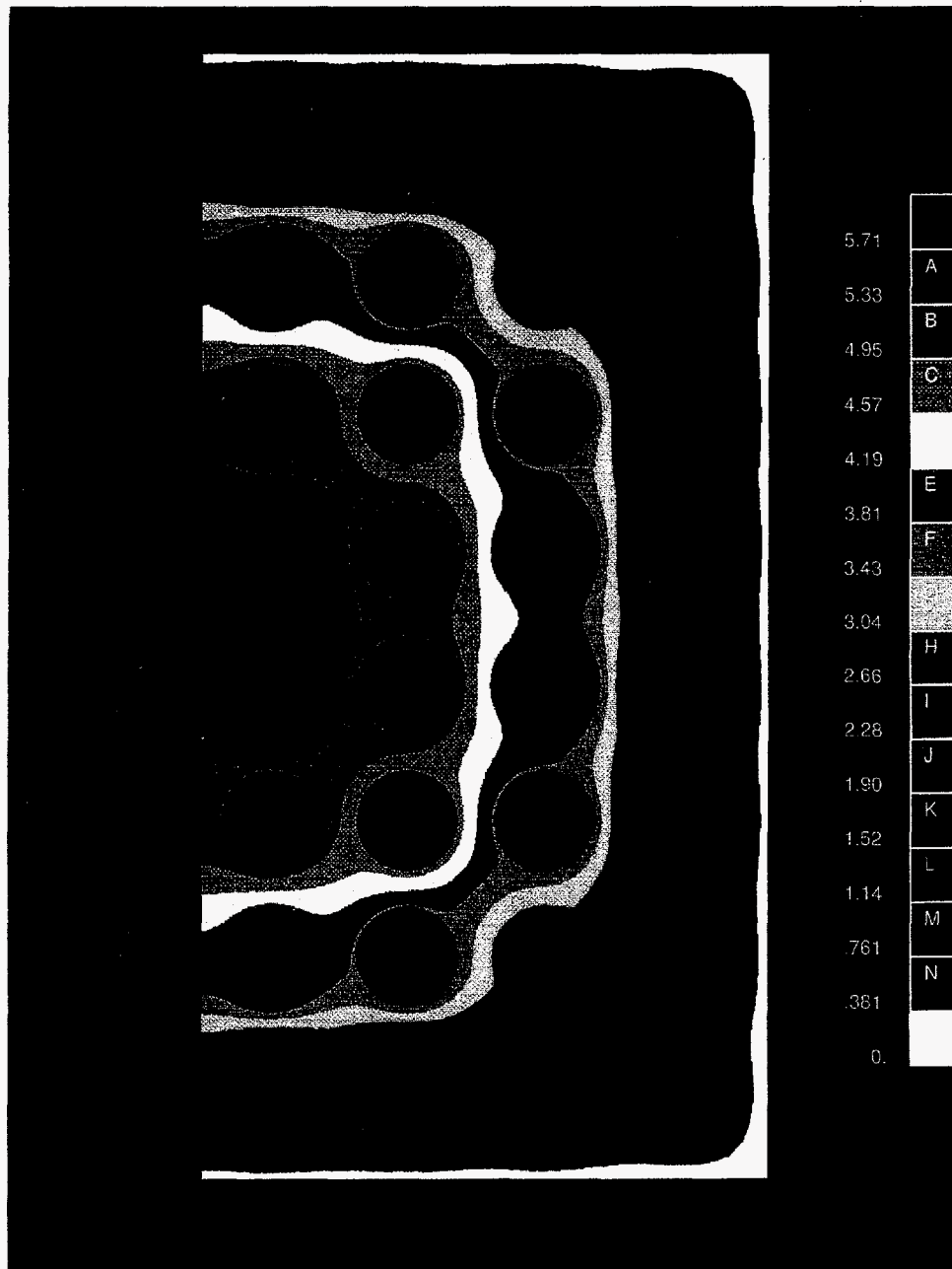


Figure 4.9 Non-dimensional temperature, $Ra_D=10$ [from Butler, (1994)]

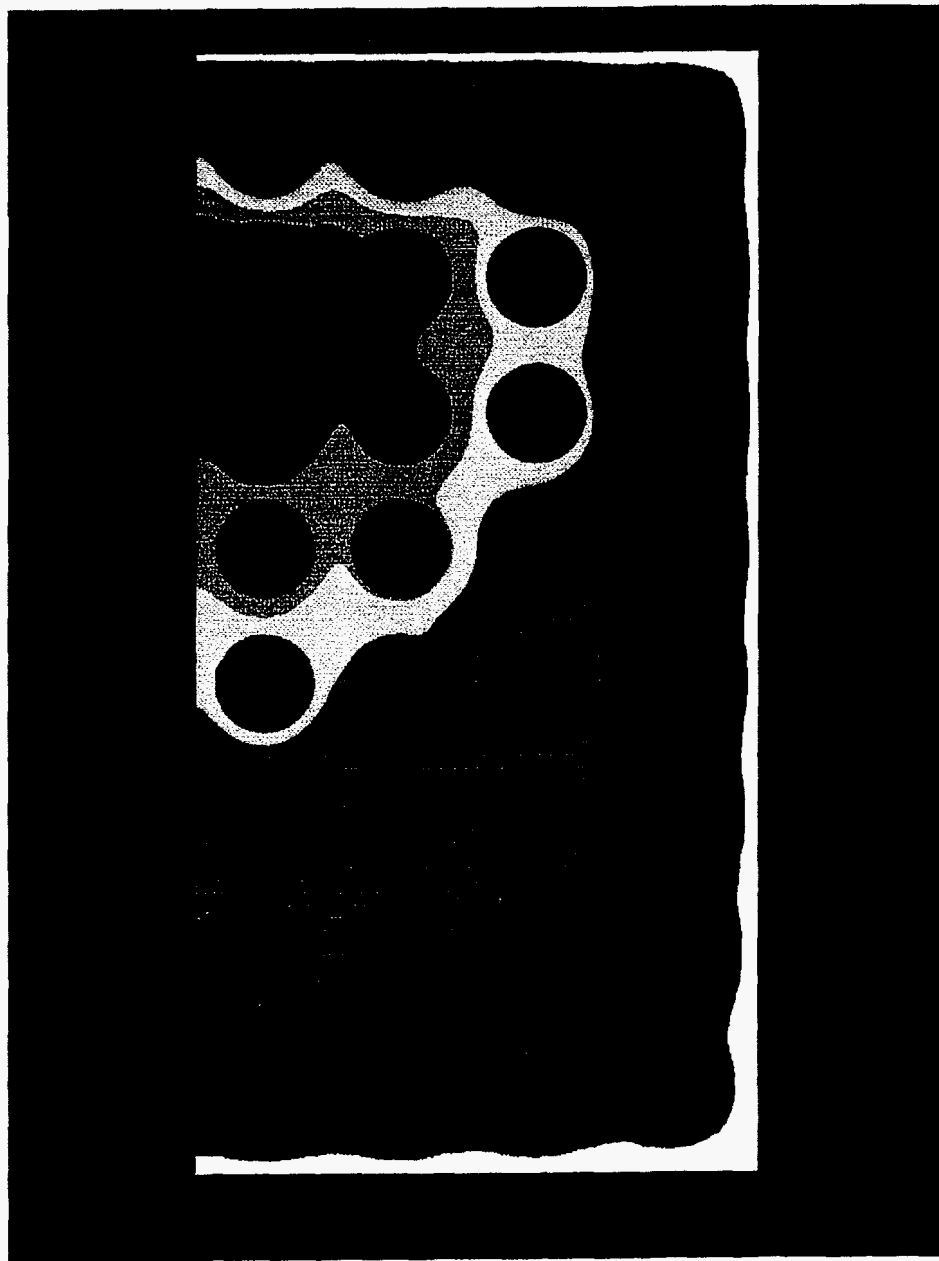


Figure 4.10 Non-dimensional temperature, $Ra_D=1,000$ [from Butler, (1994)]
{same legend as Figure 4.9}

half of the array (row 4 and down) are significantly cooler than in the $Ra_D=10$ case; whereas, rods in the upper regions of the assembly have increased in temperature. According to the rod naming convention of Figure 4.7, the maximum temperature in the array has shifted from rod B at $Ra_D=10$, to rod A at $Ra_D=1,000$. Careful examination of Figures 4.9 and 4.10 further indicates that the surface temperature of all rods in the array is very uniform, as evidenced by the curving isotherms which bend around the rods' surfaces. In fact, the circumferentially varying outer surface temperature of any rod in the assembly was found to lie within 2% of the mean rod surface temperature for all cases investigated. The vast majority of rods in the assembly were isothermal within 1% of the mean rod temperature for all Rayleigh numbers.

Figures 4.11 and 4.12 depict the rod *surface* dimensionless heat flux as a function of circumferential rod angle for rod C and rod B (see Figure 4.7), respectively. In these figures, the circumferential rod angle ϑ is measured clockwise from the top of the rod, as indicated in Figures 4.11 and 4.12. The dimensionless outer surface heat flux is presently defined as

$$q_o^* = -k^* \left[\frac{\partial \theta}{\partial r^*} \right]_{r^*=0.5} \quad (4.15)$$

and is calculated from a one-sided, three point approximation to the directional derivative at the surface of each rod, where $r^* = r/D = 0.5$. A positive value indicates flux from the rod surface at that point, and a negative value represents flux to the surface.

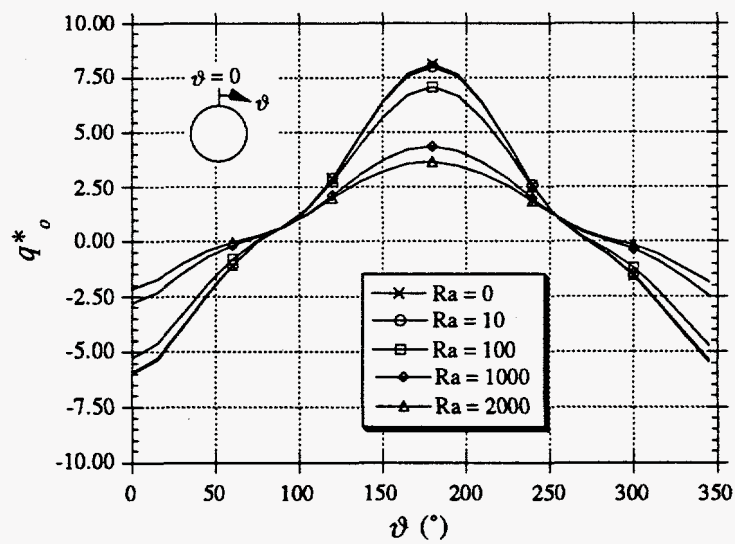


Figure 4.11 Dimensionless outer surface heat flux for rod C, (see Figure 4.7), [from Butler, (1994)]

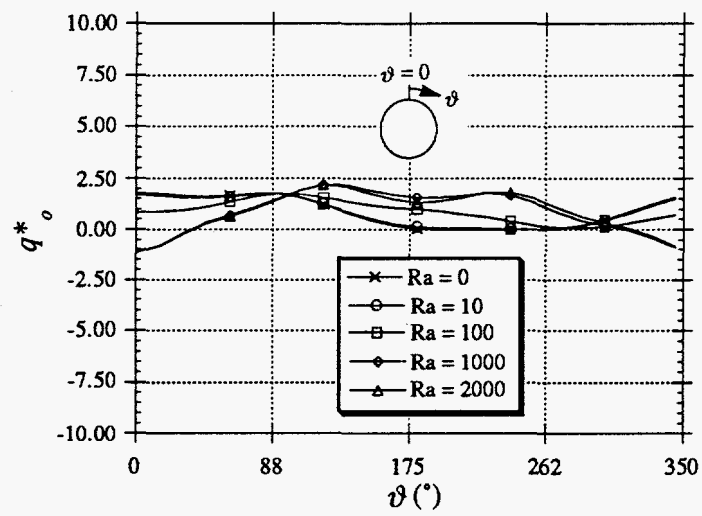


Figure 4.12 Dimensionless outer surface heat flux for rod B, (see Figure 4.7), [from Butler, (1994)]

Figure 4.11 illustrates a case in which the outer surface heat flux varies significantly about the circumference of a given fuel rod. The variation of heat flux is markedly dampened for the situation depicted by Figure 4.12. However, unlike the fuel rod surface temperature, the *minimum* variation in the outer surface heat flux about the circumference of any fuel rod was determined to be on the order of 30%, and may rise as high as 800 to 1000% of the uniform surface flux value (Butler, 1994). These results serve to substantiate the conclusions reached in previous analyses. Namely, that the fuel rod surfaces within a horizontal spent nuclear fuel assembly are best represented with an isothermal rather than a uniform heat flux boundary condition. Representation of the fuel rods (i.e. in a numerical analysis) by a uniform *surface* heat flux boundary condition would result in a fundamental alteration in the boundary layer development around the rods, thus significantly affecting the overall prediction of heat transfer and fluid flow within the fuel assembly. This is intuitively evident when one realizes that the fuel rod cladding provides a "short-circuit" path for heat generated in the center of the array to travel to the relatively cold assembly walls. Figure 4.11 well illustrates this "short-circuit" by the negative heat flux values found along the upper half of rod C ($0^\circ < \vartheta < 90^\circ$ & $\vartheta > 270^\circ$) where heat enters the rod cladding from the hot gases above the rod, subsequently travels through the low resistance cladding, and is eventually removed along the lower half of the rod where the flux is toward the assembly wall.

Thus, with regard to numerical analyses of horizontal spent fuel assemblies, the best boundary condition formulation would be to include the

cladding material in the numerical model while applying a uniform heat flux to the inner surface of the cladding. This was the approach taken here and is a practical method, given that the surface temperatures of the individual fuel rods are not known *a priori*, and indeed may be the principle objective of the analysis.

The implications of these results additionally have an impact upon the *experimental* simulation of SNF heat transfer processes. Specifically, the level of instrumentation (number and type of sensors) which is required to adequately characterize the thermal nature of SNF is affected. For example, the evidence that each of the fuel rods within a horizontal assembly is essentially isothermal will significantly reduce the number of sensors required to measure intra-assembly temperature.

The previous sections have focused upon the convective/conductive heat transfer processes within spent fuel geometries. However, it is very likely that thermal radiation will play a significant role as well. Whether or not the presence of radiation will affect the preceding conclusions will be briefly examined in the forthcoming section.

4.5 RADIATIVE/CONVECTIVE ANALYSIS OF A BWR ASSEMBLY SUBREGION

The TEXSAN thermal hydraulic code used in previous numerical simulations additionally has a thermal radiative capability (Gianoulakis, 1992). Radiation is modeled using the Net Radiation, or radiosity technique, in which an additional and separate system of discretized equations are solved for the radiosity

associated with each surface in the model (Incropera & Dewitt, 1990). The calculated radiosities are easily related to the net radiative heat flux at each surface. This energy is then treated as a heat source by adding it to the energy equation [equation (4.13)] as a source term. Thus, the net radiative heat flux at a given surface is essentially a heat flux boundary condition that is recalculated continually while the problem is being iteratively solved. All surfaces which radiatively participate are assumed to have wavelength independent properties (gray) and are further assumed to emit and reflect radiation diffusely. A sufficient number of surfaces (or sub-surfaces) should be included such that each modeled surface can be treated as isothermal and of uniform radiosity.

In order to investigate the influence of thermal radiation upon the conclusions drawn in preceding sections, TEXSAN's multimode heat transfer capability was employed. Figure 4.13 depicts the numerical model and boundary conditions relevant to the present radiative/convective study. The entire horizontal spent fuel assembly was not modeled due to the enormity of the problem and the limitations in available computational resources. Rather, the model was simplified by restricting the analysis to a subregion of a BWR fuel assembly, as indicated. Although this model is coarse in comparison to the full array described earlier (Figure 4.7), it represents a somewhat limiting case as far as thermal radiation heat transfer goes, since the corner regions of the assembly have an enhanced radiative potential due to the wide temperature range of neighboring surfaces.

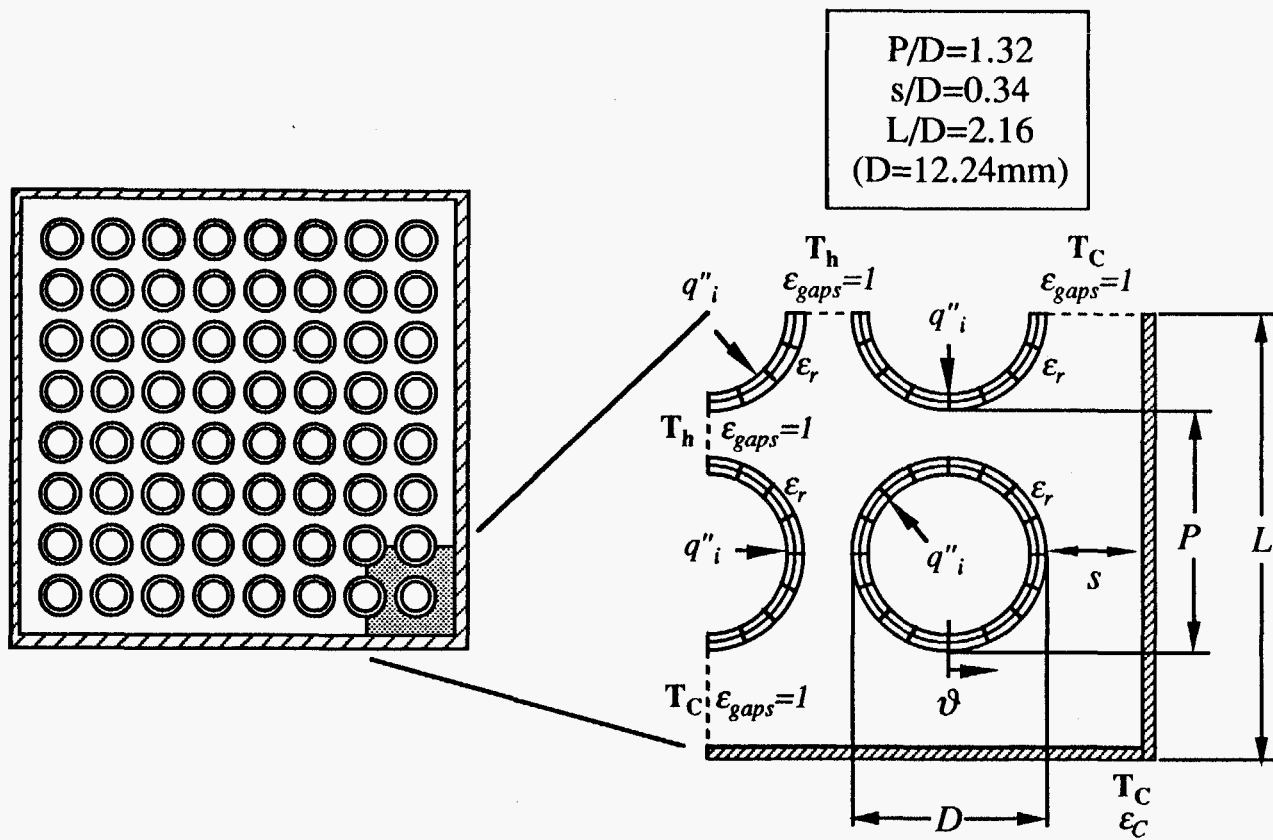


Figure 4.13 TEXSAN model for radiative/convective analysis of a BWR assembly corner region

The boundary conditions utilized in Figure 4.13 are similar to those invoked in previous numerical models. Namely, the fuel rods are treated as zircalloy cladding shells whose interior surfaces are exposed to a uniform heat flux. The assembly wall is maintained at a uniform temperature, T_C . The gaps adjacent to the assembly walls are also isothermal at T_C . However the gaps which represent the interior of the array (adjacent to the quarter rod) are at a significantly higher temperature, designated as T_h . In this investigation, a forty degree temperature difference between T_h and T_C was assumed based upon peak rod to assembly wall temperature measurements reported by Driesen *et. al.* (1980) in an actual well-aged spent fuel assembly. Specifically, $T_h = 200^\circ\text{C}$ and $T_C = 160^\circ\text{C}$.

All of the surfaces indicated in Figure 4.13 are allowed to exchange energy through radiation. Since radiation passing through the gaps is 'lost' into the interior of the assembly and is unlikely to be reflected back, the gaps between the rods and between the rods and assembly wall are considered black ($\epsilon_{gaps} = 1$). The emissivities of the fuel rods, ϵ_r , and the assembly wall, ϵ_C , are specified independently and are included as variational parameters in this study. The physical dimensions associated with this model are consistent with those given in Figure 4.7 for a typical 8X8 BWR assembly and the assembly is filled with an air backfill at atmospheric pressure.

Figure 4.14 is a plot of the dimensionless surface temperature of the corner fuel rod depicted in Figure 4.13. The temperature, θ , previously defined by equation (4.8), is plotted against the circumferential rod angle, ϑ , as

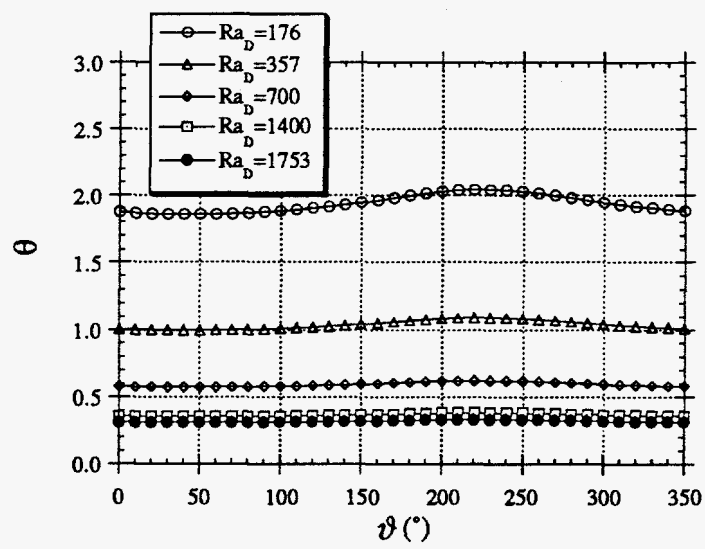


Figure 4.14 Corner rod surface temperature as a function of ϑ

given in Figure 4.13, for a range of Rayleigh number. The results indicate nothing new. Namely, that despite the presence of combined radiative/convective processes, the surface temperature of the fuel rods remains essentially isothermal.

Figure 4.15 illustrates the effect upon corner rod surface temperature as the emissivity of both fuel rod and assembly wall are perturbed. The cases plotted in Figure 4.15 correspond to those outlined in Table 4.1.

Table 4.1 Sensitivity of results to variation in surface emissivity, ($Ra_D = 1,400, T_h = 200^\circ\text{C}$ & $T_C = 160^\circ\text{C}$, [see Figure 4.15])

case	ϵ_{rod}	ϵ_C	ϵ_{gaps}
1	0.8	0.2	1.0
2	0.8	0.3	1.0
3	0.9	0.2	1.0
4	0.9	0.3	1.0
5	0.9	0.3	0.9

Based upon the results of Figure 4.15, the steady state surface temperature of the corner fuel rod is significantly more sensitive to the uncertainty associated with the assembly wall emissivity rather than that of the fuel rod emissivity. This is a direct result of the relatively large surface area associated with the walls of the surrounding enclosure. Nevertheless, the net effect upon the fuel rod's measurable average surface temperature is small in all cases. However, it should be noted that

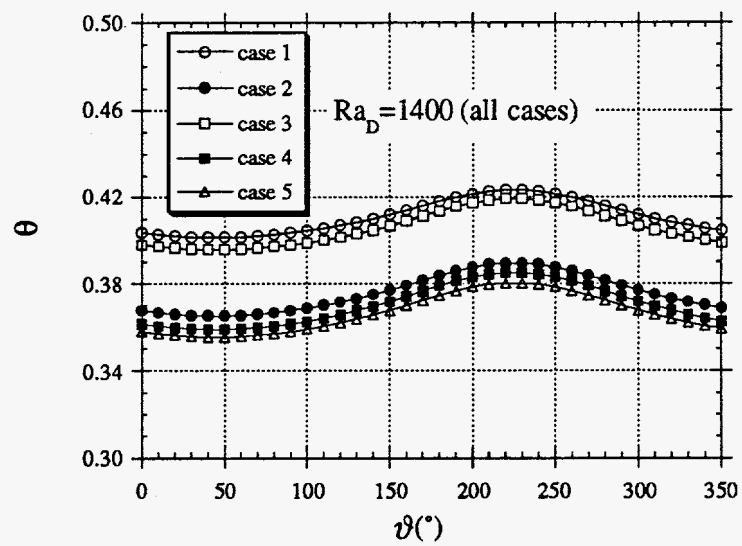


Figure 4.15 Corner rod surface temperature variation as influenced by emissivity perturbation, ($Ra_D = 1,400$, $T_h = 200^\circ\text{C}$ & $T_C = 160^\circ\text{C}$), [cases correspond to Table 4.1]

due to the coarseness of this radiative model, such conclusions may be premature. A more detailed and sophisticated analysis of thermal radiation heat transfer in SNF geometries is presented and further discussed in Chapter 8.

4.6 AXIAL ANALYSIS OF A HORIZONTAL FUEL ROD

The calculations discussed in previous sections of this chapter have treated horizontally oriented spent fuel rods as if they were of infinite length. Recall from Chapter 3.2.2., that due to the large length to height ratio of spent fuel assemblies, most thermal analyses of SNF systems are justifiably limited to two dimensions, neglecting axial effects. However, end effects will be present in essentially all fuel assembly mock-ups which are not full scale. Uncertainties can occur unless care is taken to eliminate, or reasonably mitigate, axial effects from the raw experimental data.

Much of the remainder of this dissertation will focus upon the operation and analysis of an experimental SNF assembly mock-up during simulated dry storage and/or transportation. The data obtained from this experiment will be correlated for use in two dimensional analyses; thus, it is mandatory that efforts be taken in order to ensure that the mock-up is designed and constructed from a standpoint which minimizes axial or end effects. These efforts are the subject of this section.

Figure 4.16 represents a three dimensional version of a spent fuel rod energy balance originally given in Figure 3.3. In addition to the radiative and

convective heat transfer components which are assumed to transport energy from the rod's surface, a third component associated with heat conduction through the cladding in the axial direction is indicated (q_{loss}). The magnitude of this end loss component will depend upon several factors, including the thermal conductivity of the cladding, the cross sectional cladding area through which axial conduction occurs, the specific boundary conditions at the rod tips, and the length of the rod. Of course, an infinitely long, uniformly heated rod will have no axial temperature gradient, and thus no end losses (Figure 4.17).

The basic approach of this analysis is to consider the fuel rod as a cylindrical shell with a nominal thickness of $\delta = 0.864\text{mm}$ and outer radius $r_o = 6.12\text{mm}$, typical dimensions of most BWR fuel rods. The shell approach is a viable one since the region interior to the rod's clad (UO_2 fuel) is a thermal insulator in comparison to the clad material and therefore the generation within may be conservatively expressed as a uniform heat flux incident upon the inner clad surface. The axial losses will be ascertained by treating the rod as a modified fin in that the cylindrical shell will be viewed as an "unrolled" rectangular slab with an applied heat flux on its lower surface, convection and radiation from its upper surface, and convective end or tip conditions. The relevant thermal processes imposed upon a differential element of this fin are depicted in Figure 4.18. A number of simplifying assumptions will be made however. First, only axial heat transfer will be considered. Furthermore, steady-state conditions are implied, thermal conductivity is assumed constant, and convection is uniform about the fin. Additionally, radiation will be neglected. This latter assumption

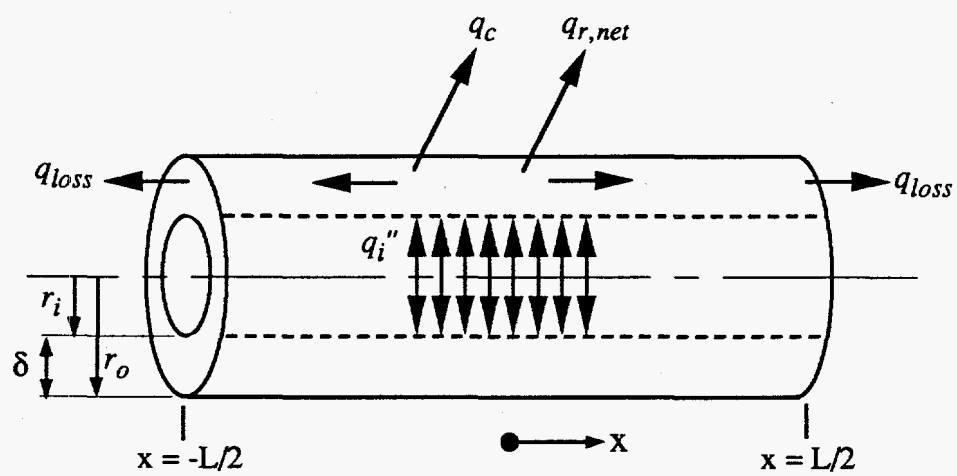


Figure 4.16 Energy balance associated with a finite length spent fuel rod

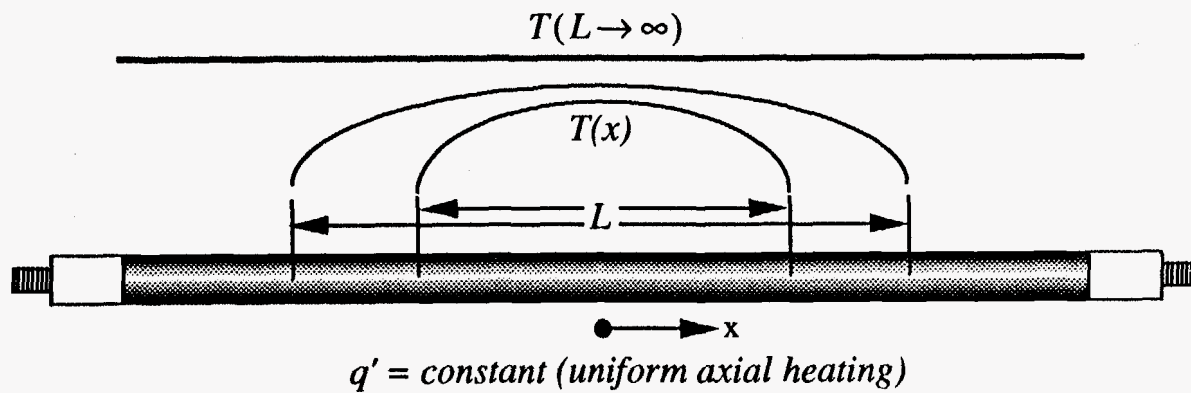


Figure 4.17 End effects as a function of rod length (uniform axial heating)

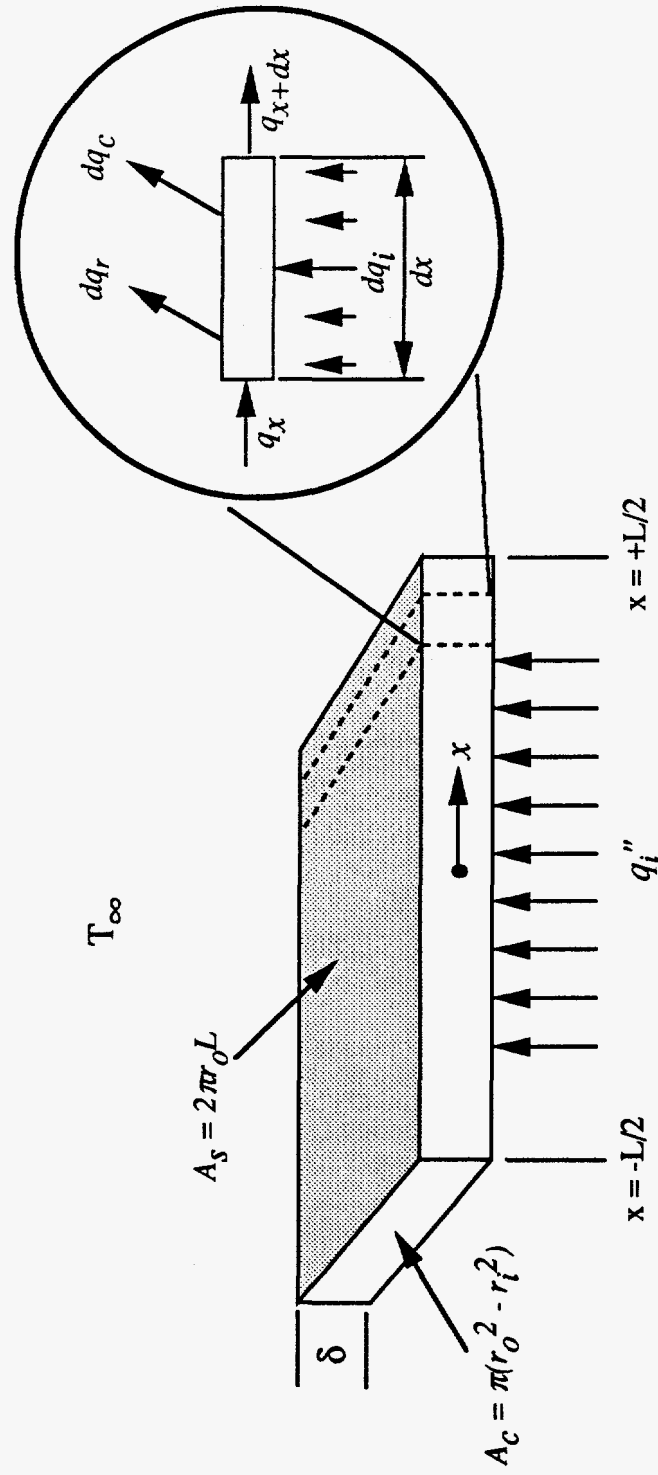


Figure 4.18 Modified fin approach to fuel rod axial analysis

will be conservative since the presence of radiative transfer will enhance thermal energy transport from the large horizontal surface, leaving less energy available for axial conduction to the rod ends. However, the assumption of an axially uniform heat transfer coefficient will not be conservative since in actuality the heat transfer coefficient will be suppressed near the rod's ends; thus enhancing end losses.

Applying the conservation of energy requirement to the differential element of Figure 4.18, one obtains the following equation:

$$q_x - q_{x+dx} + dq_i - dq_c = 0 \quad (4.16)$$

Each of the terms of equation (4.16) is subsequently defined:

$$q_x = -k_c A_c \frac{dT}{dx} \quad (4.17)$$

$$q_{x+dx} = q_x + \frac{dq_x}{dx} dx = -k_c A_c \frac{dT}{dx} - k_c A_c \frac{d}{dx} \left(\frac{dT}{dx} \right) dx \quad (4.18)$$

$$dq_c = 2\pi r_o dx h(T - T_\infty) \quad (4.19)$$

and

$$dq_i = 2\pi r_i dx q_i'' \quad (4.20)$$

Substitution of equations (4.17) through (4.20) into equation (4.16) produces the following differential equation:

$$\frac{d^2T}{dx^2} - m^2(T - T_\infty) = \frac{-q_i'' 2\pi r_i}{k_c A_c} \quad (4.21)$$

Where,

$$m^2 = \frac{2\pi r_o h}{k_c A_c} \quad (4.22)$$

Defining an excess temperature, $\theta(x) = T(x) - T_\infty$, equation (4.21) may be recast as follows:

$$\frac{d^2\theta(x)}{dx^2} - m^2\theta(x) = \frac{-q_i'' 2\pi r_i}{k_c A_c} \quad (4.23)$$

The following boundary conditions are appropriate:

• Symmetry: $\left. \frac{d\theta}{dx} \right|_{x=0} = 0 \quad (4.24)$

• Convective tips $-k_c A_c \left. \frac{d\theta}{dx} \right|_{x=L/2} = h^* A_c \theta(x=L/2) \quad (4.25)$

It should be noted that the convective coefficient h^* [equation (4.25)] may not necessarily be the same coefficient denoted by h [equation (4.22)]. The latter is the appropriate natural convective heat transfer coefficient for an infinite horizontal cylinder. The former represents the heat transfer coefficient for the vertical end surfaces of the horizontal rod. Moreover, in actuality, the fuel rods within an array must be physically supported in some manner. This is often

accomplished with gridded end plates, with which the rods are in direct physical contact. These support surfaces can increase the effective area which is available for end loss convection over that of the unsupported cladding cross sectional area, A_c . In this manner, h^* , will thus be defined in terms of an end support area correction factor, C_f , such that the support influence upon axial end loss is accounted for in the boundary condition represented by equation (4.25):

$$h^* A_c \Rightarrow h A_c C_f \quad (4.26)$$

Hence, equation (4.25) may be recast as:

$$-k_c \frac{d\theta}{dx} \Big|_{x=L/2} = h C_f \theta(x=L/2) \quad (4.27)$$

In this manner, the correction factor C_f , accounts for the geometrical peculiarities associated with the fuel rod end fittings. In order to define this constant, one may view it as a factor which multiplies the cladding cross-sectional area in order to obtain the effective end support area:

$$A_{eff} = C_f A_c \quad (4.28)$$

Thus, it only remains to determine what the effective area of the end support is for an individual fuel rod. Often, the grid spacers which hold the fuel rods in place only have 'point' physical contacts, which may in fact result in negligible conduction pathways, i.e. $C_f \approx 1$. As a very conservative estimate however, the effective area may be taken to be the fuel rod pitch squared, i.e. $A_{eff} = P^2$. In this case, the area correction factor for typical BWR assemblies (8X8) was found to be

$C_f \approx 9$. Figure 4.19 depicts these limiting cases as described. Hence, by parametrically varying C_f , the sensitivity of the fuel rod axial temperature gradient may be assessed for a wide range of conceivable end conditions.

The solution to equation (4.23), subject to the boundary conditions given by equations (4.24) and (4.27), is as follows:

$$\theta(x) = \frac{-hC_f q_i''(2\pi r_i)(\cosh mx)}{k_c^2 m^2 A_c \left[m \sinh \frac{mL}{2} + \frac{hC_f}{k_c} \cosh \frac{mL}{2} \right]} + \frac{q_i''(2\pi r_i)}{k_c m^2 A_c} \quad (4.29)$$

It should be noted that as the length of the fuel rod approaches infinity ($L \rightarrow \infty$), the first term in equation (4.29) diminishes and the resulting solution for an 'infinite' rod is:

$$\theta_{inf}(x) = \frac{q_i''(2\pi r_i)}{k_c m^2 A_c} \quad (4.30)$$

It is convenient to normalize the solution given by equation (4.29) by the infinite case solution [equation (4.30)]:

$$\theta^*(x) = \frac{\theta(x)}{\theta_{inf}(x)} \quad (4.31)$$

Subsequently, a rod with negligible end effects will have a normalized solution, $\theta^* = 1.0$.

From Figure 4.17, it can be seen that a horizontal, uniformly heated cylinder of finite length, will experience an axial temperature gradient due to end

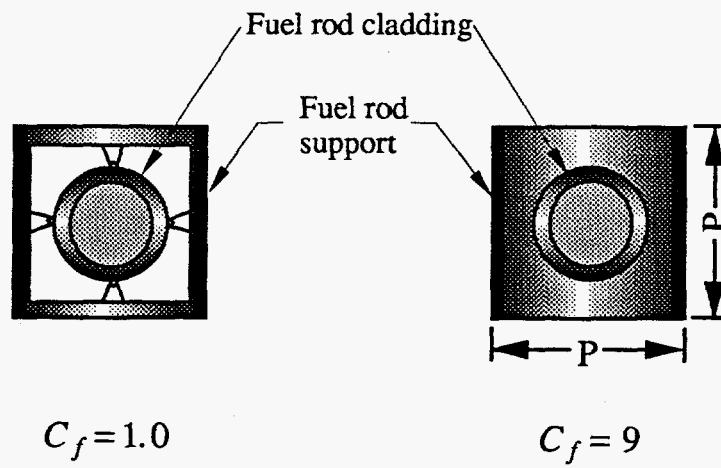


Figure 4.19 Limiting examples of fuel rod end support structures

losses. Furthermore, these end losses will likely result in surface temperatures which are less than the corresponding infinite case value. It is desirable to minimize this temperature discrepancy, and thus minimize the effects of end losses, by using simulated fuel rods (in an experimental mock-up) which are as long as reasonably achievable. Using equations (4.29) through (4.31), the effect of rod length, L , upon the non-dimensional surface temperature, θ^* , for a zircalloy clad rod is examined as shown in Figure 4.20. The ordinate is the non-dimensional surface temperature at the rod's midpoint ($x=0$), the location least affected by end losses. The average heat transfer coefficient at the rod's surface was specified to be $h=5.0\text{W/m}^2\text{K}$, which represents the lower end of data in the natural convective literature (Incropera & DeWitt, 1990). The family of curves in Figure 4.20 represents the sensitivity of the result to perturbations in the area correction factor, C_f . Even in the extraordinary and very unlikely case of $C_f=20.0$, the zircalloy rod can be considered essentially infinite at lengths exceeding $L=0.56\text{m}$. By current definition, 'essentially infinite' corresponds to a midpoint rod temperature within 0.1% of the purely infinite case where $\theta^*(0)=1.0$. Figure 4.21 illustrates the dependence of this 'essentially infinite' length, denoted as L_{inf} , on the thermal conductivity of the rod's cladding - subject to the conditions previously stated plus taking $C_f=10.0$, a conservative end loss assumption. From this figure, it is evident that as long as the thermal conductivity of the fuel rod cladding (or a simulated fuel rod) is less than $k_c \approx 65\text{W/mK}$, a rod of length $L \approx 1.0\text{m}$ is conservative with respect to midpoint temperature. However, use of a

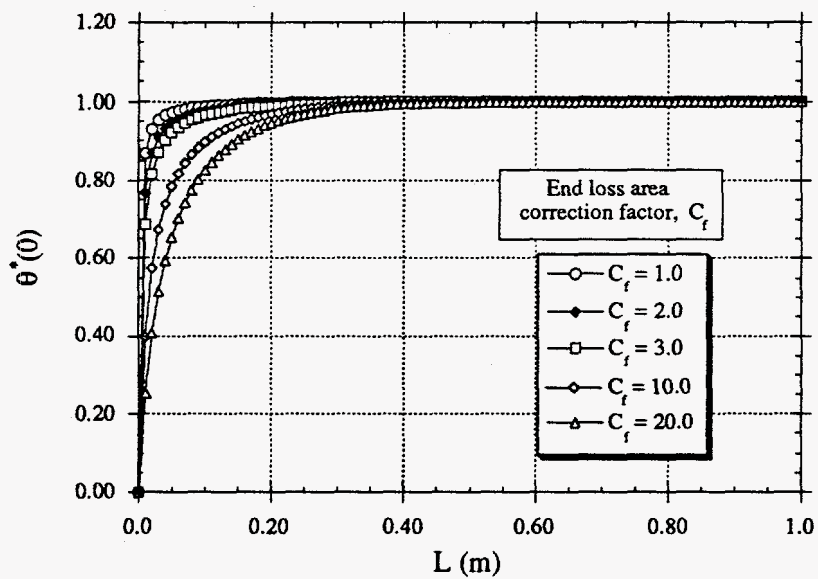


Figure 4.20 Dimensionless surface temperature at a zircalloy fuel rod's axial midpoint as a function of rod length and end condition ($h = 5.0\text{W/m}^2\text{K}$)

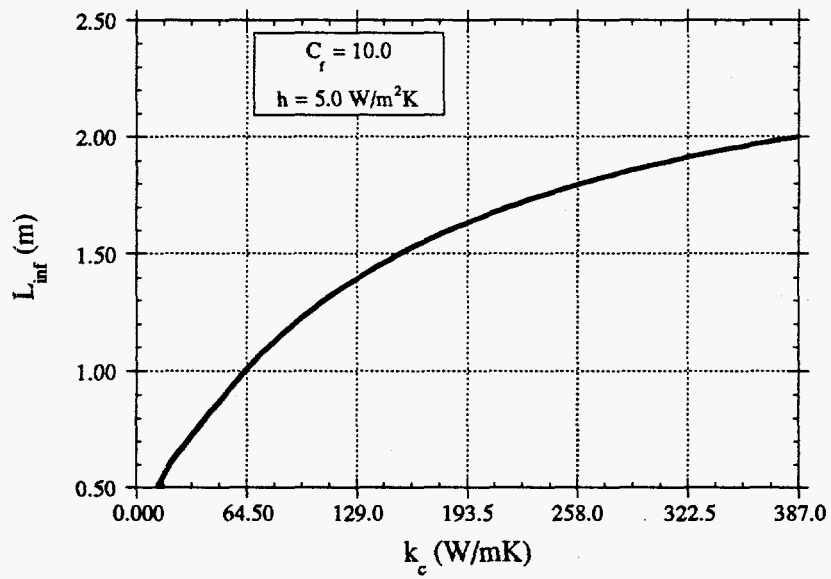


Figure 4.21 Variation of effective infinite rod length (within 1% of infinite case) with fuel rod conductivity for $C_f=10.0$ ($h = 5.0\text{W/m}^2\text{K}$)

cladding material such as copper ($k_c \approx 400 \text{ W/mK}$), would require a substantially longer rod ($L > 2.0 \text{ m}$) to minimize the effect of axial losses.

The results given by Figures 4.20 and 4.21 pertain to the effect which end losses have upon the fuel rod midpoint temperature, $\theta^*(0)$. This parameter is of interest because a given rod's midpoint is the location least affected by end loss, and is thus the best location to position temperature sensors so that two dimensional data will be obtained. However, an equally important concern involves the quantification of the actual end loss, (q_{loss}), as a function of total rod power. Recall from Chapter 3.3 the proposed experimental methodology for measuring the convective heat transfer coefficient of a horizontal cylinder. In the development which led to equation (3.25), it was assumed that the total power supplied to a given rod was dissipated from the rod's surface by combined convective and radiative processes - exclusively. In order for this methodology to be viable, the actual end loss component, q_{loss} , must be negligible. If this is not the case, the end loss component must be explicitly included in the developed energy balance. In the following chapter, which contains the experimental design description, the subject of end losses will be taken up again, specifically with regard to the chosen experimental apparatus final design. Here it will be shown that the end loss component is indeed negligible and need not be explicitly measured and/or corrected for.

4.7 SUMMARY

This chapter has consisted of a variety of scoping calculations whose intent has been essentially two-fold. First, it was hoped that a better understanding of the fundamental heat transfer mechanisms associated with horizontal SNF would be obtained. Secondly, it was desired that this insight would facilitate the design and construction of a SNF assembly mock-up. The preceding analyses allow the following conclusions to be drawn:

- Individual fuel rods within a horizontal spent fuel assembly will have surfaces which are circumferentially isothermal (within $\pm 1-2\%$ of the mean).

- The heat flux on the surface of individual fuel rods will be circumferentially non-uniform.

- Natural convection can result in significantly lower SNF assembly peak temperatures.

- Natural convection results in significant upward skewing of assembly isotherms.

- Axial end losses can be minimized through such design considerations as rod length, rod material, cladding thickness, and rod support mechanism.

These observations are of import with respect to both computational and experimental investigations of SNF systems. With regard to the latter, the lessons learned were applied to the design of an experimental apparatus which simulates a

SNF assembly during horizontal transport and/or dry storage. The hardware and software systems which comprise this design are the subject of the next chapter.

Chapter 5 - Experimental Apparatus Design Description

5.1 INTRODUCTION

In order to investigate the multimode heat transfer processes associated with the horizontal transportation and storage of spent nuclear fuel, a scale model of a standard boiling water reactor (BWR) fuel assembly (cf. Figure 1.1) has been designed and constructed at The University of Texas at Austin (UT). The design of the experimental apparatus incorporates the following features:

1. The test assembly is geometrically equivalent to a BWR fuel assembly (in a two dimensional cross section).
2. The test assembly consists of materials which are essentially thermally equivalent to spent fuel.
3. The decay heat generated in spent fuel rods is simulated using electrical coil tubular heaters.
4. The fuel channel enclosure is maintained as a constant temperature heat sink.
5. The test assembly resides within a vacuum/pressure chamber which allows substantial pressure variation of the backfill gas.

In order to meet the stated experimental objectives, the required data must include surface temperature measurements of all heater rods as well as the surrounding enclosure, power dissipation by each heater rod, and global system pressure. These measurements are obtained using an automated data acquisition system, which also serves to control the test assembly's electrical power supply. The thermal conditions within the apparatus are varied by controlling the power input to the assembly as well as the pressure of the backfill gas, either nitrogen or helium. The intention is to cover as wide a range of Rayleigh number as possible subject to the power and pressure capabilities of the experimental system.

The design of the experimental apparatus was carried out keeping in mind the lessons learned from the scoping analyses presented in the previous chapter. The following goals were established specifically with regard to the design of the test section:

1. The test assembly should be instrumented in such a manner as to ensure accurate and extensive surface temperature measurement as non-invasively as possible.
2. Experimental uncertainty in measurements of temperature, power, and pressure should be minimized at reasonable cost.
3. Test conditions should be easily controllable and easily repeatable.
4. Axial heat losses must be minimized as allowable.

5. The data acquisition system should achieve a high level of noise immunity.
6. The entire system must be assembled within budget constraints.

The UT experimental apparatus represents a thermal simulation of a standard BWR 8X8 rod spent fuel assembly. Dry storage or transport of the assembly in a horizontal orientation is simulated. The design of the apparatus consists of six major components. This chapter presents a description of the major components in the following order:

1. the electrical heater rods
2. the copper boundary enclosure (CuBE)
3. the pressure vessel and related components
4. the power system
5. the cooling system
6. the data acquisition and control system (DAQCS)

A detailed discussion of the hardware and software aspects of the above systems follows. The actual construction, configuration, and testing of the overall system is discussed later in Chapter 6.

5.2 THE HEATER RODS

5.2.1 General

The individual spent fuel rods which comprise an assembly are represented by 64 tubular electrical coil heater elements custom manufactured by Watlow Electric Mfg. Co. of St. Louis, MO. The rods have a diameter of 1.224cm (0.482") and are 92.1cm (36.25") in length. The basic heater consists of a Nichrome heater coil insulated by compacted MgO, and clad within a stainless steel (SS304) sheath. Table 5.1 compares the thermal conductivity of Watlow heater rod materials to that of an actual nuclear fuel rod, the latter consisting of a central UO₂ fuel region wrapped by a Zircalloy 2 cladding.

Table 5.1 Thermal conductivity of UT heater rods and actual BWR fuel
(W/m-K averaged from 200 °C to 1000 °C)

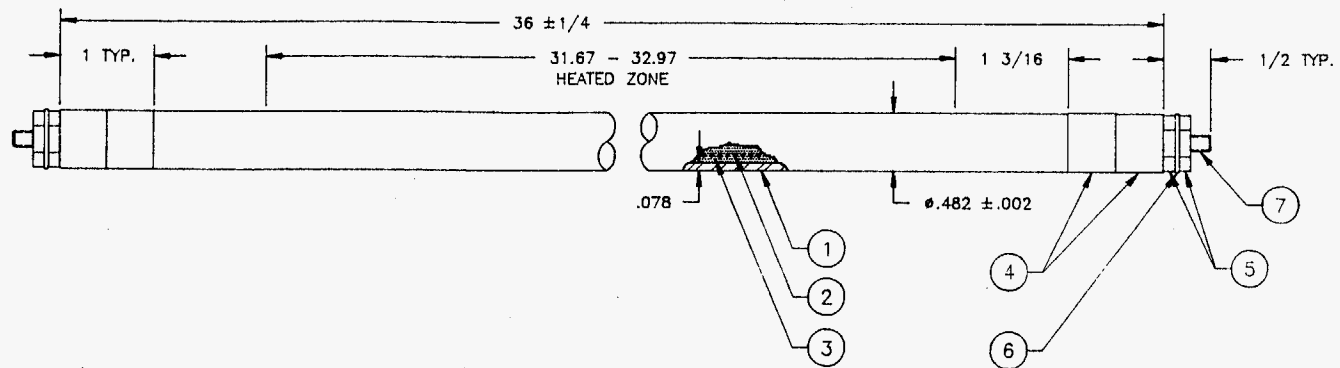
Material	<i>k</i>
MgO	2.07
SS304	15.2
UO ₂	3.60
Zircalloy 2	13.0

Three categories of Watlow heater elements were manufactured and utilized within the UT assembly:

1. Uninstrumented elements - A basic heater containing no instrumentation (thermocouples).
2. Instrumented elements containing two thermocouples - A basic heater equipped with two Type K mineral insulated metal sheath (MIMS) thermocouples (TCs) whose junctions are located at the axial midpoint of the heater. Each TC is located *within* the steel clad approximately 0.051cm (0.020") from the rod's surface. The TCs are circumferentially separated by 180°.
3. Instrumented elements containing three TCs - Identical to the elements equipped with two TCs but further instrumented with a third TC whose junction is axially offset 12.7cm (5.0") from the heater rod's midpoint.

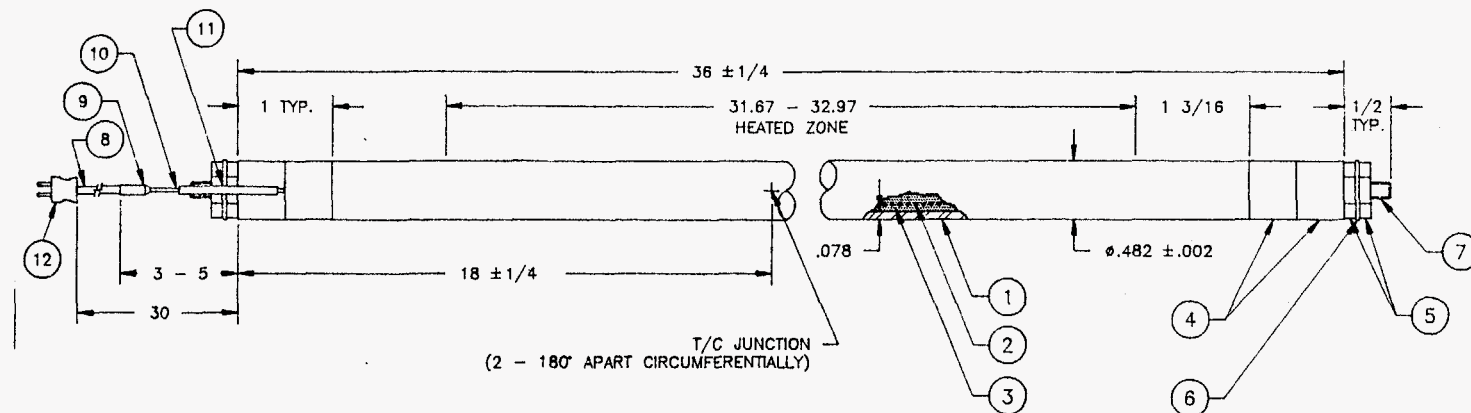
The manufacturer's drawings of each heater design are depicted in Figures 5.1-5.3. In these drawings, all dimensions and tolerances are given in terms of inches. Table 5.2 is a separate list of specifications for the instrumented rods.

Upon receipt of the heater rods, all physical dimensions were checked in house in order to ensure the stated tolerances. Watlow Co. further provided X-ray images of the heater rods such that the integrity and locations of all thermocouple junctions could be verified. The thermocouple junction positions were electro-etched on the outer surface of the instrumented rods in order to have an



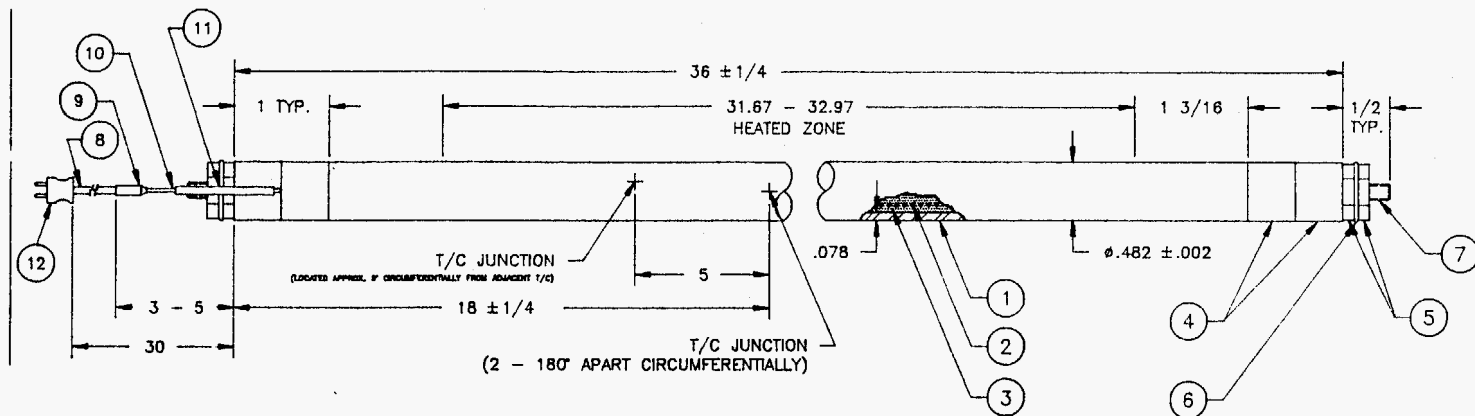
Item	Bill of Material
1	Sheath - Type 304 stainless steel
2	Resistance element - 80%Ni/20% Cr
3	Insulation - Magnesium oxide
4	Terminal insulator: mica
5	6-32 Hex nut - stainless steel
6	#6 Flat washer - stainless steel
7	6-32 Terminal - stainless steel

Figure 5.1 Watlow Co. drawing of an uninstrumented heater rod



Item	Bill of Material
1	Sheath - Type 304 stainless steel
2	Resistance element - 80%Ni/20%Cr
3	Insulation - Magnesium oxide
4	Terminal insulator - mica
5	6-32 Hex nut - stainless steel
6	#6 Flat washer - stainless steel
7	6-32 Terminal - stainless steel
8	TC lead - 24 Ga. Type K insulated wire
9	TC adapter - Type 304 stainless steel
10	TC - $\phi 0.032$ " Type K MIMS TC
11	TC insulator - rubber coated fiberglass
12	TC connector - Gordon pt. 850-K

Figure 5.2 Watlow Co. drawing of a double TC instrumented heater rod



Item	Bill of Material
1	Sheath - Type 304 stainless steel
2	Resistance element - 80%Ni/20%Cr
3	Insulation - Magnesium oxide
4	Terminal insulator - mica
5	6-32 Hex nut - stainless steel
6	#6 Flat washer - stainless steel
7	6-32 Terminal - stainless steel
8	TC lead - 24 Ga. Type K insulated wire
9	TC adapter - Type 304 stainless steel
10	TC - $\phi 0.032$ " Type K MIMS TC
11	TC insulator - rubber coated fiberglass
12	TC connector - Gordon pt. 850-K

Figure 5.3 Watlow Co. drawing of a triple TC instrumented heater rod

Table 5.2 Heater rod specifications

Sheath material	stainless steel, SS304
Resistance element	Nichrome wire (80% Ni/20% Cr)
Insulation	Magnesium oxide (MgO)
Terminal insulator	mica
Heater coil resistance (20°C)	$6\Omega \pm 0.3$
Coil to sheath insulation resistance	$> 25M\Omega$
Outer diameter	$12.24\text{mm} \pm 0.051$ (0.482" \pm 0.002)
Sheath thickness	0.198cm (0.078")
Heated length	$82.09\text{cm} \pm 1.65$ (32.32" \pm 0.65)
Thermocouple (s) [TC]	Type K MIMS
TC junction location	0.051cm (0.020") below surface
TC metal sheath diameter	0.081cm (0.032")
TC wire diameter	0.013cm (0.005")
TC wire resistance	$39.5\Omega \pm 1$

identifiable and permanent marker of their location. The heater rod coil resistance, coil to sheath insulation resistance, and TC wire resistance were also verified and recorded. The proper operation of all TCs was checked in two ways. First, a hand-held calibrator was used in order to verify that each heater rod TC was properly measuring room temperature. Secondly, a propane torch was run down the length of the heater rod (containing the TC lead wires) in order to ensure that no parasitic junctions or shorts had occurred during shipment. The TC is working properly if it responds only when the torch is passed over the junction location.

The design of each heater rod is a unique feature of the UT experimental apparatus. As such, a more detailed discussion pertaining to this topic is given in the following section.

5.2.2 Heater Rod Construction

Figure 5.4 illustrates the detailed construction of an instrumented heater rod. Instrumented rods generally contain two Type K MIMS thermocouples located at the axial midpoint of the rod, and separated circumferentially by 180°. The decision regarding the placement of heater rod TCs was made in response to the preliminary results of the scoping calculations discussed in Chapter 4. These results generally indicate that each rod within a horizontal enclosed array will be essentially circumferentially isothermal. Placing two TCs at opposing sides of each heater rod will thus allow an accurate measurement of the mean rod surface

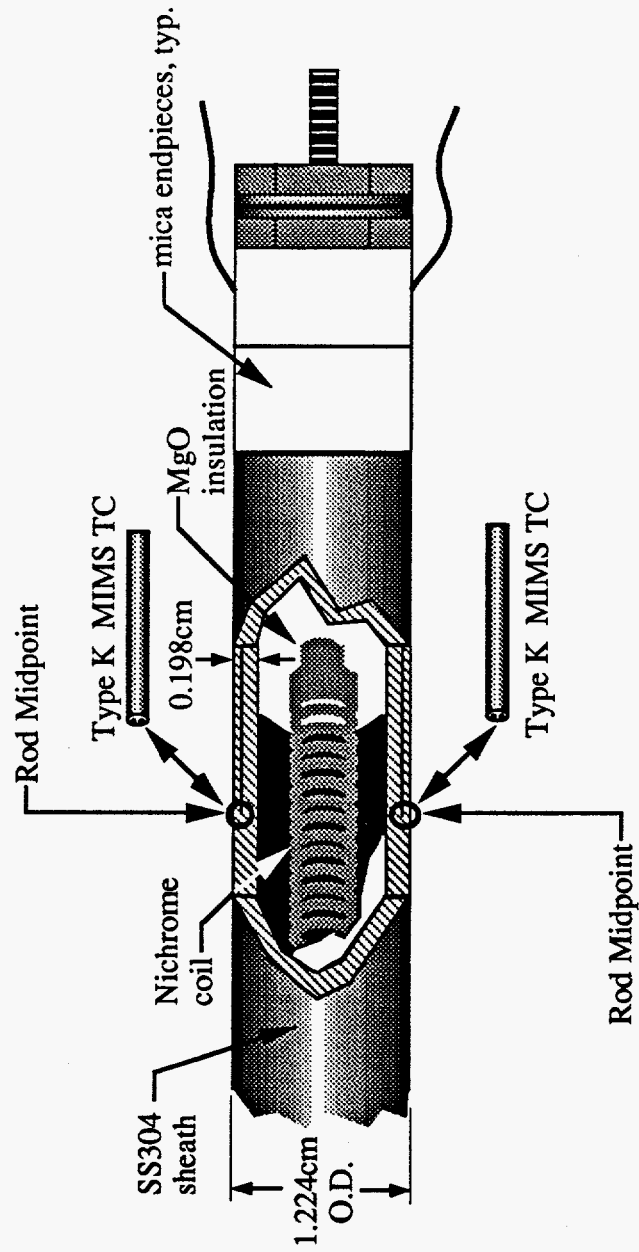


Figure 5.4 Cut-away view of an instrumented heater rod

temperature. The thermocouples are located *within* the sheath of the rod by a manufacturing process whose individual steps are shown in Figure 5.5. In step 1, a basic heater rod is made, consisting of a magnesium oxide insulated Nichrome wire coil which is wrapped in a SS304 clad. In step 2, an intermediary tube is fabricated which contains twin slots down half of its length. These slots are outfitted with the MIMS thermocouples, whose construction is essentially identical to that of the heater rod in that the 0.013cm (0.005") diameter Type K wire pair is insulated by compacted MgO and clad within a SS304 sheath. This intermediary tube containing the TCs is then fitted over the basic heater, sandwiching the TCs in position between the steel sheaths. A final steel sheath is created in step 3, and this outer tube is fitted over the heater assembly as indicated in step 4 of Figure 5.5. The assembled components are then swaged together under high pressure, resulting in a single homogeneous sheath heater rod as shown in step 5. The final rod has a 0.198cm (0.078") thick SS304 clad intimately in contact with the thermocouple, which resides approximately 0.051cm (0.020") from the rod's outer surface. The significant advantage which arises from having the TC reside entirely within the heater rod sheath is that there are no exposed wires external to the sheath which can interfere with the boundary layer flow across the rod or influence the radiative heat transfer between rod surfaces. This design also minimizes conduction heat losses in the thermocouples wires. All heater rods are of the grounded junction variety, meaning that the actual TC junction is welded to the surrounding steel thermocouple sheath. Although an ungrounded junction TC would be more immune to noise, it is

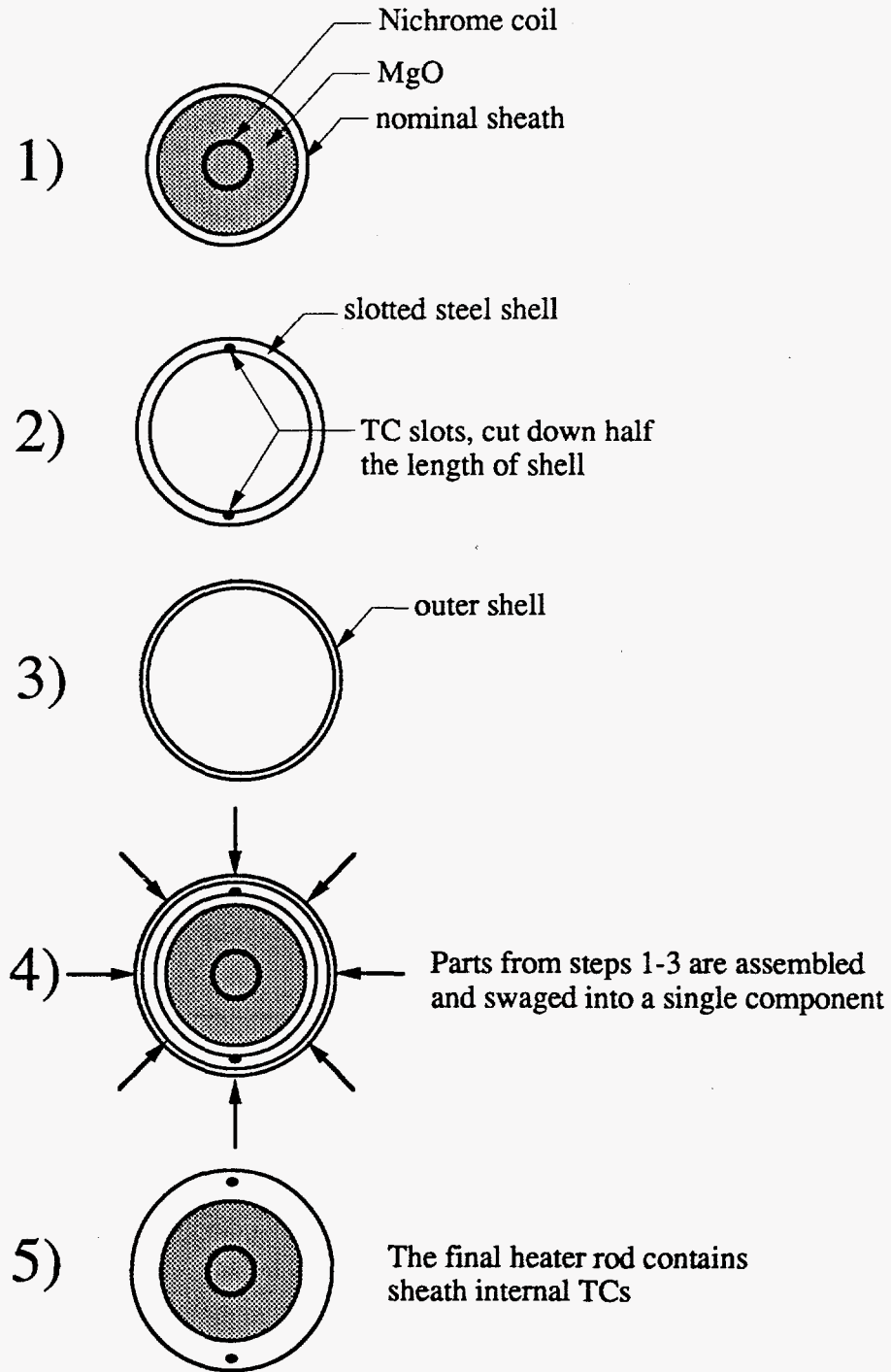


Figure 5.5 Manufacturing steps required for an instrumented rod

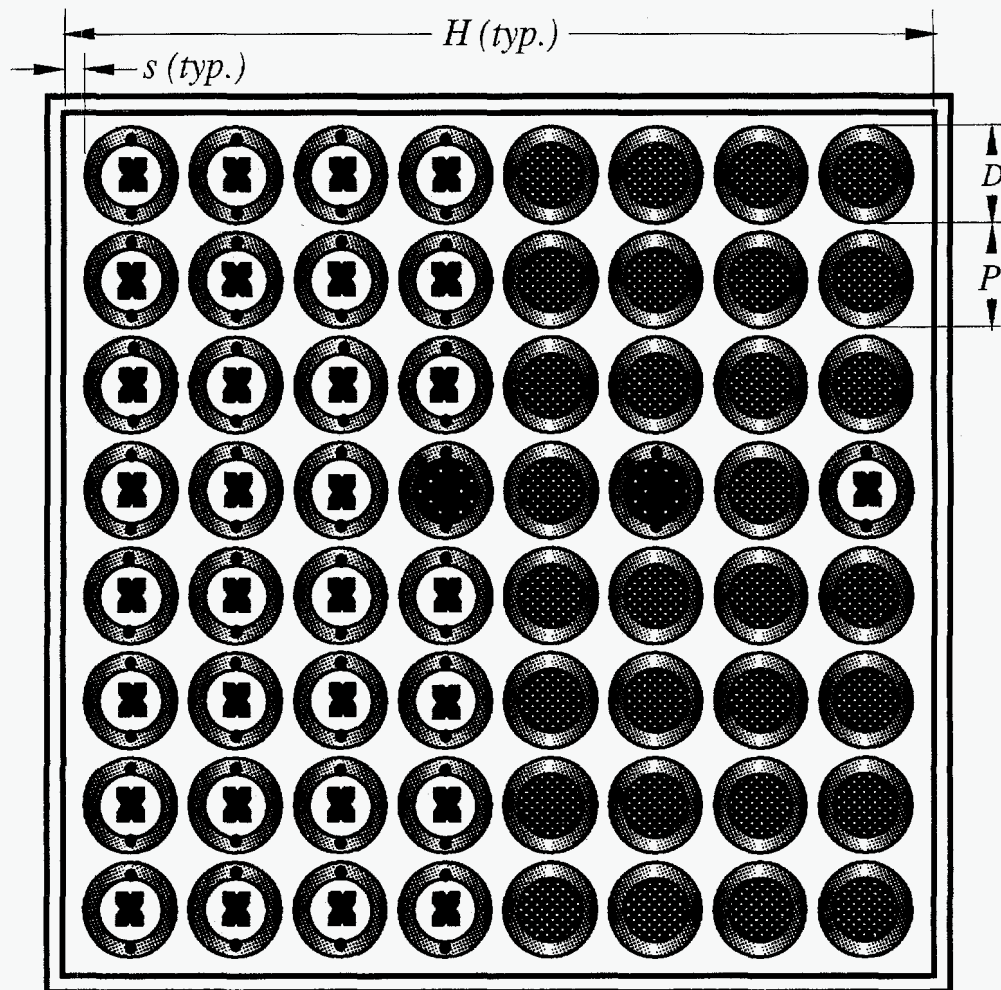
considerably more expensive and would not be in direct contact with the heater rod sheath whose temperature is sought.

The MIMS thermocouples associated with each instrumented rod emerge from the rod sheath and immediately enter twin 0.158cm (0.063") wide channels or grooves, which are bored (internally) through the rod's mica endpieces. Each heater rod contains two mica insulators on each end of the rod. The *grooved* endpieces, found only on the thermocouple end of instrumented rods, allow the MIMS TCs to pass through any rod support structure without interference or danger of pinching the TC lead wires (cf. Figures 5.2 and 5.3).

Some instrumented heater rods contain a third MIMS TC which is located 12.7cm (5.0") from the axial rod midpoint. The junction of this TC is offset approximately 9° circumferentially from its adjacent mid-rod TC (cf. Figure 5.3). This axially offset TC provides a quantitative measure of the uniformity of the axial temperature gradient. This gradient is minimized through several design features which will be discussed in Section 5.2.4 of this chapter.

5.2.3 Heater Rod Arrangement

The quantification of the fundamental heat transfer modes present within the experimental apparatus requires that the surface temperature of *all* heater rods be known. However, advantage can be taken of the system's symmetry about a vertical plane (cf. Chapter 3.2.2). Symmetry considerations led to the instrumentation scheme depicted in Figure 5.6, in which essentially half of the test






-  Uninstrumented tubular heater
-  Instrumented tubular heater with 2 TCs
(both at midpoint, 180° circumferentially apart)
-  Instrumented tubular heater with 3 TCs
(two at midpoint, 180° apart; one 12.7cm off midpoint)

Figure 5.6 Instrumentation scheme for the UT test apparatus

assembly is comprised of uninstrumented rods. This scheme provides substantial cost savings yet allows reasonable assertion of all required temperatures. The two instrumented rods located on the 'uninstrumented' side of the assembly provide a measurable means of verifying the symmetry assumption during test conditions. In total, there are seventy heater rod MIMS TCs within the rod bundle.

The UT heater rod design was guided by a desire to mimic an actual spent fuel rod as closely as possible. This was accomplished to a high degree both from a physical and a thermal perspective. The physical dimensions depicted in Figure 5.6 are identical to that of a standard General Electric 8X8 BWR assembly typical of all BWR/2, 3, 4, 5, and 6 reactors (DOE/RW-0184, 1988). Table 5.3 repeats these dimensions for all future reference.

Table 5.3 UT experimental assembly dimensions (cf. Figure 5.6)

Diameter (D)	12.24mm
Pitch (P)	16.20mm
Wall gap (s)	4.19mm
Enclosure Height (H)	134.06mm

5.2.4 End Effects Revisited

The heater rods in the UT apparatus have a heated length of $L_h = 82.09\text{cm} \pm 1.65$ ($32.32'' \pm 0.65$). The total rod length is 92.1cm ($36.25''$). This length was chosen based upon the axial analysis presented in Chapter 4.6. This analysis indicated that for fuel (heater) rods of the described design and composition (zircalloy or steel clad), a choice of $L_h \approx 1.0\text{m}$ would be essentially infinite ($\pm 0.1\%$) with respect to the midpoint rod temperature. This conclusion was obtained using conservative assumptions regarding the rod end support mechanisms. However, it was also pointed out that quantification of the actual end loss component is necessary as well. This subject will be presently addressed by specifically evaluating the end loss as a function of total supplied power for the heater rod design as specified in Table 5.2.

The first step in the prediction of the expected end loss is to calculate the axial temperature gradient for the chosen heater rod design. Using the rod specifications given in Table 5.2, and the analytical solution given by equations (4.29) through (4.31), the axial temperature profile as depicted in Figure 5.7 was determined. This plot is actually the excess temperature normalized to the infinite case value [cf. equation (4.31)]. As before, a uniform convection coefficient of $h=5.0\text{W/m}^2\text{K}$ has been assumed. Data are plotted from the rod midpoint ($x=0$) to the end of the rod's heated length, $L_h/2 = 0.41\text{m}$. Again, the area correction factor, C_f , has been varied in order to represent a wide range of possible end support

boundary conditions. By design, the UT heater rod's axial temperature gradient (and thus end loss) is minimized by the following features:

1. the choice of the heater's length
2. minimization of the clad thickness
3. insulation of each heater's end with a 2.54cm long mica endpiece
4. use of rod support plates which provide essentially a point contact with the rod's mica insulators (described in Chapter 5.3).

The last two points will determine the appropriate C_f value for the present design. Recall from Figure 4.19 that if $C_f=1.0$, then the effective area for rod tip convection (A_{eff}) is equal to that of the clad's cross sectional area (A_c). It is believed that in the present design, a value very close to $C_f=1.0$ has been obtained through the use of mica insulators and minimal-contact rod support plates. That being the case, Figure 5.7 depicts a relatively flat axial temperature profile, a good sign for anyone interested in mitigating end losses.

These losses can be easily quantified given the analytical solution for the axial temperature profile [equation (4.29)], by using Fourier's Law in order to relate the axially conducted energy to the axial temperature gradient:

$$q_{loss} = -k_c A_c \left. \frac{d\theta}{dx} \right|_{x=L_r/2} \quad (5.1)$$

The evaluation of equation (5.1) yields the following expression:

$$q_{loss} = \frac{hC_f q' \sinh\left(\frac{mL_h}{2}\right)}{k_c m \left\{ m \sinh\left(\frac{mL_h}{2}\right) + \left(\frac{hC_f}{k_c}\right) \cosh\left(\frac{mL_h}{2}\right) \right\}} \quad (5.2)$$

Figure 5.8 illustrates the end losses for the present heater rod design as a function of total supplied power, q , for a given rod. During experimentation, an individual rod power of $q \approx 6\text{W/rod}$ will not likely be exceeded. Hence, the upshot of Figure 5.8 is that the predicted end losses for the current heater rod design are essentially negligible in comparison with the total supplied power. This statement can be further quantified by scaling equation (5.2) above by the total rod power and expressing the result as a percent:

$$\frac{q_{loss}}{q} = \frac{\left(\frac{hC_f}{L_h}\right) \sinh\left(\frac{mL_h}{2}\right)}{k_c m \left[m \sinh\left(\frac{mL_h}{2}\right) + \left(\frac{hC_f}{k_c}\right) \cosh\left(\frac{mL_h}{2}\right) \right]} \quad (5.3)$$

where m is given by equation (4.22). Table 5.4 gives the percentage end loss (of the total rod power) as a function of the area correction factor, C_f .

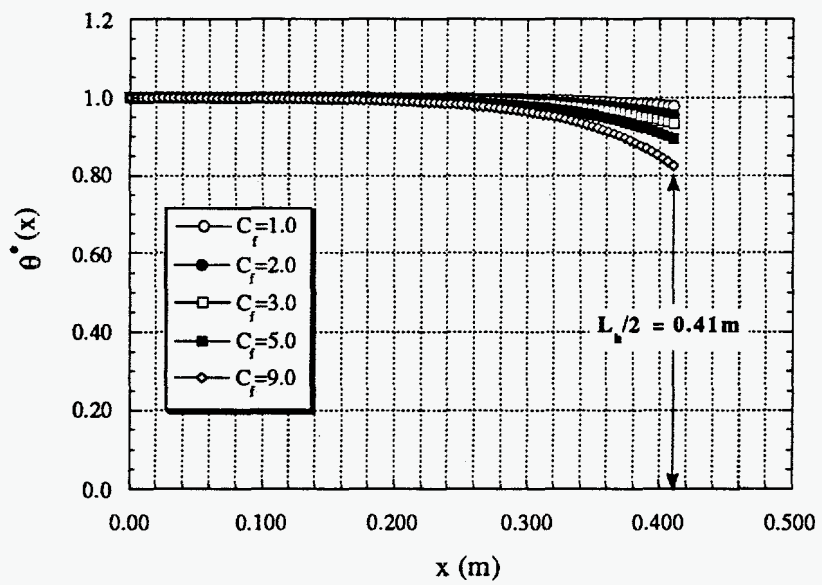


Figure 5.7 Heater rod axial temperature profile as a function of C_f

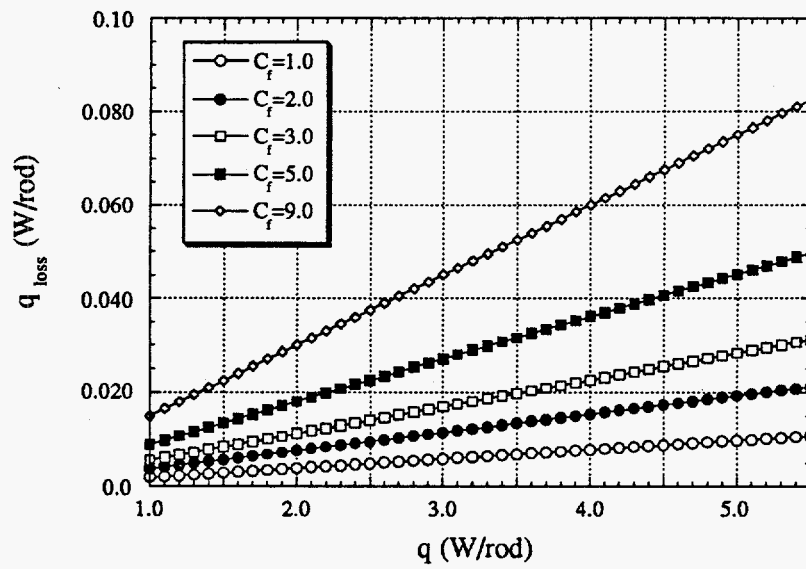


Figure 5.8 Heater rod end losses as a function of total supplied power and C_f

Table 5.4 Percentage end loss as a function of C_f

C_f	q_{loss} / q (%)
1.0	0.198
2.0	0.386
3.0	0.567
5.0	0.905
9.0	1.50

Even in the unlikely case that the rod tip boundary condition is best represented by $2 < C_f < 5$, the predicted total end loss for a given rod remains less than 1% of the total supplied power. Thus, it is asserted that end losses within the UT experimental assembly are negligible. Although certain assumptions such as a uniform rod convection coefficient may not be realistic, a good deal of conservatism has been built into the preceding calculations to lend confidence to this assertion.

5.3 THE COPPER BOUNDARY ENCLOSURE

All heater rods are assembled and enclosed within a rectangular copper boundary enclosure (the CuBE) which represents the BWR fuel channel (cf. Figure 1.1). The CuBE was custom manufactured by Century Machine Co. of Albuquerque, NM. It has an interior channel width of 13.41cm (5.278") square and an axial length of 87.31cm (34.375"). The walls of the CuBE are 1.27cm

(0.5") thick, tightly bolted together, and sealed with a high thermal conductivity grease in order to minimize circumferential temperature variation from wall to wall. The CuBE is actively water cooled during all testing in order to obtain steady state conditions within the vacuum/pressure vessel in reasonable time periods. Each wall of the CuBE is independently cooled by water flow through a 0.635cm (0.25") diameter serpentine copper tube soldered to the external CuBE surface.

Figure 5.9 depicts the engineering drawing of the CuBE from an end view. The CuBE consists of two sets of two identical copper plates. The top and bottom plates are shown in Figure 5.10; whereas, the side plates are drawn in Figure 5.11. When these pieces are assembled, a rectangular box is formed whose walls are 1.27cm (0.5") thick. The thick copper walls provide an essentially isothermal enclosure boundary condition. The CuBE sits on eight 1.91cm (0.75") ceramic legs in order to insulate the box from the steel surface upon which it rests during experimentation. The top wall of the CuBE can be easily removed in order to replace and/or service the heater rods contained within. The rods are supported within the CuBE by two heater rod support plates as seen in Figure 5.12. These plates are 0.160cm (0.063") thick brass squares, which fit over the ends of the CuBE, holding the heater rods in an 8X8 square array with a pitch-to-diameter ratio of 1.32. Each plate is tapped with sixty four 1.27cm (0.500") holes which only contact the heater rods on their 2.54cm (1.0") insulative mica endpieces (cf. Figure 5.4). Thus, there is no contact at any point between the steel heater rod surface and the CuBE support plates. The thickness of the brass support plates is

further limited in order to minimize the support area in contact with the mica and thus reduce the amount of heat conducted from the heater rods to the plates.

The inner surface temperature of the CuBE is monitored during testing by ten Omega Co. Type K foil thermocouples, bonded to the interior CuBE walls with Omegabond 200 epoxy and supported with aluminum tape. The 0.013mm (0.0005") thick, flat foil thermocouple junction provides maximum thermal coupling to the mounting surface. A thin layer (< 1mm) of Omegabond 200 high thermal conductivity epoxy is used in order to hold the TC in place with minimal conduction resistance between the TC junction and the inner CuBE surface. Figures 5.13a and 5.13b depict the locations of the CuBE foil TCs on the top/bottom plates and side plates, respectively. Eight of the ten foil TCs reside at the CuBE's midpoint, where the majority of the heater rod TCs reside. At this midpoint, there are two foil TCs on each wall of the CuBE. The remaining two foil TCs are offset 20.32cm (8.0") from the CuBE midpoint toward what is the East wall of the laboratory. Figure 5.14 is a cross sectional view of the CuBE at its midpoint, viewed from the East wall. The eight midpoint foil TCs are shown, and are designated t1; t2; N1; N2; b1; b2; S1; and S2, clockwise from the top of the CuBE.

5.4 THE PRESSURE VESSEL AND RELATED COMPONENTS

The fully loaded CuBE customarily resides within a vacuum/pressure vessel capable of maintaining either a nitrogen or helium backfill over a range of pressure statepoints. This enables conditions within the test assembly to be

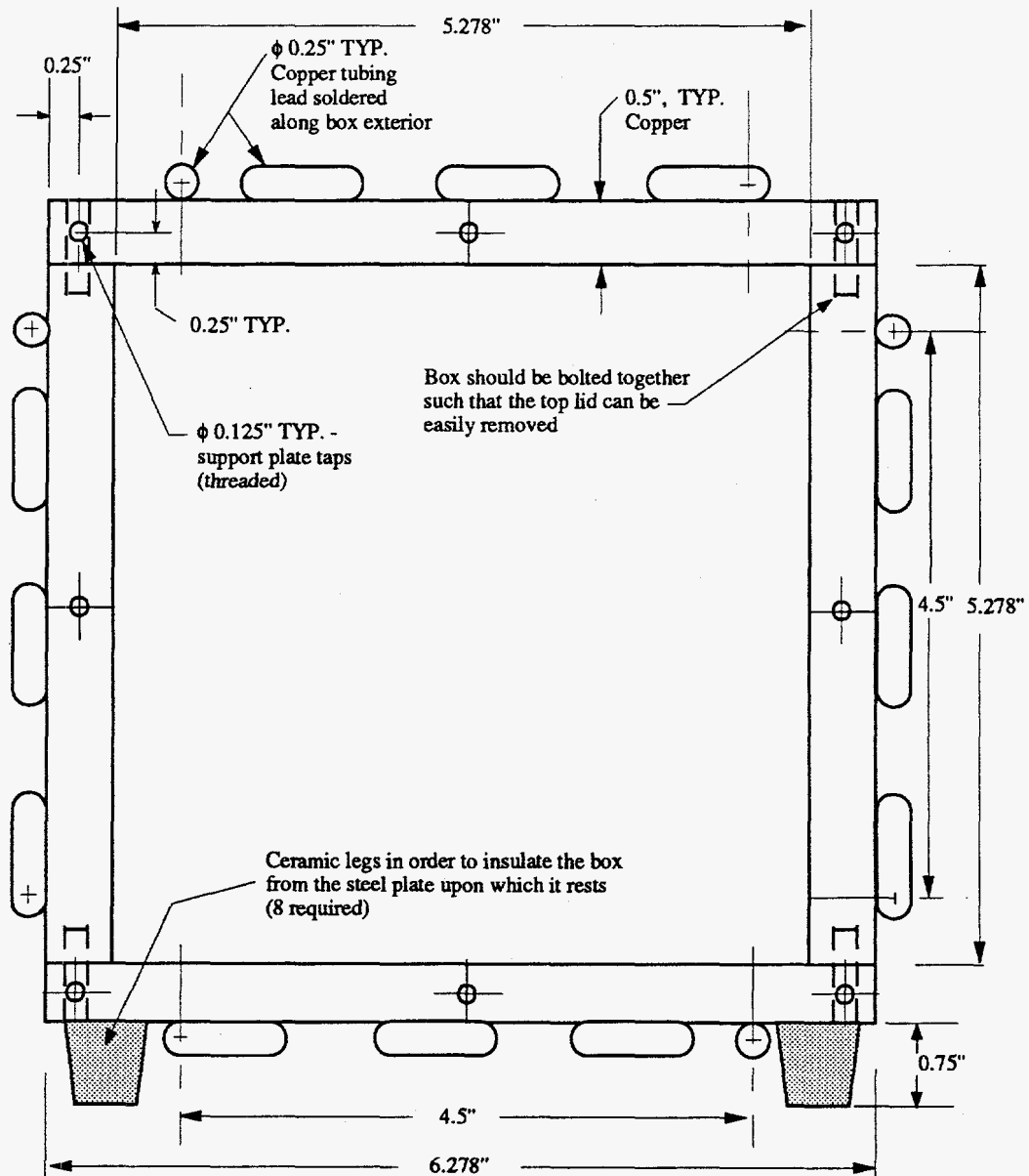


Figure 5.9 End view of CuBE (all units in inches)

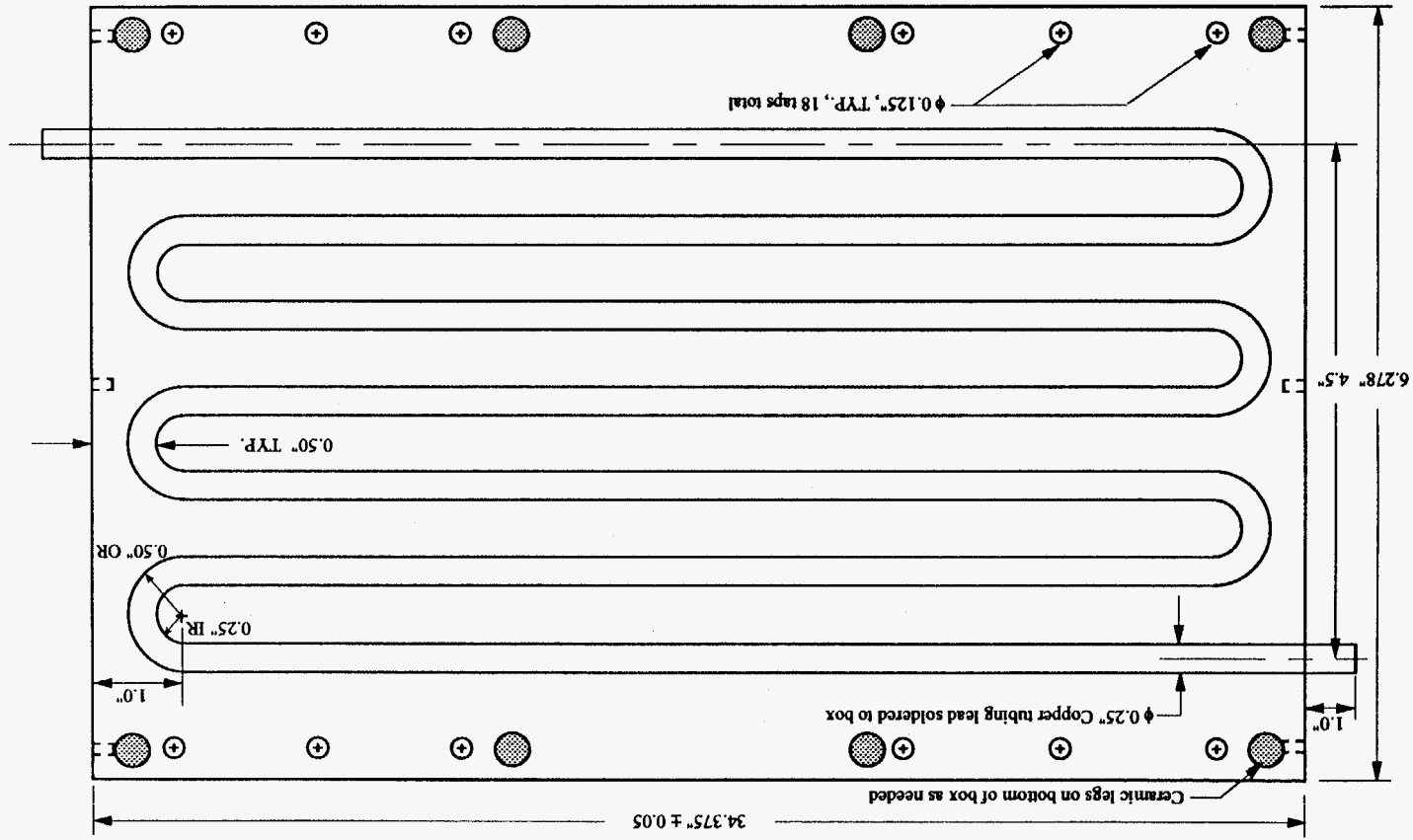


Figure 5.10 Top/bottom wall of CuBE (all units in inches)

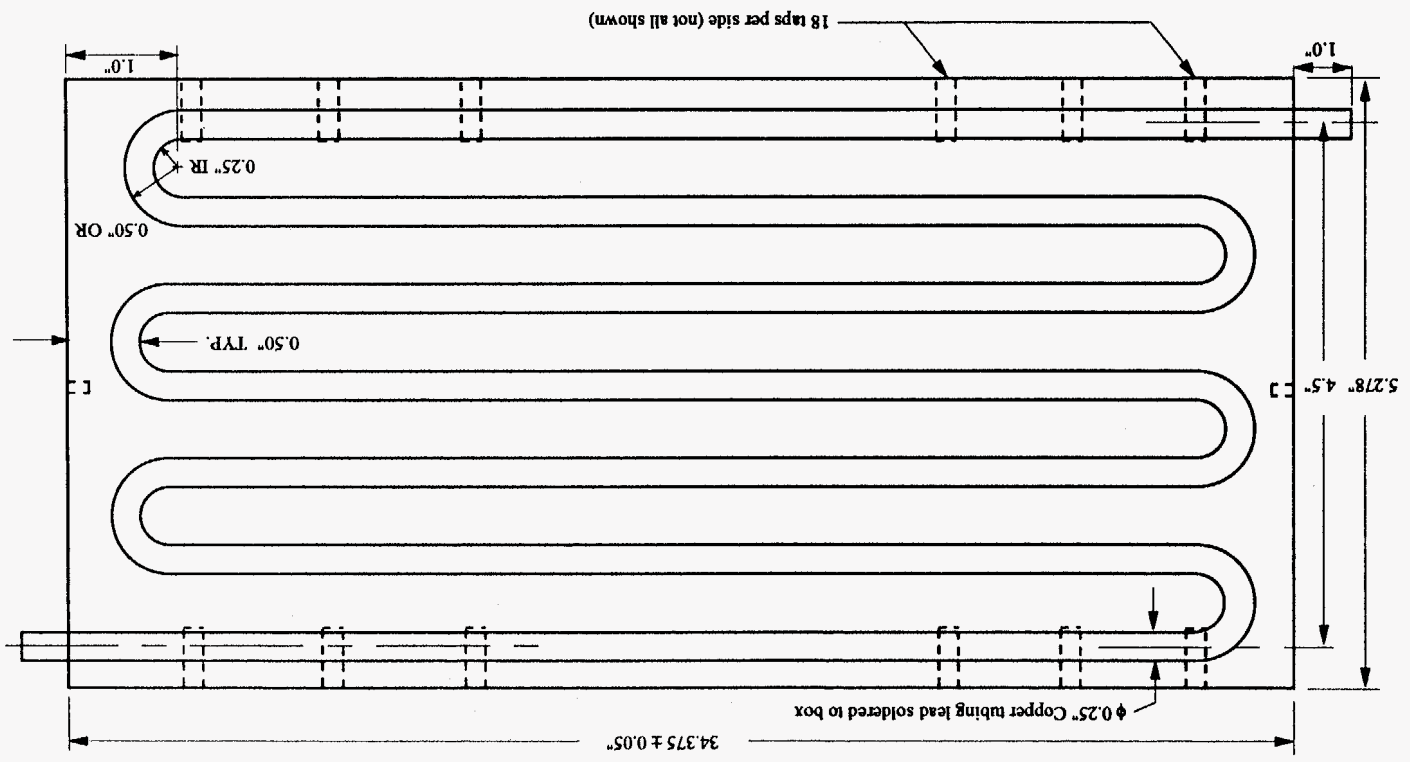


Figure 5.11 Side wall of CuBE (all units in inches)

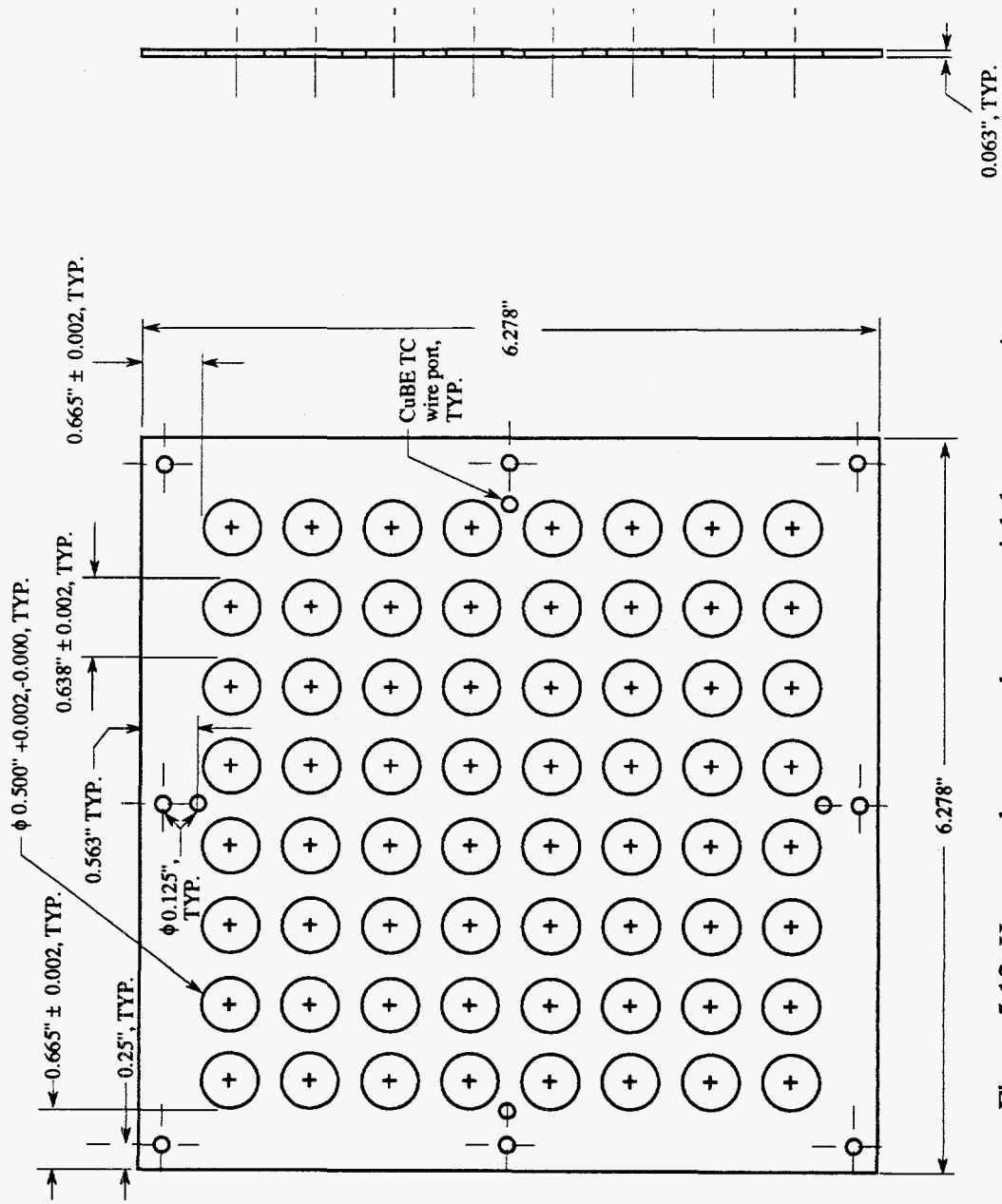


Figure 5.12 Heater rod support plate, material: brass, quantity: two
(all units in inches)

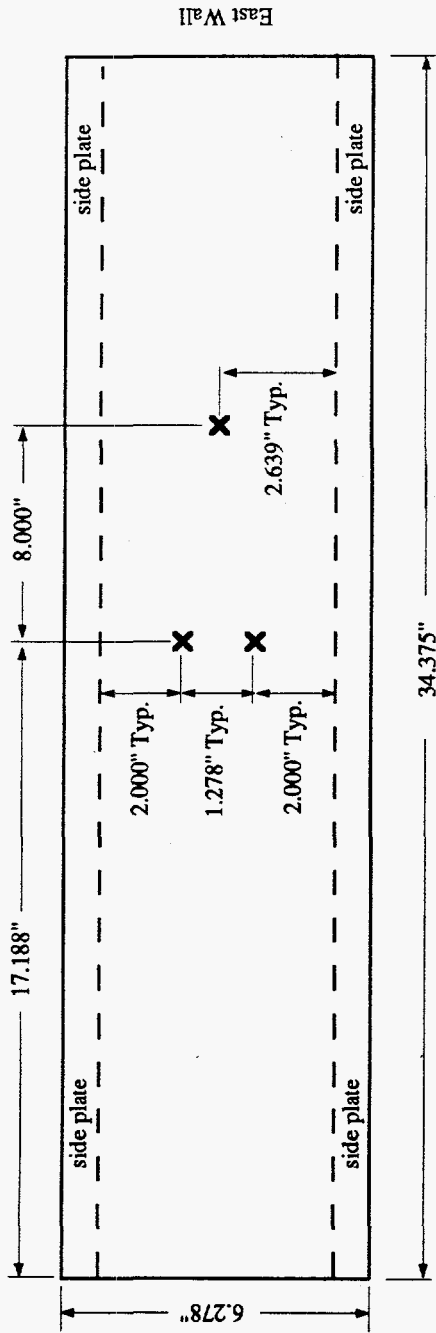


Figure 5.13a Top/bottom view of CuBE indicating inner surface mounted foil TC locations

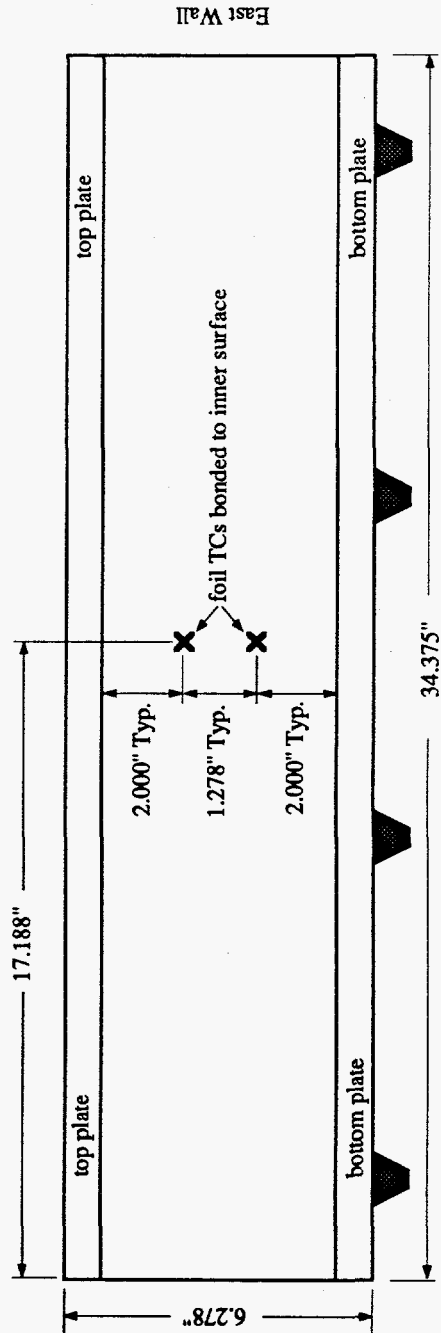


Figure 5.13b Side view of CuBE indicating inner surface mounted foil TC locations

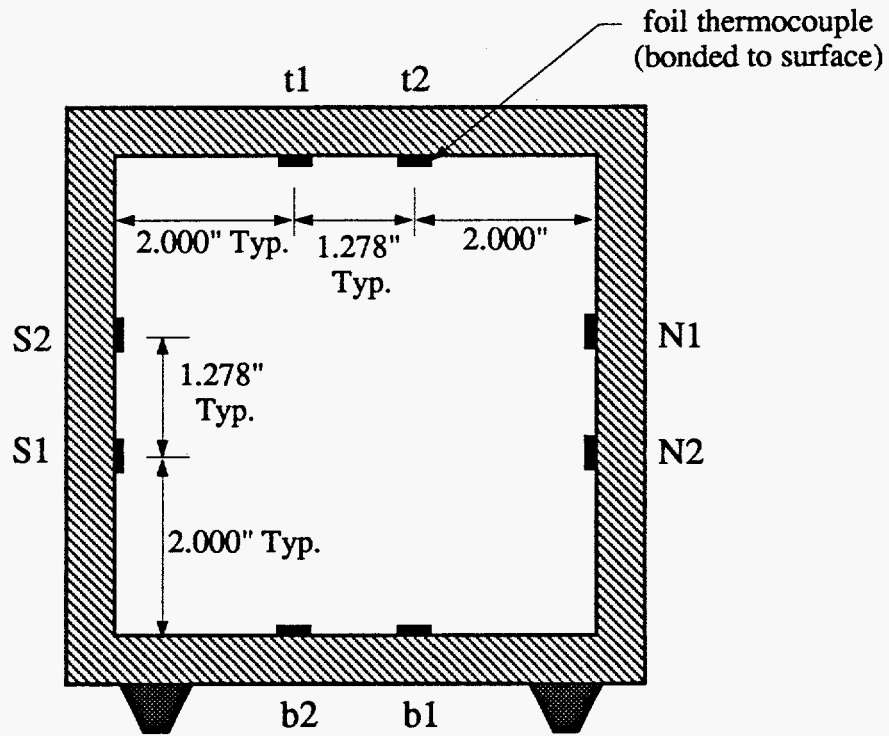


Figure 5.14 Cross sectional view of CuBE midpoint, viewed from the East wall

altered such that natural convection is either enhanced or hindered relative to atmospheric conditions, providing a substantial data range. The vessel itself is an ASME approved, 45.72cm (18.0") inner diameter flanged carbon steel (SA53-B) cylinder of total length 1.6m (63.0"). The walls are 0.953cm (0.375") in thickness and the pipe is terminated at each end with 68.1kg (150lb) SA105 carbon steel flanges. The main pipe contains thirteen, 1.91cm (0.75") NPT female threaded penetrations. It is sealed prior to experiment using compressible non-asbestos gaskets seated on a grooved lip. The pressure vessel was manufactured by Massachusetts Engineering Co. in Avon, MA. The list of specifications for the chamber is given in Table 5.5.

The CuBE rests within the pipe on a rectangular steel support surface, which is in turn welded to a track mounted along the vessel's lower interior wall. The support surface slides along the track on ball bearing assisted rollers, enabling the CuBE to be easily inserted or extracted from the pressure vessel. The sliding support additionally allows routine maintenance to be performed on the heater rod/CuBE assembly without the need to fully remove it from the pressure vessel. The CuBE's ceramic legs thermally and electrically insulate it from the vessel support surface. The support surface and its railed track were fabricated and installed within the pressure chamber by UT's Mechanical Engineering machine shop.

Table 5.5 Pressure vessel specifications [from Lovett, (1991)]

Material (pipe)	SA53B carbon steel
Material (flange)	SA105 carbon steel
Length (pipe w/o flange)	152.4cm \pm 2.54 (60" \pm 1.0)
Outside diameter	45.72cm \pm 0.25 (18.0" \pm 0.1)
Penetrations	13, 1.91cm (3/4") female NPT Locations: A. West wall: 22.86cm \pm 0.64 (9.0" \pm 0.25) from end of pipe Number: 4 circumferentially offset 90° \pm 2 B. Pipe center: 76.2cm \pm 0.64 (30.0" \pm 0.25) from West end of pipe Number: 1 at top of vessel C. East wall: 137.16cm \pm 0.64 (54.0" \pm 0.25) from West end of pipe Number: 8 circumferentially offset 45° \pm 2
Design pressure	Minimum: full vacuum Maximum: 618.1kPa \pm 6.9 (75 psig \pm 1)
Design temperature	200°C \pm 5

Figure 5.15 is a cut-away view of the pressure vessel, as viewed from the North in the laboratory in which it is located. The CuBE and its support track are visible. Ten of the pipe's thirteen penetrations are utilized during testing. Three penetrations are used for thermocouple feedthroughs; two penetrations are used for water coolant feedthroughs; one penetration is used for power line feedthroughs; one penetration is used for a pressure safety relief valve; one penetration is valved for chamber pressurization; one penetration is valved for vacuum depressurization; and one penetration contains a pressure gauge. Figure 5.16 illustrates views of the vessel and its penetrations from the East and West walls of the laboratory.

The thermocouple wire pairs from all heater rods as well as the CuBE are fitted with twin prong, plastic insulated connectors (Gordon Co., part no. 850-K). These connectors interface with a thermocouple jack panel (Omega Co., part no. OSK/MJP-580K) mounted within the pressure vessel near its East end (cf. Figure 5.15). This location is designated the TC lead end of the vessel. The corresponding West wall region of the vessel is designated the non-TC end. The TC jack panel allows easy connect/disconnect of all TC pairs such that the test assembly may be readily removed from the vessel. The jack panel contains 5 rows of TC jacks, with 16 jacks per row, for a total of 80 thermocouple connections.

Conax Buffalo Co. high density vacuum feedthroughs pass eighty pair of Type K TC extension wires from the TC jack panel through the pressure vessel

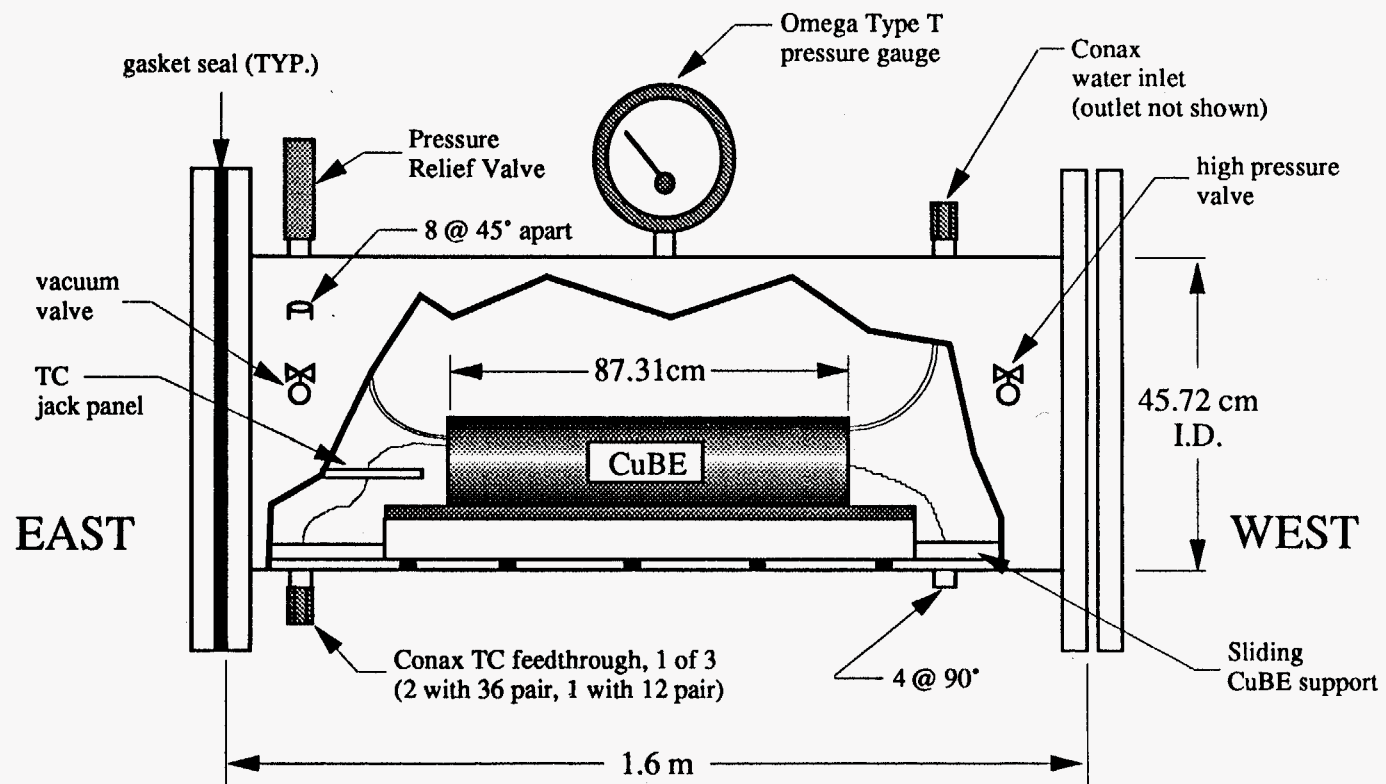


Figure 5.15 Pressure vessel cut-away viewed from the North wall

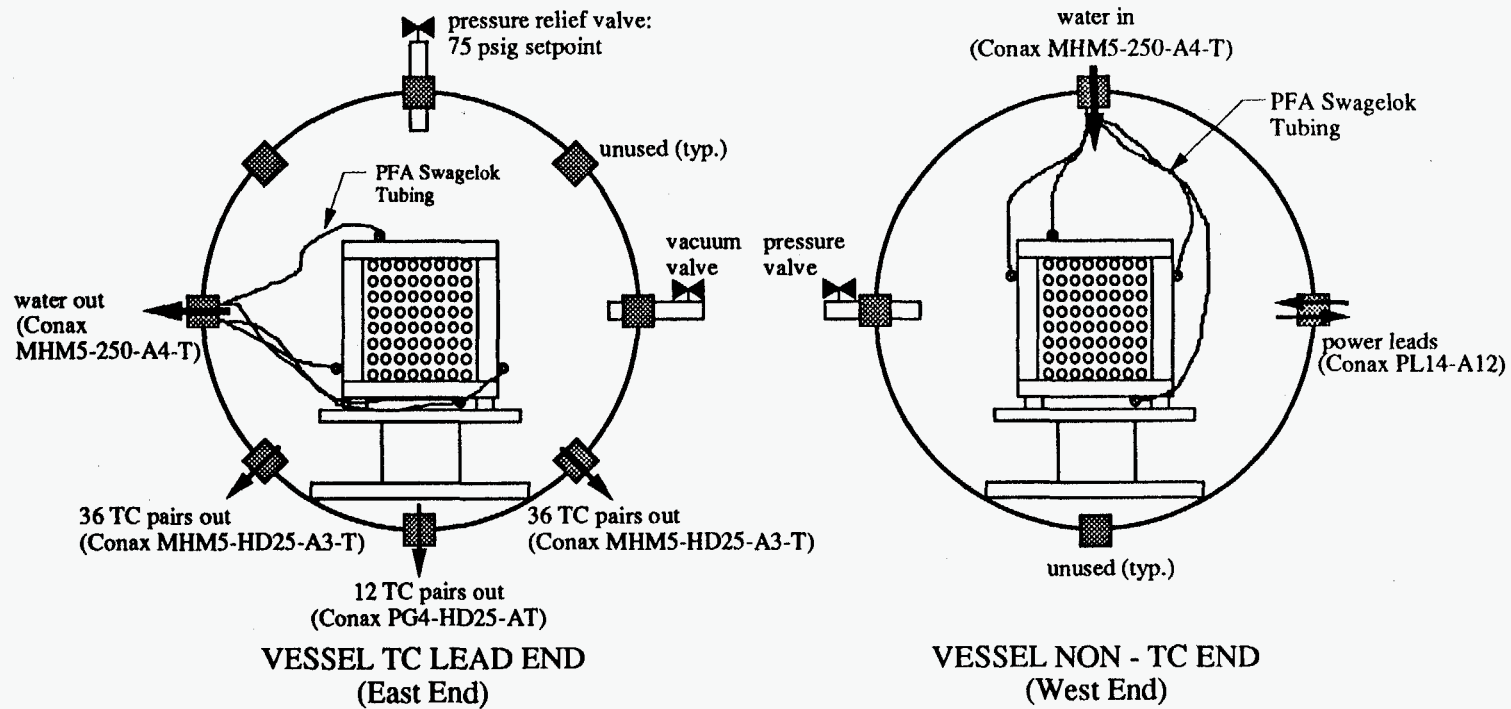


Figure 5.16 Vessel penetrations, feedthroughs, and valves within the UT apparatus

wall. Three thermocouple feedthroughs are utilized in total. Two of the TC feedthroughs are factory designated as MHM5-HD25-A5-T (cf. Figure 5.16), which each seal three separate bundles of Type K TC wire (12 pair per bundle, 36 pair per feedthrough) within a single 3/4" NPT male threaded fitting. The TC wire bundles are sealed with a Teflon sealant which is rated from full vacuum to 8,000 psi over a temperature range of -300°F to 450°F. The feedthroughs are tightened to factory recommended settings prior to testing using a torque wrench. Each pair of TC wires is custom labeled on each end of the feedthrough with a unique number which allows easy identification. The third remaining TC feedthrough is of similar design (designated PG4-HD25-AT), but only seals a single bundle of 12 thermocouple pairs. All of the numbered TC pairs are standard error limits Type K wire, 24AWG in size, and factory insulated. Four TC pairs (out of 84 total available) from the feedthroughs are unused.

Water coolant is passed into and out of the pressure vessel using two Conax Co. MHM5-250-A4-T feedthroughs. These glands are similar to those utilized for thermocouple feedthrough; however, each coolant feedthrough seals four 0.635cm (0.25") outer diameter Teflon coolant tubes. The tubing is PFA 350 material manufactured by Swagelok® Co. of Solon, OH. The quarter inch diameter tubing is thick walled [0.157cm (0.062")] and can be interfaced with Swagelok® Co. tube fittings for excellent sealing. Coolant enters the vessel in four paths (tubes) from the top penetration on the non-TC end (West), and exits from four tubes on a South side penetration of the TC lead end (East). Each of the four coolant paths is interfaced to the CuBE's copper tubing (on each end of the

CuBE) using a Swagelok® union (part no. PFA-420-6). Each wall of the CuBE is independently cooled in order to ensure an isothermal boundary condition.

The power lines which supply electrical power to the heater rods enter and exit the pressure vessel from a single feedthrough located on the non-TC end of the vessel as indicated in Figure 5.16. This feedthrough is a Conax Co. gland designated PL14-A12. This gland seals 12 mylar-insulated 14AWG copper wires from vacuum to 5,000psi over a temperature range of -300°F to 450°F. Each wire is rated 600V to 55A. Individual wires within the bundle are number labeled on both sides of the feedthrough for easy identification.

The pressure safety relief valve is an Anderson Greenwood Type 83 Safety Relief Valve (part no. 83S46-4L). The valve has a Kalrez® perfluoroelastomer O-Ring seat and is set with a lift pressure of 583.7kPa (70psig). The valve has a blowdown capacity of 0.79m³/min. (28 standard cubic feet per minute). This valve is directly installed on the pressure vessel as indicated in Figure 5.16.

The pressure vessel is depressurized using a Sargent Welch mechanical vacuum pump in order to obtain a moderate vacuum of 1torr (1000μHg). A Whitey Co. ball valve is used in order to isolate the vessel from the vacuum system. This valve is directly attached to the North side of the vessel's TC lead end. It should be noted from Figure 5.17 that a pressure of 1 torr (1000μHg) is not sufficient to eliminate gaseous conduction within the backfill gas. This pressure roughly coincides with the transition from the continuum regime to the

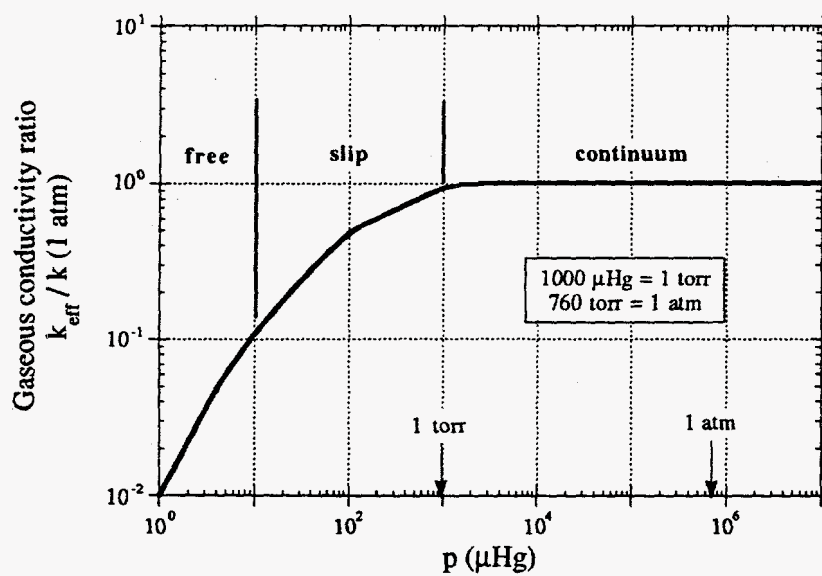


Figure 5.17 Effective gas conductivity as a function of vacuum pressure [from Manteuffel, (1991)]

slip region as indicated in Figure 5.17. Thus, no decrease in gaseous thermal conductivity (at 1 torr) can be expected relative to atmospheric pressure. However, this is not an issue in the present investigation since a true vacuum was not an objective of the experimental procedure for two reasons. First, the Rayleigh number range of interest can be obtained using a variety of gases (of varying convective potential) at pressures *greater* than atmospheric. In this study, helium was used in order to cover a low Rayleigh number range; whereas, nitrogen provided an upper Rayleigh number range (cf. Chapter 3.2.3.2). Secondly, the radiative heat transfer contribution was determined numerically, rather than experimentally. This will be discussed in Chapter 8. Hence, the sole purpose of the vacuum system in the present methodology is to purge the pressure vessel prior to changing the backfill gas in order to ensure a high purity backfill.

In order to pressurize the test chamber, a regulated high pressure cylinder gas source is utilized. A Whitey Co. ball valve located on the North side of the vessel's non-TC end isolates the vessel from the regulated source, as shown in Figure 5.16. In this study, nitrogen and helium of 99.999% purity are the chosen backfill gases. These gases not only provide a substantial Rayleigh number range, but are also the backfills currently under consideration for SNF transport and disposal. All experimentation is conducted between the pressure range of 101.4kPa and 515kPa (0psig and 60psig).

System pressure within the vessel is monitored and measured using an Omega Co. Type T Bourdon tube pressure gauge. The gauge is a compound type,

with scales ranging from full vacuum (30" Hg) to 514.9kPa (60psig). The above-atmospheric range of the gauge provides a resolution of $\pm 3.45\text{kPa}$ ($\pm 0.5\text{psi}$). The gauge's face additionally contains a mirror background in order to ensure accurate readings. The gauge is directly mounted on the top center vessel penetration as illustrated in Figure 5.16.

5.5 THE POWER SYSTEM

The power supplied to the heater rods within the pressurized vessel simulates the decay heat of radioactive species present within spent fuel assemblies. Thermally, the power input to the test section must be dissipated by both natural convective and thermal radiative processes, the distribution of which to either process is dependent upon factors such as the system pressure and the nature of the backfill gas, as well as the power level. The power supply for the present system is a *Hewlett-Packard Model 6030A DC supply, which can deliver* in excess of 1000W to the purely resistive heater rod load. A DC source was chosen in order to simplify the measurement of power and provide a low noise environment for thermocouple thermometry. Additionally, a power supply was desired which was capable of talking and listening to a controller via a general purpose interface bus (GPIB) line. In this manner, the data acquisition and control system could either interactively or programmatically control the heating rate to the test assembly, as well as receive information from the power supply regarding output voltage and current.

In addition to the power supply, the power system includes the hardware necessary to measure the power dissipated by heater rods within the experimental array. As was explained in Chapter 3, the characterization of the individual heat transfer mechanisms requires the measurement of both surface temperature and power dissipated by each *individual* heater rod. This allows an accurate energy balance to be obtained. In the UT experimental apparatus, the individual heater rod power is determined by measuring a rod's electric line current using 2A/100mV resistive shunts. The square of the measured line current multiplied by a given rod's measured resistance yields the desired rod power [cf. equation (3.17)]. A total of four shunts are presently required for line current measurement. Greater detail regarding the heater rod circuit and rod power measurement is given in Chapter 6.

5.6 THE COOLING SYSTEM

In order to obtain steady state conditions within the spent fuel assembly mock-up in reasonable time periods, the CuBE is water cooled, and thus serves as a heat exchanger. Each wall of the CuBE is independently cooled in order to ensure an isothermal inner wall boundary condition even under vigorous natural convective conditions, which will tend to preferentially heat the top wall of the enclosure. Chilled water is obtained within the laboratory at $\approx 24^{\circ}\text{C}$ (75°F), and is diverted into a four line manifold as depicted in Figure 5.18. Each of the four manifold lines consists of a horizontal tee fitting, which leads to a 3/8" Whitey Co. ball valve. A Ryan-Herco Co. rotameter gauge is mounted beyond the ball

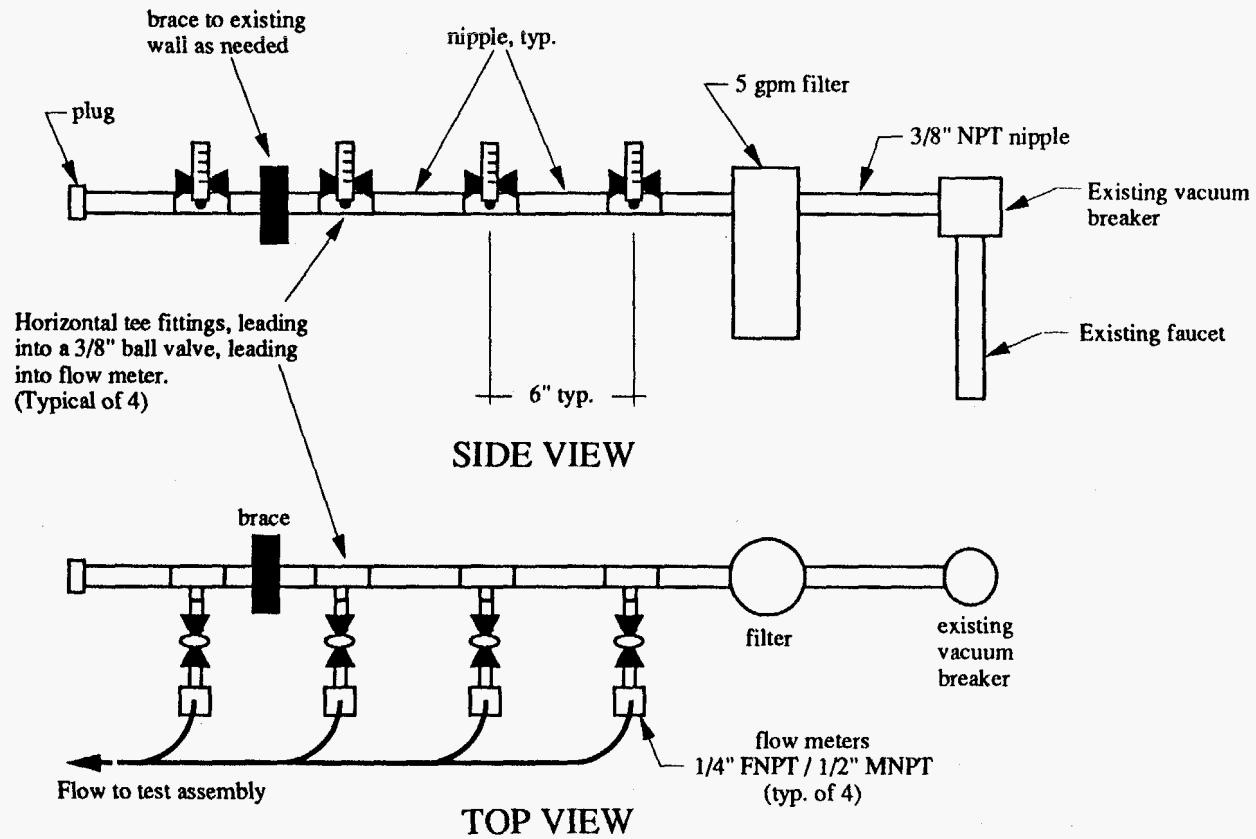


Figure 5.18 One to four line valved manifold with flow meters

valve in order to provide a measure of the cooling flow in each line. A flow rate of 1 gallon per minute is achievable in each of the four lines. A Swagelok® male connector interfaces the flow meter with the PFA flexible tubing which leads to the pressure vessel. The coolant lines enter the vessel through a Conax Co. MHM5-250-A4-T feedthrough, beyond which the lines are directly attached to the CuBE's copper tubing via Swagelok® union connectors. The cooling system is once-through, and the coolant lines exit the vessel through another Conax MHM5-250-A4-T feedthrough after passage through the CuBE's heat exchanger.

5.7 THE DATA ACQUISITION AND CONTROL SYSTEM (DAQCS)

The hardware associated with the employed data acquisition and control system (DAQCS) is illustrated in Figure 5.19. The system measures inputs consisting of thermocouple voltages and resistive current shunt potentials. The computing platform for the DAQCS is an Apple® Macintosh® personal computer equipped with two National Instruments Co. NuBus cards, one for data acquisition and one for external instrument control. The former board is the NB-MIO-16XH-42, a multifunction analog input board with 16 bit resolution and a maximum single channel sampling rate of 24,000 samples per second. Although the signals measured in the test assembly are DC and are typically sampled under steady state conditions, high speed data acquisition is important since a large number of input channels must be repeatedly averaged in order to reduce the effects of environmental noise. High resolution is additionally required since the accuracy of the resulting data depends upon the ability to measure subtle

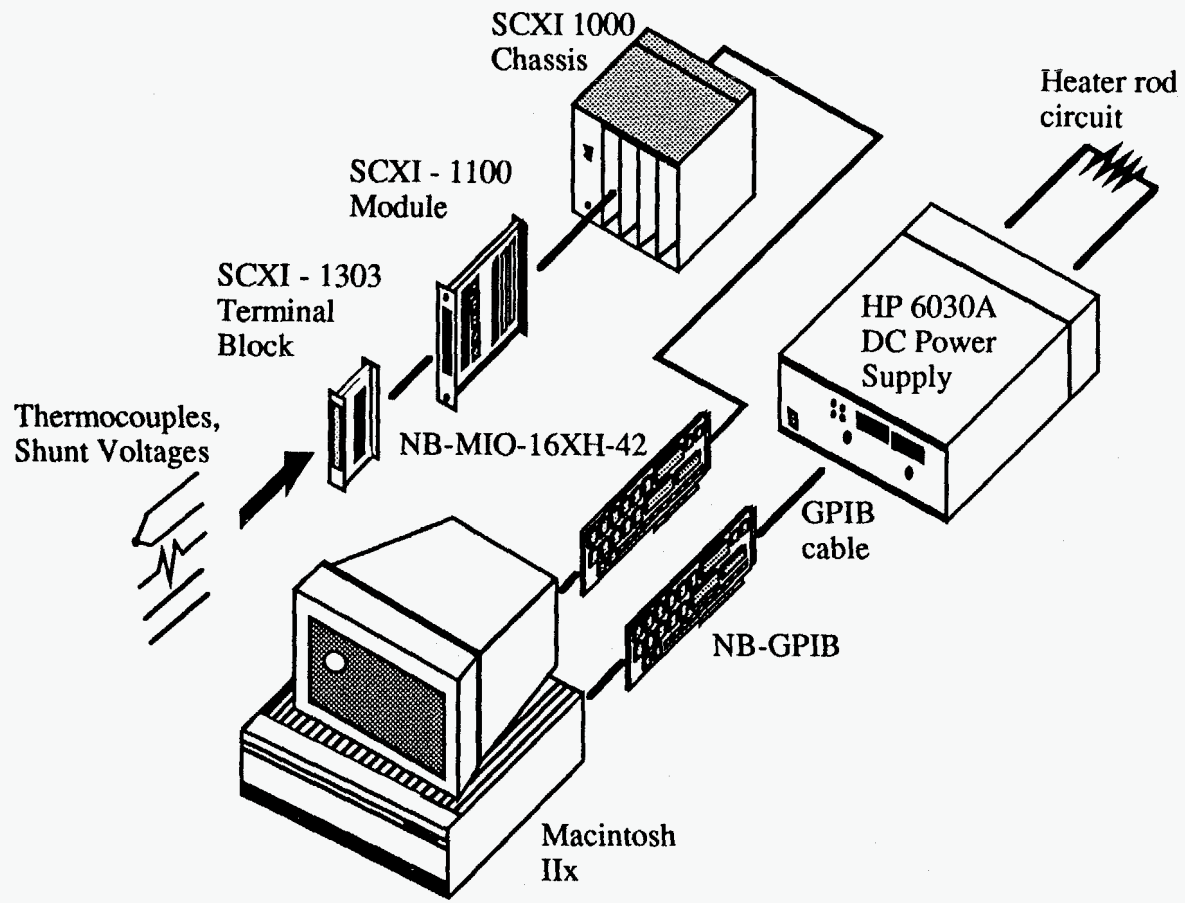


Figure 5.19 The UT data acquisition and control system

temperature differences throughout the experimental assembly. The *ideal* minimum detectable voltage swing with the current system based upon its input range, gain, and resolution is $0.30\mu\text{V}$, and thus the system is sensitive to slight variations in thermocouple output provided that appropriate efforts have been taken to minimize environmental noise. The second board installed within the Mac is the NB-GPIB, an IEEE 488 interface which provides basic Talker, Listener, and Controller functions between external stand-alone instruments and the Macintosh. In the present system, the GPIB board allows software control of the Hewlett-Packard 6030A DC power supply.

In order to multiplex and condition the incoming voltage signals, the National Instruments (NI) Signal Conditioning eXtensions for Instrumentation (SCXI) system was utilized. The UT SCXI system consists of a four slot SCXI-1000 chassis, four SCXI-1100 signal conditioning modules, and four SCXI 1303 terminal blocks. The incoming analog signals are connected directly to the SCXI-1303 terminal blocks as illustrated in Figure 5.19. The terminal block contains screw terminals for thirty two inputs, housed within a shielded enclosure. The terminal block additionally contains an on-board thermistor temperature sensor for cold junction thermocouple compensation. Each terminal block mates with an SCXI-1100 module, which is housed within the SCXI-1000 chassis. The SCXI-1100 module is a 32 differential channel multiplexer containing a software programmable gain instrumentation amplifier (PGIA) and low-pass filter. A module may be configured for thermocouple, millivolt, or voltage sources. Each SCXI-1100 module multiplexes its 32 input channels into a single channel of the

NB-MIO-16XH-42 data acquisition board installed within the Macintosh. The SCXI-1000 chassis contains a backplane bus which allows four 1100 modules to be cascaded together, resulting in a 128 (32 X 4) channel multiplexed system. The major advantage of this system stems from the fact that low level voltage signals are amplified and multiplexed within a shielded chassis which can be located close to the signal sources and therefore isolated from the noisy PC environment. Only high level conditioned signals are thus sent to the data acquisition card for analog-digital conversion and direct storage into PC memory, resulting in a greater degree of noise immunity.

The DAQCS hardware is programmed and controlled using National Instruments Co. LabVIEW® software. LabVIEW® for Macintosh allows complete programming and system control through a graphical user interface known as a virtual instrument, or VI. The virtual instrument consists of a front panel and a block diagram. The former serves as an interactive interface for supplying inputs to as well as observing real time outputs from the instrumentation system. The front panel may be tailored to emulate a particular stand-alone instrument's operating panel, or custom designed for a specific instrumentation system. The block diagram is the palette for the graphical programming structures which control the flow of data as well as provide various analysis functions and input/output operations.

Figure 5.20 is the main front panel used to interpret data from the UT spent fuel assembly mock-up. This front panel was designed specifically for the present application using LabVIEW® software. The real time compensated

output of all TCs as they are arranged within the experimental array appears in the left hand side of the panel. Since most of the instrumented heater rods contains two TCs per rod, the paired yellow-outlined indicators represent the TCs associated with a given heater rod. The red-outlined indicators represent the heater rods which are instrumented with three TCs (cf. Figure 5.6). The ten TCs associated with measurement of the CuBE interior wall are outlined in blue. The reference temperatures measured by the SCXI-1303 thermistors for cold junction TC compensation are outlined in green at the lower center of the panel. Total assembly power as well as the measured heater rod line currents are updated by digital indicators located on the upper right hand side of the front panel. A push-button titled "PLOT?" enables the operator to bring up another front panel which portrays a graphical strip chart of relevant TC channels (Figure 5.21). This feature provides a real time graphical temperature history, allowing the operator to determine whether or not the desired steady state conditions have been achieved throughout the system. The power supplied to the test assembly by the Hewlett-Packard 6030A DC power supply is controlled via the GPIB from a front panel on the Macintosh monitor as well. Figure 5.22 depicts the front panel which allows the user to input the desired operating voltage and current to the 6030A. During testing, this VI additionally provides feedback measurement of the voltage and current at the power supply's output terminals (see Figure 5.20).

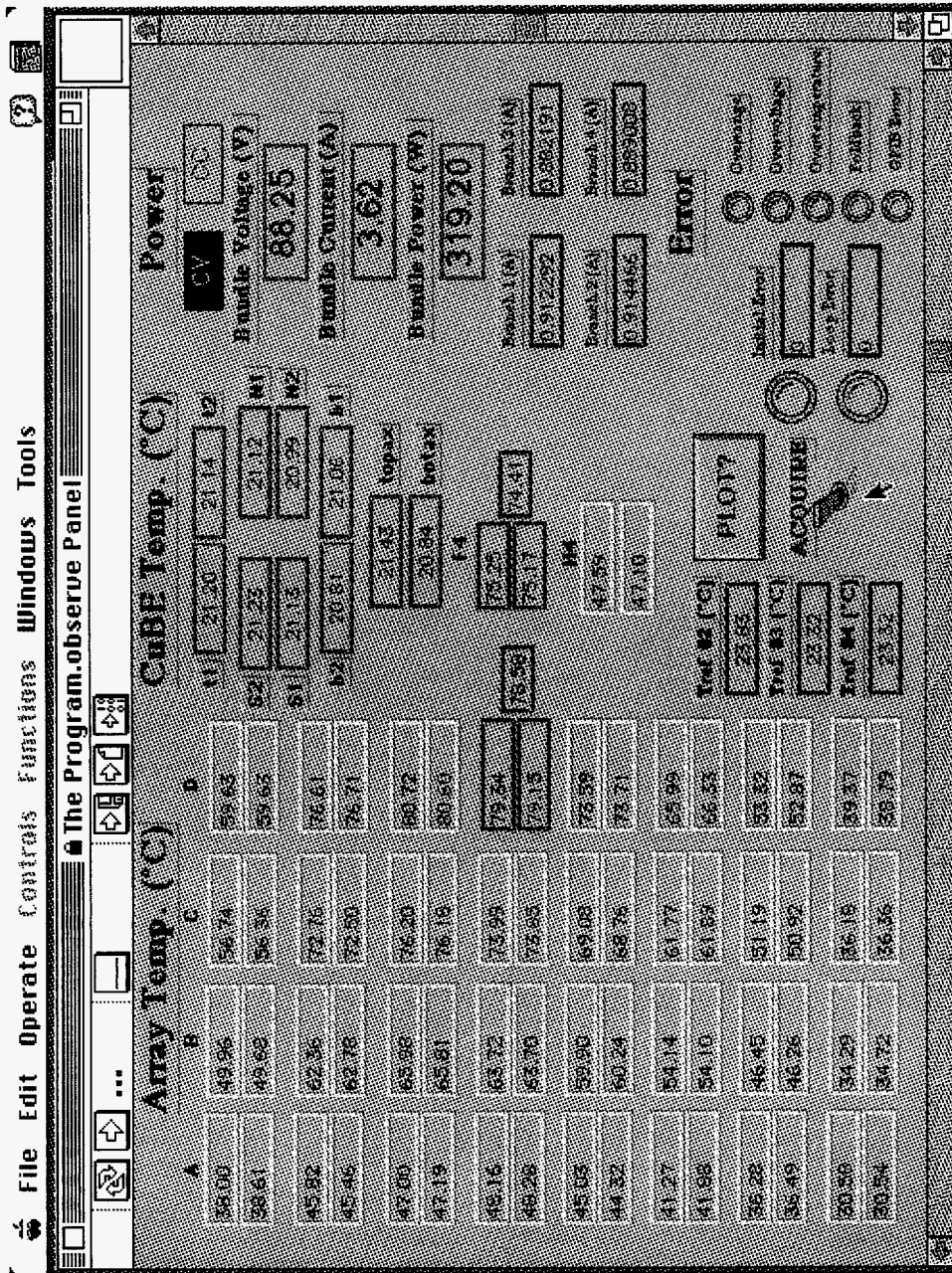


Figure 5.20 The main LabVIEW® front panel for DAQCS operation

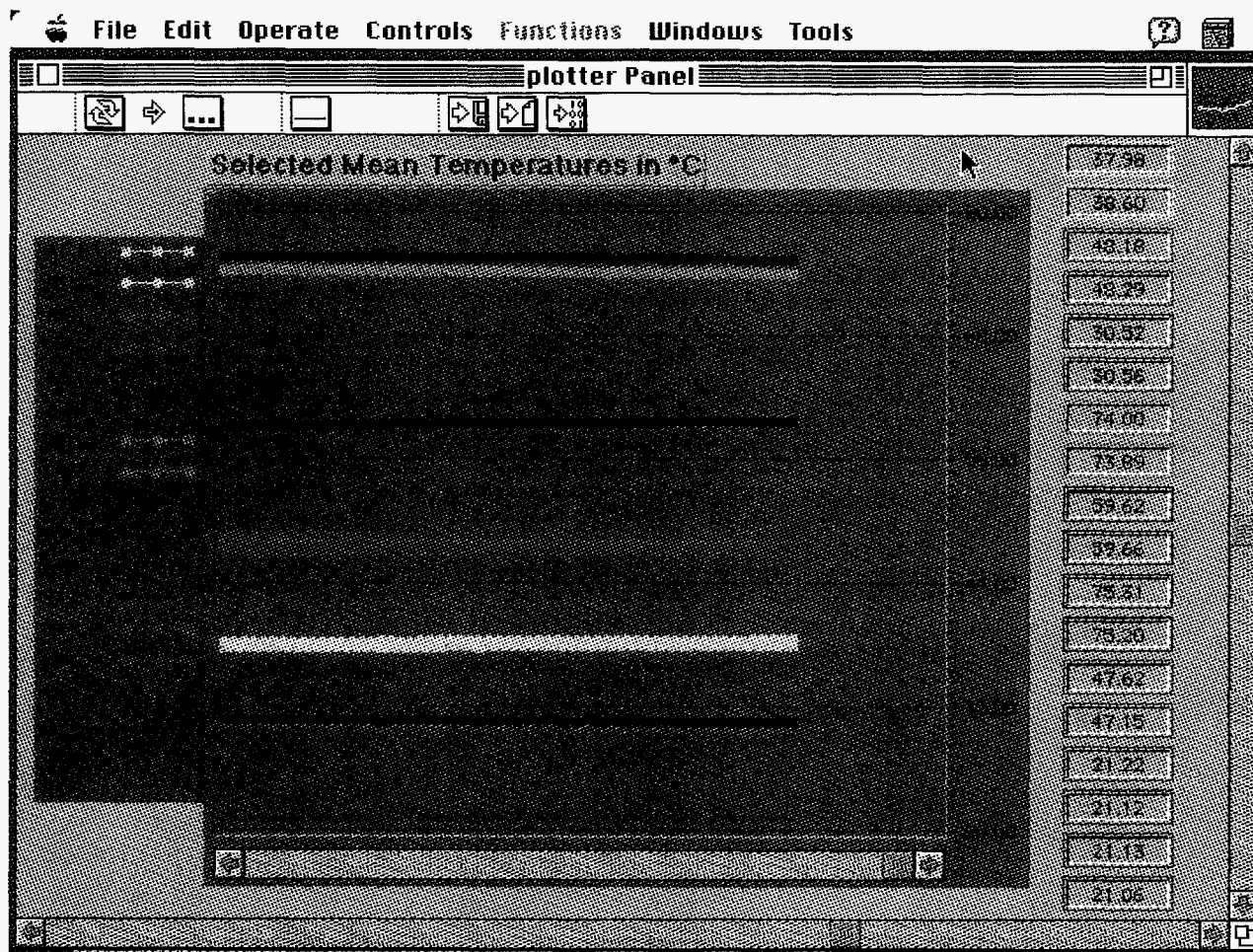


Figure 5.21 LabVIEW® strip chart for real time temperature observation

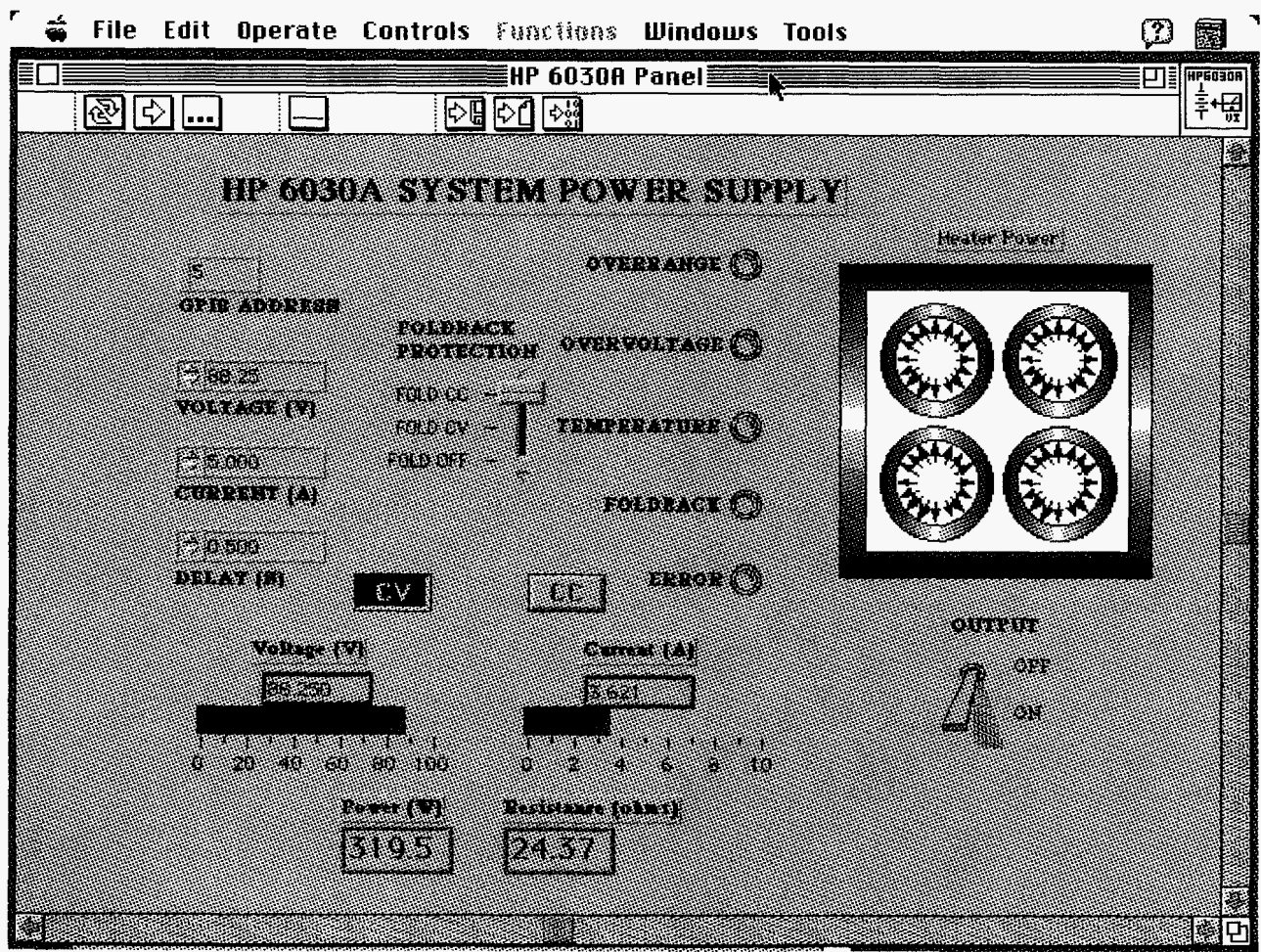


Figure 5.22 Front panel for power supply control and communication

5.8 INTEGRATED SYSTEM

Figure 5.23 depicts the integrated sub-systems which comprise the UT spent fuel assembly test apparatus. Easily identifiable in the photo are the heater rod loaded CuBE resting on its support rack; the pressure vessel including coolant, power line, and TC feedthroughs; and the data acquisition and control system. The pressure vessel is mounted on a custom designed steel table which possesses both stationary feet and wheels. The six feet are independently adjustable such that the mock assembly can be positively leveled on uneven floor surfaces. A Starrett No. 130 Precision Iron Bench Level is used in order to ensure that the test assembly is level prior to experimentation. The feet can also be retracted, in which case six wheels support the table, allowing easy transportability of the experiment.

This chapter has described the individual sub-systems which make up the experimental apparatus. Chapter 6 will focus upon the assembly, configuration and debugging of these sub-systems into a working experiment. Particular attention will be paid toward steps taken in order to minimize environmental noise, ensure proper calibration, and maximize experimental accuracy.



Figure 5.23 The overall UT experimental apparatus

Chapter 6 - Assembly, Configuration, and Debugging

6.1 OVERVIEW

The preceding chapter outlined and reviewed the major sub-systems which comprise the UT spent fuel assembly mock-up. The intention of this chapter is to describe the physical assembly and configuration of these sub-systems into an integrated operational experiment. The following topics will be discussed:

- Heater rod testing and preparation
- CuBE preparation and loading
- Electrical circuit configuration
- Heater rod power measurement
- DAQCS configuration and testing
- Initial tests and debugging

Furthermore, this chapter will present any additional information gathered during the configuration/debugging phase which is pertinent to the experimental procedure or its results.

6.2 HEATER ROD TESTING AND PREPARATION

As was discussed in Chapter 5.2, the heater rods were inspected upon receipt in order to ensure operation within the requested specifications and/or tolerances. The inspection included the following procedures:

1. Measurement of heater coil resistance at room temperature
2. Measurement of coil to sheath insulation resistance
3. Measurement of heater rod TC wire resistance (room temperature)
4. X-ray verification of TC junction integrity and location
5. X-ray verification of heated length (coil length)
6. Verification of heater rod diameter and overall length
7. Verification of TC calibration at room temperature
8. Examination of TCs for parasitic junctions (shorts) using a propane torch

It was concluded following these tests that all heater rods were within the specified design tolerances (cf. Table 5.2 and Figures 5.1-5.3) and were working properly.

The next step in the preparation of the heater rods was to paint their exterior surfaces with a coating of known radiative properties. Quantification of

the radiative heat transfer within the test assembly requires knowledge of the total hemispherical emissivity of all surfaces, as well as the temperature. For this reason, the surfaces of all heater rods (as well as the CuBE) were painted with Pyromark 2500 flat black paint manufactured by Tempil Division of Big Three Industries, South Plainfield, NJ. Pyromark 2500 is a high temperature refractory paint which has a high, stable emissivity over a large wavelength and temperature band. It has also been extensively characterized in terms of its optical properties. The coating and its properties are discussed in detail in Chapter 8.3.

Pyromark 2500 was applied to all heater rod exterior surfaces in the UT experimental apparatus. The paint is applied like an ordinary paint using a fine brush. After allowing the paint to dry overnight, the heater rod surfaces were heat cured in order to achieve Pyromark's reported specifications. Curing was done over a period of eight hours using a heat gun capable of producing heated air at approximately 150°C. After proper drying and curing, the coating will reportedly survive temperatures of 1371°C (2500°F) while retaining a high total emissivity that remains essentially stable up to 1093°C (2000°F). Needless to say, these high temperatures are not expected under the present test conditions.

6.3 CUBE PREPARATION AND LOADING

The steps taken in order to prepare the copper boundary enclosure (CuBE) for loading include the surface mounting of ten Omega Co. foil thermocouples, and the painting of the interior copper surfaces with Pyromark 2500. The foil thermocouple junctions were attached to the interior CuBE walls using a thin

layer of Omegabond 200 epoxy, a relatively high thermal conductivity epoxy which must be heat cured for proper bonding. The flat foil TCs have a junction thickness of 0.013mm (0.0005"). The design of the foil TC allows the junction and its lead wires to be bonded flush with the mounting surface, which provides maximum thermal coupling between the CuBE and the sensor, and essentially eliminates TC lead wire conduction error. The TC lead wires which stream from the foil junction were tightly secured to the CuBE using aluminum tape. Following the installation of the CuBE TCs, the interior copper surfaces were uniformly painted with Pyromark 2500 and heat cured.

The next step in CuBE preparation involved loading the instrumented and uninstrumented heater rods into the CuBE in the arrangement illustrated in Figure 5.6. This figure actually depicts the heater rod arrangement as viewed from the East wall, or TC lead end of the vessel. The heater rods were loaded into the CuBE by removing the CuBE's upper wall and sliding the heater rods through the openings in the rod support plates. A primary concern in loading the rods into the CuBE was to avoid scratching or scarring the rods' Pyromark coated surfaces. This problem was resolved by covering each rod in a cellophane wrapper prior to insertion. After a rod was positioned in the CuBE, the wrapper was easily removed.

Figure 6.1 depicts the fully loaded CuBE with top removed. As one might expect, the CuBE is most conveniently loaded from bottom to top. The thermocouple lead end of the assembly is characterized by the heater rod TC wire bundles, terminating in yellow TC connector jacks. The heater rod TCs pass out

Figure 6.1 The fully loaded CuBE with top removed



of the CuBE via 0.159cm (0.063") wide, twin grooves cut through each rod's mica endpieces. In this manner, the CuBE support plate may intimately contact the mica endpieces without actually touching the emerging thermocouple lead wires. The CuBE's ten foil thermocouples emerge from the enclosure via four 0.318cm (0.125") diameter ports drilled in the CuBE support plate, one hole per wall (cf. Figure 5.12).

6.4 POWER SYSTEM CONFIGURATION

6.4.1 Circuit Wiring and Grounding

Once the CuBE was fully loaded with its heater rod inventory, its top wall was replaced and the entire assembly was centered inside the pressure vessel on the retractable support platform. The continuity of each heater rod was checked using a Hewlett Packard 3468 Digital Multimeter. The resistance of each rod at room temperature was recorded and compared to previous resistance measurements. At this time, the heater rods in the array were connected according to the electrical configuration of Figure 6.2. In this arrangement, the heater rods are grouped in four parallel branches which contain sixteen rods in series per branch. The intention of this configuration is to provide a uniform power dissipation per heater rod subject to the specifications of the power supply and range of load resistance.

The current in the parallel branches of the heater rod circuit is measured using four 2A/100mV resistive shunts. Since the DAQCS requires that the input

voltages be within $\pm 10V$ of its chassis ground, the shunts are located 'after' the heater rod's primary voltage drop. Furthermore, the ground reference of the circuit was established as indicated in Figure 6.2 as the ground of the DAQCS by tying the negative terminals of each input channel to chassis ground. Thus, in order to eliminate the possibility of a ground loop due to local variations in building ground potential, the DC power supply is floated. Furthermore, since all input signals to the data acquisition hardware are true floating sources, the establishment of a measurement system ground as depicted provides a DC path to ground for any amplifier bias currents whose stray capacitances can result in drift and amplifier saturation (Potter, 1993).

Figure 6.3 depicts the specific manner in which the heater rods are electrically connected once inside the pressure vessel. The interconnections are made using 0.159cm (0.0625") thick copper bus bars, which are fitted over the terminal pins of each heater and secured with washers and hex nuts (size 6-32). The power lines are brought into and out of the pressure vessel through a Conax PL14-A12 vacuum feedthrough. This feedthrough seals 12 mylar-insulated 14AWG copper wires, of which only eight are utilized. Each of the wires is numerically labeled on both sides of the feedthrough for easy identification. Figure 6.3 illustrates the manner in which the individual labeled wires are connected. The wires labeled #1 and #2 constitute Branch #1 of the circuit; wires #3 and #4 are Branch #2; wires #5 and #6 are Branch #3; and wires #7 and #8 form Branch #4.

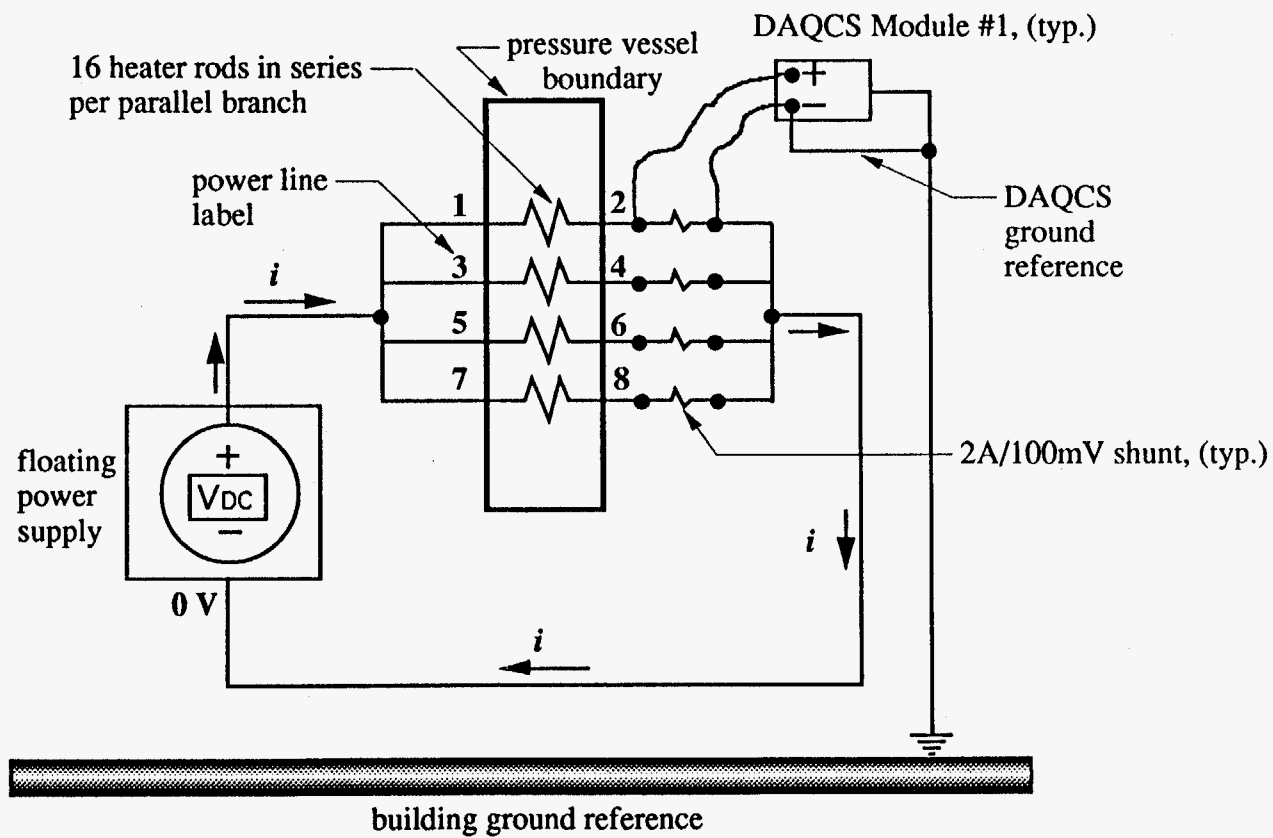


Figure 6.2 Electrical configuration of the test apparatus

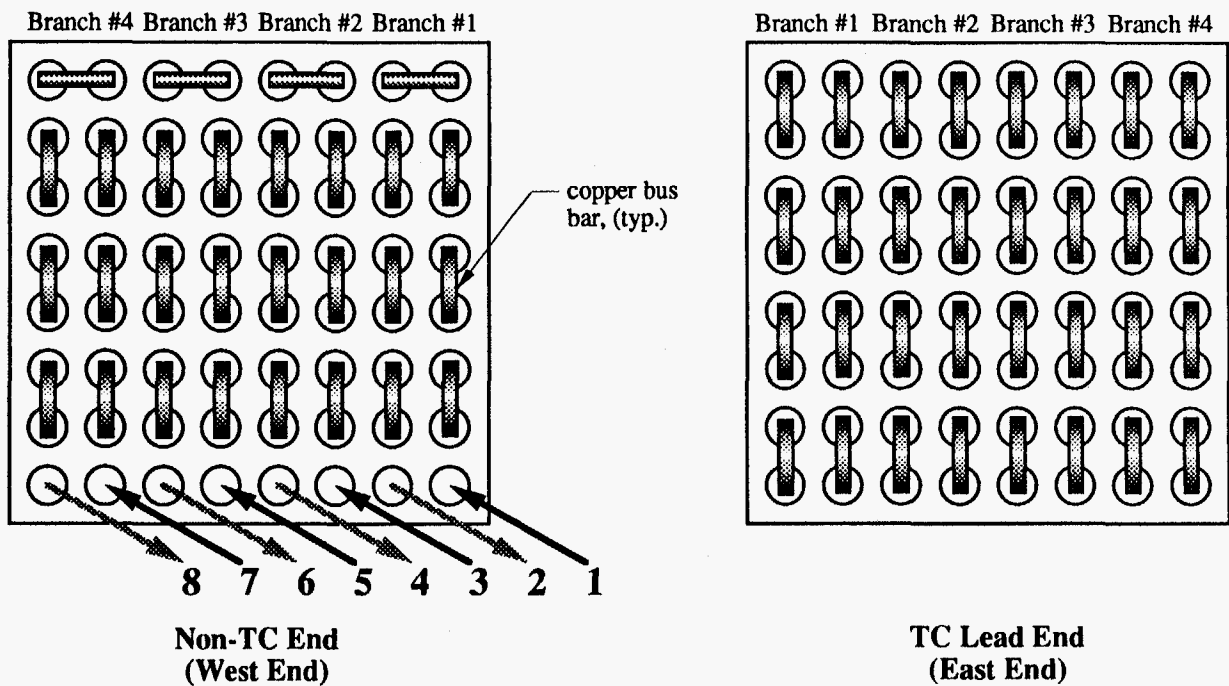


Figure 6.3 Heater rod electrical connections and power line nomenclature

6.4.2 Rod Power Measurement

As noted in previous discussions, the accurate measurement of heater rod power is of prime importance in the present study. There are several possible alternatives by which the power dissipated by the individual heater rods may be measured. The crudest method of accomplishing this task is to obtain a measurement of the total power supplied to the test assembly at the power supply terminals and divide the result by the number of heater rods. This estimate of rod power however does not account for the variations in individual rod resistance, which vary up to 5% of the nominal stated resistance (6Ω). This estimate further includes all power losses which occur in the power lines and the various electrical connections between heater rods. By contrast, the most accurate means of measuring individual rod power is to directly obtain the voltage drop over each rod and multiply the result by the measured branch current [cf. equation (3.16)]. Although the latter scheme is certainly more desirable, it proved to be impracticable to implement in the UT assembly for two reasons: a limitation on the number of wires which may be passed through the available pressure vessel penetrations, and the number of channels available on the current DAQCS.

An alternative procedure which was utilized involved measuring the current in each parallel branch of the heater rod circuit using the 2A/100mV resistive shunts, and also the value of the individual rod resistance. The square of the measured branch current multiplied by a given rod's measured resistance yields the desired rod power [cf. equation (3.17)]. The resistances of all heater

rods were measured at zero power/room temperature using the HP3468 multimeter, a 5 1/2 digit instrument capable of accurate resistance measurement ($< \pm 0.005\%$ of reading). Resistance measurements were taken twice prior to the start of experimentation and again after data collection. These values proved to be quite stable and repeatable. It should be noted that the resistance of most metallic conductors will increase linearly with the conductor's temperature, with a constant slope known as the temperature coefficient of resistance (α). Thus, the resistance of a conductor at temperature T , can be expressed in terms of its resistance at room temperature T_o , via:

$$R(T) = R_o \frac{1 + \alpha T}{1 + \alpha T_o} \quad (6.1)$$

For Nichrome wire comprised of 80% Ni and 20% Cr, Watlow Co. specifications give $\alpha = 1.11 \times 10^{-4} \text{ } 1/^{\circ}\text{C}$. Figure 6.4 depicts the Nichrome wire resistance deviation from ambient (at $T_o = 20^{\circ}\text{C}$) as a function of wire temperature, based upon equation (6.1) and the heater rod manufacturer's stated temperature coefficient of resistance. Because of Nichrome's relatively low temperature coefficient, only a 2% increase in resistance is predicted over the temperature range, $20^{\circ}\text{C} < T < 200^{\circ}\text{C}$.

In order to verify this assertion, a separate experiment was conducted. In this investigation, the coil resistance of selected heater rods was measured at power as a function of temperature. The HP3468 multimeter was used in order to directly measure the voltage drop and current over a single instrumented, insulated heater rod. The coil resistance was determined using Ohm's Law

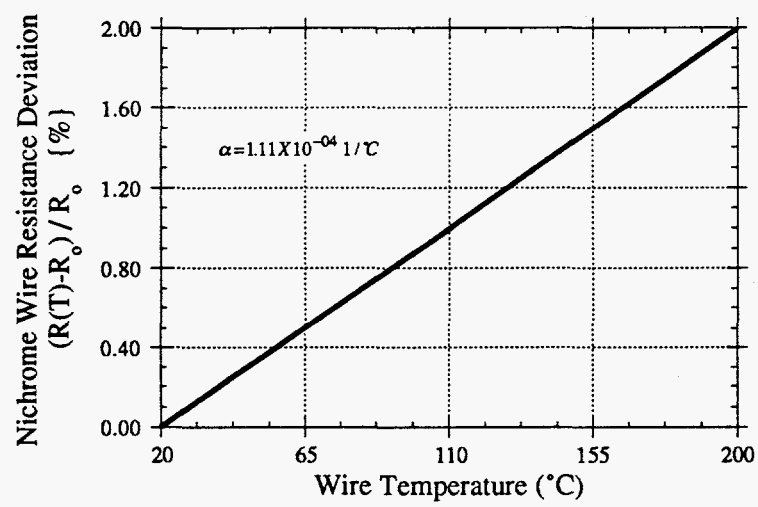


Figure 6.4 Nichrome wire resistance deviation (from $T_0 = 20^\circ\text{C}$) as a function of temperature

[$R=V/i$]. The heater rod resistance was subsequently plotted as a function of measured heater rod surface temperature. It had been previously determined using a one dimensional conduction analysis, that the difference in temperature between the heater rod's coil and the heater's steel sheath would only be of the order of one to two kelvins for the low range of rod powers which are of interest. Hence, the measured rod surface temperature is essentially the rod coil temperature. For the heater rods surveyed, the values of coil resistance varied by less than 1% (from ambient) due to the heating of the Nichrome coil over a power and temperature range of 1 to 40W/rod and 22.5 to 175°C, respectively. This measured variation in coil resistance as a function of temperature is even less than that theoretically predicted from equation (6.1). Therefore, the measured rod resistances at ambient coil temperature were not corrected for the limited temperature variation anticipated during full assembly testing. The details of the resistance measurements discussed here are elaborated upon in Chapter 9.3.2, which describes the procedure for calibrating the DAQCS for heater rod power measurement using a similar approach.

6.5 DAQCS CONFIGURATION AND TESTING

6.5.1 Overview

The measurands for which the data acquisition and control system (DAQCS) are responsible consist of: the incoming thermocouple signals from the seventy heater rod sensors and ten CuBE sensors, and the millivolt potentials

associated with the four resistive current shunts located across each branch of the heater rod circuit. The hardware and software configuration of these signal sources is the subject of the forthcoming discussions.

6.5.2 Hardware Configuration

6.5.2.1 Thermocouple Wiring, Routing, and Configuration

Figure 6.5 depicts the temperature measurement system associated with the UT test assembly. The heater rod and/or CuBE thermocouple paths originate at their junctions, which are sealed within the pressure vessel during operation. From the junctions, all TCs eventually emerge from the CuBE and are fitted with twin prong, plastic insulated connector jacks. The male connector jacks interface with their female counterparts, which are mounted on a connector jack panel located near the East wall of the pressure vessel. From the jack panel, the TC lead wires pass intact through any of three Conax thermocouple vacuum feedthroughs, and subsequently exit the pressure vessel. The TCs are then routed to the first stage of the DAQCS, which is any of four National Instruments (NI) SCXI-1303 terminal blocks containing screw terminal attachments for thirty two incoming channels each. The SCXI-1303 terminal block additionally contains an on-board thermistor temperature sensor which is maintained as the thermocouple reference.

The SCXI-1303 terminal block directly interfaces to the next stage of the DAQCS, the NI SCXI-1100 module, a thirty two differential channel multiplexer (MUX) with a software-programmable gain instrumentation amplifier (PGIA).

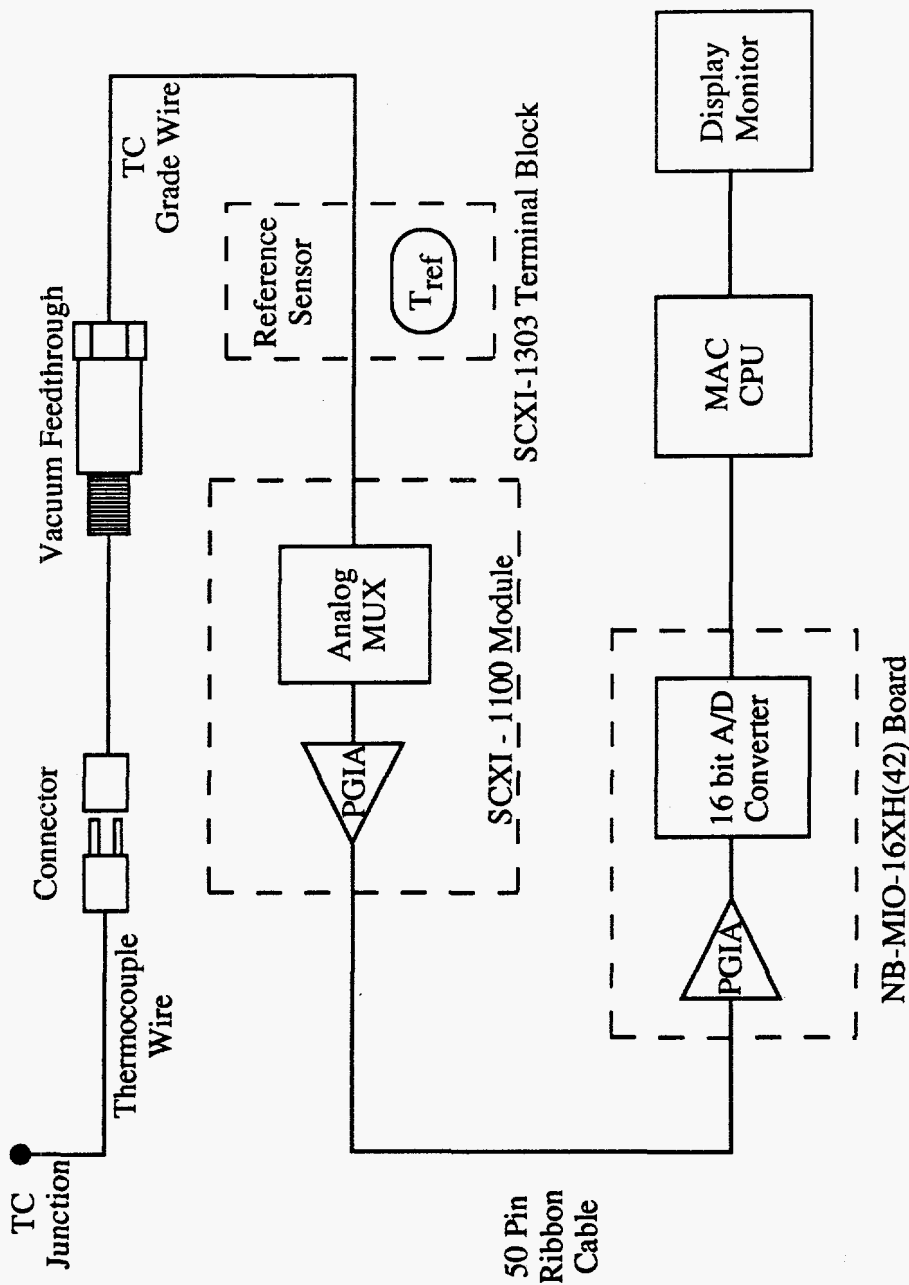


Figure 6.5 Temperature measurement aspects of the UT DAQCS

Each SCXI-1100 module multiplexes thirty two channels into a single channel of the data acquisition board. In the UT DAQCS, four such modules are cascaded together in order to multiplex up to 128 (32X4) channels into a single data acquisition board channel. The input multiplexers of the SCXI-1100 module have an input range of $\pm 10V$. The PGIA of each module can be software configured for gains ranging from 1 to 2,000 with a settling time between channels of $7\mu s$ at gains up to 100. All four SCXI-1100 modules reside within the SCXI-1000 chassis, which provides shielding as well as the electronic buses needed for directing signals and transferring data between modules.

The amplified, high-level conditioned signals which are produced by the SCXI system are routed through a 50 pin ribbon cable from the SCXI-1000 chassis to an Apple® Macintosh® Iix personal computer equipped with a NI NB-MIO-16XH(42) data acquisition board. This high resolution board contains its own PGIA as well as a 16 bit analog-to-digital (A/D) successive approximation converter. The maximum sampling rate for the NB-MIO-16XH(42) is 24,000 samples per second at a relative accuracy of $\pm 1LSB$ (least significant bit). The gain error and offset error associated with the PGIA can be completely nulled out using software controlled calibration hardware which allows the amplifier inputs to be grounded and auto-zeroed. This feature is also available for the PGIAs located within the SCXI-1100 modules.

Figure 6.6 depicts the view of the heater rod array as seen from the TC lead end (East end) of the pressure vessel. This figure is similar to Figure 5.6 in

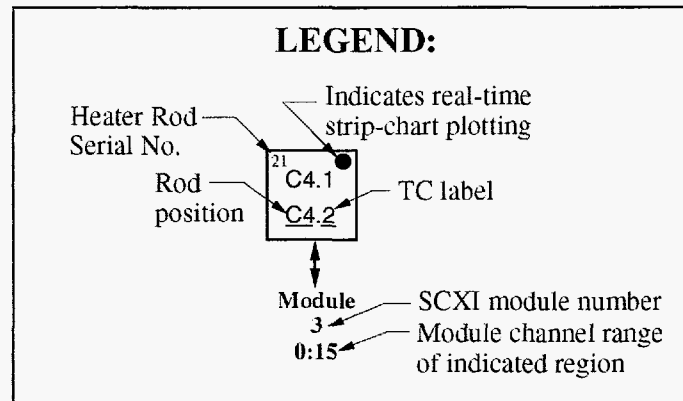
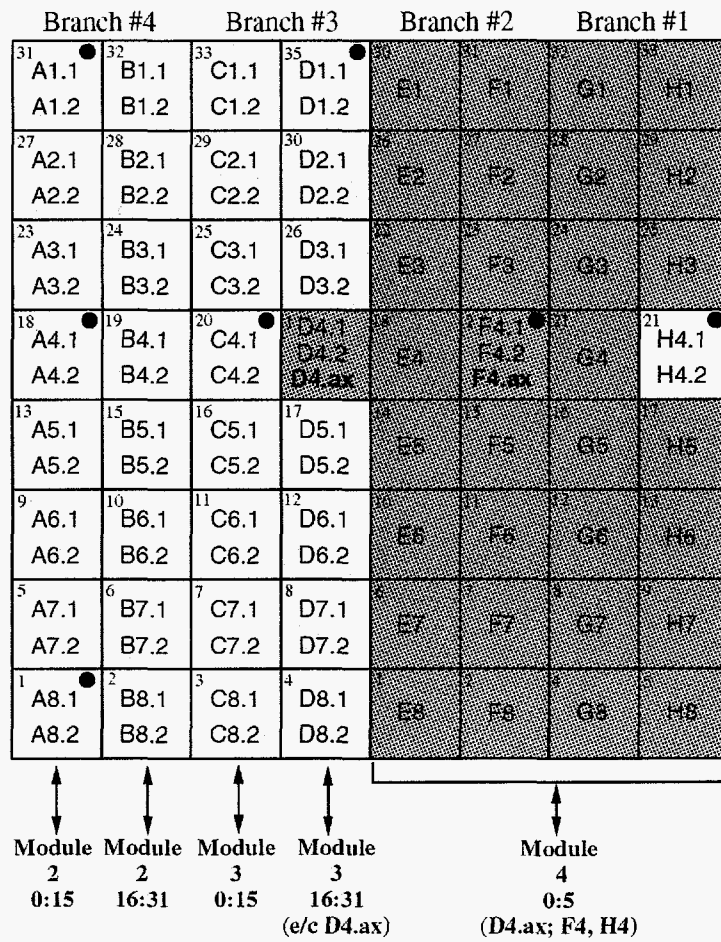
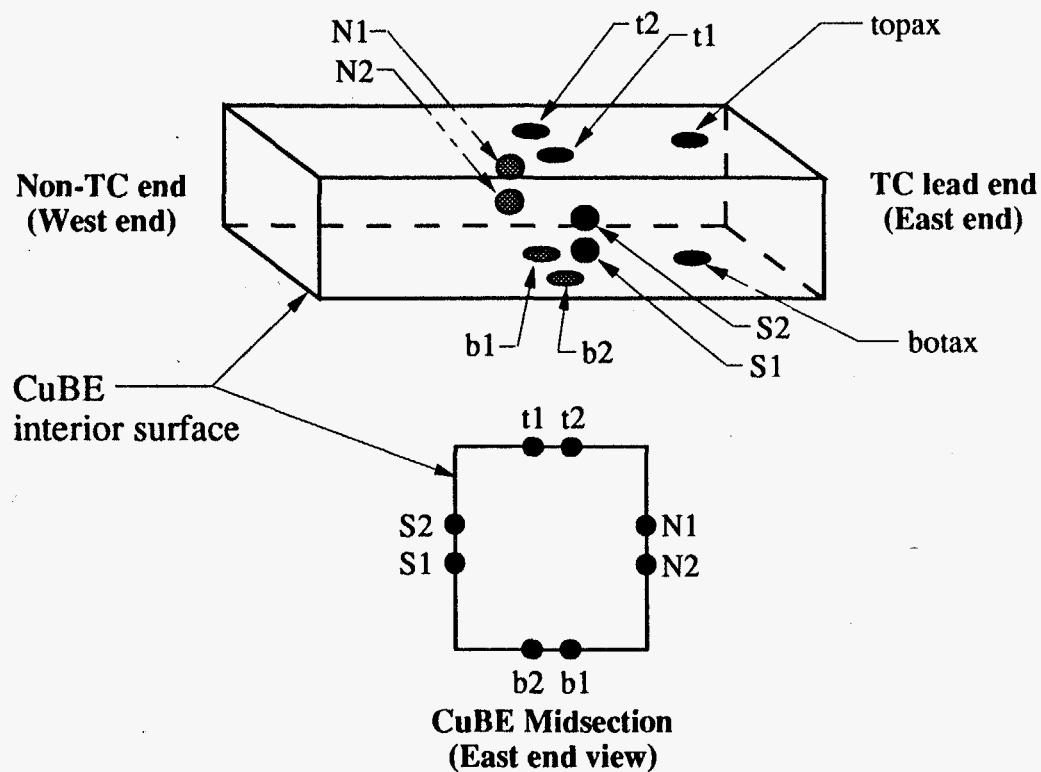


Figure 6.6 DAQCS configuration legend for heater rod TCs
[view of the assembly from the TC lead end (East end)]

that instrumented rods containing two TCs are represented in yellow; instrumented rods containing three TCs are in red; and uninstrumented rods are blue. However, this figure additionally portrays the wiring and configuration legend for all thermocouple connections to the DAQCS. The figure is interpreted as follows: Each column of the 8X8 array is designated by a letter, A-H; whereas, each row of the array is denoted by a numeral, 1-8. Consider heater rod position C4. This rod position contains an instrumented heater (serial number #20) with two sheath thermocouples, designated C4.1 and C4.2, respectively. These TCs are routed to SCXI Module 3 (the modules are labeled for identification), and are physically wired to channels #6 and #7 of the Module 3 terminal block. Each SCXI module can condition up to 32 thermocouple inputs. These inputs are labeled from #0 to #31. Counting down from the top of column C places C4.1 and C4.2 at channels #6 and #7, respectively.

Only Modules 2, 3, and 4 are used for TC inputs. Module 1 is reserved for shunt potential measurement. Note from Figure 6.6 that while Modules 2 and 3 have all 32 of their inputs used for thermocouples, Module 4 only contains TC inputs corresponding to three heater rods. For example, Module 4 - channel #0, is wired to D4.ax (the axially offset TC mounted on D4's triple instrumented heater rod). In a similar manner, channels #1; #2; #3; #4; and #5 (of Module 4), are respectively wired to thermocouples F4.1; F4.2, F4.ax; H4.1; and H4.2. Channels #6-16 of Module 4 are also utilized; however, they are reserved for the ten CuBE mounted thermocouples. The wiring configuration for the CuBE TCs is depicted in Figure 6.7.



Module 4; channel:	6	7	8	9	10	11	12	13	14	15
TC:	N1	t1	S1	b1	topax	botax	N2	t2	S2	b2

Figure 6.7 DAQCS configuration legend for CuBE TCs

The gains applied to all SCXI modules as well as the NB-MIO-16X are software programmable, meaning that the gains are assigned programmatically using the LabVIEW® software which controls and directs the data acquisition. SCXI Modules 2, 3, and 4, which first receive and amplify the TC inputs, are given a gain of 1,000. Since the DAQCS is limited to an input range of -10 to +10V, +10mV is the largest allowable thermocouple input signal with a gain of 1,000. This signal (+10mV) corresponds to a temperature of approximately 250°C for Type K TCs, a value well within the temperature limits expected during full assembly testing. The NB-MIO-16X data acquisition board also contains a PGIA whose gain is software configured. However, in the present application, the data acquisition board's gain is set to one, allowing the SCXI modules to perform all amplification.

6.5.2.2 Shunt Wiring, Routing, and Configuration

A shunt is essentially a resistor which is used in order to measure electric current. The voltage drop over the shunt is linearly proportional to its current. Typically, shunt resistors have a low resistance rating such that the shunt itself does not significantly alter the current value. In order to measure the current through each heater rod in the UT assembly, four portable shunts are utilized which are rated 2A/100mV. Thus, the shunts have a nominal resistance of 0.05Ω. By measuring the potential across each shunt, the current may be easily and accurately determined.

All shunt potentials are measured in the present DAQCS using SCXI Module 1. Thus, of the 32 inputs available on this module, only four are utilized. The Module 1 channels are configured as follows: Channel #0 is wired to the Branch #1 shunt; channel #1 to Branch #2; channel #2 to Branch #3; and channel #3 to Branch #4. The heater rods connected to each of the four parallel branches are denoted at the top of Figure 6.6. All channels of Module 1 are assigned a gain of 100. For a signal input range of -10 to +10V, and a shunt gain of 100, 100mV is the maximum input voltage to the DAQCS. It is not expected during experimentation to exceed a branch current of 2.0A (which corresponds to 100mV).

6.5.3 Software Configuration

LabVIEW® (National Instruments, Austin, TX.) is a graphical programming system for data acquisition and control, data analysis, and data presentation. In the present application, LabVIEW® is used in order to configure the DAQCS hardware, control and monitor the power circuit, and acquire/display data. Programming in the LabVIEW® environment makes use of a total graphical user interface in order to assemble software modules known as virtual instruments, or VIs. The graphical VI consists of both a front panel and a block diagram. The front panel serves as an interactive interface for supplying inputs to and observing outputs from the instrumentation system. A front panel may be assembled with virtual knobs, switches, digital displays, graphs, and strip charts, allowing the user to control as well as receive real-time feedback from the

instrumentation system. To program the VI, a block diagram is graphically constructed. Virtual wires are used to direct the flow of data from one block diagram structure to another. These structures may be simple arithmetic structures, advanced acquisition and analysis routines, or file input/output operations that store or retrieve data in numerous formats. LabVIEW® programs use the graphical VIs in a hierarchical nature, much like textual programs make use of written subroutines. Thus, the complexity of large programs may be effectively hidden in low level block diagrams while retaining access to intermediate values through the front panel.

Figure 6.8 is a flow chart of the LabVIEW® program written for the present application. This program is utilized in order to configure the experimental hardware, as well as acquire and process data obtained from the UT test assembly. Three of the program's front panels (multiple front panels are possible) are illustrated in Figures 5.20-5.22. These front panels are primarily used to display real-time data. However, before data acquisition can begin, the user must provide the program with required input, which includes the gain applied to each SCXI module, the data sampling rate, and the total data quantity desired. Other prefatory information is also required such as the total number of SCXI modules to scan, the channel scan list, and the computer bus addresses of component hardware. This information is entered graphically from another front panel, depicted in Figure 6.9.

Once the required information has been entered, data acquisition is initiated when the user toggles the "ACQUIRE" switch seen in the front panel of

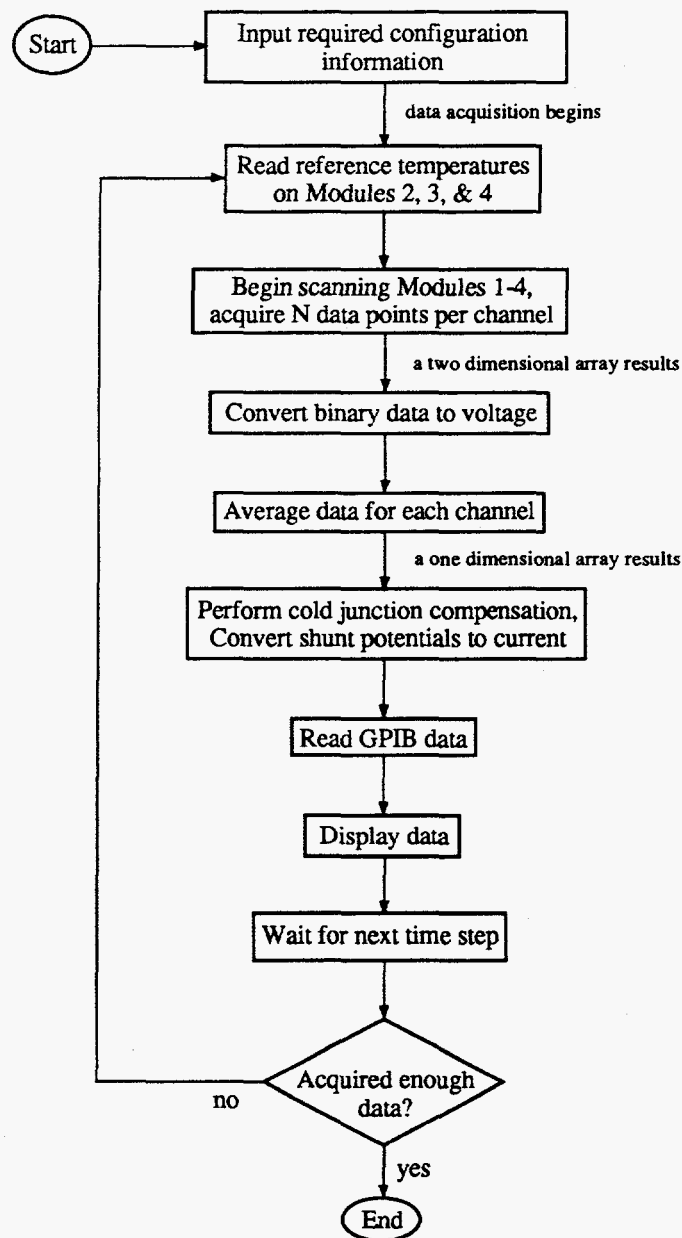


Figure 6.8 LabVIEW® data acquisition program flow chart

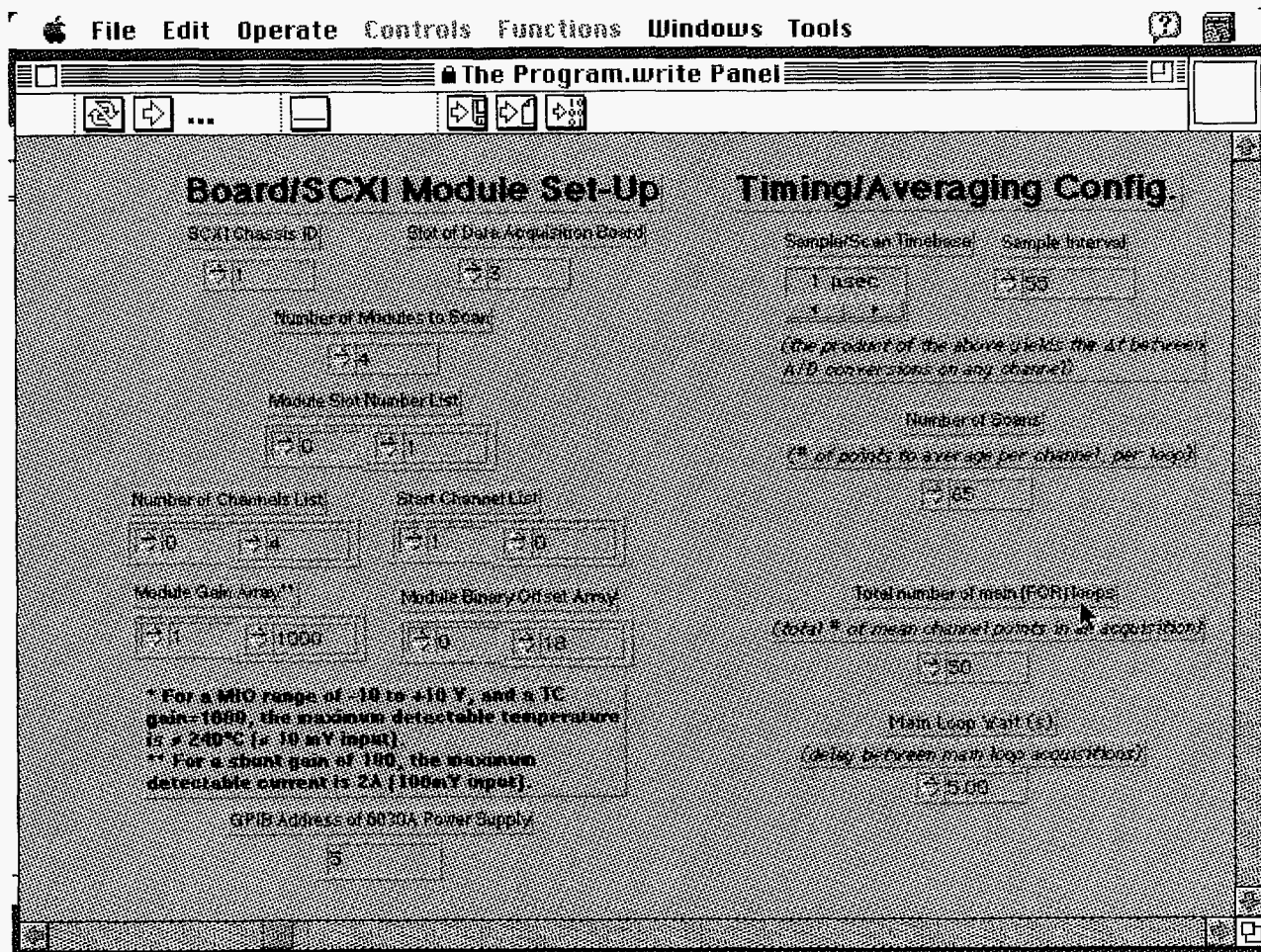


Figure 6.9 Front panel for DAQCS configuration/timing input

Figure 5.20. Programmatically, the first step in the data acquisition process is the sampling of reference temperatures. The reference temperature for all TCs connected to SCXI Module 2 is obtained from the Module 2 thermistor; for all TCs connected to Module 3 the reference temperature is obtained from the Module 3 thermistor, and so on. Each thermistor is rapidly sampled 100 times and the results are averaged. Next, the scanning of all input channels begins. Starting with SCXI Module 1- channel #0, all modules and channels are sequentially scanned as they are specified in the channel scan list. The channels are repeatedly scanned until the specified number of data points have been acquired. In the present application, the data sampling rate is 18,182 samples per second. Although the data acquisition board has a specified sampling rate of 24,000 samples per second, this rate is only available for gains up to 100. For higher gains (> 100), the sampling rate is limited to 20,000S/s in order to allow the PGIA time to settle, thereby avoiding amplifier saturation and maintaining specified accuracy.

It should be noted that the stated sampling rate of 18,182S/s is the composite A/D conversion rate for all channels. The effective sampling rate *per channel* is this value scaled by the total number of input channels, or $18,182/84 = 216.45\text{S/s}$. Thus, during scanning, each input channel is scanned at a rate of 216.45 times per second. Each input channel is sampled at this rate until the specified number of data points have been obtained. This parameter, designated as "Number of Scans" in the front panel of Figure 6.9, is presently set to 65. Therefore, all 84 input channels are scanned until 65 data points per channel have

been acquired. This operation results in a two dimensional array of data in which there are 84 rows (for each channel) by 65 columns (for each scan). The number of data points acquired in a scanning operation and the rate of their acquisition were chosen such that data could be averaged over an integral number of power line cycles. Since power line noise is typically 60Hz in frequency, averaging the acquired data over an integral number of line cycles minimizes the precision error of the measurement.

The two dimensional array of binary values created after scanning is next converted to an equivalent array of voltages using the following relation:

$$\text{volts} = \frac{(\text{binary value})(20V)}{2^{16}[\text{gain}]} \quad (6.2)$$

Note that the DAQCS's input range is -10 to +10V, and that this range is coded by 2^{16} divisions (the data acquisition board of 16 bit resolution). After conversion, the array of voltage values is averaged for each channel over all scans. This operation results in a one dimensional array whose size is equal to the total number of channels (84).

The next step in the flow chart of Figure 6.8 involves thermocouple cold junction compensation. Here, the channels which contain thermocouple signals are separated from the four channels which contain shunt voltages. The first step in TC cold junction compensation is to convert the reference temperature(s) to a voltage (emf). A ninth order polynomial based upon NIST Monograph 175 (taken from the 1993 ASTM Fourth Edition manual) is utilized:

$$E = C_0 + C_1T + C_2T^2 + \dots + C_nT^n + C_0e^{C_1(T-126.9686)^2} \quad (6.3)$$

Here, T is in °C and E is in mV. The resulting value is then added to the thermocouple measured voltages. Then, the reference compensated voltage is converted back to temperature via:

$$T = C_0 + C_1E + C_2E^2 + \dots + C_nE^n \quad (6.4)$$

The stated uncertainty of these relations for Type K wire is less than 0.05°C.

In a similar fashion, the measured shunt potentials are converted to current. The conversion relation for the 2A/100mV shunts is as follows:

$$i(A) = \frac{(2A)(shunt\ voltage)}{0.100V} \quad (6.5)$$

The next action of the data acquisition program calls a VI which communicates with the power supply through the GPIB. This communication may involve listening, such as receiving current/voltage data from the power supply; or talking, such as supplying the power supply with new instructions.

Finally, all of the obtained data is displayed in the front panels for the user, who has only been waiting on the order of milliseconds for the preceding tasks to be accomplished. Then, the entire process is repeated after a user specified time delay, until all the desired data have been obtained. Presently, the time delay is set to 5.0 seconds (see the "Main Loop Wait" control in Figure 6.9), and the total number of scanning sequences (see the "Total number of main loops"

control in Figure 6.9) is set to 50. Thus, at the *end* of program execution, 50 data points have been obtained per channel (each point is actually an average of 65 measurements) at an effective Δt between points of 5.0s. This results in a total data acquisition time period of approximately four and a half minutes. Data are only obtained under steady state experimental conditions.

6.6 INITIAL TESTING AND DEBUGGING

After the assembly and configuration of the major experimental sub-systems described above, the UT SNF assembly mock-up was ready for initial testing. The evaluation of the initial testing phase primarily centered around the performance of the DAQCS, as most of the other experimental sub-systems had either previously been proven or a good deal of confidence was held in their abilities. Prior to the initial test of the DAQCS, all wiring was checked and re-checked using the digital multimeter in a resistance or continuity mode. The power circuit was checked in this manner as well. All wiring was found to be intact and secure.

The initial test of the DAQCS consisted of shorting all of the thermocouple inputs at the jack connector panel (cf. Figure 6.5). In this scenario, the DAQCS should indicate all TCs measuring ambient temperature. This would in effect test all components of the DAQCS with the exception of the TC wires within the heater rods and the CuBE. This test was conducted with the power supply off and was fully successful. In fact, all TCs indicated room temperature within $\pm 0.1^\circ\text{C}$.

In order to ensure that the thermocouples within the heater rods were still viable, another data set were taken with the shorts removed and the heater rod TCs plugged into the TC connector panel. Again, with the power supply off, the DAQCS indicated room temperature for all input channels within $\pm 0.1^\circ\text{C}$.

The next test of the system was essentially a calibration procedure. A Biddle Co. thermocouple calibrator was used in order to input a known signal into the DAQCS, beginning at the TC connector panel. The calibration signal is then acquired using the remaining components of the data acquisition system. This calibration was carried out using each of the SCXI modules employed in thermocouple measurement. Multiple channels from each module were involved. Readings were taken with the power supply off in 20°C increments ranging from 26 to 200°C . The difference between the temperature measured using the DAQCS and the calibrator setpoint constitutes the system error. Figure 6.10 shows the LabVIEW® front panel which is used to perform individual channel calibrations. This VI takes 1,000 samples from a specified, single input channel on a given module at high speed ($>18\text{kS/s}$) and displays the measurements graphically. In this manner, noise or other sources of error are readily visible. The results of the calibration procedure are discussed in detail in the uncertainty analysis given in Chapter 9.2.1; however, in summary, the DAQCS performed very well. All channels calibrated were within $\pm 1.5^\circ\text{C}$ of the calibrator setpoint over the temperature range, $26^\circ\text{C} < T < 200^\circ\text{C}$.

The last system check to be performed was a full power test with the apparatus wired as it would be during actual experimentation. All thermocouples

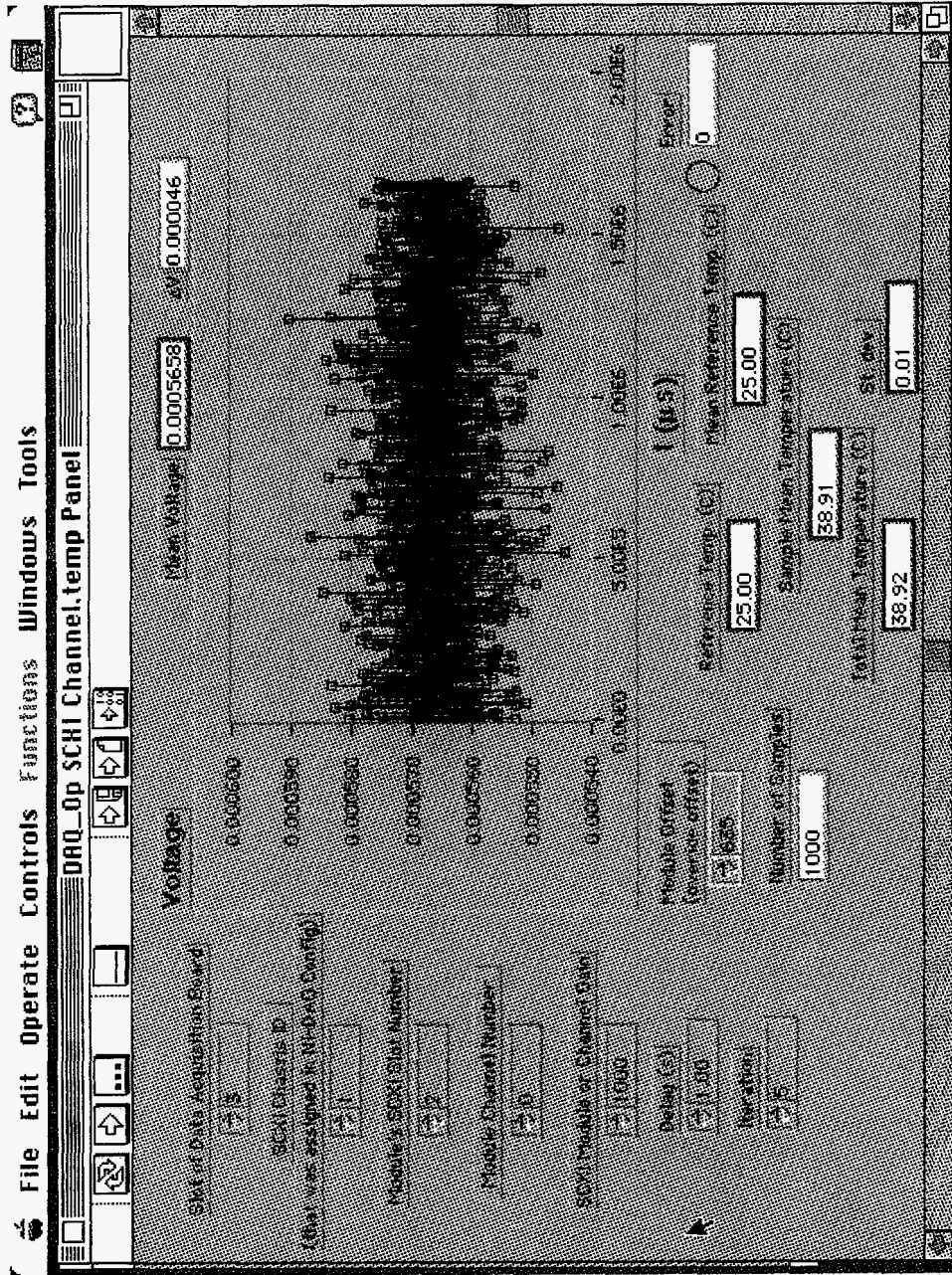


Figure 6.10 Front panel used for single channel thermocouple calibrations

were connected, the power circuit was activated, and coolant flow to the CuBE was established. However, as soon as data acquisition was initiated, a significant problem was encountered. All thermocouple readings were grossly in error. It was quickly discovered however, that when the power supply was shut off, the TC readings rapidly returned to normalcy. An indisputable coupling between the power supply and the thermocouple measurement process existed.

The first step in the investigation of this coupling was to use the Biddle thermocouple calibrator (in a measurement mode) in order to compare its readings with those returned by the DAQCS. The Biddle readings were accomplished by removing a thermocouple jack from the TC connector panel and subsequently interfacing the particular channel with the Biddle device. For all channels tested, it was found that the Biddle yielded the correct measurement while the DAQCS produced one which was grossly in error. Hence, problems associated inherently with the heater rod and/or CuBE TCs were tentatively ruled out. The problem appeared to be strictly related to the data acquisition system alone. It should be noted that DAQCS readings must be taken with all TCs (for which the system is configured) plugged in. Otherwise, when the multiplexer encounters an open channel, the amplifier may saturate and not have time to properly settle before multiplexing to the next channel. This can result in measurement error on other channels.

The next procedure in the debugging process was to set up a circuit involving only *one* instrumented heater rod and the power supply. One of the

instrumented rod's thermocouples was input to the Biddle, while the remaining TC was directly wired to the DAQCS. It was found that when data acquisition was attempted with the power supply on, the same coupling was present with the one rod circuit as was evident in the 64 rod circuit. The Biddle measured a reasonable temperature while the DAQCS returned temperatures which were in error anywhere from 10°C to 100°C, depending upon heater power level. With the power supply off, the Biddle and the DAQCS yielded essentially identical measurements.

Finally, it was observed that when the power supply is on, a potential difference between the heater rod sheath and ground occurs. The charge which builds up on the heater rod sheath is proportional to the power delivered by the DC supply. For power levels expected during experimentation ($\approx 1\text{-}5\text{W/rod}$), a potential in excess of +10V was observed between the heater rod sheath and the DAQCS ground. As soon as the power supply was shut off however, this sheath voltage decayed rapidly to zero. The charge which builds up on the heater rod sheath is believed to be capacitative in nature. Induction is not a likely culprit because the heater rod circuit is entirely direct current and the system power supply is a high quality DC source with a low ripple component.

The problem with having a charge present on the heater rod sheath during data acquisition stems from the common mode voltage limitation of the DAQCS. Despite the fact that the DAQCS measures a differential voltage between its thermocouple inputs, both inputs to a given channel (with the current system) must be within $\pm 10\text{V}$ of chassis (DAQCS) ground. If an input exceeds this

limitation, the amplifier is likely to saturate, producing an error on the particular channel being scanned (cf. Figure 6.11a). This error can propagate to other channels, even if their common mode values are within the $\pm 10\text{V}$ limits, since a saturated amplifier may not have time to properly settle before the next channel is multiplexed. Hence, during full array testing, it is asserted that the common mode voltage limitation of $+10\text{V}$ was exceeded on several channels, which subsequently produced amplifier saturation, interfered with amplifier settling, and in general resulted in highly variable and erroneous results.

The solution to the problem described above is to eliminate the build up of charge on the heater rod sheath. Then, the common mode voltage for the heater rod thermocouple inputs would be less than the 10V limit of the present system. It should be noted that this common mode limitation is strictly a feature of the particular data acquisition system employed. Recall that when the Biddle calibrator was used in order to measure a TC input with the rod sheath charged, no error resulted. This is due to the fact that the Biddle device has a much higher common mode voltage limitation than the current DAQCS (National Instruments manufactures an SCXI module with up to $+240\text{V}$ common mode protection, although it is significantly more expensive).

In order to eliminate the potential difference between the heater rod sheath and ground, all that is necessary is to establish an electrical link between the sheath and the DAQCS chassis ground. A simple copper wire attached to the heater sheath at one end and wired to ground on the other will suffice. In otherwords, *all* TC-instrumented heater rod sheaths must be grounded to the

DAQCS chassis ground (cf. Figure 6.11b). However, in the UT test assembly, this seemingly called for extracting the CuBE, removing its top wall, and subsequently welding a ground wire to the sheaths of all instrumented rods - a task involving considerable effort. Fortunately though, it was realized that the proper ground connections could be made by simply wiring the ground to the *thermocouple* sheaths at a point external to the CuBE. Since the heater rod TCs have metal sheaths which are in contact with the actual rod sheath, grounding the thermocouple sheath is equivalent to grounding the heater rod sheath.

Using insulated copper wires with pincher-like wire connectors on either end, a secure connection was established between the sheath of one thermocouple on each instrumented heater rod and the DAQCS chassis ground, effectively grounding all TC-instrumented rods. Furthermore, the pressure vessel itself was wired to chassis ground, thus shielding internal thermocouple wiring against electro-magnetic radiation induced noise. Aluminum foil shielding containing a ground wire was wrapped around the TC wire bundles emerging from the pressure vessel feedthroughs as well. The shields are only grounded on one end in order to prevent the occurrence of ground loops due to possible differences in ground potentials.

After the implementation of the described grounding procedures, the entire system was re-tested over a range of supplied power. No unusual readings were encountered. Accuracy was verified by again interfacing selected channels to the Biddle calibrator and subsequently comparing the Biddle readings to those of the DAQCS. Discrepancies no larger than those observed with the power supply off

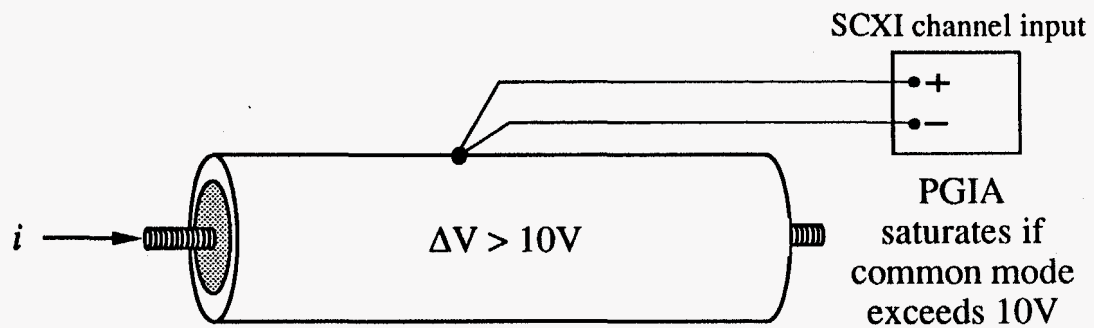


Figure 6.11a Power supply/heater rod coupling results in amplifier saturation

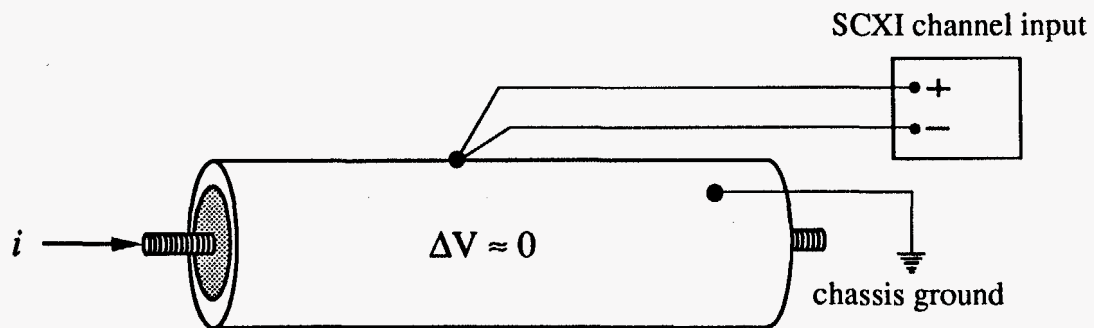


Figure 6.11b Grounding the rod sheath resolves the problem

were recorded. In fact, in all cases, the measured temperature error was less than that calculated using the DAQCS manufacturer's supplied specifications (cf. Chapter 9.2). Thus, it was concluded that the UT apparatus was fully operational and ready for experimentation over its designed pressure and power ranges. The details of the experimental procedure leading to data acquisition, as well as the techniques for data reduction, are the subjects of the next chapter.

Chapter 7 - Experimental Procedure and Data Reduction

7.1 OVERVIEW

The objective of this chapter is two-fold. First, the step-by-step procedure followed during the course of all experimental data acquisition is described. Secondly, the data processing and analysis tools which allow data reduction and presentation are outlined. The definitions of key variables and non-dimensional parameters which will be used in order to present the results in later chapters are given as well.

7.2 TEST MATRIX

The principal variables which affect the relative rates of conduction, convection, and thermal radiation heat transfer within the UT spent fuel assembly mock-up are the backfill gas, the heater rod power, and the system pressure. These three variables are controlled during the course of experimental testing in order to investigate a wide range of thermal environments of interest to SNF transportation and storage. Table 7.1 represents the primary experimental test matrix chosen for the present investigation. This matrix contains a total of 42 experimental data sets, each one representing a steady state thermal equilibrium statepoint for which data were acquired and analyzed. To attain the final 42 data

sets, over 160 experimental runs were conducted in order to obtain statistically meaningful data as well as verify the repeatability of all measurements.

Table 7.1 The primary experimental test matrix (pressures are absolute)

	101.3kPa	170.2kPa	239.1kPa	308.0kPa	376.9kPa	445.9kPa	514.8kPa
1W/rod	N ₂ ; He	N ₂ ; He	N ₂ ; He	N ₂ ; He	N ₂ ; He	N ₂ ; He	N ₂ ; He
3W/rod	N ₂ ; He	N ₂ ; He	N ₂ ; He	N ₂ ; He	N ₂ ; He	N ₂ ; He	N ₂ ; He
5W/rod	N ₂ ; He	N ₂ ; He	N ₂ ; He	N ₂ ; He	N ₂ ; He	N ₂ ; He	N ₂ ; He

With regard to the backfill gas, the present study utilizes nitrogen and helium due to the wide range in Rayleigh number which these gases offer (cf. Chapter 3.2.3) Furthermore, these gases have been given foremost consideration among proposed SNF cask backfills due to their non-reacting and non-toxic nature. All power/pressure statepoints in the current experimental matrix are subjected to both nitrogen and helium backfills.

As discussed in previous chapters, the power supplied to the test assembly is controlled programmatically using a 1200W DC power supply. In this manner, the resistive dissipation of electrical energy simulates the thermal energy produced from the decay of spent nuclear fuel radionuclides. Powers ranging from approximately 1 to 5W per heater rod are applied during experimentation.

7.3 EXPERIMENTAL PROCEDURE

After the successful completion of the preliminary tests at atmospheric pressure (in air) which were described in the previous chapter, the UT experimental apparatus was deemed ready for full pressure experimentation. The first step in the required experimental procedure is to seal the pressure vessel. Both ends of the vessel are equipped with 0.159cm (0.063") thick, non-asbestos compressible gaskets, seated on a 2.54cm (1.0") grooved lip. Each gasket is seated between the flanged pressure vessel end and a 1.91cm (0.75") thick, 63.5cm (25.0") diameter hinged circular door (cf. Figure 5.15). The hinged circular doors are secured to the vessel with 32 bolts (total), 2.86cm (1.13") in diameter and 12.7cm (5.0") long. After the flange bolts are securely tightened, the pressure vessel is fully sealed by closing all penetrating valves and tightening the feedthroughs to their manufacturer's specified torque using a 150ft-lb torque wrench.

After the pressure vessel is sealed, a moderate vacuum is established within the chamber by activating the Sargent-Welch mechanical vacuum pump and opening the vacuum valve (cf. Figure 5.16). The pump is run until a vacuum of approximately 1torr (1000 μ Hg) is established, at which time the vacuum valve is closed. The desired backfill gas (either nitrogen or helium) is fed into the chamber by first opening the high pressure gas cylinder's regulator valve and then gradually opening the vessel's pressure valve (cf. Figure 5.16). Initially, the vessel is pressurized to full pressure at 515kPa absolute (60psig). During the

initial pressurization, the pressure vessel is leak tested by allowing it to remain at 515kPa (60psig) for a period of eight hours. During all subsequent experimental runs, no observable decrease in system pressure occurred during this time period.

After pressurization, the vessel is again purged by restarting the vacuum pump and re-opening the vacuum valve. Again, a vacuum of 1torr is achieved. The vacuum valve is then closed and the chamber re-pressurized using the backfill gas cylinder source. Pressurization continues until the chamber reaches atmospheric pressure [101.3kPa (0psig)]. The purging process described ensures that the test chamber is pressurized with a known backfill of high purity. Nitrogen and helium gas cylinders whose contents are 99.999% purity are obtained from Liquid Air Co. Inc., Austin, TX.

Once the backfill gas is established in the vessel at atmospheric pressure, the power supply is turned on, and the LabVIEW® data acquisition program is booted on the DAQCS personal computer. Using the power supply control front panel depicted in Figure 5.22, the desired voltage and maximum expected current are input into the VI. The power supply is then activated by running the program. The power level supplied to the test assembly is indicated to the user on the VI front panel.

Next, coolant flow to the CuBE is established by fully opening each of the four ball valves on the coolant manifold (cf. Figure 5.18). The resulting flow rates in each line are recorded. Typically, each line maintains a flow rate of approximately 0.4gpm. An advantage of limiting testing to above atmospheric

pressure is that if a coolant leak were to occur inside the pressure vessel, flooding and significant damage would not likely result. During the course of all experimental runs, it was determined that the CuBE remains essentially isothermal (within $\pm 0.25^\circ\text{C}$) regardless of the flow distribution in each of the four manifold lines. In other words, preferential cooling of the CuBE's top wall is not required, as long as reasonable flow rates in each manifold line are maintained.

At this point in the experimental start up, it is a good idea to check the performance of the DAQCS. This requires turning the SCXI system on and allowing it to warm up for a period of 15 minutes. Once the system is warmed up, the primary LabVIEW® front panel is booted (cf. Figure 5.20). This is the VI which indicates the temperature of all thermocouple channels, the branch currents as measured from the resistive shunts, and the total power at the terminals of the power supply. If all is going well, the experimenter should see the characteristic warm up of the heater rod TCs. The CuBE TCs should indicate that the enclosure is essentially isothermal.

It was observed during the course of experimentation that approximately three to four hours are required in order for the system to reach steady state. Steady state conditions are verified by activating the VI represented by the front panel of Figure 5.21. This front panel is a strip chart of 18 TC channels, which includes 7 heater rods uniformly distributed throughout the array as well as four TCs from the CuBE. The time interval along the x-axis of the strip chart represents approximately 10 minutes. Thus, at the effective data acquisition rate, enough data are collected in order to easily ascertain whether or not the system

has achieved steady state. Furthermore, the temperature scale on the right side of the strip chart may be interactively re-scaled during data acquisition in order to focus in on the behavior of one or a few TC channels. For conservatism, no data sets were taken sooner than six hours following a power/pressure adjustment.

Once steady state behavior is verified at the desired power and pressure, the acquisition of data can begin. Data sets are taken in two modes in order to ensure reproducibility. First, the rod bundle is brought to steady state at a given power and pressure. With the bundle held at constant power, the pressure is repeatedly increased, with a data set taken at each newly achieved equilibrium statepoint. After the maximum pressure is reached (515kPa) and data recorded, the trend is reversed, with data being taken at constant bundle power while the pressure is repeatedly *reduced*. This process is then repeated at a new bundle power level.

Secondly, data are recorded by keeping the system at a constant pressure and repeatedly varying the power input to the rod bundle. After all power statepoints have been achieved, the pressure is brought to a new level and the process is repeated. Following the recording of all raw data, redundant data sets are averaged in order to reduce the data to 42 sets. When the LabVIEW® program acquires data, it can be stored directly into a spreadsheet format. In the present program, all data are stored in a Microsoft® Excel® worksheet. In this form, the worksheet may be customized in order to perform a wide variety of data analysis and reduction tasks. The nature and scope of these tasks are the subject of the following section.

7.4 DATA REDUCTION

The result of an experimental data acquisition is a Microsoft® Excel® worksheet which consists of a two dimensional array with 84 columns and 50 rows. The 84 columns represent the 84 total input channels to the DAQCS. Seventy of these channels are heater rod TC inputs, 10 are CuBE TC inputs, and the remaining four channels are the measured branch currents. The rows of the data array correspond to the 50 independent data points acquired every five seconds per channel. Each of these data points is actually an average of 65 independent scanning measurements. Data analysis and reduction is carried out by creating a custom Excel® worksheet, known as a template, into which the two dimensional data array can be pasted. This custom worksheet performs a wide variety of analysis and reduction functions. The template is then renamed and saved as a standard worksheet. All data sets are processed in this manner.

Figure 7.1 depicts the various analysis functions performed by the data reduction worksheet. The analysis functions are boxed in the figure; whereas, the required inputs are indicated with arrows. The raw data which must be pasted into the worksheet template consist of the 84X50 array of thermocouple measured temperatures and branch currents. Once the data are pasted, the worksheet performs a statistical analysis of the data by calculating the maximum value, minimum value, mean value, standard deviation, and precision error (95% confidence), for each input channel. Once the 50 data points for each channel are averaged, the worksheet determines the mean heater rod and CuBE temperatures

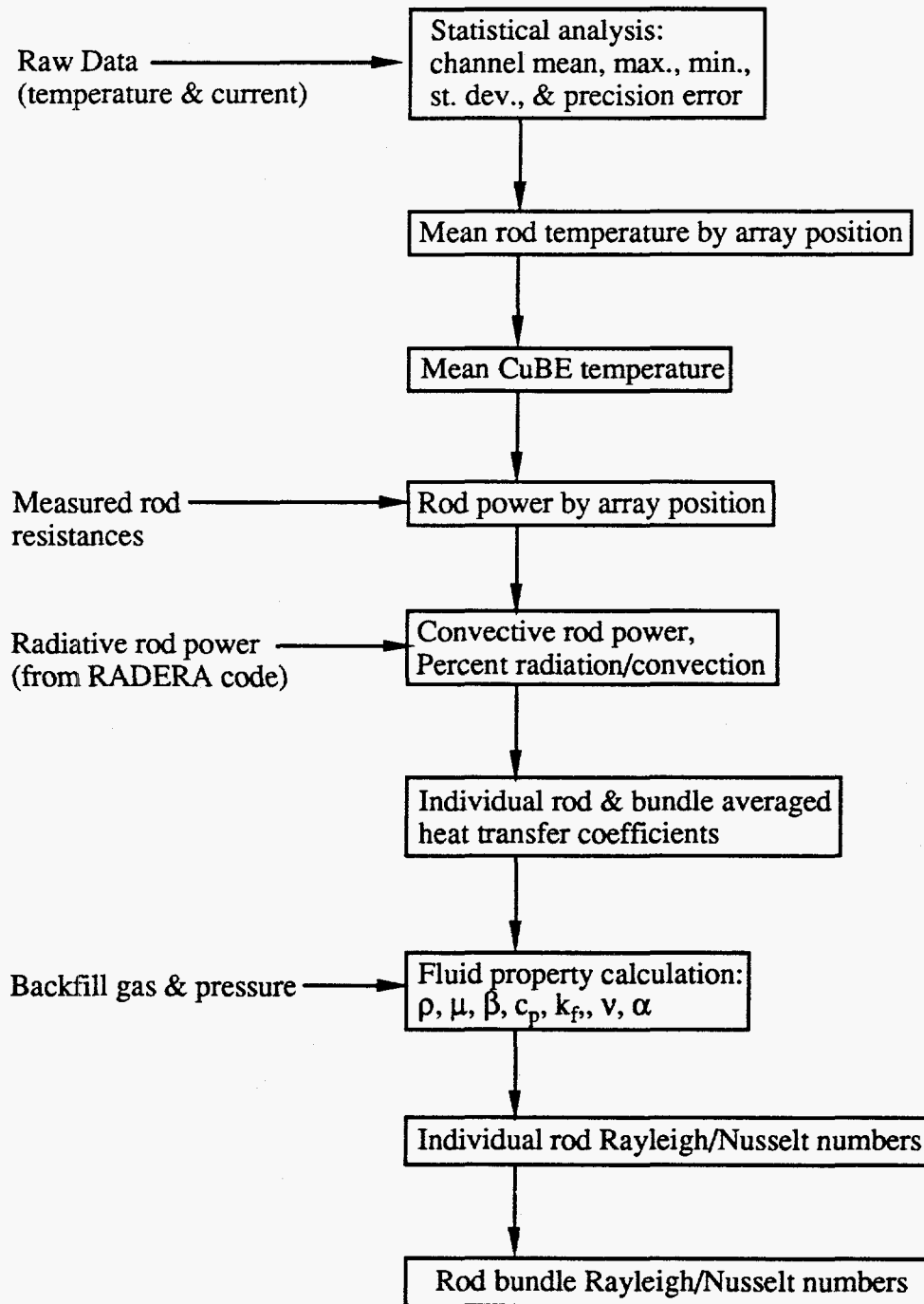


Figure 7.1 Data analysis and reduction using an Excel® worksheet

by averaging the appropriate channels. The mean rod temperatures are displayed on the worksheet in the 8 row by 8 column pattern in which the rods are positioned within the heater array.

In order to calculate the power dissipated by each rod, the measured heater rod resistance values must be input to the worksheet. The resistances which are utilized in the worksheet represent an average of rod resistance measurements taken throughout the course of experimentation. These resistances are given in Appendix 5 according to rod position. Rod power is then calculated based upon equation (3.17), using the measured branch currents and rod resistances.

The worksheet additionally calculates the convective rod power using equation (3.15). The convective power is the total power minus the radiative contribution. However, the radiative rod powers must be input into the worksheet externally. The RADERA code (RADiation in Enclosed Rod Arrays) is a stand-alone finite element based algorithm which numerically calculates the individual rod radiative power based upon experimentally measured temperatures. RADERA must be executed for *each* experimental statepoint and its results subsequently input into the analysis worksheet. Thus, radiation is corrected for in each experimental dataset. The determination of the radiative component using RADERA is described in detail in Chapter 8.

The convective heat transfer coefficients for individual rods within the assembly as well as for the rod bundle as an average are calculated in the Excel®

worksheet as well. The convective heat transfer coefficient for individual rods is given by:

$$h = \frac{q'_c}{\pi D \Delta T} \quad (7.1)$$

where q'_c is the convective rod power per unit length, D is the rod diameter, and $\Delta T = T_r - T_C$. The individual rod characteristic temperature difference, ΔT , is the difference between a given rod's mean temperature, (T_r), and the mean temperature of the surrounding CuBE, (T_C).

The convective heat transfer coefficient for the rod bundle as an average is given by the following expression:

$$h_b = \frac{Q'_c}{4H \Delta T_b} \quad (7.2)$$

where Q'_c is the total rod bundle power due to convection per unit length, H is the height of the CuBE, and $\Delta T_b = T_{r,b} - T_C$. The characteristic temperature difference for the rod bundle, ΔT_b , is defined as the difference between the mean temperature of all rods in the bundle, ($T_{r,b}$), and the mean CuBE temperature.

A heat transfer coefficient may also be defined for the entire array based upon the maximum characteristic temperature difference, where $\Delta T_{max} = T_{max} - T_C$:

$$h_{max} = \frac{Q'_c}{4H \Delta T_{max}} \quad (7.3)$$

where T_{max} is the peak rod temperature in the bundle.

The data reduction worksheet is programmed to calculate required fluid properties such as backfill density, specific heat at constant pressure, thermal conductivity, and absolute viscosity. The required input for these computations is the type of backfill gas (nitrogen or helium) and the measured system pressure. The properties are calculated using semi-empirical correlations obtained from the fourth edition of *The Properties of Gases and Liquids* (Reid, Prausnitz, & Poling; 1987). These properties are needed to specify convection results in terms of the appropriate non-dimensional parameters. All fluid properties are evaluated at some reference temperature. For individual rods in the array, the reference temperature is given by equation (7.4); for the rod bundle as an average, equation (7.5) is appropriate.

$$T_f = \frac{T_r + T_C}{2} \quad (7.4)$$

$$T_{f,b} = \frac{T_{r,b} + T_C}{2} \quad (7.5)$$

Convective results are generally presented in terms of non-dimensional parameters; namely, the Rayleigh and Nusselt numbers (cf. Chapter 3.2.3.2). In this work, individual rod Rayleigh/Nusselt correlations are presented for all rod positions in the 8X8 rod bundle. Furthermore, full array correlations are developed. These parameters are also calculated within the framework of an Excel® worksheet. The individual rod Rayleigh and Nusselt numbers are defined by equations (7.6) and (7.7) respectively.

$$Ra = \frac{g\beta\Delta T D^3}{\nu\alpha} \quad (7.6)$$

$$Nu = \frac{hD}{k_f} \quad (7.7)$$

A full array Rayleigh and Nusselt number based upon the mean bundle characteristic temperature difference (ΔT_b) are respectively defined by equations (7.8) and (7.9).

$$Ra_b = \frac{g\beta\Delta T_b H^3}{\nu\alpha} \quad (7.8)$$

$$Nu_b = \frac{h_b H}{k_f} \quad (7.9)$$

A full array Rayleigh and Nusselt number, based upon the maximum characteristic temperature difference (ΔT_{max}), are given by equations (7.10) and (7.11):

$$Ra_{max} = \frac{g\beta\Delta T_{max} H^3}{\nu\alpha} \quad (7.10)$$

$$Nu_{max} = \frac{h_{max} H}{k_f} \quad (7.11)$$

Furthermore, a full array Rayleigh number can be alternatively defined in terms of the total convective heat rate per unit length, (Q'_c), rather than a characteristic temperature difference:

$$Ra_Q = \frac{g\beta Q'_c H^4}{4H\nu\alpha k_f} \quad (7.12)$$

7.5 LOOKING AHEAD

The experimental procedure followed during the course of this investigation has been outlined and discussed. The handling of the resulting data using a custom spreadsheet program was detailed as well. The spreadsheet program provides essentially all of the data analysis and reduction functions required for data presentation in later chapters. An exception however, concerns the analysis of the radiative heat transfer within the assembly. In this work, the radiative heat transfer component is determined numerically using a finite element method in which the radiative transport equation is solved for the incident radiative flux vector at each node within the numerical mesh. The utilized form of the radiation transport equation does not include the scattering/absorption terms normally associated with the application of this equation in participating media. The following chapter reviews the theory and analytical techniques involved in the determination of the radiative component in enclosed rod arrays. This discussion is followed by an uncertainty analysis of all experimental systems in Chapter 9. Finally, the results of all data acquisition and analysis are presented in Chapter 10.

Chapter 8 - Determination of the Radiative Heat Transfer Component

8.1 BACKGROUND

In order to isolate the convective process and subsequently produce experimental results which are system independent with regard to surface properties, the radiative component of multimode heat transfer must be fully removed from the presented Nusselt vs. Rayleigh number correlations. This is accomplished by subtracting the radiative heat transfer rate from the total rate in order to obtain only the convective heat transfer rate (all per unit length) on a rod by rod basis:

$$q'_c = q' - q'_{r,net} \quad (8.1)$$

The total rate of heat transfer can be measured experimentally rather easily through direct measurement of applied electric power; however, experimental determination of the independent radiative component is a significantly more strenuous exercise. In order to accomplish the latter in a horizontal rod array, a hard vacuum must be established corresponding to *each* power/pressure equilibrium statepoint at which convection previously occurred. The vacuum must be sufficient to effectively eliminate convective and conductive processes within the backfill medium (generally $< 10^{-03}$ torr, cf. Figure 5.17). Since the radiative heat transfer for a given rod in the bundle is dependent upon the rod

surface temperature distribution throughout the array, the exact temperature distribution seen at a steady state convective statepoint must be reproduced under vacuum conditions. This can only be accomplished by controlling the applied power to each heater rod such that the bundle temperature distribution *at pressure* is duplicated under vacuum conditions. Once this condition has been achieved, the measured electrical power applied to each rod is the rod radiative power for the given bundle temperature distribution. Thus, the difference in measured rod power between conditions of convection/conduction (uniform bundle power) and vacuum (independently controlled rod power) equates to a given rod's convective heat transfer rate. Needless to say, the experimental implementation of the above procedure requires an automated approach in order to achieve both accuracy and efficiency. Regardless of control system however, this approach is costly in terms of both capital and required time. The complexity of such a control system may be reduced by grouping the rods into temperature bins and subsequently controlling the power supplied to each bin under vacuum conditions. However, doing so can introduce a significant error into the measured radiative power. Thus, under conditions in which radiation is significant for a given rod relative to the total supplied power, large uncertainties and errors in the determined heat transfer coefficient may result.

Alternatively, it is possible to determine the individual rod radiative transfer rates numerically, based upon experimentally measured temperature data (at pressure). Recent advances in the computational speed and memory capacity of computer hardware make such numerical determinations increasingly practical

and very accurate. For these reasons, as well as the numerous difficulties and costs associated with experimental radiation determination in rod bundles, the numerical approach was selected for the present work.

8.2 NUMERICAL COMPUTATION OF THERMAL RADIATION IN ROD ARRAYS

8.2.1 Introduction

Numerical determination of the radiative heat transfer rate on a rod to rod basis within horizontal rod arrays has been reported by several authors using a variety of techniques (Klepper, 1963; Watson, 1963; Cox, 1976; and Irino *et al.*, 1986). All of these reported approaches have implemented methods which invoke the following assumptions:

- Nonparticipating media within an enclosure
- Isothermal surfaces
- Diffuse, gray, opaque surfaces
- Uniform surface radiosity
- Temperature independent radiative properties

Cox's work, which is undoubtedly the most referenced publication relating to radiation heat transfer in the rod bundle geometry, employs formulations to the problem in which the rod array temperature field is sought given the net radiative heat transfer rate for each surface. Numerical implementations of the Net Radiation method, Hottel's Script f method, and Gebhart's method are reported. The numerical results are compared to experimental data (utilizing a 217 rod

hexagonal rod bundle), obtained within a suitable vacuum such that the applied rod power was solely radiative. As Cox realized, a key factor in the accuracy of radiative solutions in this geometry regards the assumption of uniform radiosity. When using *rod to rod* view factors, which inherently assumes that each rod's surface is subject to circumferentially uniform radiosity, Cox notes a substantial discrepancy between numerically and experimentally obtained results. The assumption of uniform radiosity for an entire rod's surface is poor despite the fact that each rod's surface is essentially isothermal. This is due to the reflected portion of the radiosity which is highly non-uniform due to the circumferential non-uniformity of a given rod's incident irradiation. However, by numerically subdividing the entire rod's surface into an increasing number of sub-surfaces, the uniform radiosity assumption becomes progressively better. In the cited work by Cox, subdivision of a each rod's surface into 30° increments (12 individual sub-surfaces per rod), results in a *maximum* 7% discrepancy between experimental and calculated values.

8.2.2 Finite Element Based Radiation Methods

The finite element technique has been applied to a broad range of physical phenomena related to structural mechanics, fluid dynamics, and thermal analysis. A significant benefit of the method regards the manner in which a numerical mesh may be elegantly created for geometrically complex models. A large number of commercial software packages are currently available which utilize finite element techniques for pre- and post-processing tasks as well as for direct numerical

evaluation of combined mode thermal processes. However, most of these commercial finite element thermal-hydraulic codes are primarily oriented toward advective and/or conductive analyses. Software which does include radiative models typically employ very approximate methods and thus their capability for accurate radiative modeling often falls short of state-of-the-art radiative methods.

Burns (1995) has developed a finite element based numerical technique which can be adopted in order to model combined mode heat transfer within enclosures containing participating surfaces and absorbing/scattering media. The method further allows for spectral and temperature dependent radiative properties. An adaptation of this technique is applied to the present, enclosed rod bundle geometry in order to determine the net radiative heat transfer rate for each rod within the UT experimental assembly - given the experimentally measured temperature of each heater rod and the surrounding enclosure temperature. The technique described by Burns was significantly simplified for the present implementation by invoking the assumptions outlined in the following section.

8.2.3 Assumptions Relevant to the Applied Finite Element Model

Assumption 1: Nonparticipating media within an enclosure - The standard BWR fuel assembly contains an 8 X 8 square matrix of fuel rods surrounded by a square enclosure or fuel channel. Typical backfills include gases such as nitrogen and helium. In the UT experimental apparatus, this geometry is preserved and only non-participating media are involved (nitrogen and helium).

Assumption 2: Gray, diffuse, opaque surfaces - All surfaces within the UT experimental assembly were uniformly coated with Pyromark Series 2500 flat black paint manufactured by Tempil Division of Big Three Industries, South Plainfield, NJ. The optical properties of Pyromark 2500 black paint have been well characterized in studies by NASA (Wade & Slemple, 1962) and Sandia National Laboratories (Longenbaugh, Sanchez, & Mahoney, 1990). When applied to a smooth metallic surface such as stainless steel or copper, this paint provides a diffuse, opaque coating, that to a reasonable approximation can be considered gray as well. Measurements by SNL (see Section 8.2.7 which follows) of the spectral emissivity of Pyromark 2500 applied to a smooth inconel substrate at 100°C and 300°C, indicate little spectral variation ($< \pm 0.1$ units from a typical mean value of $\epsilon = 0.85$) over the measured range, $0 < \lambda < 20 \mu\text{m}$. For a representative experimental array temperature of 100°C, this spectral range contains over 85% of the energy emitted by a blackbody at the same temperature. Since neighboring surfaces within the array do not vary significantly in temperature, the spectral range of a given surface's irradiation will likely be similarly focused. Because of the consistency of the measured spectral emissivity over a large wavelength band, which contains most of a typical heater surface's emission and irradiation, the gray surface approximation is rational.

Assumption 3: Temperature independent radiative properties - The finite element model applied to the present geometry, requires only one surface property to be specified, that being the total hemispherical emissivity of each surface within the model. The total hemispherical emissivity for Pyromark 2500 coated surfaces is

very stable over a significant temperature range, varying by less than 0.02 units from the mean over the interval, $25 < T < 1000^{\circ}\text{C}$ (Longenbaugh, Sanchez, & Mahoney, 1990). This, in conjunction with the limited variations of temperature seen within the UT rod bundle ($23^{\circ}\text{C} < T < 150^{\circ}\text{C}$), allows the temperature dependence of the input emissivity to be inconsequential.

8.2.4 Derivation of the Applied Finite Element Formulations

This section provides a detailed development of a finite element formulation for radiation heat transfer within rod arrays subject to the assumptions given in the previous section. The final numerical model is utilized in order to determine the radiative heat transfer component within the UT experimental assembly based upon measured temperatures and known surface properties. The governing radiative transport equation will be provided and discussed in this section; however, for a more detailed account of the method itself and its applicability to a broader problem set, namely participating media with non-constant properties, the reader is encouraged to consult the work outlined by Burns (1995). Remaining sections of this chapter outline the structure and use of the developed numerical routine and several benchmark calculations are reviewed.

The essence of the numerical routine utilized in this work lies in the determination of the radiative flux vector, (q_r'') , for each node within the finite element mesh. As indicated in Figure 8.1, the radiative flux vector represents the total radiant flux incident upon a surface dA from surrounding surfaces, due to both direct emission and diffuse reflection. In this figure, \hat{n} is a unit vector

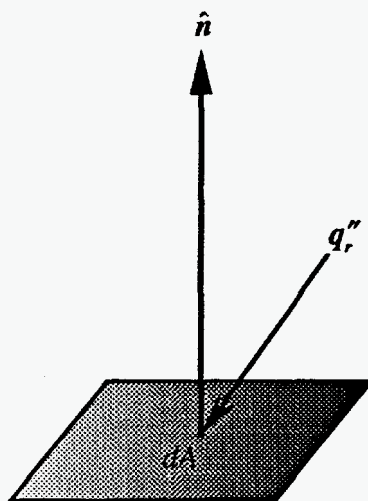


Figure 8.1 The radiative flux vector associated with dA

normal to dA , which can be oriented in any direction. As outlined in Siegel and Howell (1992), the flux vector can be related to the intensity of incident thermal radiation. Consider the quantities illustrated in Figure 8.2. The unit vector \hat{s} is in the S direction and thus the dot product between this vector and the surface normal is $\hat{n} \cdot \hat{s} = \cos \varphi$, where φ is the angle from the normal of dA to the direction of the incident intensity i . The total intensity is defined as the rate of radiant energy, per unit solid angle, which crosses dA , per unit area normal to i , integrated over all wavelengths. Hence, the rate of radiant energy, dq_r , crossing dA in Figure 8.2 is:

$$dq_r = i dA \cos \varphi d\omega \quad (8.2)$$

where $d\omega$ is a differential solid angle. With the above expressed as a heat flux associated with dA , equation (8.2) becomes:

$$dq_r'' = \frac{dq_r}{dA} = i \cos \varphi d\omega \quad (8.3)$$

This relation may now be integrated over all solid angles of interest in order to obtain the radiative flux crossing dA as a result of intensities incident from all directions:

$$q_r'' = \int_{4\pi} i \cos \varphi d\omega \quad (8.4)$$

Note however, that the above expression is actually only one component of the total radiative flux vector, q_r'' . It is in fact the normal component in the \hat{n}

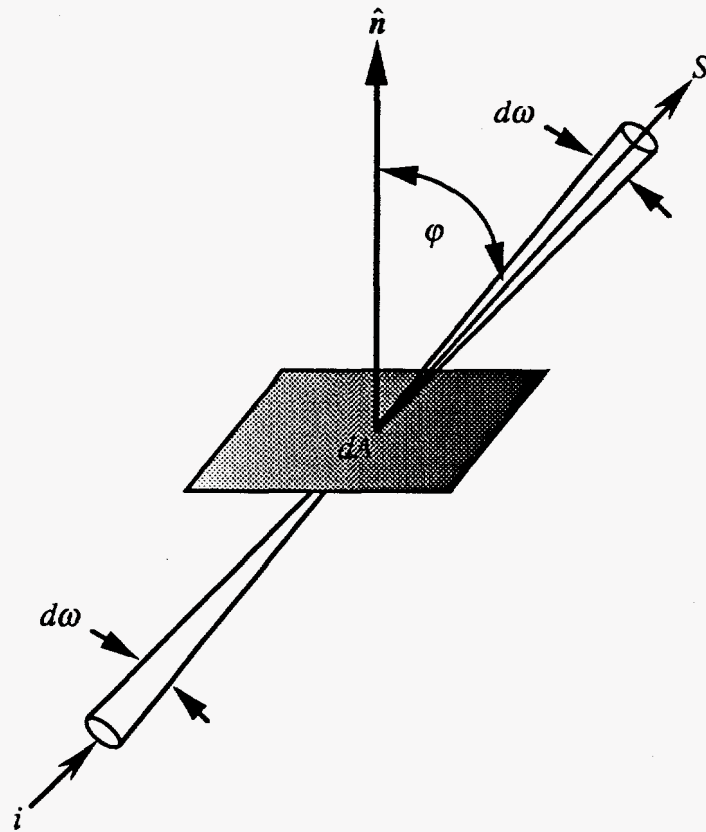


Figure 8.2 Quantities relating the intensity to the radiative flux vector

direction, as only this component can actually interact radiatively with dA . Thus, equation (8.4) is better expressed as:

$$q''_{r,n} = \int_{4\pi} i \cos \varphi d\omega = q''_r \cdot \hat{n} \quad (8.5)$$

Since $\hat{n} \cdot \hat{s} = \cos \varphi$,

$$q''_{r,n} = \int_{4\pi} i \hat{n} \cdot \hat{s} d\omega = q''_r \cdot \hat{n} \quad (8.6)$$

Thus, the total radiative flux *vector* is related to the directionally dependent intensity as:

$$q''_r = \int_{4\pi} i \hat{s} d\omega \quad (8.7)$$

Now consider the radiant exchange between two nodes, i and j , in the Cartesian coordinate system of Figure 8.3. Note that the quantities defined by Figure 8.2 have been superimposed upon the differential surface da_j associated with node j . The intensity of incident radiation at node i can be expressed in terms of its two components: 1) the intensity associated with direct emission from da_j , and 2) the intensity associated with surface reflection from da_j . For the special case of gray, diffuse surfaces, these components of intensity take the following form:

$$i(r_i) = \frac{1}{\pi} \left[\epsilon_j \sigma T^4(r_j) + \{q''_r(r_j) \cdot \hat{n}\} (1 - \epsilon_j) \right] \quad (8.8)$$

Note that the reflected portion of the intensity incident at node i is expressed in terms of the normal component of the radiative flux vector incident at node j .

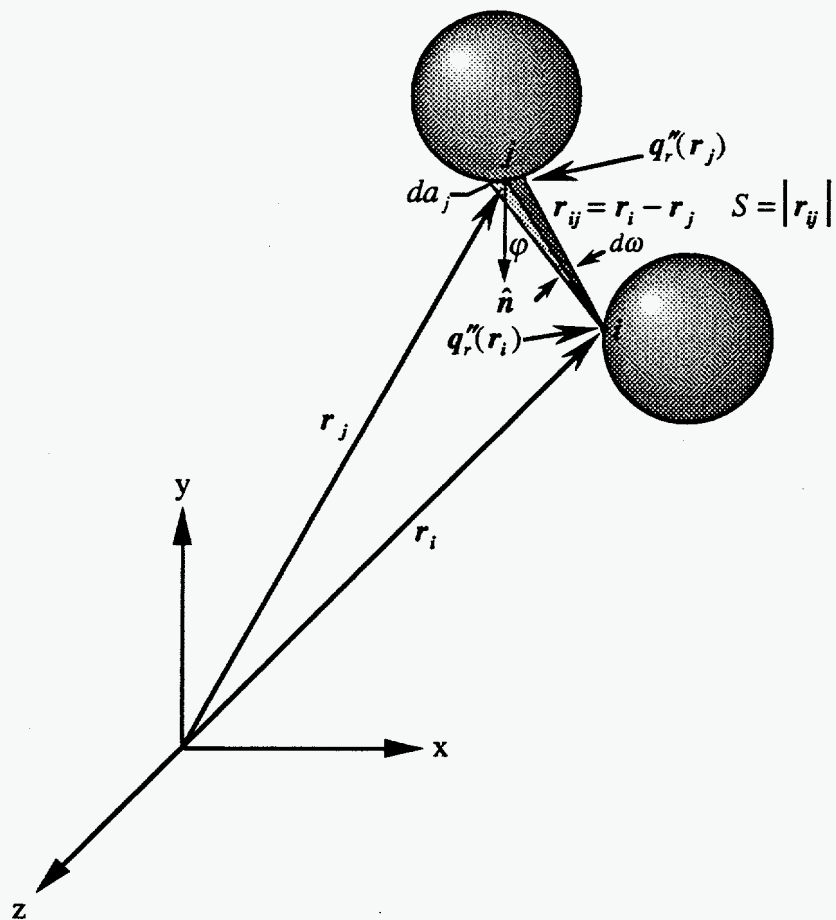


Figure 8.3 Radiant exchange between nodes i and j in Cartesian coordinates

Substituting the above expression into the definition of the radiative heat flux given by equation (8.7), the radiative flux vector associated with node i is given as follows:

$$\mathbf{q}_r''(\mathbf{r}_i) = \frac{1}{\pi} \int_{\partial\omega} \left[\varepsilon_j \sigma T^4(\mathbf{r}_j) + \{ \mathbf{q}_r''(\mathbf{r}_j) \cdot \hat{\mathbf{n}} \} (1 - \varepsilon_j) \right] \hat{\mathbf{s}} d\omega \quad (8.9)$$

In the three dimensional geometry of Figure 8.3, the intensity emitted and reflected from da_j , incident at node i , travels in the direction given by vector $\mathbf{r}_{ij} = \mathbf{r}_i - \mathbf{r}_j$, which has a pathlength $S = |\mathbf{r}_i - \mathbf{r}_j|$. The unit vector along S is given as:

$$\hat{\mathbf{s}} = \frac{\mathbf{r}_i - \mathbf{r}_j}{|\mathbf{r}_i - \mathbf{r}_j|} = \frac{\mathbf{r}_{ij}}{|\mathbf{r}_{ij}|} \quad (8.10)$$

The quantity $\cos \varphi$ is again the dot product of the unit normal $\hat{\mathbf{n}}$, and the unit vector $\hat{\mathbf{s}}$ along S , so that:

$$\cos \varphi = \hat{\mathbf{n}} \cdot \hat{\mathbf{s}} = \hat{\mathbf{n}} \cdot \frac{\mathbf{r}_{ij}}{|\mathbf{r}_{ij}|} \quad (8.11)$$

The solid angle that da_j subtends when viewed from node i is thus:

$$d\omega = \frac{da_j \cos \varphi}{S^2} = da_j \hat{\mathbf{n}} \cdot \frac{\mathbf{r}_{ij}}{|\mathbf{r}_{ij}|} \frac{1}{|\mathbf{r}_{ij}|^2} = da_j \hat{\mathbf{n}} \cdot \frac{\mathbf{r}_{ij}}{|\mathbf{r}_{ij}|^3} \quad (8.12)$$

Substituting equations (8.10) and (8.12) into equation (8.9) has the following effect:

$$\mathbf{q}_r''(r_i) = \frac{1}{\pi} \oint_{\partial\Omega} \left[\varepsilon_j \sigma T^4(r_j) + \{\mathbf{q}_r''(r_j) \cdot \hat{\mathbf{n}}\} (1 - \varepsilon_j) \right] (\hat{\mathbf{n}} \cdot \mathbf{r}_{ij}) \frac{\mathbf{r}_{ij}}{|\mathbf{r}_{ij}|^4} da_j \quad (8.13)$$

Radiative relations of this type are derived in Siegel and Howell for participating media within gray diffuse boundaries and are also given for more general situations by Lin (1988). The significance of this form of the radiative flux vector over the formulation given previously by equation (8.9) lies in the manner in which the angular integration over a solid angle domain has been transformed into a surface integration. Thus, no additional information other than the nodal connectivity data, typically available from a finite element model, is required. Equation (8.13) can be put into final solution form by expressing the vector, \mathbf{r}_{ij} , as a unit vector, i.e. $\mathbf{r}_{ij} = \hat{\mathbf{r}}_{ij} |\mathbf{r}_{ij}|$. Thus, the following expression is obtained:

$$\begin{aligned} \mathbf{q}_r''(r_i) = & \frac{1}{\pi} \oint_{\partial\Omega} \left[\varepsilon_j \sigma T^4(r_j) \right] (\hat{\mathbf{n}} \cdot \hat{\mathbf{r}}_{ij}) \frac{\hat{\mathbf{r}}_{ij}}{|\mathbf{r}_{ij}|^2} da_j \\ & + \frac{1}{\pi} \oint_{\partial\Omega} \left\{ \mathbf{q}_r''(r_j) \cdot \hat{\mathbf{n}} \right\} (1 - \varepsilon_j) (\hat{\mathbf{n}} \cdot \hat{\mathbf{r}}_{ij}) \frac{\hat{\mathbf{r}}_{ij}}{|\mathbf{r}_{ij}|^2} da_j \end{aligned} \quad (8.14)$$

The above expression represents the radiative flux vector at a point r_i for the diffuse, gray surface case in a non-participating media. Note that each of the integrals contained within equation (8.14) is a vector with direction given by $\hat{\mathbf{r}}_{ij}$. The numerical problem is thus to evaluate equation (8.14) at all nodes belonging to surfaces within the computational domain, ($\partial\Omega$). The nodal radiation configuration factors which determine nodal visibility within a given

computational domain are imbedded within equation (8.14) and will be subsequently derived.

In order to implement a finite element formulation in the numerical determination of radiative heat transfer, each of the unknowns of equation (8.14) must be expressed in terms of a linear combination of finite element *basis functions*. In the Galerkin approximation, the solution is then restricted to a finite Hilbert function space which is represented by a set of basis functions, $\Psi_j(\mathbf{r})$, typically low order piecewise continuous polynomials defined over a set of subregions or *elements*. The basis functions which will be required in this formulation are given as follows, where N is the number of nodes in the mesh:

$$\mathbf{q}_r''(\mathbf{r}) = \sum_{j=1}^N \mathbf{q}_{r,j}'' \Psi_j(\mathbf{r}) \quad (8.15)$$

$$T^a(\mathbf{r}) = \sum_{j=1}^N T_j^a \Psi_j(\mathbf{r}) \quad (8.16)$$

The latter expansion given by equation (8.16) is known as the Swartz-Wendroff approximation. The coefficients of the above expansions respectively represent the values of the radiative flux vectors and temperatures at the nodal locations, j , which define each of the elements of the computational mesh.

In order to derive the appropriate finite element formulation for the determination of the radiative flux vector, subject to the assumptions previously outlined, the expansions given by equations (8.15) and (8.16) are substituted into

the expression for the flux vector given by equation (8.14). The *discretized* result is given by equation (8.17):

$$\begin{aligned} q''_{r,i} = & \sum_{j=1}^N \sigma \epsilon T_j^4 \left\{ \frac{1}{\pi} \oint_{\partial\Omega} \Psi_j(r) [\hat{n} \cdot \hat{r}_{ij}] \frac{\hat{r}_{ij}}{|\hat{r}_{ij}|^2} da_j \right\} \\ & + \sum_{j=1}^N q''_{r,j} \cdot (1 - \epsilon) \left\{ \frac{1}{\pi} \oint_{\partial\Omega} \Psi_j(r) \hat{n} [\hat{n} \cdot \hat{r}_{ij}] \frac{\hat{r}_{ij}}{|\hat{r}_{ij}|^2} da_j \right\} \end{aligned} \quad (8.17)$$

Note that the coefficients of the discrete finite element expansions are nodal quantities and may thus be moved outside of the integrals in the above expression. Also note that the first integral of equation (8.17) is a vector while the second integral contains a tensor quantity. Equation (8.17) represents a closed set of simultaneous equations for the radiative flux vector which are evaluated by a series of vector matrix products. The integral quantities do not depend on the solution itself as long as the assumption of constant material properties is upheld; thus, these "bracketed" quantities may be evaluated once for a given computational mesh and stored in memory for subsequent use. Expressed in a more convenient form, equation (8.17) becomes:

$$q''_{r,i} = q''_{r,j} \cdot (1 - \epsilon) \bar{R}_{q_{ij}} + \sigma \epsilon T_j^4 E_{q_{ij}} \quad (i, j = 1, N) \quad (8.18)$$

where in three dimensions:

$$E_{q_{ij}} = \frac{1}{\pi} \oint_{\partial\Omega} \Psi_j(\hat{n} \cdot \hat{r}_{ij}) \frac{\hat{r}_{ij}}{|\hat{r}_{ij}|^2} da_j \quad (8.19)$$

$$\bar{R}_{q_{ij}} = \frac{1}{\pi} \oint_{\partial\Omega} \Psi_j \hat{n}(\hat{n} \cdot \hat{r}_{ij}) \frac{\hat{r}_{ij}}{|\hat{r}_{ij}|^2} da_j \quad (8.20)$$

Equation (8.18) is a vector equation for each of the components of the radiative flux vector at node i . The components of the $(N \times N)$ $E_{q_{ij}}$ matrix are vectors, and the components of the $\bar{R}_{q_{ij}}$ matrix are second order tensors. Furthermore, the $E_{q_{ij}}$ matrix can be viewed as consisting of the direct emission geometrical 'configuration factors' between nodes i and j ; whereas, the $\bar{R}_{q_{ij}}$ matrix can be said to contain the indirect, or diffuse surface reflection 'configuration factors'. For a given finite element mesh, equations (8.19) and (8.20) need only be evaluated once. Solutions for the radiative flux vector given by equation (8.18) may then be obtained for varying temperature boundary conditions and surface emissivities without having to repeat the computationally intensive matrix evaluations. Note that the terms ϵ and $(1-\epsilon)$ have been removed from these matrices. Since all surfaces within the experimental assembly (to be modeled) are uniformly coated with paint having essentially constant properties, there is no need to retain these terms within the integrals.

Equations (8.19) and (8.20) are valid for three dimensional geometries; however, they will only be applied to a two dimensional mesh. Nevertheless, since radiation heat transfer is inherently a three dimensional process, contributions from the third or "z" dimension must be accounted for. The trigonometry involved in this transformation is detailed by Burns (1995), with the two dimensional result given by the following:

$$E_{q_{ij}} = \frac{1}{2} \oint_{\partial\Omega} \Psi_j (\hat{n} \cdot \hat{s}_{ij}) \frac{\hat{s}_{ij}}{|s_{ij}|} da_j \quad (8.21)$$

$$\bar{R}_{q_{ij}} = \frac{1}{2} \oint_{\partial\Omega} \Psi_j \hat{n} (\hat{n} \cdot \hat{s}_{ij}) \frac{\hat{s}_{ij}}{|s_{ij}|} da_j \quad (8.22)$$

Also note that the vector s_{ij} and its unit vector are merely the two dimensional projections of r_{ij} onto the x, y plane. Thus, the final formulation required for solution of the nodal *incident* radiation flux vector associated with a "two dimensional" enclosure consisting of diffuse gray surfaces is given by equations (8.18), (8.21), and (8.22). Note, however, that in order to properly isolate the convective contribution according to equation (8.1), it is the *net* radiative heat transfer rate which is desired. The net transfer rate associated with node i can be related to the incident radiative flux vector and the surface emissive power by conducting an energy balance on a differential area surrounding node i as illustrated in Figure 8.4. The results of such a balance yield the following:

$$q''_{r,net,i} + \epsilon (q''_{r,i} \cdot \hat{n}) - \epsilon \sigma T_i^4 = 0 \quad (8.23)$$

Rearranging in order to solve for the net flux at node i gives,

$$q''_{r,net,i} = \epsilon \left[\sigma T_i^4 - (q''_{r,i} \cdot \hat{n}) \right] \quad (8.24)$$

Finally, to obtain the desired net radiative rate *per heater rod*, the expression given by equation (8.24) must be integrated about the circumference of a given heater rod:

$$q_{r,net} = \oint_{rod\ m} q''_{r,net,i} da \quad i = 1, N \quad (8.25)$$

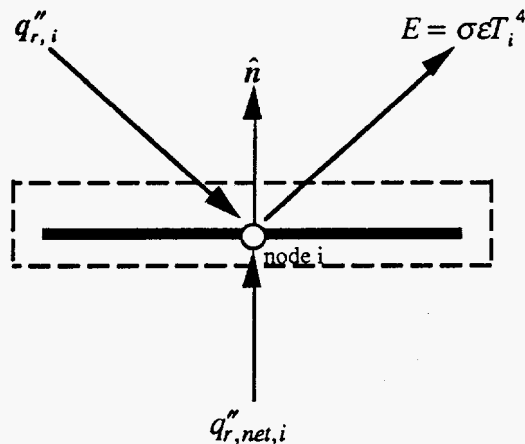


Figure 8.4 Determination of the nodal net radiative heat rate

8.2.5 Visibility Considerations: Shadowing and Line of Symmetry

In order to somewhat abate the computational burden associated with the solution of equations (8.21) and (8.22) for an enclosed rod bundle, two techniques were employed which take advantage of this specific geometry: shadowing and line of symmetry.

8.2.5.1 Shadowing

Recall that in essence, equations (8.21) and (8.22) represent matrices whose respective components may be interpreted as the direct emission and diffuse reflection configuration factors for all nodes within the computational mesh. A computational model which consists of N nodes will have of the order of N^2 configuration factor relations between the nodes. Furthermore, if there are M

potential obstructing surfaces within the model, then there will be of the order of N^2M visibility tests which must be conducted in order to obtain the mesh connectivity for radiation heat transfer. In the enclosed rod bundle, where abundant obstructing surfaces consisting of simple geometric shapes are present, the N^2M visibility tests consist of calculations to find intersections between obstructing surfaces and line segments joining two points for which line of sight (configuration factor) is to be determined. Consider the geometry illustrated in Figure 8.5. Generally, the calculation of configuration factors between two points in the computational domain, say i and j , begins by casting a ray between the two points as illustrated. In this case, i and j may not necessarily represent nodal locations, but rather the location of Gauss-Legendre integration points. The contribution of each integration point is then assimilated through the Gaussian integration process over entire finite elements associated with each node. Hence, configuration factors represented by the components of E_{q_u} and \bar{R}_{q_u} are discussed in terms of nodal representations and the relationship of visibility to the integration points is understood.

Shadowing occurs when some opaque object or concavity within the domain intersects the ray r_{ij} constructed between Gauss points. The visibility test objective is then to compare the ray r_{ij} to each possible obstruction in the most efficient manner possible. This test is actually implemented in two parts. Initially, it is determined whether or not the ray containing i and j intersects a

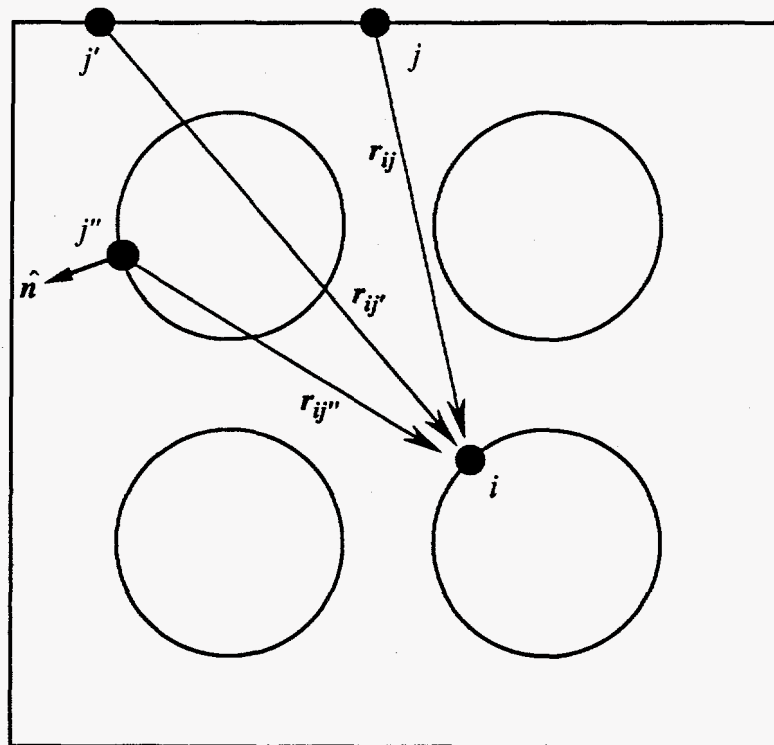


Figure 8.5 Shadowing related visibility tests

given obstructing surface. Secondly, the test evaluates whether or not the intersection lies between i and j . When an obstructing surface is found to exist between i and j , no further testing is required and the configuration factor between the two Gauss points is set equal to zero. If no obstruction is found, the configuration factor is calculated [via equation (8.21) or (8.22)] and the next i, j pair is tested.

Although this can be done using only the finite element mesh information, if the number of obstructions (M) is large, then the number of visibility tests may be significantly decreased by describing the obstructing surfaces independently. In the particular case regarding enclosed rod bundles, increased efficiency is obtained by creating an input file, independent from the finite element mesh file (known as the neutral file), in which the locations of all heater rod's centroids are given relative to the coordinate axis established in the neutral file. Since in this case all obstructing surfaces (rods) are circular, they are represented by the simple mathematical equation for a circle of radius r about the specified centroid. This method is implemented in the present work in order to take specific advantage of the relative geometric simplicity of the obstructing surfaces. Further expediency is obtained by performing a "pre-shadowing" test in order to eliminate i, j pairs which have no hope of "seeing" each other radiatively. Consider in Figure 8.5 the nodal pair given by i and j ". A constituent of the configuration factor calculation between i and j " involves the outward facing normal, \hat{n} , associated with j ". Intuitively, in order for radiation originating at j " to directly reach point i , the surface associated with point j " must be facing node i . Thus, the simple test,

$\hat{n} \cdot r_{ij} < 0$, indicates that radiation from node j cannot "see" node i , and thus no further visibility tests are necessary.

8.2.5.2 Line of Symmetry

Since the memory requirements and computational operations associated with thermal radiative modeling generally scale as N^2 , significant computational burden may be relieved by exploiting solution symmetry in any numerical procedure. A line of symmetry in the present analysis is equivalent to a perfectly insulating, perfectly reflecting mirror along the "boundary" corresponding to the symmetry line. The numerical implementation of this condition in the rod bundle geometry and its effect on visibility will be briefly discussed here.

Figure 8.6 represents a computational domain in which only the surfaces to the right-hand side of the indicated symmetry line are explicitly modeled. In order to limit computations to the right-hand side of this domain, a boundary condition must be implemented at the symmetry line such that radiation incident upon this line ("surface") is specularly reflected. Recall that for an enclosed horizontal rod bundle participating in multimode heat transfer, a thermal line of symmetry exists about the vertical centerline. If only radiative and/or conductive processes were at work, the rod bundle would be 1/8 symmetric; however, the presence of advection results in a skewing of isotherms upward (against the gravity vector) such that only vertical symmetry is justifiable.

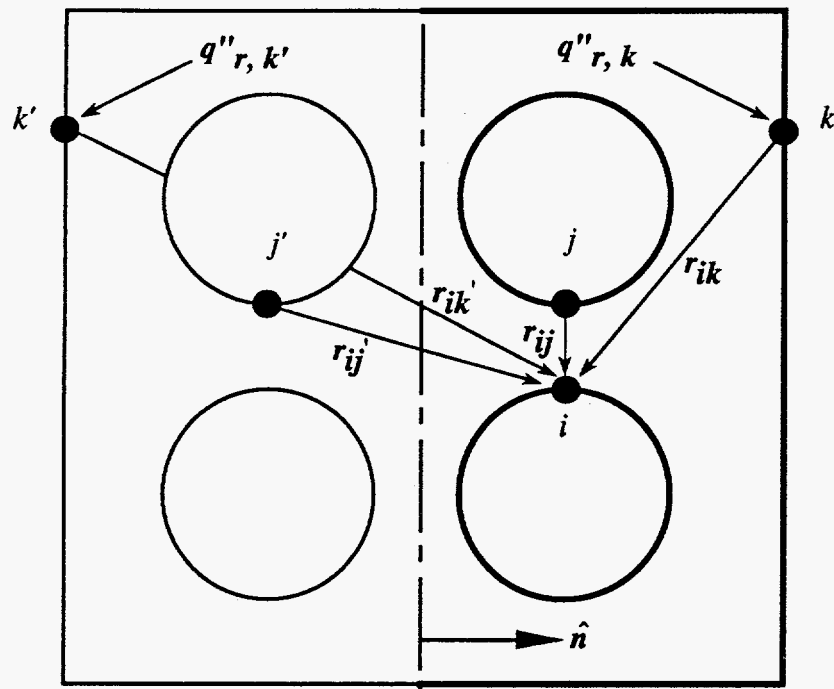


Figure 8.6 Line of symmetry considerations in visibility calculations

To implement the specular reflection boundary condition at the vertical symmetry line, the radiative contributions of direct emission and diffuse reflection will be considered separately, which is consistent with the previous development leading to expressions for $E_{q_{ij}}$ and $\bar{R}_{q_{ij}}$. Observe point j in Figure 8.6 and its "reflection", point j' . Based upon the formulations previously derived for the radiative flux vector, it can be shown that the effect of points j and j' on the *directly* incident flux at point i may be expressed in terms of the temperatures at j and j' as follows:

$$q''_{r,direct,i} = \epsilon \sigma T_j^4 E_{q_{ij}} + \epsilon \sigma T_{j'}^4 E_{q_{ij'}} \quad (8.26)$$

where it has been assumed that all participating surfaces have uniform surface properties. Here, $E_{q_{ij}}$ and $E_{q_{ij'}}$ respectively represent the direct emission configuration factors between nodes j and i , and nodes j' and i . By symmetry, it is asserted that $T_j = T_{j'}$, and therefore equation (8.26) may be expressed as

$$q''_{r,direct,i} = \epsilon \sigma T_j^4 (E_{q_{ij}} + E_{q_{ij'}}) \quad (8.27)$$

Thus, it is not necessary to explicitly include the temperature of node j' in the calculation of the radiative transport; although, it *is* necessary to evaluate the configuration factor $E_{q_{ij'}}$.

The effect of diffuse surface *reflection* presents an additional complication beyond that previously discussed in that diffuse reflection involves the incident radiative flux vector at each point with which node i interacts [cf. equation (8.18)]. Again consider the geometry of Figure 8.6 where point k may interact

with node i via both direct emission and diffuse reflection; whereas, the point k' may only interact with node i by reflection. The contribution to the incident radiative flux at node i due to diffuse reflection from points k and k' is given by:

$$q''_{r,indirect,i} = (1 - \varepsilon) \left[q''_{r,k} \cdot \bar{R}_{q_{ik}} + q''_{r,k'} \cdot \bar{R}_{q_{ik'}} \right] \quad (8.28)$$

where \bar{R}_q is the diffuse reflection tensor of equation (8.22) for a two dimensional domain. It is important to note that the visibility between nodes i and k , and i and k' must be calculated independently since it is not difficult to imagine a case in which no line of sight exists between node i and k' though there is between i and k , or vice-versa.

The above relations briefly summarize the essential ingredients required in order to exploit solution symmetry for radiative transport within the rod bundle geometry. The computational effort associated with the modeling procedure is significantly reduced when symmetry is used to simplify the problem.

8.2.6 Solution Procedure and Code Structure

8.2.6.1 Solution Procedure

In order to apply the previously discussed numerical procedures in such a manner that the radiative heat transfer component within enclosed rod bundles may be calculated, the RADERA code was developed (RADIation in Enclosed Rod Arrays). A listing of the code is included in Appendix 1. This algorithm is an adaptation of the finite element based formulation developed by Burns (1995),

which employs the Swartz-Wendroff approximation to evaluate the radiative heat transfer within enclosures characterized by gray, constant properties. The crux of this routine involves the determination of the configuration factor matrices given by equations (8.21) and (8.22) for a given finite element model, and the subsequent determination of the radiative flux vector at each node, expressed in terms of the aforementioned matrices by equation (8.18). The code is structured such that known, experimentally measured rod temperatures serve as input, along with the total hemispherical emissivities of all surfaces. Given the "nodal" temperatures, the incident radiative flux vector is determined using an iterative technique. Regardless of the iterative method employed (several are viable), all of the components of the configuration factor matrices in equations (8.21) and (8.22) are evaluated and stored in memory throughout the iterative solution. Beginning with an initial guess for the flux vector in equation (8.18) and the known nodal temperatures, the iterative procedure is repeated until the maximum change in the calculated flux vector is less than some small specified convergence criterion. After this criterion has been achieved, the net radiative flux at each node is determined via equation (8.24). Then, these quantities are integrated over the entire rod in order to determine the net rod radiative linear heat rate using equation (8.25). Finally, an energy balance is conducted in which the net radiative heat rate from all rods is summed and compared to the net rate received by the boundary enclosure. The internal error arising from the energy balance is expressed as a percent of the average radiant heat rate for the entire bundle:

$$e_{int} = \left[\frac{\sum_{m=1}^{N_{rods}} q'_{r,net,m} - |q'_{r,net,CuBE}|}{\bar{q}'_{r,net,tot}} \right] * 100 \quad (8.29)$$

where,

$$\bar{q}'_{r,net,tot} = \frac{\sum_{m=1}^{N_{rods}} q'_{r,net,m} + |q'_{r,net,CuBE}|}{2} \quad (8.30)$$

and $q'_{r,net,CuBE}$ is the net radiative heat rate integrated over the entire enclosure surface.

8.2.6.2 RADERA Code Structure

Figure 8.7 is a flowchart of the RADERA algorithm employed in the determination of the radiative heat transfer component for all experiments conducted with the UT BWR assembly mock-up. In order to use this code, one must first create a suitable finite element mesh using a pre-processing program such as PATRAN, distributed by PDA Engineering in Costa Mesa, CA. The result of this operation is a 'neutral file', which contains all node/element connectivity information, node locations, and boundary conditions. Other required input includes a file containing the *experimentally measured* average temperatures of all heater rods as well as the CuBE inner surface temperature. The total hemispherical emissivities of all surfaces are included in this file as well. As discussed previously in Section 8.2.5.1, an input file, distinct from the neutral file, containing the locations of heater rod centroids and radii, is utilized to

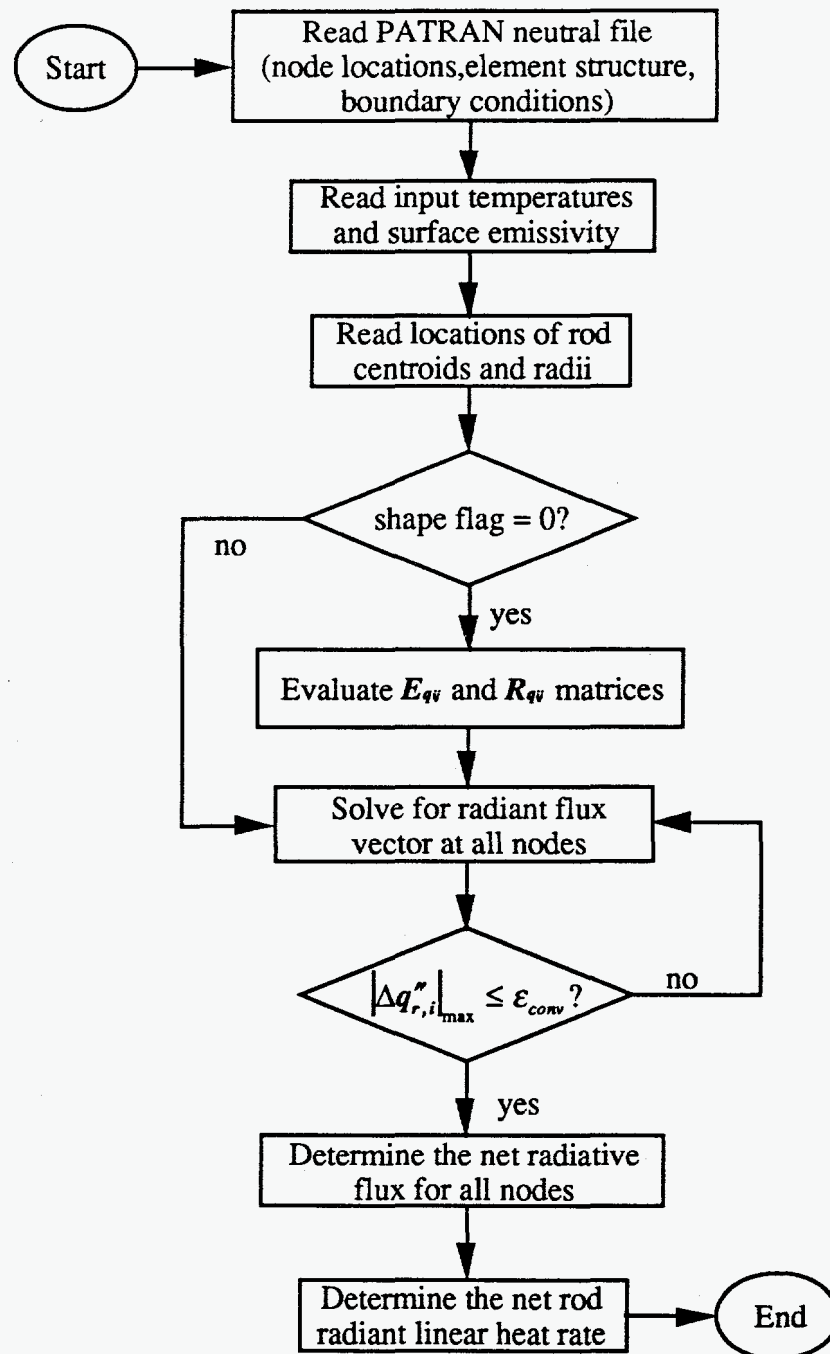


Figure 8.7 RADERA algorithm structure

conduct visibility tests. Once all input files have been created, RADERA execution is begun. If the shape factor flag value is equal to zero, then the $E_{q,q}$ and $\bar{R}_{q,q}$ matrices are calculated. If these matrices have been already determined for a given finite element mesh, then the flag value is set equal to one and the previously determined matrices are reused. With the configuration factors at hand, the incident radiative flux vector is determined at each node via equation (8.18). This is a transcendental equation in which the known temperatures are entered along with an initial guess for the flux vector. A Picard iteration method is utilized in order to iterate until the maximum change in the calculated flux vector is below some small convergence criterion, typically 10^{-12} . After such convergence has been obtained for all nodes, equation (8.24) is employed in order to determine the net nodal radiative heat flux. Integrating about the circumference of each heater rod via equation (8.25) yields the desired net radiant heat rate per heater rod. The internal error of the model is expressed as previously discussed by conducting an energy balance between the total radiant energy leaving all heater rods and the total radiant energy received by the CuBE. This error is reported in the RADERA code's output file, which also consists of a listing of the net radiative heat rates for each heater rod within the assembly as well as for the surrounding enclosure (per unit length).

8.3 DETERMINATION OF TOTAL HEMISPHERICAL EMISSIVITIES

As with all numerical techniques, the RADERA algorithm will produce results which contain some degree of error. Some of this error can be associated

with the numerical method itself, for example, due to the finite mesh spacing employed. However, as will be shown in the uncertainty analysis of Chapter 9, a more significant source of potential error is the uncertainty allied with the correct value of the surface emissivity. This is especially true under experimental conditions in which radiation is dominant (i.e. nitrogen backfill at low pressure and high power). Under such conditions, the emissivity uncertainty can overwhelm errors introduced by all of the theoretical and numerical approximations. Thus, it is vitally important that the accepted values for surface emissivity (to be used in all radiation calculations) be ones which have been carefully measured and characterized, and thus possess low values of experimental uncertainty. In order to achieve this condition, all participating surfaces within the UT experimental array were coated with Pyromark 2500 flat black paint manufactured by Tempil Division of Big Three Industries, South Plainfield, NJ. Pyromark 2500 flat black paint is a high temperature silicon based refractory paint and is available commercially. The paint contains finely ground chromium oxide powders which produce the flat black finish. The paint also contains a small amount of graphite, a silicate binder, and an organic vehicle. The paint is applied like an ordinary paint by brushing or spraying. After allowing time for sufficient drying, the paint must be heat-cured in order to achieve its reported specifications. After proper drying and curing, the coating will reportedly survive temperatures of 2500°F while retaining a high total normal emissivity that remains essentially stable up to 2000°F. A large range of optical properties for Pyromark 2500 have been documented by researchers in numerous past studies. The following section discusses two salient characterizations of

Pyromark paint conducted by Sandia National Laboratories (SNL) and NASA, respectively. The emissivity data produced by these efforts were further validated by direct measurement at UT using a thermal imaging camera, as will be reviewed in Section 8.3.3 of this chapter.

8.3.1 Reported Emissivity for Pyromark 2500 Coated Surfaces

The optical properties of Pyromark 2500 black paint have been extensively characterized in studies by both SNL (Longenbaugh, Sanchez, & Mahoney, 1990) and NASA (Wade & Slemper, 1962). When applied to a smooth metallic surface such as stainless steel or copper, this paint provides a diffuse, opaque coating that to a reasonable approximation can be considered gray as well. Furthermore, detailed measurements of this paint's spectral and total emissivity as a function of temperature have been made on various metallic substrates using sophisticated measurement techniques. The two studies cited above report results which are very compatible and contain acceptable levels of experimental uncertainty.

8.3.1.1 SNL Reported Emissivity Values

Emissivity measurements by SNL for Pyromark 2500 coated surfaces were obtained using both portable and laboratory based instruments (see reference above). The portable 'field type' instrument was used in order to measure painted components too large to measure in the laboratory; whereas, the laboratory measurements were conducted using small, specially prepared painted specimens

under controlled conditions. The field instrument was a portable infrared reflectometer, Model DB-100, manufactured by Gier-Dunkle, Inc. This reflectometer is designed in order to measure the normal infrared emissivity of flat, opaque samples placed over its measurement port. The DB-100 actually measures the infrared reflectivity (emissivity = $1.0 - \text{reflectivity}$, for opaque samples) by viewing the sample with a single detector while the surface is alternately irradiated with black body radiation from a rotating slit-cavity at differing temperatures. When calibrated to a known standard, the measurement uncertainty for this detector is within ± 0.03 reflectivity units for typical metallic samples, as reported by Pettit & Mahoney (1980). Emissivity measurements using this instrument were taken for samples at 100 and 300°C.

In the SNL laboratory measurements, Pyromark coated surfaces were optically characterized using two devices, each capable of measurement over a given wavelength range. Covering the wavelength range from 0.265 μm to 2.400 μm , the hemispherical spectral reflectivity properties of Pyromark 2500 coated substrates were measured using a Beckman 5270 spectrophotometer equipped with an integrating sphere accessory. All data obtained using this instrument were referenced to NBS (National Bureau of Standards) calibrated standard material and have a reported measurement uncertainty of ± 0.005 reflectivity units (1.000 reflectivity units = 100% reflectance). For optical properties covering the wavelength range from 2.400 μm to 20.0 μm , a Perkin-Elmer Model 1800 FTIR (Fourier Transform Infrared) spectrophotometer was modified using an integrating sphere arrangement which enables the measurement

of hemispherical spectral reflectivity over the near to mid-infrared wavelength region (Tardy & Dunn, 1987). The laboratory data obtained using these two instruments were later merged such that the optical properties over the range $0.265\mu\text{m} \leq \lambda \leq 20.0\mu\text{m}$ were characterized to within a measurement uncertainty of ± 0.010 units. Using the spectral information obtained from the two laboratory spectrophotometers, the total reflectivity values over the combined wavelength range were determined as a function of temperature based upon the following relation:

$$\rho = \frac{\int_{\lambda_1}^{\lambda_2} \rho(\lambda) E_{bb}(\lambda, T) d\lambda}{\int_{\lambda_1}^{\lambda_2} E_{bb}(\lambda, T) d\lambda} \quad (8.31)$$

where ρ is the total hemispherical reflectivity at temperature T , $\rho(\lambda)$ is the *measured* spectral hemispherical reflectivity, and E_{bb} is the Planck black body distribution function at T . In the case of the combined data, $\lambda_1=0.265\mu\text{m}$ and $\lambda_2=20.0\mu\text{m}$. Since all samples were opaque, the total hemispherical emissivity, ϵ , is obtained via:

$$\epsilon = 1 - \rho = \frac{\int_{\lambda_1}^{\lambda_2} \{1 - \rho(\lambda)\} E_{bb}(\lambda, T) d\lambda}{\int_{\lambda_1}^{\lambda_2} E_{bb}(\lambda, T) d\lambda} \quad (8.32)$$

The SNL measurements for 'as-rolled' mild stainless steel substrate uniformly coated with Pyromark 2500 are summarized in Table 8.1 for the temperature range of interest in the present experimental investigation.

Table 8.1 SNL measurements of total hemispherical emissivity for a Pyromark coated mild steel substrate [from Longenbaugh, Sanchez, & Mahoney, (1990)]

Instrumentation	Temperature (°C)	ϵ
Field	100	0.82 ± 0.03
Field	300	0.81 ± 0.03
Laboratory	27	0.82 ± 0.01
Laboratory	77	0.83 ± 0.01

The emissivity values given in Table 8.1 were measured using integrating sphere spectrophotometers, which obtain spectral measurements over the range $0.265 < \lambda < 20.0 \mu\text{m}$. For temperatures seen within the UT experimental rod bundle, this bandwidth contains between 85% and 90% of the total emitted thermal radiation; thus, the SNL reported values are a good representation of the desired total emissivity. Furthermore, over this wavelength band, the reported spectral variation of the measured emissivity is slight, within 10% of the mean. In order for a surface to be considered gray, the emissivity (absorptivity) must be essentially independent of wavelength over the spectral range in which emission

and irradiation occur. Since surfaces within the UT experimental array emit and receive thermal radiation over essentially the same infrared waveband ($0.265 < \lambda < 20.0 \mu\text{m}$), the gray approximation is a good one.

8.3.1.2 NASA Reported Emissivity Values

Additional emissivity measurements of Pyromark flat black paint on steel and Inconel substrates are reported in an earlier NASA study (Wade & Slemple, 1962). In this study, an instrumentation system was employed which utilized a thermocouple equipped, heavily oxidized, Inconel baffled cone as a 'reference black body'. The emissive power of a vertically suspended Pyromark coated test specimen was measured using a thermopile pyrometer. Subsequent comparison to the radiant flux emitted by the reference black body at the same temperature allowed determination of the specimen's emissivity. The pyrometer was mounted on a pivoted arm, which allowed flux measurements at varying angles of observation from the normal. The total emissivity of the coated samples was characterized over a temperature range of 600°F to 2000°F. Figure 8.8 depicts the NASA measured total normal emissivity values for Pyromark coated stainless steel and Inconel specimens. Note that the measured values are both temperature and substrate dependent. For the SS 321 substrate, the measured total normal emissivity at 600°F ($\approx 315^\circ\text{C}$) is $\epsilon = 0.78$. This value is slightly lower than the SNL measurements at similar temperatures. Note that if the coated surface emits diffusely, then the normal measured emissivity can be considered a close approximation of the hemispherical value. This condition was investigated by

Wade and Slemph by measuring the specimen's emitted radiant flux incrementally from the normal view. Figure 8.9 illustrates the result of this test by plotting the ratio of the measured flux at a given angle to the measurement obtained at 0° (the normal position). The measured radiant flux values, analogous to equation (8.3), have been corrected for the variation in surface area viewed. The solid line sketched on the figure represents Lambert's cosine law for a perfectly diffuse surface. As shown, the Pyromark coated surfaces are very close to being perfectly diffuse and thus the normal values given in Figure 8.8 can be interpreted as being total hemispherical.

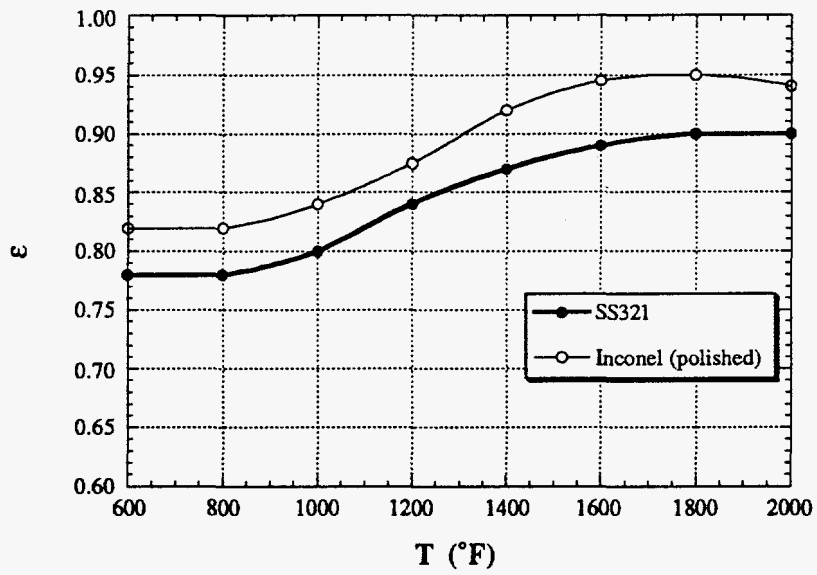


Figure 8.8 Variation of the total normal emissivity of Pyromark coated surfaces [from Wade & Slemple, (1962)]

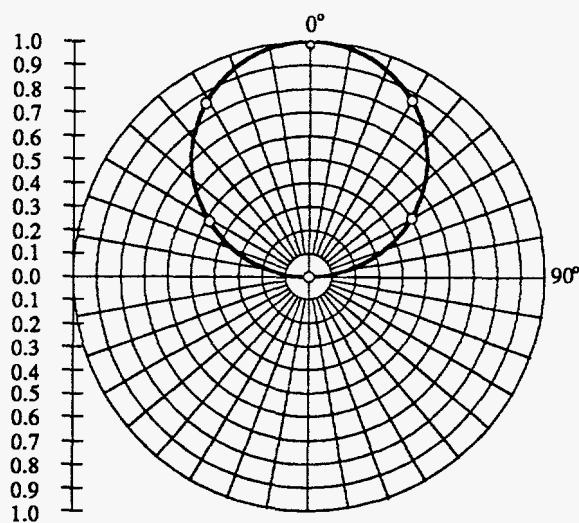


Figure 8.9 Comparison of the radiant flux of a Pyromark coated SS-321 surface with Lambert's Cosine Law for diffuse emission (solid line), [from Wade & Slem, (1962)]

8.3.2 Summary of Reported Emissivity Values for Pyromark 2500

The emissivity data supplied by the SNL and NASA studies were obtained using sophisticated techniques under controlled laboratory conditions, resulting in accurate measurements with low experimental uncertainties. Data were obtained for a significant range of surface temperatures and for a variety of substrate materials. It is from these data that the total hemispherical emissivity values required for input to the RADERA code were determined. In the UT BWR simulations, all surfaces which were coated with Pyromark 2500 were held below 200°C and often the difference between the cooled boundary enclosure and the maximum heater rod surface temperature was less than 100°C. For this range of conditions, the SNL data of Table 8.1 predict a total hemispherical emissivity of $\epsilon \approx 0.82$. The NASA data of Figure 8.8 indicate constant values below 600°F of $\epsilon \approx 0.78$. Thus, for the purpose of modeling (radiatively) the UT array using the RADERA algorithm, a total hemispherical emissivity of $\epsilon = 0.80 \pm 0.02$ was selected, with the stated uncertainty having been chosen in order to bridge the gap between the NASA and SNL reported values. Nevertheless, as a double check of the potentially sensitive emissivity value, an experimental emissivity measurement was taken (at UT) of a Pyromark 2500 coated SS304 plate. The results of this study are discussed in the following section.

8.3.3 Experimental Measurements of Emissivity at UT

In order to obtain additional confidence with regard to the use of literature reported emissivity values for Pyromark coated metallic surfaces, a thermal imaging system available at UT was utilized for direct emissivity measurement. This system consisted primarily of an Inframetrics Model 600L camera calibrated to operate in the 8 to 12 μ m infrared waveband and its associated control unit. The 600L camera contains a Mercury-Cadmium-Telluride (Hg-Cd-Te) detector whose electrical conductivity changes proportionally with the total radiant power received. The voltage obtained from a resistance bridge configuration is translated into gray level intensity, which can be displayed on a monitor. The infrared (IR) detector in the 600L camera is cooled with liquid nitrogen to a temperature of 77K using a closed cycle microcooler which operates in a Stirling cycle. This camera can operate continuously and can be positioned at any angle with respect to the target surface. IR cameras of this type have been previously employed in order to measure the emissivity of various surfaces (Aliaga, 1992). For this study, the emissivity of a smooth SS304 surface, coated uniformly with Pyromark 2500 paint, was determined using the configuration indicated in Figure 8.10. In this arrangement a foil, Type K thermocouple was mounted on a thin SS304 plate, facing the camera. The back of the plate was equipped with a hot plate consisting of a flexible coil heater manufactured by Watlow of St. Louis, MO. The camera was mounted approximately 0.5m from the plate in a position normal to the plate's surface. The stainless steel plate was then heated until a steady state temperature was achieved. The uniform heating provided by this

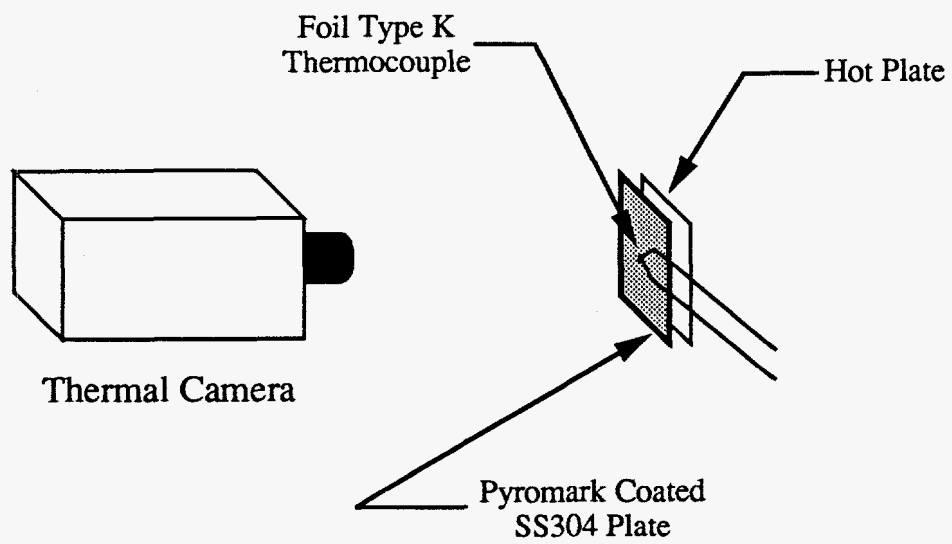


Figure 8.10 Arrangement for experimental emissivity measurement using an IR camera

configuration resulted in a near isothermal condition for the plate surface facing the camera, a fact verified by imaging with the thermal camera. In order to measure the coated plate's emissivity, the emissivity parameter in the infrared system (a control) was entered and adjusted until a match between the temperature reading from the foil thermocouple and the IR system was attained. All measurements were obtained with the plate at a steady temperature of 150°F (66°C), a value which is representative of experimental test conditions. It is important to note that the plate temperature must be substantially higher than its surroundings so that the reflected component of the surface's total radiative power is relatively small compared to the emitted component. The results of the UT measurement using the IR system yielded a normal emissivity of $\epsilon = 0.8$, which is consistent with the literature reported values and thus corroborates the value chosen for RADERA implementation. Aliaga (1992) maintains an emissivity uncertainty of ± 0.02 units for this type of measurement using identical equipment. Aliaga further reports that there is virtually no effect of the angle of camera inclination on the measurement within 20 degrees from the normal position.

8.4 BENCHMARKING AND RADERA CODE ASSESSMENT

8.4.1 The Concentric Annulus

In order to determine the viability of the RADERA code with regard to the evaluation of 'two dimensional' radiative heat transport between diffuse, gray

surfaces, a benchmark problem is sought which will assay the code's shadowing and symmetry features as well as indicate the algorithm's general accuracy. The benchmark should have an analytical solution which can be easily solved for a number of different input parameters. The concentric annulus shown in Figure 8.11 meets all of these criteria.

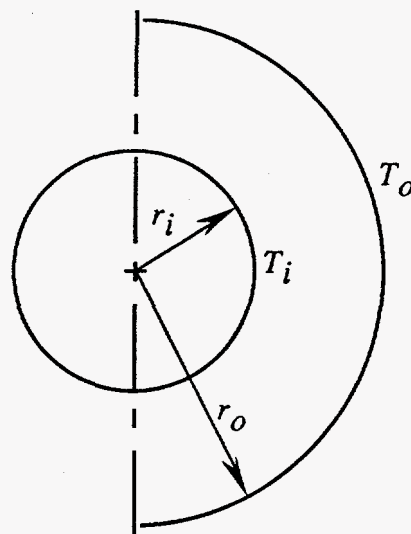


Figure 8.11 The concentric annulus benchmark problem

In this problem, the inner cylinder surface is isothermal at temperature, T_i ; whereas, the surrounding outer cylinder is uniformly at temperature, T_o . All surfaces have a total hemispherical emissivity, ϵ , which is temperature independent. Furthermore, the surfaces are diffuse and gray in nature. Note that

the geometry pictured in Figure 8.11 is one which will utilize the symmetry and shadowing capabilities of the RADERA code described previously.

Since the radiosities over the inner and outer cylinders are uniform, the net radiative heat flux over each cylinder may be evaluated from elementary viewfactor analysis. The solution to this problem may be expressed in a non-dimensional form by scaling the dimensions of the annulus in terms of the gap width, $L = r_o - r_i$; thus, a dimensionless radius is given as $R = r/L$. The temperatures may also be scaled in terms of the inner cylinder temperature such that $\theta = T/T_i$. Hence, the dimensionless radiative heat rate leaving each cylinder is given by the following:

$$q_{r,net}^* = \frac{2\pi R_i R_o \varepsilon (\theta_i^4 - \theta_o^4)}{R_o + (1 - \varepsilon) R_i} \quad (8.33)$$

Table 8.2 illustrates the accuracy of the heat flux calculations by comparing the RADERA generated results with those obtained using the analytical solution represented by equation (8.33). The numerical results were obtained using quadratic rod-type finite elements in which each element is composed of three nodes. The modeled cylinder pair has an aspect ratio of 1.6 and therefore $R_i=0.625$ and $R_o=1.625$. The temperature ratio, $\theta_o = 0.5$; hence, there is heat transfer to the outer cylinder. The emissivity of the cylinders is $\varepsilon = 0.5$. Results are presented for four cases representing variations in the mesh spacing, which is measured by the number of nodes used to discretize the inner cylinder (twice as many nodes comprise the outer cylinder).

Table 8.2 Concentric annulus analysis using RADERA with $\theta_o = 0.5$ and $\varepsilon = 0.5$

N_i	$e_{abs} (\%)$ [equ. 8.34]	$e_{int} (\%)$ [equ. 8.29]
5	-1.7	4.03
9	0.05	-0.16
21	-0.05	0.21
29	-0.04	0.16

Using the latter mesh spacing of Table 8.2, which contains 29 nodes for the inner cylinder and 58 nodes for the outer cylinder, the emissivity was varied for the case in which $\theta_o = 0.2$. These results are given in the following table:

Table 8.3 Concentric annulus analysis with $\theta_o = 0.2$ and $N_i=29$

ε	$e_{abs} (\%)$ [equ. 8.34]	$e_{int} (\%)$ [equ. 8.29]
0.5	0.11	0.55
0.8	0.04	0.27
0.9	0.03	0.22
1.0	-0.28	0.18

The internal RADERA error, e_{int} , is obtained based upon the fact that since radiation is the only mode of heat transfer considered, the sum of the net radiative heat rates from all surfaces must equal zero. An analogous form of equation (8.29) for a concentric annulus was used in order to obtain this quantity. The absolute error, e_{abs} , expresses the deviation of the RADERA obtained result to that of the analytical solution given by equation (8.33):

$$e_{abs} = \left[\frac{q_{r,net,RADERA}^* - q_{r,net,eq. 8.33}^*}{q_{r,net,eq. 8.33}^*} \right] * 100 \quad (8.34)$$

Based upon studies conducted by Burns (1995), results obtained using quadratic finite element basis functions are preferred over those obtained using linear functions. This is due to the ability of the quadratic elements to better conform to the shape of the cylinders compared to the piecewise linear approximation of the linear elements.

The results of the RADERA code for the geometry of Figure 8.11 are in general quite accurate, providing evidence for the validity of the algorithm's fundamental formulations and methodology. This is of course dependent of upon the determination of the appropriate mesh spacing for the problem at hand. Furthermore, the viability of the symmetry and shadowing features of the code have been established as well. In the concentric annulus problem described here, approximately 30% of the nodal configuration factors were zero due to the obstruction of the center cylinder. This fraction is expected to increase as the

annulus gap decreases, or if the modeled geometry is even more restricted, such as in the tightly packed rod arrays considered in the next section.

8.4.2 The Enclosed Rod Array

The enclosed rod array is the precise problem for which RADERA was conceived and created. The following discussion will focus upon the code's applicability and functionality in this complex, restricted geometry. Unfortunately, there is no analytical solution for this problem and thus numerical results can only be *directly* assessed by comparison with experimental data. Such experimental data must conform to the following requirements, however, in order to be useful for code validation:

- 1) Data must exist for the precise geometry considered.
- 2) Temperature data must be carefully and accurately measured. (low uncertainty)
- 3) All surfaces within the experimental array must have well known optical properties (emissivity). Surfaces must be opaque, diffuse, gray, and to a large degree isothermal.
- 4) Radiation should be the only mode of heat transfer.

In order to accomplish the last condition, a perfect vacuum must be attained within the experimental environment. Then, there would be no gas to conduct the thermal energy and the only possible heat transfer mechanism would be radiation. A perfect vacuum however is essentially impossible to achieve and thus a

compromise must be struck in the determination of how 'hard' a vacuum is actually required in order to reasonably eliminate gaseous conduction effects. Thus, the realization of the listed prerequisites is not a task to be taken for granted. In the present work, suitable experimental vacuum data was not obtainable which would allow the *direct* assessment of RADERA's efficacy in the enclosed rod bundle geometry. This is due to the fact that the hardest vacuum obtainable in the UT facility is of the order of 1 torr, a level which does not acceptably eliminate gaseous conduction (cf. Chapter 5.4). Nevertheless, a great deal may be learned about the viability of RADERA by *indirect*, or non-experimental means. Namely, the code's performance may be characterized by evaluating such numerical parameters as the internal error given by equation (8.29), which appraises the degree in which the following energy balance is conserved:

$$\sum_{m=1}^{M \text{ total surfaces}} q_{r,net_m} = 0 \quad (8.35)$$

where M is the total number of surfaces within the enclosed rod bundle. Further characterization of any numerical routine's accuracy is obtained by performing mesh independence studies in which the effect of mesh spacing and structure on the code's solution is assessed.

Figure 8.12 represents the RADERA model used for all radiative heat transport calculations involving the UT experimental assembly. Vertical symmetry assumptions have been taken into account and therefore only half of the assembly cross section is explicitly modeled. The appropriate boundary

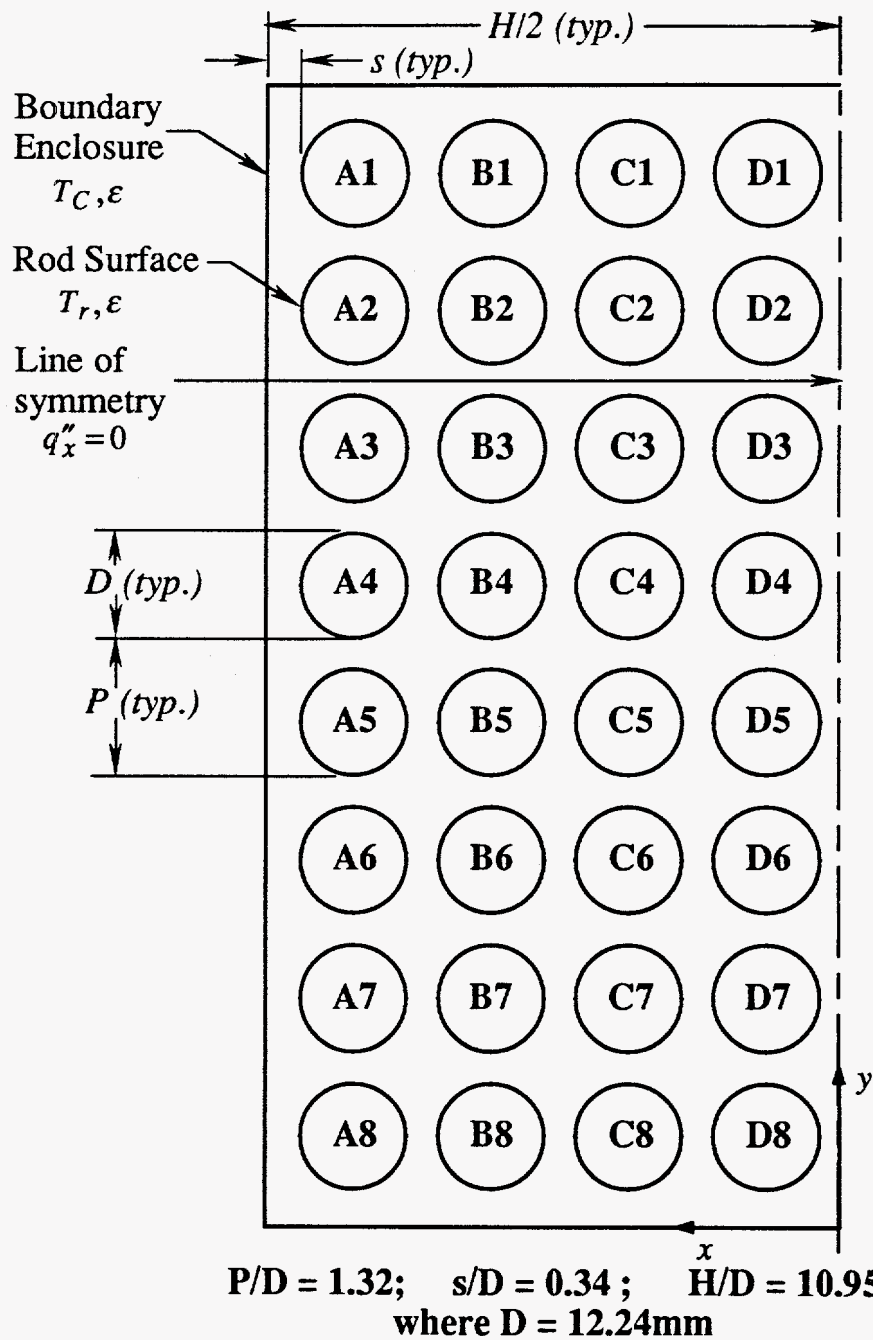


Figure 8.12 RADERA model for radiative transport analysis

conditions for the radiative model include specification of the mean surface temperature for each rod within the bundle (designated T_r), and specification of the mean CuBE temperature (designated T_C). The physical dimensions of the numerical model are consistent with the UT apparatus (and a GE BWR fuel assembly). The rod positions in Figure 8.12 are labeled using an alpha-numeric nomenclature where a capital letter denotes the column and the following numeral denotes the row. This nomenclature of Figure 8.12 will be used throughout the remainder of this dissertation in order to reference specific rod positions.

The objective of this model, as it is to be applied in the analysis of experimentally measured data, is to determine the net radiative heat transfer rate per unit length for all surfaces indicated, given the experimentally measured surface temperatures and emissivity values. As previously noted, separation of the radiative heat transfer component from the total supplied power is crucial to the experimental determination of *system independent* Nusselt-Rayleigh correlations for the natural convection process within the assembly. The highly conductive cladding of each fuel rod allows each rod to be treated as an isothermal cylinder, a fact verified by both numerical prediction and experimental measurement (cf. Chapter 3). All surfaces further possess the same total emissivity, a consequence of the stability of the Pyromark coating over the limited temperature range seen within the UT assembly.

The initial run using RADERA with the geometry of Figure 8.12 employed a coarse finite element mesh which consisted of 12, three-noded bar elements to discretize each fuel pin and 64 bar elements to discretize the surrounding shroud. Using this mesh and a set of representative temperatures, the internal error given by equation (8.29) was found to be 30.6% of the total assembly heat transfer. By increasing the number of elements to 16 elements per fuel rod and 120 elements for the shroud wall, the internal error was decreased to 11%. Further refinement in the computational mesh would result in additional reduction of the internal error; however, the resulting increase in the number of unknowns poses a significant burden on the computational requirements for the problem. Realizing however that the integrals in equation (8.17) are essentially calculated between integration point locations, increasing the number of integration points per element should also decrease the error without increasing the number of unknowns. Employing this line of thought, the integration order was increased from four point to eight point Gauss-Legendre integration, and using the previous mesh with 16 elements per rod, a decrease in the internal error from 11% to 0.9% was observed. Any internal error less than 1% was deemed acceptable. As demonstrated, increasing the integration order provides increased accuracy for complex visibility problems without increasing the overall size of the problem.

The RADERA algorithm is employed in order to determine the radiative heat transfer component of individual heater rods within the UT experimental array, given the experimentally measured heater rod/CuBE temperatures, and the

radiative surface properties. The radiative analysis is carried out using the nominal mesh discussed above, which possesses a total of 1265 nodes. The results of the RADERA calculations for each experimental statepoint are reported in Appendix 4. The radiation corrected Nusselt/Rayleigh number correlations are presented and discussed in Chapter 10. During the course of all RADERA runs, for both helium and nitrogen backfills, it was found that the internal error given by equation (8.29) remained below the 1% established acceptance criterion. The lingering error arises from internal numerical uncertainties introduced during the solution procedure. For example, the mesh spacing in any numerical model must be limited in order to obtain convergence in a reasonable time period. If it were possible to decrease the mesh spacing to an infinitesimally small value, then the numerical prediction would in theory approach the exact solution. This is not strictly true in the present case, as other factors such as truncation error, round-off error, and code convergence also affect the result. However, these errors are typically small in RADERA's implementation as a high level integration order is employed, double precision units are utilized throughout the calculation, and the code's convergence criteria is set to a very small value (10^{-12}). Thus, the *internal* numerical uncertainty in the calculated result is assumed to be most dependent upon the appropriateness of the chosen finite element mesh.

In order to determine the 'uncertainty' in the calculated results due to this mesh spacing, a finer mesh was created by doubling the number of nodes in each heater rod. This fine mesh thus contained 64 nodes per rod (32 elements per rod) and 513 nodes in the CuBE, for a total of 2561 nodes. The difference in the

calculated radiative heat transfer corresponding to the fine and implemented (nominal) mesh spacings was used in order to estimate an 'uncertainty' associated with the nominal mesh. This difference (in individual rod radiative heat rates) was found to be acceptably small (< 0.01 W/m), giving confidence in the results obtained using the nominal mesh spacing (1265 total nodes). This study is described in more detail in Chapter 9.5.

Errors which arise from sources *external* to the code itself are those due to the uncertainty inherent in the specification of the required input parameters, namely the total hemispherical emissivity of all surfaces and the associated surface temperature. These factors can produce errors which overwhelm all other sources. This is due to the fact that these values must be experimentally measured and thus may possess significant levels of uncertainty.

A complete error analysis was conducted pertaining to the RADERA code's implementation in the enclosed rod array geometry, taking into account all sources of estimated uncertainty outlined above. The details of this investigation are given in Chapter 9. It was determined in this analysis that a *conservative* uncertainty estimate in the calculation of the net radiative heat rate, for a given rod, is of the order of ± 0.1 W/m, which represents approximately 0.03% of the total array power for the cases in which radiation heat transfer was deemed most important (nitrogen backfill at high power and low pressure).

8.5 SUMMARY

In order to produce Nusselt-Rayleigh correlations applicable to spent fuel systems in transportation or storage configurations, it is vital to separate the convective heat transfer from the radiative component. This can be done experimentally or numerically; however, the experimental implementation involves significant cost and effort and may require simplifications in procedure which can sacrifice accuracy. For these reasons, a numerical approach was chosen for the present study. This approach involves the radiative modeling of a horizontal rod array using a finite element based mesh and solution procedure. The RADERA code is the result of these efforts and serves as a tool from which the radiative heat transfer on a rod-to-rod basis may be predicted, based upon experimental temperature measurements. The accuracy of the code was tested using both the enclosed rod array geometry and a concentric annulus, the latter of which has an analytical solution which is easily obtained. An error analysis indicates that the primary sources of RADERA uncertainty stem from individual input parameter uncertainty, as well as the selection of an appropriate finite element numerical mesh. However, the error analysis also indicates that for the conditions under which the code was implemented, the final uncertainty levels are within acceptable limits.